INTERFACIAL ELECTRON TRANSFER FOR SOLAR ENERGY CONVERSION: KINETIC AND MECHANISTIC INSIGHTS

Rachel E. Bangle

A dissertation submitted to the faculty at the University of North Carolina at Chapel Hill in partial fulfillment of the requirements for the degree of Doctor of Philosophy in the Department of Chemistry.

Chapel Hill
2021

Approved by:

Gerald J. Meyer

Jillian L. Dempsey

Alexander J. M. Miller

James F. Cahoon

Joanna M. Atkin

ABSTRACT

Rachel E. Bangle: Interfacial Electron Transfer for Solar Energy Conversion: Kinetic and Mechanistic Insights
(Under the direction of Gerald J. Meyer)

The ubiquity of sunlight makes solar energy a promising alternative to carbon fuels, but wide-spread applications will require solar energy storage. To this end, solar energy and earth-abundant chemical feedstocks might be converted to liquid fuels in devices termed dye-sensitized photoelectrosynthesis cells (DSPECs). This Dissertation seeks to build fundamental understandings of interfacial electron transfer (IET) reactions between molecular sensitizers and metal oxide (MOx) nanocrystals important to DSPEC optimization. Chapter 1 outlines the chemical processes involved in DSPEC operation and the semi-classical theories which describe IET.

Chapters 2 develops a novel method to sensitize MOx materials through diazonium electrografting. Diazonium-substituting Ru-bis-terpyridine sensitizers were successfully anchored to MOx surfaces through alkaline-stable, covalent bonds. Though diazonium-electrografted photoelectrodes produced small photocurrents relative to traditional anchoring groups in acidic conditions, they achieved sustained photocurrents at pH 12.

In Chapter 3, the IET mechanisms of dye-sensitized MOx core|shell materials generated through atomic layer deposition are discussed. Structural and kinetic analysis of Ru-polypyridyl-sensitized $ZrO_2|TiO_2$ and $SnO_2|TiO_2$ materials demonstrated that the rate and mechanism of IET could be controlled by the shell thickness and morphology.

Chapters 4-7 explore IET reactions in dye-sensitized transparent conducting oxides (TCOs), which exhibit metallic behavior. In Chapter 4, a TCO displayed both anodic and cathodic capabilities, as the direction of photo-initiated IET with Ru-polypyridyl or Ru-bipyrazine sensitizers was controlled by applied potentials and sensitizer excited state localization. In Chapters 5-7, Marcus-Gerischer kinetic analysis allowed quantification of IET reorganization energies (λ). This showed that for a Ru water oxidation catalyst, proton-coupled IET exhibited a 0.4 eV larger λ than did electron transfer alone (Chapter 5). Marcus-Gerischer analysis also showed λ to increase systematically with IET distance for Ru-polypyridal and tri-aryl amine complexes located at defined positions within the TCO electric double layer (EDL) by layered ionic bridges (Chapter 6). In fact, within the outer-Helmholtz plane, IET was nearly activationless ($\lambda \approx 0.1$ eV). This was attributed to electric fields in the EDL which drastically decreased the dielectric response of the polar solvents. Further, insensitivity to solvent dynamics between water, acetonitrile, methanol, and benzonitrile indicated IET was non-adiabatic, even at the smallest distances (Chapter 7).

To the mentors and friends along the way.

ACKNOWLEDGEMENTS

My grandmother, Joan Harwood Bangle, was always excited by my academic accomplishments, to a degree that in retrospect seems frankly outsized for grade school report cards. But she was so proud every time and was determined that I would be educated to the fullest extent possible. Though I didn't have the presence of mind to wonder why when I could still ask, I think now that it was the same reason that she hated "The Beverley Hillbillies" for making poor and rural people the butt of a joke. She never wanted people to have a reason to think of her as ignorant, foolish, or naïve. She instilled in me the value of education and, in some ways, taught me how to feel self-assurance and pride in your own accomplishments, and for that I would like to thank her.

Joan Bangle was the first in a long line of people that have supported my education during my childhood and adolescence to whom I owe an inexpressible debt of gratitude today. In countless small ways, my teachers and members of my church community created a fostering environment—Kelly Biggers, Donna Bowers, Ed Lipe, Mrs. Efird, and Mr. Shaw each influenced and supported me. And in much bigger ways, I would never have been able to reach the point of writing this Dissertation without my family. I cannot thank enough my mom, Teresa; my dad, Ray Jr.; and my brother John for their care, love, and unfaltering support. I am especially grateful to my mom for taking on the weight of our family hardships, both in the last few years and in the two decades prior, to allow me the space to continue learning and focusing on school. Not only in middle and high school did she unbegrudgingly give me the time to study and thrive, but also in my adult life, when she would have been

fully within her rights to ask me to come home to share the burden, she never did. She never made me feel guilty for taking the indulgence of five extra years of graduate school, she has worked incredibly diligently and generously for our family, and I am incredible grateful for the privileges that she has afforded me.

Though they have been a part of my life for less time, I also am incredibly grateful to the Waugh and Martin families, who have made me feel supported and whole-heartedly accepted over the last decade. Lisa, David, and Nancy have been there for now three graduations, and have steadily cheered me on, always expressing excitement and interest in my education and my career. I am particularly grateful to Lisa for being such a painless roommate, for sharing career advice, and for actively engaging in my scientific interests. And even more than this, I would like to thank Tyler Waugh for being my most direct and powerful source of support and comfort through the course of this Dissertation work. He has been an infinite well of kindness, patience, and love through everything, making sure that I make room for fun and joy in my life along with the work. I owe Tyler a huge thanks for the late nights and the lost weekends, for being a listening ear and a shoulder to cry on when I've needed one, and, most of all, for helping me build a vision for a future that all of this work has been leading towards.

Beyond my family and community, I would like to acknowledge and thank the scientific collaborators that have been such an integral part of this journey. I was first introduced to research by Dr. Alvin Crumbliss and Dr. Claire Siburt, who I have felt incredibly fortunate not only to count as mentors but also as friends. I would like to thank them both deeply for their time, attention, and patience as they took me on as a fledgling chemist. I have been advised in this Dissertation work by Dr. Gerald Meyer, and he has not

only been generous with his time and expertise, but has also helped me to develop as a writer, communicator, mentor, and overall scientist. I am appreciative for the scientific freedom that Jerry has allowed me and for the sense of ownership of my work that this has afforded me. I also would like to thank him for his purposeful efforts to advance my career, often above and beyond what is required of an advisor. I have also felt incredibly fortunate to work with talented scientists outside of my lab through the EFRC, especially Dr. Jillian Dempsey, who has been a thoughtful and generous mentor and collaborator.

Finally, I would like to acknowledge the lab mates that I have spent so much time with over the last five years. Being a part of this team has truly been the most rewarding part of my Dissertation work, and I want to convey to everyone how much they have impressed and touched me through the years. Though everyone who I have worked with has helped me in some way, a few people deserve special recognition. I came in in the same year as Yuting Lin and Michael Turlington. Yuting is one of the only people I have ever met who I can call unique—darkly funny without relying on memes, empathetic to a fault, creative, and resilient. I cannot say enough good things about Yuting, and I owe her so much for the time we spent together. Michael has also been a huge support through the last five years, and I couldn't ask for a nicer person to have the desk next to mine. He has been thoughtful and caring and has gone out of his way on multiple occasions to help me in rough times, and I would like to offer him a heartfelt thanks. I also owe a huge debt to two post-docs, Ludovic Troain-Gautier and Jenny Schneider, who I worked with extensively and can truly call not only mentors, but also friends. Ludo took me under his wing when I first started and taught me the passion and hard work that being a successful scientist would require. Jenny was my closest collaborator, was a delight to work with, and always pushed me to make the most of

myself. Both of them are brilliant scientists and were incredibly formative to me during my Dissertation work, and I would like to thank them. I would like to thank Erica James for her friendship and kindness, for dinners at her apartment and allowing me to be a part of her life. I would also like to thank Eric Piechota for teaching me to love electron transfer theory, for sharing his problems with me and listening to mine, and for being a much-needed distraction on long days. Matt Brady and Sara Wehlin made the lab much more socially cohesive in the time that they were here, and I thank them for that. It has been a privilege to know each of them, and I wish them all the best.

TABLE OF CONTENTS

LIST OF TABLES

LIST OF FIGURES

CHAPTER 1: INTERFACIAL ELECTRON TRANSFER FOR SOLAR ENERGY CONVERSION

1.1 Meeting Global Energy Demands

Near consensus on the need to decrease greenhouse emissions and address climate change has developed in recent years. In 2016, the United Nations Framework Convention on Climate Change signed what is commonly known as the "Paris Agreement," a multi-national strategy to hold global warming to 2 °C above pre-industrial levels.[1] This is an exigent task, as in 2019 the average global temperature was already 1 °C above the 20th century average, and projections show that continuation of the energy economy of 2000-2010 would result in > 4 °C warming by the end of the century (Fig. 1.1).[2,3] As such, the Paris Agreement outlined aggressive but necessary steps to avert the worst projected climate disasters—for global emissions to peak by 2025 and to be decreased by half by 2050.[1,4–6] To achieve these goals equitably, wealthy nations will need to move even faster, cutting greenhouse emissions a staggering 55% by 2030.[5]

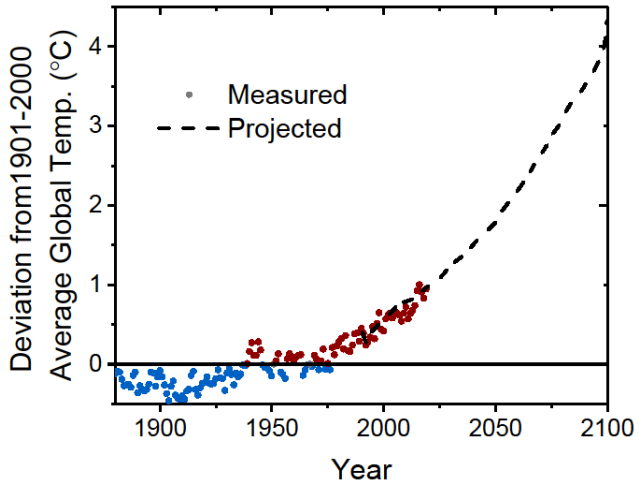

Figure 1.1. The deviation in the annual global temperature from the average temperature of the 20th century. Points are historical data. The dashed line is the projected temperature change assuming acceleration of fossil fuel use equivalent to that of 2000-2010.

While climate change mitigation necessitates rapid elimination of fossil fuels, extreme poverty eradication and global population growth will require significant energy.[7] In 2018, global energy consumption was 1.8 x 10^5 terrawatt hours (TWh), and current trends project this will likely increase 44% to ~ 2.6 x 10^5 TWh by 2050.[8] To produce this energy would require 3.3 x 10^{10} tonnes of coal in 2050 alone, which would generate 2.1 x 10^{14} lbs of CO_2, in addition to other toxins and greenhouse gases.[9] To meet energy demands and simultaneously mitigate climate change will require rapid adoption of current renewable energy technologies and development of new carbon-neutral energy generation capabilities.

1.1.1 The Case for Solar Energy

The International Energy Agency projects that achievement of the Paris Agreement goals will require significant electrification of sectors currently powered by fossil fuels. At the same time, success is predicted to require that 75% of the world's electricity be produced by renewable sources. This represents a drastic increase from the ~ 30% renewable electricity generated in 2020.[6,8] Though currently hydrothermal electricity generation accounts for the largest portion of the renewable energy supply, the abundance of solar energy presents a

clear advantage.[8] The average solar flux onto Earth is ~ 1.7 x 10^5 TW, meaning that the sun provides enough energy in a little more than an hour to meet current global energy demands for a year.[10] Capture of some portion of this energy is made possible by the maturation of silicon photovoltaic (Si-PV) devices, which generally produce solar electricity with ~ 20% conversion efficiency.[11] Governmental incentives and both public and private market investments have led to drastically lowered Si-PV manufacturing and installation costs, while technological developments have improved device lifetimes. This has made solar the fastest growing form of renewable electricity.[8,12] In fact, in many countries development of new large-scale Si-PV electricity generation is less expensive than equivalent coal or gas plants.[12]

Cost-effectiveness, however, does not necessarily mean that rapid expansion of solar energy generation is without challenges. Because photovoltaics are preeminent, captured solar energy is almost exclusively converted to electricity. Though electrification of sectors such as domestic heating and passenger transport is cost-efficient and ongoing, electrification of many industrial processes is difficult.[6] This leaves current solar energy conversion technologies, and electricity generated by any renewable source, inadequate to meet these specific demands. Further, the diurnal, seasonal, and weather-dependent sunlight fluctuations are problematic for consistent and reliable electricity generation.[13] Energy storage is required to accommodate for irregularities in solar flux, but batteries are expensive, heavy, and frequently have lifetimes shorter than Si-PVs. Instead, solar electricity could be stored by powering turbines that pump water uphill or, but impractically large volumes of water would be required daily to meet current demands.[14] A third possibility is to use solar energy not to generate electricity, but instead to drive chemical reactions to form bonds in energy-dense solar fuels, which will be discussed in the next section.[4,14–20]

1.1.2 Solar Fuels as Energy Storage

Solar fuels are inspired by natural photosynthesis, which is in fact the process that created today's fossil fuels. Visible light absorption by chlorophylls in Photosystems (PS) I and II separate charges that are vectorially transferred through electron transport chains with free energy gradients to catalytic sites that oxidize water or reduce $NADP^+$ to NADPH. The NADPH subsequently enters the Calvin cycle to produce carbohydrates with atmospheric CO_2 as the carbon source.[17] Researchers have envisioned artificial photosynthetic assemblies in which solar photons are absorbed and separated into redox equivalents that drive fuel-forming reactions and water oxidation.[4,14–20] Reduction of CO_2 to form a liquid fuel is exceptionally desirable, as carbon fuels are easily integrated into our present energy infrastructure. Both water oxidation and CO_2 reduction, however, are complex, multielectron processes that are thermally and kinetically difficult to couple with solar light absorption.

Fujishima and Honda published the first example of human-engineered solar fuels generation in 1972 (Fig. 1.2a).[21] An illuminated TiO_2 thin film electrically connected to a platinum dark cathode split water into oxygen and hydrogen gases. Hydrogen has been widely proposed as a prominent energy source in a future 'hydrogen economy'. Fujishima and Honda used ultraviolet (UV) light to initiate bandgap excitation of TiO_2 to generate valence band (VB) holes energetically competent to oxidize H_2O to O_2. The conduction band (CB) electrons were directed through an external circuit to the Pt electrode where proton reduction to H_2 occurred with a pH gradient. Since this seminal example, many other metal oxide (MOx) semiconductors have been found to act as photo-initiated water oxidation catalysts (WOCs).[17,22–25] In theory, any MOx with a VB energetically positive of the formal reduction potential of water ($E°$ = 1.23 V vs NHE at pH 0) could serve as an anode in water

splitting photoelectrosynthesis cells.[17,24] Unassisted water splitting, however, requires CB electrons that are thermodynamically capable of proton reduction. Currently, $SrTiO_3$ is the only single-material photoanode that fulfills both of these requirements.[26]

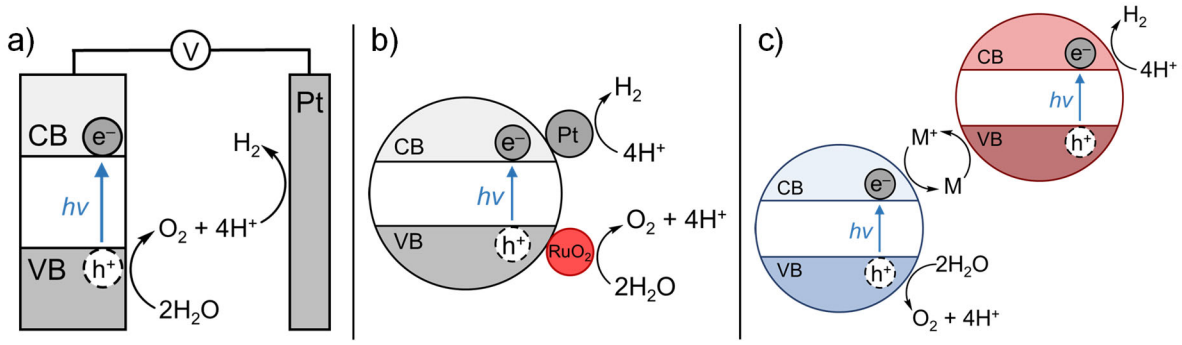

Figure 1.2. Solar fuels generation with MOx semiconductor light absorbers and WOCs. a) Photo-generated holes in a MOx VB split water while a Pt dark cathode reduces protons to H_2. b) A MOx nanoparticle is deposited with a Pt hydrogen evolution site and RuO_2, a WOC, both activated by light excitation of the MOx. c) Tandem MOx nanoparticles can exchange photo-generated holes and electrons via a redox mediator M while they split water or reduce protons.

Single MOx semiconductor photoanodes suffer, however, from the necessity that the MOx be the light absorber, electron transport medium, and catalyst simultaneously. Each process requires optimization, with sometimes conflicting demands on the MOx. As such, researchers have sought to decouple the necessary processes and optimize materials for each. In an early example, Grätzel derivatized TiO_2 nanoparticles with deposits of Pt and RuO_2, Fig. 1.2b.[27] Here again, photo-generated electrons are transported through TiO_2 to the Pt, which acts as a hydrogen evolution catalyst (HEC), while holes generated in proximity of the RuO_2 activate the WOC. Alternatively, Bard employed multiple MOx nanoparticles in a tandem architecture with a redox mediator, which separated the two catalytic half reactions.[28] These strategies spread the demands of solar fuel generation across more chemical components, yet neither attained high catalytic efficiencies. This is in part due to the reliance on MOx as light absorbers, as the large band gaps required for catalysis also necessitate high-

energy excitation.[24] For example, the anatase TiO_2 band gap is ~ 3.2 eV, which leads to a fundamental excitation at ~ 390 nm.[17,24,29] Reliance on UV absorption disregards the vast majority of the solar spectrum.

Though a few other semiconductors, such as gallium arsenide and cadmium selenide, are capable of visible light absorption, they are unstable when illuminated in aqueous solution.[24,30] As such, integration of molecular light absorbers, called sensitizers, with metal oxides represents a promising strategy to widen the wavelength range accessible for solar fuels generation.[4,14,16–18,24,31,32] The use of molecular sensitizers was prompted by flash photolysis studies of $[Ru^{II}(bpy)_3]^{2+}$, where bpy is 2,2′-bipyridine, which coupled sensitizer light absorption with electron transfer (ET).[24] Visible light excitation of $[Ru^{II}(bpy)_3]^{2+}$ promotes an electron from the Ru metal center to a ligand-localized π^* orbital. A molecular acceptor Q—often methyl viologen or similar—then quenches the excited state (ES) through ET to generate the oxidized $[Ru^{III}(bpy)_3]^{3+}$ (Eq. 1.1).[33,34]

$$[Ru^{II}(bpy)_3]^{2+} + h\nu \rightarrow [Ru^{III}(bpy)_2(bpy^{-\bullet})]^{2+*} + Q \rightarrow [Ru^{III}(bpy)_3]^{3+} + Q^- \quad (1.1)$$

Though $[Ru(bpy)_3]^{3+}$ is thermally capable of water oxidation, completion of the 4 e^- process in single electron steps is kinetically sluggish.[33,34] Further, sensitizers which are strong photooxidants or photoreductants suitable for catalysis frequently are ineffective solar light harvesters. Thus, neither MOx nor molecular sensitizers alone are adequate to efficiently generate solar fuels. Use of the two together, however, enables optimization of each process individually to alleviate the weaknesses encountered when only a single MOx is utilized.

1.2 Dye-Sensitized Solar and Photoelectrosynthesis Cells

Integration of molecular sensitizers with semiconductor electron transport materials forms the basis of modern dye-sensitization. In 1991, Grätzel and O'Regan reported the first high-efficiency dye-sensitized solar cell (DSSC) made from TiO_2 deposited on a conductive glass substrate with a trimeric ruthenium sensitizer.[17,35] Grätzel and O'Regan's key advance was the use of a mesoporous thin film composed of interconnected TiO_2 nanocrystals that increase the surface area for sensitizer binding (Fig. 1.3a). The surface areas of these thin films are about 1000 times that of a planar surface, which enables effective solar light harvesting. In a generalized DSSC, visible light excitation of the sensitizers (often Ru(II) polypyridyl complexes) generates a reducing ES, which transfers an electron to an acceptor state in the MOx (usually TiO_2) on pico- to femtosecond timescales, a process called injection.[36,37] The electrons in the MOx generate a photovoltage by raising the quasi-Fermi level towards the vacuum level. The MOx also transports injected electrons through the thin films to an external circuit where they ultimately reduce redox mediators (typically I_3^-) at a Pt electrode (Fig. 1.3b).[35,38] The Grätzel and O'Regan DSSC achieved a conversion efficiency of 7%, but optimization of the sensitizer, electrolyte, and mediator have since resulted in up to ~15% efficiencies.[17,39]

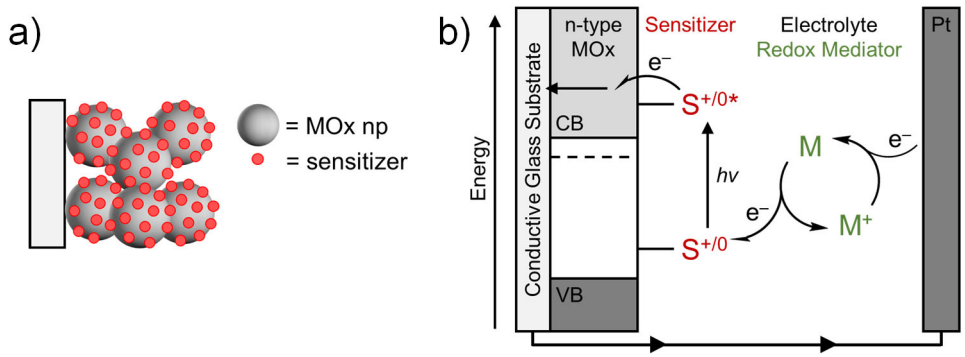

Figure 1.3. a) MOx nanoparticles form high surface area mesoporous thin films that are sensitized to visible light with surface-anchored sensitizers. b) A general depiction of a DSSC in which light excitation of a sensitizer S initiates electron injection into the MOx CB. Transport through the MOx translates electrons into an external circuit and a Pt cathode where they reduce a redox mediator M^+. M transfers an electron to S^+ to regenerate the initial redox state of the sensitizer. Energies are not to scale.

A molecular WOC can serve in place of the redox mediators in DSSCs to form dye-sensitized photoelectrosynthesis cells (DSPEC, Fig. 1.4). A common type of DSPEC splits water rather than generating electricity.[17,18,20,24,32] Sensitizer excitation causes injection as in DSSCs, but the oxidized sensitizer is regenerated by ET from a WOC. Repeated ET events accumulate oxidizing equivalents and activate the WOC to oxidize water to O_2. The injected electrons and protons are utilized at a Pt electrode for proton reduction to yield H_2 gas (Fig. 1.4a). Dye-sensitized water splitting remains inefficient, < 1% under AM 1.5 solar illumination, but Faradaic efficiencies for both H_2 and O_2 formation can exceed 50%.[40–46]

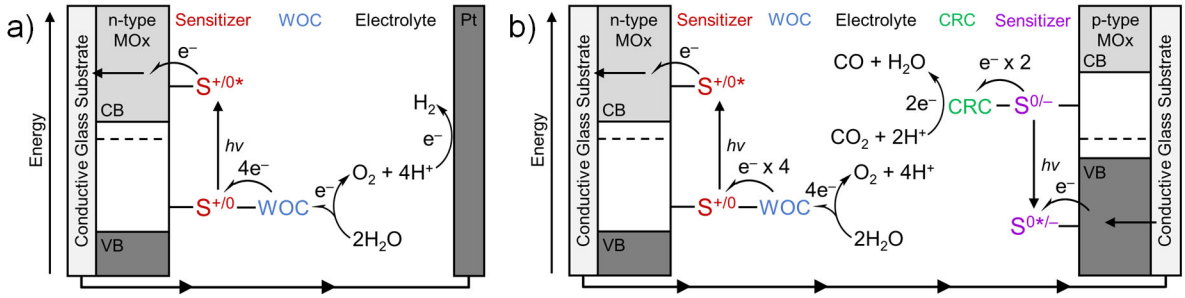

Figure 1.4. a) A DSPEC in which sensitizer excitation results in electron injection. Transport through the MOx to an external circuit and a Pt electrode where protons are reduced to H_2. ET from a WOC regenerates the initial sensitizer state and collects oxidizing equivalents that activate the WOC. b) A tandem DSPEC in which the Pt electrode is replaced by a dye-sensitized photocathode. Sensitizer excitation results in an ES that accepts an electron from the VB of the MOx. Subsequent ET events activate a CRC. Energies are not to scale.

In tandem DSPECs, dye-sensitized water oxidation photoanodes are paired with dye-sensitized photocathodes which use light to perform CO_2 (or other) reduction reactions (Fig. 1.4b).[4,20,24,47,48] At the dye-sensitized photocathode, sensitizer excitation generates an ES which accepts an electron from the VB of the MOx. The electrons on the reduced sensitizer are funneled through subsequent ET events to a CO_2 reduction catalyst (CRC). The activated CRC transforms CO_2 to CO or, preferably, to more reduced, higher-nuclearity carbon fuels. The use of two photons in the tandem DPSEC may one day enable the generation of liquid carbon-based fuels that are more valuable than H_2.

The DSSCs and DSPECs operate through a cumulative series of excitation, interfacial electron transfer (IET), electron transport, and intermolecular electron transfer steps. Each of these reactions have specific chemical and physical demands, which provide a myriad of ways in which the solar cell performance can be tuned and optimized. In the remainder of this section, the chemistry and physics of the essential DSPEC components will be discussed with a focus on efficiency and longevity.

1.2.1 Metal Oxide Electrodes

Though the earliest solar fuels generation utilized only MOx semiconductors,[21] it is widely thought that separate light absorbers, electron transport materials, and catalysts individually optimized for their own tasks will ultimately result in higher efficiencies. This removes some burden from the MOxs, which serve primarily as electron donors/acceptors and electron transport materials. Electron transport physically separates photo-generated holes and electrons and lengthens the lifetimes of charge separated states. Several properties of MOx electrodes are necessary for high efficiency: 1) large surface areas to anchor sensitizers and optimize solar light harvesting, 2) a sufficient density of redox-active states energetically aligned with the sensitizer excited state reduction potential ($E^{\circ\,+/0*}$) to allow IET, and 3) high electron mobility for rapid electron transport through the MOx and away from the interface. Additionally, high MOx transparency in the visible region is desirable for spectroscopic analysis in a transmission mode.

Transparency to visible light requires a band gap ≥ 3.2 eV.[24] This includes a great many MOx materials from which highly transparent, high surface area nanocrystalline films have been successfully prepared.[17,25] These nanocrystalline thin films are typically produced by doctor blading colloidal sol-gel suspensions of MOx nanoparticles onto a conductive substrate. Special care is taken to prevent nanoparticle aggregation and thus light scatter within the films. After doctor-blading, the films are annealed at high temperatures to sinter nanoparticles and oxidize away organic polymer additives. The film thickness and porosity (frequently 40–60% by volume), as well as nanoparticle diameter, are readily controllable and determine the overall surface area.[49] Monolayer surface coverages of molecular species

on these films generally correspond to ~ 10^{-7} – 10^{-8} mol cm^{-2}, which allows for significant absorption of visible light even for sensitizers with low extinction coefficients.[24,49–53]

Photoanodes are constructed from n-type MOxs, for which electrons are the primary free carriers, while photocathodes are constructed from p-type MOxs, for which holes are the primary free carriers.[54,55] To date, p-type MOx materials have largely been limited to NiO. Dye-sensitized NiO solar cells, however, are highly inefficient, behavior attributed to slow hole transfer and a high defect density.[56–62] Explorations of new p-type materials for dye-sensitized photocathodes are ongoing, and Chapter 4 of this Dissertation provides a possible alternative class of materials that might serve in place of p-type MOx as photocathodes.

The use of n-type MOx semiconductors, however, is much better characterized and is historically far more successful. Many MOx semiconductors have been explored as dye-sensitized photoanodes, but by far the best studied are TiO_2, SnO_2, and ZnO. Not only was the anatase polymorph of TiO_2 the first MOx employed for dye-sensitized photoanodes, but it has also performed most optimally in DSSC applications.[63] Interest in ZnO stems from its electronic similarity to TiO_2. The two materials have virtually identical CB edges, E_{CB}, positive on an electrochemical scale of common sensitizer $E°\ S^{+/0}*$ values.[17,25,63–67] For SnO_2, the E_{CB} is even more favorable, reported to be ~ 0.5 V more positive than that of TiO_2 (Fig. 1.5a).[63,64,68–70] The value of E_{CB} relative to $E°\ S^{+/0}*$ has been used to define the driving force for injection, and the larger driving force for dye-sensitized SnO_2 is reflected in more rapid kinetics and higher injection yields from sensitizers that are weak excited state reductants.[63–65] Further, high electron mobilities in ZnO and SnO_2 lead to rapid charge transport, which one would expect to extend the lifetimes of charge separated states.[63,71,72] Despite this, however, TiO_2 is still the champion DSSC material.

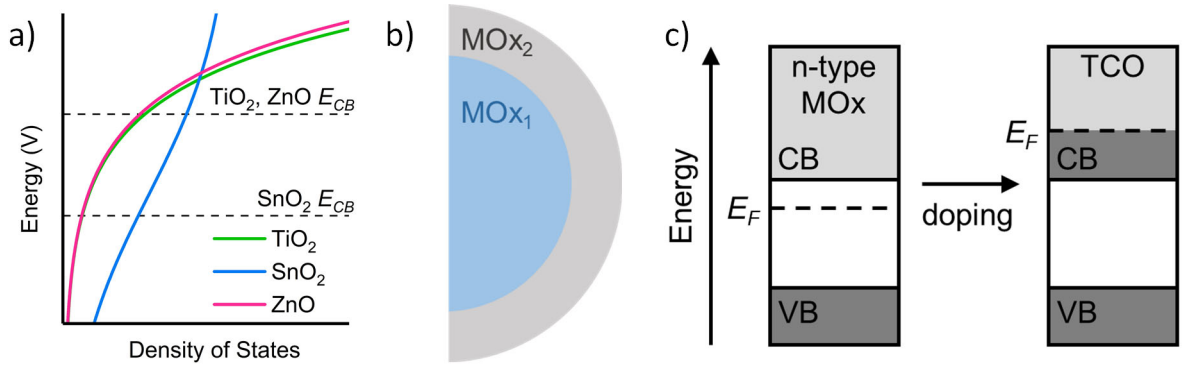

Figure 1.5. a) The density of acceptor states in TiO_2, SnO_2, and ZnO, where the states below E_{CB} have been assigned as trap states. b) Core-shell nanostructures with an MOx_1 core and a MOx_2 shell. c) The position of the Fermi level E_F in a n-type semiconductor and a transparent conducting oxide (TCO).

These MOx materials are also frequently thought to contain trap states—localized redox-active states in the band gap identifiable in electrochemical experiments (Fig. 1.5a).[66–69,73,74] These localized states have been invoked as the main determinant of photo- and electrochemical behavior of MOx materials for applications in DSSCs.[75–79] In a commonly accepted mechanism, after excited state injection, the electrons relax from the CB into lower-energy trap states. Then thermally-activated escape from these states either into the CB or into nearby traps is required for either electron transport or transfer.[70,80–83] The possibility of multiple trapping/detrapping events has been invoked in kinetic models to account for non-exponential electron transport and electron transfer kinetics in nanocrystalline TiO_2, though the physical origins of these kinetics are not definitively known.[82,84] Trap states are thus frequently thought to be important in defining the lifetimes of photo-generated charge separated states in DSSCs and DSPECs.

One strategy to improve MOx materials is to generate more complex nanostructures. An important example is a "core|shell" architecture, in which a MOx nanocrystalline thin film is coated through atomic layer deposition (ALD) with another MOx (Fig. 1.5b), the morphology of which is controlled by post-deposition heat treatments.[85–88] The ALD layer

serves to passivate surface trap states and can instantiate a physical and energetic barrier to recombination in the photo-generated charge separated state.[20,89–97] With these enhancements, DSPECs composed of SnO_2|TiO_2 core|shell materials oxidize water more efficiently than those made of either SnO_2 or TiO_2 alone.[42,93] Efforts to elucidate the effects of ALD layers on the mechanism of IET from the MOx to a molecule are detailed in Chapter 3 of this Dissertation.

A final class of useful MOx materials are transparent conducting oxides (TCOs) such as tin-doped indium oxide (Sn:In_2O_3, ITO), aluminum-doped zinc oxide (Al:ZnO, AZO), and fluorine-doped tin oxide (F:SnO_2, FTO). In these materials, n-type doping raises the Fermi level (E_F) of the into the CB (Fig. 1.5c). Moderate doping (5-10%) results in free carrier densities in excess of 10^{21} cm^{-3}, which leads to high electron mobility; low, temperature dependent resistivity; and an infrared localized surface plasmon resonance.[98–100] The TCOs thus behave electrically like a metal while still maintaining high transparency to visible light. Though TCOs have historically been utilized for spectral and electrochemical analysis of dye-sensitized electrodes, their high density of carriers results in very small dye-sensitized photovoltages and hence low power conversion efficiencies. Recently, however, interest in TCOs for DSSCs has been piqued by reports that TCOs can serve as either photoanodes or photocathodes (see Chapter 4) and can generate long-lived photoinduced charge separated states.[57,101–103] Further, the metallic behavior of TCOs allows experimental control of the IET driving force, which allows fundamental kinetic studies that have been utilized in Chapters 5-7 of this Dissertation.[104,105]

1.2.2 Surface-Anchoring Strategies

The transparency of the MOx to visible light necessitates sensitizers capable of excited state interfacial electron transfer with the MOx. To concentrate sensitizers at the MOx/electrolyte interface and encourage IET, sensitizers are generally chemically anchored to the MOx surface. Additionally, molecular WOCs and CRCs must be localized near the sensitizers to be efficiently activated. As such, strategies to stably anchor molecular species to MOx surfaces are vital to DSSC and DSPEC performance. Sensitizers are generally anchored through appended functional groups, often substituents at the 4,4′ positions of a 2,2′-bipyridine.[106] The most commonly utilized substituents are carboxylic and phosphonic acids, which are proposed to form dative bonds with the metal ions in the MOx (Fig. 1.6).[107–109] Evidence from IR spectra suggest that both carboxylic and phosphonic acids likely anchor in a bidentate fashion, though binding modes have not been conclusively established.[106] Though carboxylic and phosphonic acids are stable in a wide range of organic solvents, they are vulnerable to hydrolysis in neutral or alkaline aqueous electrolytes. Carboxylic acid anchors are especially unstable and desorb within minutes in pH $\geq$ 4 solutions.[106,110,111] Phosphonic acid anchors are stable at pH < 7, but they are still not suitable for the alkaline conditions desirable for water oxidation.[24] Recently, silatrane and hydroxamic acid groups (Fig. 1.6) have stably anchored sensitizers in a wide range of aqueous solutions, pH 2-11.[106,112,113] Though they have not yet been well characterized, these groups may present important advances in DSSC and DSPEC surface anchoring. The electrografting of diazonium-functionalized sensitizers to form alkaline-stable covalent bonds with a variety of MOx materials is reported in Chapter 2 of this Dissertation.

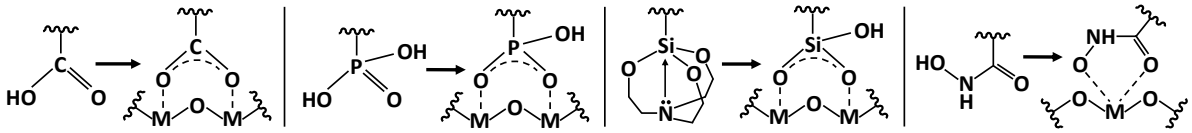

Figure 1.6. Substituents commonly employed as sensitizer anchors and likely anchoring modes on an MOx surface suggested from IR spectroscopy.

Sensitizer anchors also influence DSSC and DSPEC performance by establishing electronic coupling between the sensitizer and MOx. Large coupling, which promotes rapid IET, results from orbital delocalization from the sensitizer onto the anchoring group.[106] Experimental comparisons of injection yields and rate constants give insights into relative sensitizer/MOx coupling through carboxylic, phosphonic, and hydroxamic acids.[112,114,115] Excited state injection rate constants were measured to be more than twice as large when sensitizers were anchored through carboxylic versus phosphonic acid.[114] The sp^3-hybridized P atom in the phosphonic acid disallows orbital delocalization onto the anchor, and as such sensitizer/MOx coupling is small. The opposite is true for the sp^2-hybridized carbon in carboxylic acid. Injection rate constants have not to my knowledge been measured for hydroxamic acid-anchored sensitizers, but they have similar injection yields to carboxylic acid-anchored sensitizers.[112,115] This suggests hydroxamic acids also generate relatively large sensitizer/metal oxide coupling. Injection yields and rate constants for silatrane-anchored sensitizers have yet to be established.

Catalysts are sometimes co-anchored to MOx surfaces alongside sensitizers, but the demands of catalyst anchors differ. Where anchored sensitizers should promote excited state IET with a large electronic coupling, anchored catalysts should promote intermolecular ET between the catalyst and sensitizer. In fact, IET between MOx and catalysts represents a major deactivation pathway.[24] As such, catalysts are often anchored to the sensitizer rather than to the MOx itself either through synthesis of covalent sensitizer-catalyst assemblies or

through van der Waals interactions between hydrophobic groups on both molecular species.[17,18,24,32,116]

1.2.3 Sensitizer Excited State Photophysics

Sensitizer development has focused extinction coefficient optimization over large spectral ranges, especially in the red and near IR regions. Several classes of molecular sensitizers, reviewed by Hagfeldt, *et. al*,[10] have become prominent. Porphyrins, phthalocyanines, and a variety of conjugated organic molecules have been successfully utilized to sensitize MOx, but metal complexes, which frequently exhibit metal-to-ligand charge transfer (MLCT) absorbances in the visible region, are most common. Coordination complexes of Fe, Re, Cu, Os, and Pt have been used as sensitizers, but Ru coordination complexes have been studied most extensively. Ruthenium(II) complexes with bipyridine, terpyridine, heterocyclic, or phenanthroline ligands exhibit MLCT transitions in the visible region with extinction coefficients generally on the order of 10^4 M^{-1} cm^{-1}.[10,34,117] Though Ru-based sensitizers exhibit limited absorbance in the near-IR, careful ligand design has led to a number of panchromatic Ru sensitizers, most notably those with thiocyanate ligands.[10,118–120]

Sensitizers must also be energetically competent to undergo ES interfacial electron transfer with the MOx CB (or VB) to generate a charge-separated state (Eq. 1.2).

$$\mathrm{MOx|–S} + h\nu \rightarrow \mathrm{MOx|–S^*} \rightarrow \mathrm{MOx(e^-)|–S^+} \quad \text{(anode)} \qquad (1.2)$$
$$\rightarrow \mathrm{MOx(h^+)|–S^-} \quad \text{(cathode)}$$

The oxidized/reduced sensitizers must then be energetically appropriate for regenerative ET with the catalyst or redox mediator. These thermodynamic demands are often contrary to the need to absorb visible and near-IR light, however. At a photoanode, for example, excited state injection requires the sensitizer $E°\ S^{+/0*}$ be more negative on an electrochemical scale

than E_{CB}, which for TiO_2 is -0.1 V vs NHE at pH 0 with a -59 mV/pH shift as the electrolyte is made more alkaline.[24] Because $E°\ S^{+/0}*$ is related to the sensitizer ground state reduction potential, $E°\ S^{+/0}$ through the free energy stored in the excited state, ΔG_{ES} (Eq. 1.3), injection is promoted by a small or negative $E°\ S^{+/0}$ and a large ΔG_{ES}.

$$E°\ S^{+/0}* = E°\ S^{+/0} - \Delta G_{ES} \quad (1.3)$$

Successful regeneration, however, requires that the sensitizer $E°\ S^{+/0}$ be more positive than the reduction potential of the WOC or the redox mediator. Further, a large ΔG_{ES}, requires high energy photons, in clear conflict with the desire for visible and near-IR absorption.[24] As such, sensitizers must balance energetic and light absorption requirements.

1.2.4 Water Oxidation and CO_2 Reduction Catalysts

In DSPECs, oxidized or reduced sensitizers are regenerated through ET with a WOC or CRC (Eq. 1.4). Repeated photon absorption and regenerative ET then serves to build oxidizing or reducing equivalents and activate the catalysts.

$$MOx(e^-)|–S^+–WOC \rightarrow MOx(e^-)|–S–WOC^+ \quad \text{(anode)} \quad (1.4)$$

$$MOx(h^+)|–S^-–CRC \rightarrow MOx(h^+)|–S–CRC^- \quad \text{(cathode)}$$

Charge recombination (see below) limits DSPEC efficiency, as both water oxidation and CO_2 reduction are kinetically slow relative to the unwanted recombination. This manifests as relatively small turn-over frequencies (TOFs) for many WOCs and CRCs.[16–19,24] Because water oxidation is mechanistically complex yet very important, much research has focused on the individual steps in the composite mechanism and the identification of structure-function relationships. Ruthenium-based WOCs have been the most studied, though Ir-, Co-, and Fe-centered catalysts have also been successful.[18] In general, transition metal-based WOCs accumulate oxidizing equivalents to generate high-valent metal oxo (M=O)

intermediates that have been proposed to initiate O–O bond formation. Both nucleophilic water attack on the M=O bond and the coupling of two M=O in a radical-like reaction have been proposed.[18] Mechanistic studies have allowed significant progress since the first molecular WOC was reported in 1982—a μ-oxo bridged dinuclear Ru complex known as the "Blue Dimer" with a turn-over number (TON) of 13 and a turn-over frequency (TOF) of 0.0042 s^{-1}.[121] The most successful catalysts in use today are Sun-type catalysts based on a single-site Ru complex with a 2,2′-bipyridine-6,6′-dicarboxylate ligand.[122] For select examples of these WOCs, turn over numbers (TONs) greater than 100,000 and TOFs > 1000 s^{-1} have been reported.[18,123] The kinetic influence of proton involvement in WOC ET reactivity is addressed in Chapter 5 of this Dissertation.

Numerous CRCs have also been reported since the 1970s, frequently transition metal complexes with macrocyclic or porphyrin ligands.[18,124,125] Development of molecular CRCs has strived not only to improve stability, TOF, and overpotential, but also to enable selectivity, as CO_2 reduction can lead to multiple products (CO, formate, oxylate, alcohols, alkanes, etc.). In addition, CO_2 reduction is often kinetically competitive with proton and/or O_2 reduction. CRCs with first-row, earth-abundant metals are known to be stable and efficient. A notable example is an Fe-porphyrin catalyst that reduces CO_2 to CO with Faradaic efficiencies > 90%, TOF > 1,000,000 s^{-1}, and no observable degradation over days.[126,127] From these highly successful catalysts, current efforts focus on catalysis that yields higher-value carbon products.

1.2.5 Productive and Detrimental Electron Transfer Events

It is thus clear that DSPEC operation requires a daunting number of chemical processes, illustrated for a photoanode in Fig. 1.7: 1) sensitizer excitation, 2) excited state

injection, 3) electron relaxation into MOx trap states, 4) electron transport through the MOx, 5) sensitizer regeneration, and 6) catalysis. These productive steps, however, compete kinetically with detrimental pathways which limit efficiency.[10,24,128] Generation and maintenance of charge-separated states for the long timescales required for catalysis can fail due to a) ES decay, b) back electron transfer (BET), and c) charge recombination (CR).

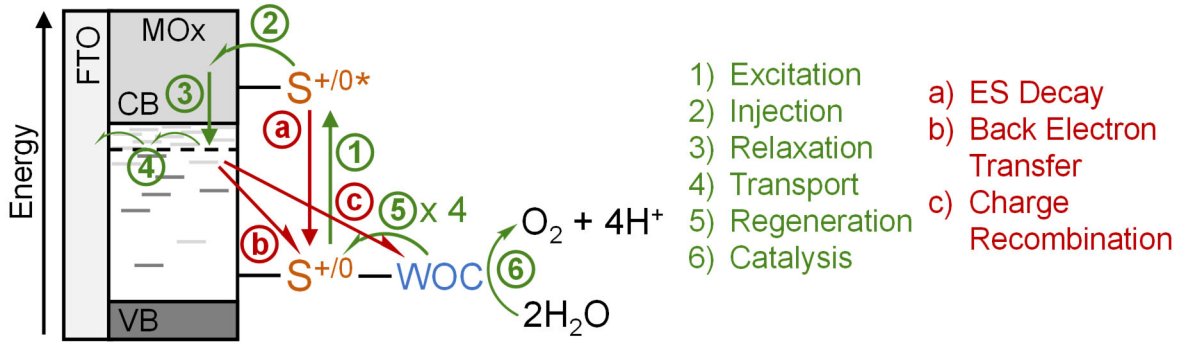

Figure 1.7. Productive (green) and detrimental (red) processes in DSPEC photoanode function. Energies are not to scale.

A generalized DSSC which utilizes TiO_2 sensitized with Ru-polypyridyl light absorbers and the iodide/iodine couple as a redox mediator provides a useful illustration of how these detrimental processes can limit efficiency. For Ru-polypyridyl sensitizers, excited state decay generally occurs on nanosecond timescales, which competes kinetically with femto- and picosecond injection and can limit the injection yield. After injection, the oxidized sensitizer is then susceptible to BET with the electron in the TiO_2 (Eq. 1.5).

$$MOx(e^-)|–S^+ \rightarrow MOx|–S \quad (1.5)$$

This BET competes kinetically with regeneration with iodide, both of which occur on micro- to millisecond timescales. After regeneration, the charge separated state comprised of the reduced TiO_2 and the oxidized mediator is susceptible to CR on the microsecond to second timescales (Eq. 1.6).

$$MOx(e^-)|–S + M^+ \rightarrow MOx|–S + M \quad (1.6)$$

This CR is a particularly potent threat in DSPECs which utilize catalysts rather than redox mediators, as catalysis requires multiple redox equivalents and frequently occurs over seconds. Deceleration and minimization of these detrimental processes, especially BET and CR, are important to DSPEC efficiency.

1.3 Electron Transfer Kinetics

At the heart of DSSC and DSPEC operation are two interfacial electron transfer reactions: productive excited state electron/hole injection to generate a charge-separated state and detrimental recombination of separated holes and electrons. The rates of these IET reactions are important determinants of the overall yields, and as such to understand and control them is crucial for DSSC and DSPEC optimization. Further, IET between MOx nanoparticles and surface-anchored sensitizers is of fundamental interest, as surface attachment generates unique reaction environments that affect kinetic parameters.[54,129] Fundamental theories to predict the rate constants for IET have been developed from analogous inter- and intramolecular electron transfer theories.

1.3.1 Marcus Theory

Inter- and intramolecular ET alter bond lengths and solvent structure, which changes potential energy. This fundamental assertion is a starting point for transition state theory, in which chemical reactants and products represent minima on a potential energy surface (PES). Conversion of reactants to products thus requires crossing a saddle point, which represents a transition state, in the multi-dimensional surface. The energy input to move from the reactant minimum to the transition state, called the Gibbs free energy of activation ($-\Delta G^{\ddagger}$), then dictates the rate constant and equilibrium constant for the reaction. Though the historical

development of transition state theory through the late 19th and early 20th centuries was tremendous, the modern semi-classical expression (Eq. 1.7) was developed by Rudolph Marcus in the 1950s.[130,131]

$$k_{ET} = \frac{2\pi}{\hbar}|H_{ab}|^2 \frac{1}{\sqrt{4\pi\lambda k_b T}} \exp\left(-\frac{(\lambda+\Delta G°)^2}{4\lambda k_b T}\right) \quad (1.7)$$

This expression describes the ET rate constant, k_{ET}, in terms of three physical parameters: the Gibbs free energy change of the reaction ($\Delta G°$), colloquially called the driving force ($-\Delta G°$); the electronic coupling between the donor and acceptor wave functions (H_{ab}); and the reorganization energy (λ).[129–135]

In the Marcus picture of electron transfer, the multi-dimensional reaction PES is simplified to two parabolas, one that describes the reactant and the other that describes the product, which represent harmonic oscillators (Eq. 1.8 and 1.9, Fig. 1.8a).

$$G_R = \frac{1}{2} f X^2 = \lambda X^2 \quad (1.8)$$

$$G_P = \frac{1}{2} f (X-1)^2 + \Delta G° = \lambda (X-1)^2 + \Delta G° \quad (1.9)$$

Here, G_R and G_P are the Gibbs free energies for the reactant and product, respectively; X is the nuclear configuration of the bonds and solvent; and f is the Hooke's Law force constant, equivalent in Marcus Theory to 2λ. The fundamental kinetic parameters in Eq. 1.7 can then be mapped onto these parabolas (Fig. 1.8a).

The free energy difference between the reactant and product PES minima shows $\Delta G°$. This is typically measured experimentally by the difference in the donor and acceptor reduction potentials. Electronic coupling H_{ab} is illustrated by mixing of the two parabolas at the reactant/product intersection. Values of H_{ab} are defined by the distance between the donor and acceptor (R), the innate coupling ($H_{ab}°$) when the donor and acceptor are at the van der

Waals separation ($R°$), and a decay parameter (β) dependent on the intervening medium (Eq. 1.10).

$$H_{ab} = H_{ab}° \exp\left(-\frac{\beta}{2}(R - R°)\right) \quad (1.10)$$

The height of the cusp at the reactant/product intersection which must be crossed at the instant of thermal ET is $\Delta G^{\ddagger}$. This is defined in terms of the other Marcus parameters (Eq. 1.11).

$$\Delta G^{\ddagger} = \frac{(\Delta G° + \lambda)^2}{4\lambda} \quad (1.11)$$

Finally, the free energy difference between the reactant and the product PES at the nuclear configuration of the reactant minimum defines λ (Fig. 1.8).[130,131] Physically, this is the energy stored in the destabilized solvent and bonds of the Frank-Condon state, dictated by the Born-Oppenheimer approximation to occur upon instantaneous light-inducted ET. Some energy λ is then required to alter the bond lengths and reorient the solvent molecules in response to the change in charge distribution upon ET.

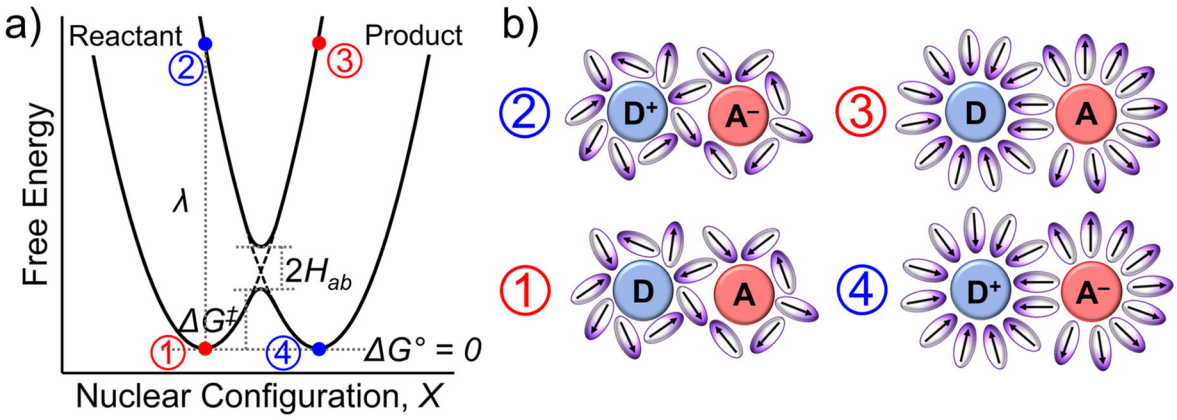

Figure 1.8. a) Reactant and product PESs for a self-exchange reaction as described by Marcus Theory. The parameters $\Delta G°$, λ, H_{ab}, and $\Delta G^{\ddagger}$ are indicated. b) Points marked on the reactant (red) and product (blue) PES correspond to particular bond and solvent configurations for the reactant and product minima (1 and 4) and the Frank-Condon states upon reactant or product excitation (2 and 3).

The total reorganization energy is often taken as a sum of inner-sphere (λ_i) and outer-sphere (λ_o) components such that $\lambda = \lambda_i + \lambda_o$. The inner-sphere component arises because bond length displacements accompany electron transfer. The energy of a given bond *j* with force constant f_j is described by Hooke's law, and the total λ_i is the summation of the energy change across all bonds (Eq. 1.12).

$$\lambda_i = \frac{n}{2}\sum_j f_j\,(l_P - l_R)^2 \tag{1.12}$$

Here *n* is the number of bonds, and l_P and l_R are the product and reactant bond lengths.[130,131] The outer-sphere component arises from the solvent dielectric response to changes in charge distribution upon ET (Eq. 1.13).[130,131,136]

$$\lambda_o = \frac{e^2}{4\pi\varepsilon_0}\left(\frac{1}{2r_D} - \frac{1}{2r_A} + \frac{1}{R}\right)\left(\frac{1}{\varepsilon_{op}} - \frac{1}{\varepsilon_{st}}\right) \tag{1.13}$$

Here, *e* is the elementary charge, ε_{op} and ε_{st} are the optical and static dielectric constants, and r_D and r_A are the donor and acceptor radii. Values of λ_i tend to be small without Jahn-Teller or other distortions in the transition state, and thus λ_o often dwarfs λ_i ($\lambda \approx \lambda_o$).

One of the most salient and unexpected features of Marcus Theory is the parabolic dependence of $\Delta G^{\ddagger}$ and k_{ET} on driving force, $-\Delta G°$, to produce three distinct kinetic regimes (Fig. 1.9a).[130,131,133] When $-\Delta G° < \lambda$, called the normal region, , k_{ET} is predicted to increase with $-\Delta G°$. A k_{ET} maximum is reached in the activationless region when $-\Delta G° = \lambda$ and $\Delta G^{\ddagger} = 0$. Significantly, when $-\Delta G° > \lambda$ the magnitude of k_{ET} is predicted to decrease with driving force to result in what is often called the Marcus inverted region. The experimental realization of inverted electron transfer kinetics by Closs and Miller (Fig. 1.9b) cemented Marcus's work as the foundation of modern ET Theory.[137] Notably, however, the observed decay of k_{ET} in the inverted region was less steep than predicted by Eq. 1.7. In the Closs-Miller experiment, when $-\Delta G°$ was large, coupling between vibrational excited states of the

acceptor and the donor wave function allowed quantum tunneling through the activation barrier. A quantum mechanical expression which sums over all vibrational modes (ω) in a Frank-Condon weighted density of states (Eq. 1.14) accounted for this tunneling and adequately modelled the experimental data.[133,134,137]

$$k_{ET} = \frac{2\pi}{\hbar}|H_{ab}|^2 \frac{1}{\sqrt{4\pi\lambda k_b T}} \sum_{\omega=0}^{\infty} \frac{e^{\frac{-\lambda_i}{h\nu}} \frac{-\lambda_i}{h\nu}^{\omega}}{\omega!} \exp\left(-\frac{(\Delta G° + \lambda_i + \omega h\nu)^2}{4\lambda k_b T}\right) \quad (1.14)$$

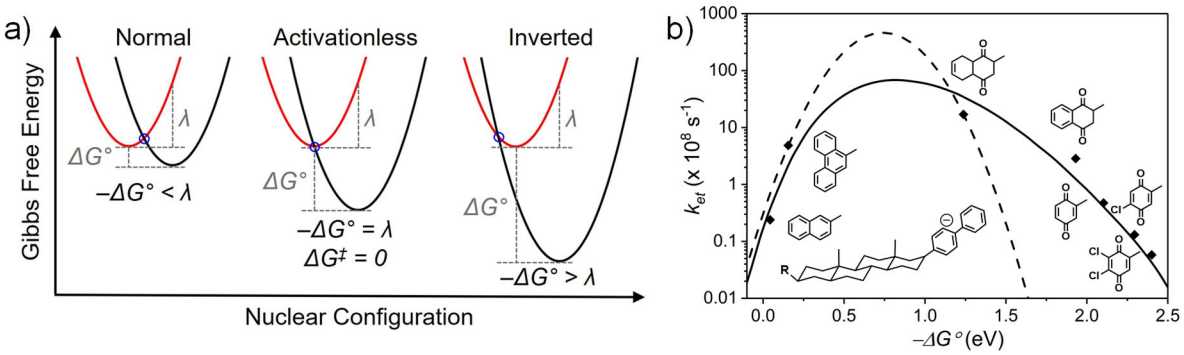

Figure 1.9. a) PES with constant λ and negligible H_{ab} illustrate the parabolic dependence of $\Delta G^{\ddagger}$ on $-\Delta G°$, which divides ET into three regions. b) The first experimental observation of inverted kinetics for intramolecular ET in the pictured donor-bridge-acceptor molecules (ref. [137]). The acceptor identity, pictured for each data point, tuned $-\Delta G°$. The dashed parabola shows a fit to Eq. 1.7, while the solid curve shows a fit to Eq. 1.14.

1.3.2 Adaptation of Marcus Theory for Interfacial Electron Transfer

Because the three fundamental Marcus parameters suggest predictable kinetic responses, they are valuable to control electron transfer kinetics both in solution and at interfaces. For instance, in DSPECs catalysts are frequently positioned far from the MOx surface to minimize H_{ab} and limit charge recombination.[24,102,116] Precise control of λ and H_{ab}, however, necessitates that they be experimentally measured. Because donor and acceptor reduction potentials can be controlled with substituents, experiments in which $-\Delta G°$ is systematically tuned are often used to determine λ and H_{ab} for intra- and intermolecular ET.[137–139] These experiments are complicated for interfacial electron transfer is DSSCs and DSPECS, however, as values of $-\Delta G°$ are often ambiguous for reactions with defect-rich,

nanocrystalline MOx semiconductors.[84,140–146] In the absence of defect states, $-\Delta G°$ for IET from a semiconductor MOx donor to a molecular acceptor with a formal reduction potential $E°'$ that lies with the forbidden bandgap is defined by $-\Delta G° = eE°' - E_{CB}$. In practice, however, estimates of E_{CB} often rely on reported flat band potentials for MOx single crystals which may not be equivalent to nanocrystalline materials. This also discounts the possibility that low-energy MOx trap states are involved in IET. As such, Marcus analysis of IET with traditional semiconducting metal oxides has seen limited success.

Values of $-\Delta G°$ are better defined for IET reactions between molecular species and conductive electrodes. For a conductive electrode donor and a molecular acceptor, $-\Delta G°$ is determined by the molecular $E°'$ and the electrode Fermi level (E_F) which is in turn controlled by an externally applied potential (E_{app}) (Eq. 1.15).

$$-\Delta G^o = eE°' - E_F = e\left(E°' - E_{app}\right) \quad (1.15)$$

This is the basis for voltammetry experiments, in which E_{app} predictably initiates electrochemical reduction or oxidation of a molecular species at a conductive electrode.[54] Interfacial electron transfer reactions, however, are fundamentally different than intra- and intermolecular ET reactions described by Marcus Theory. Within a conductive electrode, a continuum of redox-active states exist that may act as an electron donor or acceptor, and IET can occur from a range of states within the continuum. For example, in the case of an electrode donor and a molecular acceptor, individual IET events can occur from the highest-energy occupied electrode state at the Fermi level ($\rho(E_F)$) and from the occupied states in the continuum below. In analogy to Marcus Theory, each state in the continuum can be conceptualized as a reactant PES (Fig. 1.10a), and IET from each state proceeds with a rate constant determined by an individual barrier. The observed interfacial electron transfer rate

constant (k_{IET}) reflects a summation of these individual IET events across the electrode continuum as expressed by Marcus-Gerischer Theory (Eq. 1.16).[54,147–151]

$$k_{IET} = \frac{2\pi}{\hbar} H_{ab}^2 \int_{-\infty}^{\infty} \rho(E) f(E, E_F) W(E) dE \quad (1.16)$$

Here, H_{ab} is the electronic coupling between the electrode and molecular species, $\rho(E)$ is the density of the electrode states, $f(E,E_F)$ is the Fermi-Diraac distribution that describes the occupancy of the electrode states relative to E_F, and $W(E)$ is the activation barrier for IET from each state.[54,147–152] Values of $W(E)$ form a Gaussian distribution relative to the molecular $E°'$ (Eq. 1.17) equivalent to the activation term in the semiclassical Marcus expression.

$$W(E) = \frac{1}{\sqrt{4\pi\lambda k_B T}} \exp\left(\frac{-(\Delta G°(E)+\lambda)^2}{4\lambda k_B T}\right) \quad (1.17)$$

The overall k_{IET} is thus determined by the energetic overlap between $\rho(E)f(E,E_F)$ and $W(E)$, often depicted as in Fig. 1.10b, where the electrode continuum of states is shown on the left, occupied states are denoted in gray, and the $W(E)$ distribution is shown on the right.

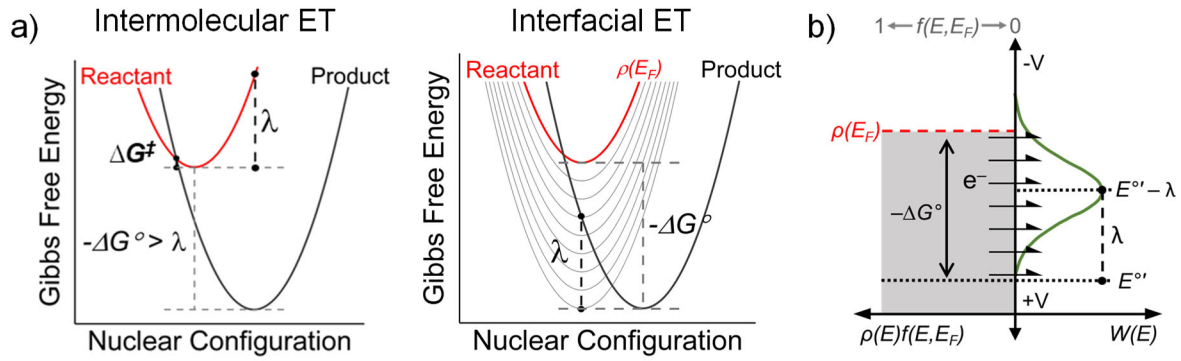

Figure 1.10. a) Marcus Theory for intermolecular (left) and interfacial (right) ET with equivalent $-\Delta G°$ and λ. H_{ab} is small in both cases. The continuum of electrode states involved in IET is shown as nested PESs, each with $\Delta G^{\ddagger}$ dictated by its intersection with the product PES. The Fermi level state is represented as $\rho(E_F)$. b) A depiction of Marcus-Gerischer Theory which illustrates the energetic overlap between the electrode states $\rho(E)f(E,E_F)$ and $W(E)$, the distribution of IET activation energies. $W(E)$ is positioned relative to the molecular $E°'$, and its width is defined by λ. Single-headed arrows show IET reactivity.

Like the semiclassical Marcus expression, $W(E)$ is maximized when $-\Delta G° = \lambda$. However, Marcus-Gerischer Theory predicts a quite different kinetic response to $-\Delta G°$ than does Marcus Theory. Because it is proportional to the integral of $W(E)$, k_{IET} is sigmoidal with $-\Delta G°$, and $-\Delta G° = \lambda$ represents the inflection point of the curve (Fig. 1.11). This means that though k_{IET} growth decelerates with $-\Delta G°$ when $-\Delta G° > \lambda$, no inverted region is predicted. Instead, k_{IET} continues to increase until the overlap of $\rho(E)f(E,E_F)$ and $W(E)$ is unity— when $-\Delta G° > 2\lambda$. Under these conditions, k_{IET} reaches a maximum attainable value (k_{IET}^{max}) defined by H_{ab} (Eq. 1.18).

$$k_{IET}^{max} = \frac{2\pi}{\hbar} {H_{ab}}^2 \rho \tag{1.18}$$

This expression assumes that $f(E,E_F)$ is in the low-temperature limit and that $\rho(E)$ is independent of energy. Substitution of Eq. 1.18 allows Eq. 1.16 to be expressed in a form convenient for least-squares regression (Eq. 1.19) which is useful for experimental quantification of λ from the IET kinetic response to $-\Delta G°$.[104,105]

$$\frac{k_{IET}}{k_{IET}^{max}} = \frac{1}{2}\left[1 - \mathrm{erf}\left(\frac{\Delta G° + \lambda}{2\sqrt{\lambda k_B T}}\right)\right] \tag{1.19}$$

For IET, λ_o is predicted to depend on the solvent dielectric response, the distance between the electrode and molecule (R_{IET}), and the molecular radii (r) (Eq. 1.20).[54,131,153]

$$\lambda_{o,IET} = \frac{e^2}{8\pi\varepsilon_0}\left(\frac{1}{\varepsilon_{op}} - \frac{1}{\varepsilon_{st}}\right)\left(\frac{1}{r} - \frac{1}{2R_{IET}}\right) \tag{1.20}$$

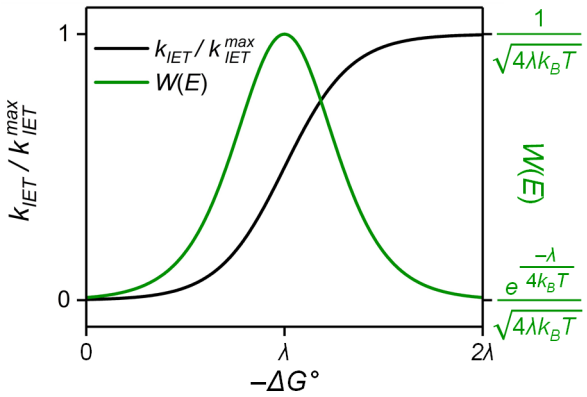

Figure 1.11. The Marcus-Gerischer prediction of k_{IET}/k_{IET}^{max} vs. $-\Delta G°$ for IET (black). The derivative of this curve gives the Gaussian distribution of activation barriers $W(E)$ (green).

In celebrated examples by Chidsey, Finklea, Hanshew, and others, the kinetic response predicted by Eq. 1.16 and 1.19 has been observed experimentally, most commonly for molecules tethered to gold electrodes by long-chain alkane thiol self-assembled monolayers.[154–157] In Chapters 5-7 of this Dissertation, this kinetic analysis will be applied to photo-initiated reactions at conductive interfaces to experimentally determine λ and H_{ab} for IET reactions relevant to DSSCs and DSPECs.

1.3.3 Complications of Adiabaticity

A subtlety of Eqs. 1.7 and 1.16 is the assumption that the reaction is non-adiabatic, with small values of H_{ab} relative to λ and k_bT. In fact, the PES in Figs. 1.9 and 1.10 are presented with negligibly small H_{ab}. In this case, the cusp at the intersection of the reactant and product PESs, which must be crossed for ET, is sharp, and oscillations in the nuclear configuration move the system along the reactant PES. The system passes frequently through the transition state but spends little time in this configuration. Here, movement onto the product PES requires a low-probability instantaneous hop from the reactant PES at the intersection. Some ET reactions, however, are adiabatic, with molecular orbital delocalization that causes significant overlap of the donor and acceptor wave

functions.[129,131,133,158–164] For intra- and intermolecular ET, this manifests in mixing of the reactant and product PESs, which lowers and broadens the intersection cusp (Fig. 1.8a). In this case, continuous progress along the nuclear configuration is unlikely to result in a return to the reactant minimum. The probability of movement onto the product PES from the transition state thus approaches unity.

The defining feature of adiabatic ET is that electronic motion becomes correlated with nuclear solvent and inner-sphere motions in violation of the Born-Oppenheimer approximation. Because of this, kinetics of adiabatic ET are much more mathematically complex than those of non-adiabatic ET.[158–162] This means that the solvent not only acts as a static energy dump through λ_o, but dynamically contributes to changes in charge distribution on the time scale of electronic motion. Solvent dynamics are frequently quantified by the solvent longitudinal relaxation time (τ_L), the time required for solvent dipoles to undergo dielectric response to changes in charge distribution (Eq. 1.21).[136,165,166]

$$\tau_L = \frac{\varepsilon_\infty}{\varepsilon_{st}} \tau_D \tag{1.21}$$

Values of τ_L are proportional to the solvent viscosity and defined in terms of the Debye relaxation time (τ_D) measured from dielectric response spectra and the static and high-frequency dielectric constants (ε_{st} and ε_∞). To account for adiabaticity, k_{ET} can be defined with a transmission coefficient κ and a nuclear frequency ν_n (Eq. 1.22).

Here κ is the probability of movement from the transition state to the product PES determined by H_{ab}, and ν_n is commonly assigned as a relevant solvent rotation or intramolecular vibration. Both κ and ν_n depend on τ_L. This results in an ET rate constant k_{et} which deviates from the purely non-adiabatic rate constant k_{NA} defined in Eq. 1.7 by an adiabaticity parameter γ (Eq. 1.23).[158–162]

$$k_{et} = \kappa \nu_n \exp\left(\frac{-(\Delta G^\circ + \lambda)^2}{4\lambda k_B T}\right) = \frac{\gamma}{1+\gamma} \nu_n \exp\left(\frac{-(\Delta G^\circ + \lambda)^2}{4\lambda k_B T}\right) = \frac{k_{NA}}{1+\gamma} \quad (1.22)$$

$$\gamma = \frac{4\pi {H_{ab}}^2 \tau_L}{\hbar \lambda} \quad (1.23)$$

When $\gamma \ll 1$, Eq. 1.22 simplifies to $k_{et} \approx k_{NA}$, and the reaction is in the non-adiabatic limit. Adiabatic ET is signified by $\gamma \gg 1$. From Eq. 1.23, it is apparent that an ET reaction will be pushed towards adiabaticity not only by large H_{ab}, but also by small λ and slowly relaxing solvents (large τ_L). Adiabaticity manifests experimentally in τ_L-dependent kinetics, as k_{et} is depressed in "slow," viscous solvents. It also results in k_{et} values independent of ET distance, as when $\gamma \gg 1$, ${H_{ab}}^2$ factors out of Eq. 1.22.

In parallel to these expressions which describe adiabatic intra- and inter- molecular ET, robust theoretical treatments of adiabatic IET at electrode surfaces have been developed.[167–174] Within these treatments, adiabaticity can be described by a transmission coefficient at *each* intersection of the reactant and product PESs. The multiple transition states allowed by the many PES intersections are offset by small coupling in each individual case. The IET adiabaticity parameter γ_{IET} then accounts for the continuum of states by inclusion of $k_B T \rho$, where ρ is the electrode density of states assumed to be energy independent (Eq. 1.24).[167]

$$\gamma_{IET} = \frac{4\pi k_B T \rho {H_{ab}}^2 \tau_L}{\hbar \lambda} \quad (1.24)$$

Here adiabaticity not only predicts τ_L dependence and distance independence, but also kinetic insensitivity to ρ, which factors out of the non-adiabatic k_{IET} in Eq. 1.16 along with H_{ab} when $\gamma_{IET} \gg 1$. [169,175] This means adiabatic IET kinetics should be insensitive to the composition of the electrode.

Each of the experimental indications of adiabaticity described above have been observed for IET reactions at metallic electrodes. Electrochemical IET reactions have been reported to be solvent viscosity/τ_L dependent[176–178] and electrode independent.[175,179] Further, researchers have reported electrochemical IET to be distance-independent when anchored molecular species are positioned very near a metal electrode to promote H_{ab}. These experiments, however, were hindered by instability and poor ordering in self-assembled monolayers of short hydrocarbon chains.[180,181] Despite this evidence for adiabatic IET at metal electrodes, IET reactions involving semiconducting MOx are generally considered to be non-adiabatic. At dye-sensitized interfaces, however, surface-anchored molecular species are forced into close proximity with the electrode surface, which might be expected to promote sensitizer/MOx coupling and thus adiabaticity. The possibility of adiabatic IET in a dye-sensitized MOx will be explored in Chapter 7 of this Dissertation.

1.4 Final Remarks

The use of solar photons to drive fuel forming chemical reactions in DSPECs would provide an avenue to store solar energy in the form of solar fuels. The overall function of a DSPEC, however, is chemically complex and requires the optimization of multiple electron transfer events and other chemical processes. Of particular importance are interfacial electron transfer reactions that either generate or destroy photo-initiated charge separated states. In order to enhance productive, and minimize detrimental, processes this Dissertation seeks to develop fundamental understanding of IET between metal oxide nanocrystalline thin films and anchored molecular species. In Chapter 2, attempts are detailed to improve the chemical anchors themselves by covalently binding sensitizers to MOx surfaces via diazonium

electrografting. Chapter 3 develops a deep mechanistic understanding of IET in core|shell MOx nanostructures with a focus on how these materials can slow unproductive back electron transfer and charge recombination. Chapters 4-7 describe a variety of IET reactions that involve transparent conducting oxides. It is shown that the electronic structure of TCOs allows them to act as both a photoanode and a photocathode (Chapter 4). The TCOs are also utilized as tools to experimentally quantify the fundamental Marcus parameters described above, most importantly λ (Chapters 5-7). Special focus is given in this Dissertation to how the distance between the MOx and a molecule influences IET kinetics.

REFERENCES

(1) Paris Agreement | Climate Action https://ec.europa.eu/clima/policies/international/negotiations/paris_en#tab-0-1 (accessed Feb 25, 2021).

(2) Lindsey, R.; Dahlman, L. Climate Change: Global Temperature. *ClimateWatch Magazine*. 2020.

(3) Herring, D. Climate Change: Global Temperature Projections. *ClimateWatch Magazine*. 2012.

(4) House, R. L.; Iha, N. Y. M.; Coppo, R. L.; Alibabaei, L.; Sherman, B. D.; Kang, P.; Brennaman, M. K.; Hoertz, P. G.; Meyer, T. J. Artificial Photosynthesis: Where Are We Now? Where Can We Go? *J. Photochem. Photobiol. C Photochem. Rev.* **2015**, *25*, 32–45.

(5) 2030 climate & energy framework https://ec.europa.eu/clima/policies/strategies/2030_en#tab-0-0 (accessed Feb 25, 2021).

(6) World Energy Outlook 2020 https://www.iea.org/reports/world-energy-outlook-2020 (accessed Feb 25, 2021).

(7) Cilluffo, A.; Ruiz, N. G. World population growth is expected to nearly stop by 2100 | Pew Research Center https://www.pewresearch.org/fact-tank/2019/06/17/worlds-population-is-projected-to-nearly-stop-growing-by-the-end-of-the-century/ (accessed Feb 25, 2021).

(8) International Energy Outlook 2019 www.eia.gov/outlooks/ieo (accessed Feb 25, 2021).

(9) Hong, B. D.; Slatick, E. R. *Carbon Dioxide Emission Factors for Coal*; Washington, DC, 1994.

(10) Hagfeldt, A.; Boschloo, G.; Sun, L.; Kloo, L.; Pettersson, H. Dye-Sensitized Solar Cells. *Chem. Rev.* **2010**, *110*, 6595–6663.

(11) Crystalline Silicon Photovoltaics Research https://www.energy.gov/eere/solar/crystalline-silicon-photovoltaics-research (accessed Feb 26, 2021).

(12) Renewables 2020 – Analysis and forecast to 2025 https://www.iea.org/reports/renewables-2020 (accessed Feb 26, 2021).

(13) Lewis, N. S. Research Opportunities to Advance Solar Energy Utilization. *Science.* **2016**, *351* (6271), 1920–1920.

(14) Lewis, N. S.; Nocera, D. G. Powering the Planet: Chemical Challenges in Solar Energy Utilization. *Proc. Natl. Acad. Sci. U. S. A.* **2006**, *103* (43), 15729–15735.

(15) Harriman, A. Prospects for Conversion of Solar Energy into Chemical Fuels: The Concept of a Solar Fuels Industry. *Philos. Trans. R. Soc. A Math. Phys. Eng. Sci.* **2013**, *371* (1996), 0415.

(16) Gust, D.; Moore, T. A.; Moore, A. L. Solar Fuels via Artificial Photosynthesis. *Acc. Chem. Res.* **2009**, *42* (12), 1890–1898.

(17) Berardi, S.; Drouet, S.; Francàs, L.; Gimbert-Suriñach, C.; Guttentag, M.; Richmond, C.; Stoll, T.; Llobet, A. Molecular Artificial Photosynthesis. *Chem. Soc. Rev.* **2014**, *43* (22), 7501–7519.

(18) Zhang, B.; Sun, L. Artificial Photosynthesis: Opportunities and Challenges of Molecular Catalysts. *Chem. Soc. Rev* **2019**, *48*, 2216–2264.

(19) Kärkäs, M. D.; Verho, O.; Johnston, E. V.; Åkermark, B. Artificial Photosynthesis: Molecular Systems for Catalytic Water Oxidation. *Chem. Rev.* **2014**, *114* (24), 11863–12001.

(20) Brennaman, M. K.; Dillon, R. J.; Alibabaei, L.; Gish, M. K.; Dares, C. J.; Ashford, D. L.; House, R. L.; Meyer, G. J.; Papanikolas, J. M.; Meyer, T. J. Finding the Way to Solar Fuels with Dye-Sensitized Photoelectrosynthesis Cells. *J. Am. Chem. Soc.* **2016**, *138*, 13085–13102.

(21) Fujishima, A.; Honda, K. Electrochemical Photolysis of Water at a Semiconductor Electrode. *Nature* **1972**, *238* (5358), 37–38.

(22) Li, J.; Wu, N. Semiconductor-Based Photocatalysts and Photoelectrochemical Cells for Solar Fuel Generation: A Review. *Catal. Sci. Technol.* **2015**, *5* (3), 1337–1384.

(23) Hisatomi, T.; Kubota, J.; Domen, K. Recent Advances in Semiconductors for Photocatalytic and Photoelectrochemical Water Splitting. *Chem. Soc. Rev* **2014**, *43*, 7535.

(24) Ashford, D. L.; Gish, M. K.; Vannucci, A. K.; Brennaman, M. K.; Templeton, J. L.; Papanikolas, J. M.; Meyer, T. J. Molecular Chromophore-Catalyst Assemblies for Solar Fuel Applications. *Chem. Rev.* **2015**, *115* (23), 13006–13049.

(25) Hagfeldt, A.; Gratzel, M. Light-Induced Redox Reactions in Nanocrystalline Systems. *Chem. Rev* **1995**, *95* (1), 49–68.

(26) Wrighton, M. S.; Ellis, A. B.; Wolczanski, P. T.; Morse, D. L.; Abrahamson, H. B.; Ginley, D. S. Strontium Titanate Photoelectrodes. Efficient Photoassisted Electrolysis of Water at Zero Applied Potential. *J. Am. Chem. Soc.* **1976**, *98* (10), 2774–2779.

(27) Duonghong, D.; Borgarello, E.; Gratzel, M. Dynamics of Light-Induced Water Cleavage in Colloidal Systems. *J. Am. Chem. Soc.* **1981**, *103* (16), 4685–4690.

(28) Bard, A. J. Photoelectrochemistry and Heterogeneous Photo-Catalysis at

Semiconductors. *J. Photochem.* **1979**, *10* (1), 59–75.

(29) Chen, S.; Wang, L. W. Thermodynamic Oxidation and Reduction Potentials of Photocatalytic Semiconductors in Aqueous Solution. *Chem. Mater.* **2012**, *24* (18), 3659–3666.

(30) Jun, H. K.; Careem, M. A.; Arof, A. K. Quantum Dot-Sensitized Solar Cells-Perspective and Recent Developments: A Review of Cd Chalcogenide Quantum Dots as Sensitizers. *Renew. Sustain. Energy Rev.* **2013**, *22*, 148–167.

(31) Harriman, A. Artificial Light-Harvesting Arrays for Solar Energy Conversion. *Chem. Commun.* **2015**, *51* (59), 11745–11756.

(32) Kärkäs, M. D.; Johnston, E. V.; Verho, O.; Akermark, B. Artificial Photosynthesis: From Nanosecond Electron Transfer to Catalytic Water Oxidation. *Acc. Chem. Res.* **2014**, *47* (1), 100–111.

(33) Meyer, T. J. Chemical Approaches to Artificial Photosynthesis. *Acc. Chem. Res.* **1989**, *22* (5), 163–170.

(34) Juris, A.; Balzani, V.; Barigelletti, F.; Campagna, S.; Belser, P.; von Zelewsky, A. Ru(II) Polypyridine Complexes: Photophysics, Photochemistry, Eletrochemistry, and Chemiluminescence. *Coord. Chem. Rev.* **1988**, *84*, 85–277.

(35) O'Regan, B.; Gratzel, M. A Low-Cost, High-Efficiency Solar Cell Based on Dye-Sensitized Colloidal TiO_2 Films. *Nature* **1991**, *353*, 737–740.

(36) Ardo, S.; Meyer, G. J. Photodriven Heterogeneous Charge Transfer with Transition-Metal Compounds Anchored to TiO_2 Semiconductor Surfaces. *Chem. Soc. Rev.* **2009**, *38* (1), 115–164.

(37) Kelly, C. A.; Meyer, G. J. Excited State Processes at Sensitized Nanocrystalline Thin Film Semiconductor Interfaces. *Coord. Chem. Rev.* **2001**, *211* (1), 295–315.

(38) Troian-Gautier, L.; Swords, W. B.; Meyer, G. J. Iodide Photoredox and Bond Formation Chemistry. *Acc. Chem. Res.* **2018**, *52*, 170–179.

(39) Burschka, J.; Pellet, N.; Moon, S. J.; Humphry-Baker, R.; Gao, P.; Nazeeruddin, M. K.; Grätzel, M. Sequential Deposition as a Route to High-Performance Perovskite-Sensitized Solar Cells. *Nature* **2013**, *499* (7458), 316–319.

(40) Sherman, B. D.; Sheridan, M. V; Dares, C. J.; Meyer, T. J. Two Electrode Collector−Generator Method for the Detection of Electrochemically or Photoelectrochemically Produced O_2. *Anal. Chem.* **2016**, *88*, 7076–7082.

(41) Xu, P.; Huang, T.; Huang, J.; Yan, Y.; Mallouk, T. E. Dye-Sensitized

Photoelectrochemical Water Oxidation through a Buried Junction. *Proc. Natl. Acad. Sci.* **2018**, *115* (27), 6946–6951.

(42) Wang, D.; Wang, L.; Brady, M. D.; Dares, C. J.; Meyer, G. J.; Meyer, T. J.; Concepcion, J. J. Self-Assembled Chromophore−Catalyst Bilayer for Water Oxidation in a Dye-Sensitized Photoelectrosynthesis Cell. *J. Phys. Chem. C* **2019**, *123*, 30039–30045.

(43) Alibabaei, L.; Sherman, B. D.; Norris, M. R.; Brennaman, M. K.; Meyer, T. J.; Mccusker, J. K. Visible Photoelectrochemical Water Splitting into H_2 and O_2 in a Dye-Sensitized Photoelectrosynthesis Cell. *Proc. Nat. Acad. Sci.* **2015**, *112* (19), 5899–5902.

(44) Wang, D.; Niu, F.; Mortelliti, M. J.; Sheridan, M. V.; Sherman, B. D.; Zhu, Y.; McBride, J. R.; Dempsey, J. L.; Shen, S.; Dares, C. J.; Li, F.; Meyer, T. J. A Stable Dye-Sensitized Photoelectrosynthesis Cell Mediated by a NiO Overlayer for Water Oxidation. *Proc. Natl. Acad. Sci.* **2020**, *117* (23), 12564–12571.

(45) Suryani, O.; Higashino, Y.; Mulyana, J. Y.; Kaneko, M.; Hoshi, T.; Shigaki, K.; Kubo, Y. A Near-Infrared Organic Photosensitizer for Use in Dye-Sensitized Photoelectrochemical Water Splitting. *Chem. Commun.* **2017**, *53*, 6787.

(46) Volpato, A. G.; Marasi, M.; Gobbato, T.; Valentini, F.; Sabuzi, F.; Gagliardi, V.; Bonetto, A; Marcomini, A.; Berardi, S.; Conte, V.; Bonchio, M.; Caramori, S.; Galloni, P.; Sartorel, A. Photoanodes for Water Oxidation with Visible Light Based on a Pentacyclic Quinoid Organic Dye Enabling Proton-Coupled Electron Transfer. *Chem. Commun.* **2020**, *56*, 2248–2251.

(47) Alibabaei, L.; Luo, H.; House, R. L.; Hoertz, P. G.; Lopez, R.; Meyer, T. J. Applications of Metal Oxide Materials in Dye Sensitized Photoelectrosynthesis Cells for Making Solar Fuels: Let the Molecules Do the Work. *J. Mater. Chem. A* **2013**, *1*, 4133–4145.

(48) House, R. L.; Heyer, C. M.; Meyer, G. J.; Papanikolas, J. M.; Meyer, T. J. The University of North Carolina Energy Frontier Research Center: Center for Solar Fuels. *ACS Energy Lett.* **2016**, *1*, 872–874.

(49) Dimarco, B. N.; Motley, T. C.; Balok, R. S.; Li, G.; Siegler, M. A.; O 'donnell, R. M.; Hu, K.; Meyer, G. J. A Distance Dependence to Lateral Self-Exchange across Nanocrystalline TiO_2. A Comparative Study of Three Homologous $Ru^{III/II}$ Polypyridyl Compounds. *J Phys Chem C* **2016**, *120*, 14226–14235.

(50) Argazzi, R.; Bignozzi, C. A.; Heimer, T. A.; Castellano, F. N.; Meyer, G. J. Enhanced Spectral Sensitivity from Ruthenium(II) Polypyridyl Based Photovoltaic Devices. *Inorg. Chem.* **1994**, *33*, 5741–5749.

(51) Desilvestro, J.; Gratzel, M.; Kavan, L.; Moser, J. Highly Efficient Sensitization of Titanium Dioxide. *J. Am. Chem. Soc.* **1985**, *107*, 2988–2990.

(52) Vlachopoulos, N.; Liska, P.; Augustynski, J.; Gratzel, M. Very Efficient Visible Light Energy Harvesting and Conversion by Spectral Sensitization of High Surface Area Polycrystalline Titanium Dioxide Films. *J. Am. Chem. Soc.* **1988**, *110* (4), 1216–1220.

(53) Trammell, S. A.; Meyer, T. J. Diffusional Mediation of Surface Electron Transfer on TiO_2. *J. Phys. Chem. B* **1999**, *103* (1), 104–107.

(54) Bard, A. J.; Faulkner, L. R. *Electochemical Method: Fundamentals and Applications*, 2nd ed.; Harris, D., Swain, E., Robey, C., Aiello, E., Eds.; Wiley, 2000.

(55) Cox, P. A. *The Electronic Structure And Chemistry Of Solids*, 1st ed.; Oxford Science Publications, 1987.

(56) He, J.; Lindstrom, H.; Hagfeldt, A.; Lindquist, S.-E. Dye-Sensitized Nanostructured p-Type Nickel Oxide Film as a Photocathode for a Solar Cell. *J. Phys. Chem. B* **1999**, *103*, 8940–8943.

(57) Huang, Z.; He, M.; Yu, M.; Click, K.; Beauchamp, D.; Wu, Y. Dye-Controlled Interfacial Electron Transfer for High-Current Indium Tin Oxide Photocathodes. *Angew. Chemie Int. Ed.* **2015**, *54* (23), 6857–6861.

(58) Flynn, C. J.; McCullough, S. M.; Li, L.; Donley, C. L.; Kanai, Y.; Cahoon, J. F. Passivation of Nickel Vacancy Defects in Nickel Oxide Solar Cells by Targeted Atomic Deposition of Boron. *J. Phys. Chem. C* **2016**, *120* (30), 16568–16576.

(59) Ji, Z.; He, M.; Huang, Z.; Ozkan, U.; Wu, Y. Photostable P-Type Dye-Sensitized Photoelectrochemical Cells for Water Reduction. *J. Am. Chem. Soc* **2013**, *125*, 11696–11699.

(60) Bachmeier, A.; Hall, S.; Ragsdale, S. W.; Armstrong, F. A. Selective Visible-Light-Driven CO_2 Reduction on a p-Type Dye-Sensitized Nio Photocathode. *J. Am. Chem. Soc.* **2014**, *136* (39), 13518–13521.

(61) Hongjun, Z.; Hagfeldt, A.; Boschloo, G. Photoelectrochemistry of Mesoporous NiO Electrodes in Iodide/Triiodide Electrolytes. *J. Phys. Chem. C* **2007**, *111* (47), 17455–17458.

(62) Huang, Z.; Natu, G.; Ji, Z.; He, M.; Yu, M.; Wu, Y. Probing the Low Fill Factor of NiO P-Type Dye-Sensitized Solar Cells. *J. Phys. Chem. C* **2012**, *116* (50), 26239–26246.

(63) Tiwana, P.; Docampo, P.; Johnston, M. B.; Snaith, H. J.; Herz, L. M. Electron Mobility and Injection Dynamics in Mesoporous ZnO, SnO_2 , and TiO_2 Films Used in Dye-Sensitized Solar Cells. **2011**, *5* (6), 5158–5166.

(64) Fessenden, R. W.; Kamat, P. V. Rate Constants for Charge Injection from Excited Sensitizer into SnO_2, ZnO, and TiO_2 Semiconductor Nanocrystallites. *J. Phys. Chem.* **1995**, *99*, 12902–12906.

(65) Katoh, R.; Furube, A.; Yoshihara, T.; Hara, K.; Fujihashi, G.; Takano, S.; Murata, S.; Arakawa, H.; Tachiya, M. Efficiencies of Electron Injection from Excited N3 Dye into Nanocrystalline Semiconductor (ZrO_2, TiO_2, ZnO, Nb_2O_5, SnO_2, In_2O_3) Films. *J. Phys. Chem. B* **2004**, *108*, 4818–4822.

(66) Berger, T.; Monllor-Satoca, D.; Jankulovska, M.; Lana-Villarreal, T.; Gómez, R. The Electrochemistry of Nanostructured Titanium Dioxide Electrodes. *Chem. Phys. Chem.* **2012**, *13* (12), 2824–2875.

(67) Ozgur, U.; Alivov, Y. I.; Liu, C.; Teke, A.; Reshchikov, M. A.; Dogan, S.; Avrutin, V.; Cho, S.-J.; Morkoc, H. A Comprehensive Review of ZnO Materials and Devices. *J. Appl. Phys.* **2005**, *98*, 041301.

(68) Jarzebski, Z. M.; Marten, J. P. Physical Properties of SnO_2 Materials II. Electrical Properties. *J. Electrochem. Soc.* **1976**, *123* (9), 299C-310C.

(69) Barr, T. J.; Sampaio, R. N.; DiMarco, B. N.; James, E. M.; Meyer, G. J. Phantom Electrons in Mesoporous Nanocrystalline SnO_2 Thin Films with Cation-Dependent Reduction Onsets. *Chem. Mater.* **2017**, *29*, 3919–3927.

(70) Knauf, R. R.; Brennaman, M. K.; Alibabaei, L.; Norris, M. R.; Dempsey, J. L. Revealing the Relationship between Semiconductor Electronic Structure and Electron Transfer Dynamics at Metal Oxide-Chromophore Interfaces. *J. Phys. Chem. C* **2013**, *117*, 25259–25268.

(71) James, E. M.; Bennett, M. T.; Bangle, R. E.; Meyer, G. J. Electron Localization and Transport in SnO_2/TiO_2 Mesoporous Thin Films: Evidence for a $SnO_2/Sn_xTi_{1-x}O_2/TiO_2$ Structure. *Langmuir* **2019**, *35* (39).

(72) Green, A. N. M.; Palomares, E.; Haque, S. A.; Kroon, J. M.; Durrant, J. R. Charge Transport versus Recombination in Dye-Sensitized Solar Cells Employing Nanocrystalline TiO_2 and SnO_2 Films. *J. Phys. Chem. B* **2005**, *109*, 12525–12533.

(73) Batzill, M.; Diebold, U. The Surface and Materials Science of Tin Oxide. *Prog. Surf. Sci.* **2005**, *79* (2–4), 47–154.

(74) Diebold, U. The Surface Science of Titanium Dioxide. *Surf. Sci. Rep.* **2003**, *48*, 53–229.

(75) Bisquert, J.; Fabregat-Santiago, F.; Mora-Seró, I.; Garcia-Belmonte, G.; Barea, E. M.; Palomares, E. A Review of Recent Results on Electrochemical Determination of the Density of Electronic States of Nanostructured Metal-Oxide Semiconductors and Organic Hole Conductors. *Inorganica Chim. Acta* **2008**, *361* (3), 684–698.

(76) Closs, G. L.; Calcaterra, L. T.; Green, N. J.; Penfield, K. W.; Miller, J. R. Distance, Stereoelectronic Effects, and the Marcus Inverted Region in Intramolecular Electron Transfer

in Organic Radical Anions. *J. Phys. Chem.* **1986**, *90* (16), 3673–3683.

(77) Wang, H.; He, J.; Boschloo, G.; Lindstro, H.; Hagfeldt, A.; Lindquist, S.-E. Electrochemical Investigation of Traps in a Nanostructured TiO_2 Film.

(78) Bisquert, J.; Vikhrenko, V. S. Interpretation of the Time Constants Measured by Kinetic Techniques in Nanostructured Semiconductor Electrodes and Dye-Sensitized Solar Cells. *J. Phys. Chem. B* **2004**, *108* (7), 2313–2322.

(79) Snaith, H. J.; Schmidt-Mende, L. Advances in Liquid-Electrolyte and Solid-State Dye-Sensitized Solar Cells. *Adv. Mater.* **2007**, *19* (20), 3187–3200.

(80) Huber, R.; Spo, S.; Moser, J. E.; Gra, M.; Wachtveitl, J. The Role of Surface States in the Ultrafast Photoinduced Electron Transfer from Sensitizing Dye Molecules to Semiconductor Colloids. *J. Phys. Chem. B* **2000**, *104*, 8995–9003.

(81) Boschloo, G.; Hagfeldt, A. Activation Energy of Electron Transport in Dye-Sensitized TiO_2 Solar Cells. *J. Phys. Chem. B* **2005**, *109* (24), 12093–12098.

(82) Nelson, J.; Haque, S. A.; Klug, D. R.; Durrant, J. R. Trap-Limited Recombination in Dye-Sensitized Nanocrystalline Metal Oxide Electrodes. *Phys. Rev. V* **2001**, *63* (20), 205321.

(83) Haque, S. A.; Tachibana, Y.; Willis, R. L.; Moser, J. E.; Grätzel, M.; Klug, D. R.; Durrant, J. R. Parameters Influencing Charge Recombination Kinetics in Dye-Sensitized Nanocrystalline Titanium Dioxide Films. *J. Phys. Chem. B* **2000**, *104*, 538–547.

(84) Nelson, J.; Chandler, R. E. Random Walk Models of Charge Transfer and Transport in Dye Sensitized Systems. *Coord. Chem. Rev.* **2004**, *248*, 1181–1194.

(85) Xie, Q.; Jiang, Y. L.; Detavernier, C.; Deduytsche, D.; Van Meirhaeghe, R. L.; Ru, G. P.; Li, B. Z.; Qu, X. P. Atomic Layer Deposition of TiO_2 from Tetrakis-Dimethyl-Amido Titanium or Ti Isopropoxide Precursors and H2O. *J. Appl. Phys.* **2007**, *102* (8), 083521.

(86) James, E. M.; Barr, T. J.; Meyer, G. J. Evidence for an Electronic State at the Interface between the SnO_2 Core and the TiO_2 Shell in Mesoporous SnO_2/TiO_2 Thin Films. *ACS Appl. Energy Mater.* **2018**, *1* (2), 859–867.

(87) Mortelliti, M. J.; Wang, A. N.; Dempsey, J. L. Atomic Layer Deposition of SnO_x onto Mesoporous, Nanocrsytalline TiO_2 and SnO_2 Thin Films. *Polyhedron* **2019**, *171*, 433–437.

(88) Schneider, J.; Bangle, R. E.; Swords, W. B.; Troian-Gautier, L.; Meyer, G. J. Determination of Proton-Coupled Electron Transfer Reorganization Energies with Application to Water Oxidation Catalysts. *J. Am. Chem. Soc.* **2019**.

(89) Knauf, R. R.; Kalanyan, B.; Parsons, G. N.; Dempsey, J. L. Charge Recombination Dynamics in Sensitized SnO_2/TiO_2 Core/Shell Photoanodes. *J. Phys. Chem. C* **2015**, *119*,

28353–28360.

(90) Prasittichai, C.; Avila, J. R.; Farha, O. K.; Hupp, J. T. Systematic Modulation of Quantum (Electron) Tunneling Behavior by Atomic Layer Deposition on Nanoparticulate SnO_2 and TiO_2 Photoanodes. *J. Am. Chem. Soc.* **2013**, *135* (44), 16328–16331.

(91) Li, W.; Elzatahry, A.; Aldhayan, D.; Zhao, D. Core-Shell Structured Titanium Dioxide Nanomaterials for Solar Energy Utilization. *Chem. Soc. Rev.* **2018**, *47* (22), 8203–8237.

(92) Pang, A.; Sun, X.; Ruan, H.; Li, Y.; Dai, S.; Wei, M. Highly Efficient Dye-Sensitized Solar Cells Composed of TiO_2@SnO_2 Core-Shell Microspheres. *Nano Energy* **2014**, *5*, 82–90.

(93) Wee, K. R.; Sherman, B. D.; Brennaman, M. K.; Sheridan, M. V.; Nayak, A.; Alibabaei, L.; Meyer, T. J. An Aqueous, Organic Dye Derivatized SnO_2/TiO_2 Core/Shell Photoanode. *J. Mater. Chem. A* **2016**, *4* (8), 2969–2975.

(94) Alibabaei, L.; Farnum, B. H.; Kalanyan, B.; Brennaman, M. K.; Losego, M. D.; Parsons, G. N.; Meyer, T. J. Atomic Layer Deposition of TiO_2 on Mesoporous NanoITO: Conductive Core-Shell Photoanodes for Dye-Sensitized Solar Cells. *Nano Lett* **2014**, *14*, 3255–3261.

(95) Karlsson, M.; Jõgi, I.; Eriksson, S. K.; Rensmo, H.; Boman, M.; Boschloo, G.; Hagfeldt, A. Dye-Sensitized Solar Cells Employing a SnO_2-TiO_2 Core-Shell Structure Made by Atomic Layer Deposition. *Chimia (Aarau).* **2013**, *67* (3), 142–148.

(96) Sherman, B. D.; Ashford, D. L.; Lapides, A. M.; Sheridan, M. V; Wee, K.-R.; Meyer, T. J. Light-Driven Water Splitting with a Molecular Electroassembly-Based Core/Shell Photoanode. *J. Phys. Chem. Lett* **2015**, *6*, 3213–3217.

(97) Avila, J. R.; Katz, M. J.; Farha, O. K.; Hupp, J. T. Barrier-Layer-Mediated Electron Transfer from Semiconductor Electrodes to Molecules in Solution: Sensitivity of Mechanism to Barrier-Layer Thickness. *J. Phys. Chem. C* **2016**, *120* (1), 20922–20928.

(98) Klein, A. Transparent Conducting Oxides: Electronic Structure-Property Relationship from Photoelectron Spectroscopy with in Situ Sample Preparation. *J. Am. Ceram. Soc.* **2012**, *96* (2), 331–345.

(99) Edwards, P. P.; Porch, A.; Jones, M. O.; Morgan, D. V.; Perks, R. M. Basic Materials Physics of Transparent Conducting Oxides. *Dalt. Trans.* **2004**, No. 19, 2995.

(100) Garcia, G.; Buonsanti, R.; Runnerstrom, E. L.; Mendelsberg, R. J.; Llordes, A.; Anders, A.; Richardson, T. J.; Milliron, D. J. Dynamically Modulating the Surface Plasmon Resonance of Doped Semiconductor Nanocrystals. *Nano Lett.* **2011**, *11* (10), 4415–4420.

(101) Farnum, B. H.; Morseth, Z. A.; Lapides, A. M.; Rieth, A. J.; Hoertz, P. G.;

Brennaman, M. K.; Papanikolas, J. M.; Meyer, T. J. Photoinduced Interfacial Electron Transfer within a Mesoporous Transparent Conducting Oxide Film. *J. Am. Chem. Soc.* **2014**, *136* (6), 2208–2211.

(102) Sampaio, R. N.; Troian-Gautier, L.; Meyer, G. J. A Charge-Separated State That Lives for Almost a Second at a Conductive Metal Oxide Interface. *Angew. Chemie* **2018**, *130* (47), 15616–15620.

(103) Farnum, B. H.; Nakada, A.; Ishitani, O.; Meyer, T. J. Bias-Dependent Oxidative or Reductive Quenching of a Molecular Excited-State Assembly Bound to a Transparent Conductive Oxide. *J. Phys. Chem. C* **2015**, *119* (45), 25180–25187.

(104) Farnum, B. H.; Morseth, Z. A.; Brennaman, M. K.; Papanikolas, J. M.; Meyer, T. J. Application of Degenerately Doped Metal Oxides in the Study of Photoinduced Interfacial Electron Transfer. *J. Phys. Chem. B* **2015**, *119*, 7698–7711.

(105) Farnum, B. H.; Morseth, Z. A.; Brennaman, M. K.; Papanikolas, J. M.; Meyer, T. J. Driving Force Dependent, Photoinduced Electron Transfer at Degenerately Doped, Optically Transparent Semiconductor Nanoparticle Interfaces. *J. Am. Chem. Soc.* **2014**, *136* (45), 15869–15872.

(106) Materna, K. L.; Crabtree, R. H.; Brudvig, G. W. Anchoring Groups for Photocatalytic Water Oxidation on Metal Oxide Surfaces. *Chem. Soc. Rev.* **2017**, *46*, 6099–6110.

(107) Brown, D. G.; Schauer, P. A.; Borau-Garcia, J.; Fancy, B. R.; Berlinguette, C. P. Stabilization of Ruthenium Sensitizers to TiO_2 Surfaces through Cooperative Anchoring Groups. *J. Am. Chem. Soc* **2013**, *135*, 1692–1695.

(108) Hanson, K.; Brennaman, M. K.; Luo, H.; Glasson, C. R. K.; Concepcion, J. J.; Song, W.; Meyer, T. J. Photostability of Phosphonate-Derivatized, Ru^{II} Polypyridyl Complexes on Metal Oxide Surfaces. *ACS Appl. Mater. Interfaces* **2012**, *4*, 1462–1469.

(109) Raber, M. M.; Brady, M. D.; Troian-Gautier, L.; Dickenson, J. C.; Marquard, S. L.; Hyde, J. T.; Lopez, S. J.; Meyer, G. J.; Meyer, T. J.; Harrison, D. P. Fundamental Factors Impacting the Stability of Phosphonate-Derivatized Ruthenium Polypyridyl Sensitizers Adsorbed on Metal Oxide Surfaces. *ACS Appl. Mater. Interfaces* **2018**, *10* (26), 22821–22833.

(110) Bae, E.; Choi, W.; Park, J.; Shin, H. S.; Kim, S. Bin; Lee, J. S. Effects of Surface Anchoring Groups (Carboxylate vs Phosphonate) in Ruthenium-Complex-Sensitized TiO_2 on Visible Light Reactivity in Aqueous Suspensions. *J. Phys. Chem. B* **2004**, *108*, 14093–14101.

(111) Brennan, B. J.; Llansola Portolés, M. J.; Liddell, P. A.; Moore, T. A.; Moore, A. L.; Gust, D. Comparison of Silatrane, Phosphonic Acid, and Carboxylic Acid Functional Groups for Attachment of Porphyrin Sensitizers to TiO_2 in Photoelectrochemical Cells. *Phys. Chem.*

Chem. Phys. **2013**, *15*, 16605–16614.

(112) McNamara, W. R.; Milot, R. L.; Song, H.; Snoeberger III, R. C.; Batista, V. S.; Schmuttenmaer, C. A.; Brudvig, G. W.; Crabtree, R. H. Water-Stable, Hydroxamate Anchors for Functionalization of TiO_2 Surfaces with Ultrafast Interfacial Electron Transfer. *Energy Environ. Sci.* **2010**, *3*, 917–923.

(113) Materna, K. L.; Brennan, B. J.; Brudvig, G. W. Silatranes for Binding Inorganic Complexes to Metal Oxide Surfaces. *Dalt. Trans.* **2015**, *44* (47), 20312–20315.

(114) Ernstorfer, R.; Gundlach, L.; Felber, S.; Storck, W.; Eichberger, R.; Willig, F. Role of Molecular Anchor Groups in Molecule-to-Semiconductor Electron Transfer. *J. Phys. Chem. B* **2006**, *110* (50), 25383–25391.

(115) Martini, L. A.; Moore, G. F.; Milot, R. L.; Cai, L. Z.; Sheehan, S. W.; Schmuttenmaer, C. A.; Brudvig, G. W.; Crabtree, R. H. Modular Assembly of High-Potential Zinc Porphyrin Photosensitizers Attached to TiO_2 with a Series of Anchoring Groups. *J. Phys. Chem. C* **2013**, *117* (28), 14526–14533.

(116) Wang, J. C.; Hill, S. P.; Dilbeck, T.; Ogunsolu, O. O.; Banerjee, T.; Hanson, K. Multimolecular Assemblies on High Surface Area Metal Oxides and Their Role in Interfacial Energy and Electron Transfer. *Chem. Soc. Rev.* **2018**, *47*, 104–148.

(117) Sutin, N.; Creutz, C. Properties and Reactivities of the Luminescent Excited States of Polypyridine Complexes of Ruthenium(II) and Osmium(II). In *Advances in Chemistry*; UTC, 1978; Vol. 168, pp 1–27.

(118) Anderson, P. A.; Strouse, G. F.; Treadway, J. A.; Richard Keene, F.; Meyer, T. J. Black MLCT Absorbers. *Inorg. Chem.* **1994**, *33* (18), 3863–3864.

(119) Nazeeruddin, M. K.; Kay, A.; Rodicio, I.; Humphry-Baker, R.; Muller, E.; Liska, P.; Vlachopoulos, N.; Gratzel, M. Conversion of Light to Electricity by Cis-X_2Bis(2,2'-Bipyridyl-4,4'-Dicarboxylate)Ruthenium Charge-Transfer Sensitizers (X = Cl^-, Br^-, I^-, CN^-, and SCN^-) on Nanocrystalline TiO_2 Electrodes. *J. Am. Chem. Soc* **1993**, *115*, 6382–6390.

(120) Nazeeruddin, M. K.; Péchy, P.; Grätzel, M. Efficient Panchromatic Sensitization of Nanocrystalline TiO_2 Films by a Black Dye Based on a Trithiocyanato-Ruthenium Complex. *Chem. Commun.* **1997**, No. 18, 1705–1706.

(121) Gersten, S. W.; Samuels, G. J.; Meyer, T. J. Catalytic Oxidation of Water by an Oxo-Bridged Ruthenium Dimer. *J. Am. Chem. Soc.* **1982**, *104*, 4029–4032.

(122) Duan, L.; Fischer, A.; Xu, Y.; Sun, L. Isolated Seven-Coordinate Ru(IV) Dimer Complex with $[HOHOH]^-$ Bridging Ligand as an Intermediate for Catalytic Water Oxidation. *J. Am. Chem. Soc.* **2009**, *131* (30), 10397–10399.

(123) Wang, L.; Duan, L.; Wang, Y.; Ahlquist, M. S. G.; Sun, L. Highly Efficient and Robust Molecular Water Oxidation Catalysts Based on Ruthenium Complexes. *Chem. Commun.* **2014**, *50* (85), 12947–12950.

(124) Elgrishi, N.; Chambers, M. B.; Wang, X.; Fontecave, M. Molecular Polypyridine-Based Metal Complexes as Catalysts for the Reduction of CO_2. *Chem. Soc. Rev.* **2017**, *46* (3), 761–796.

(125) Dalle, K. E.; Warnan, J.; Leung, J. J.; Reuillard, B.; Karmel, I. S.; Reisner, E. Electro- and Solar-Driven Fuel Synthesis with First Row Transition Metal Complexes. *Chem. Rev.* **2019**, *119* (4), 2752–2875.

(126) Costentin, C.; Drouet, S.; Robert, M.; Savéant, J. M. A Local Proton Source Enhances CO_2 Electroreduction to CO by a Molecular Fe Catalyst. *Science.* **2012**, *338* (6103), 90–94.

(127) Azcarate, I.; Costentin, C.; Robert, M.; Savéant, J. M. Through-Space Charge Interaction Substituent Effects in Molecular Catalysis Leading to the Design of the Most Efficient Catalyst of CO_2-to-CO Electrochemical Conversion. *J. Am. Chem. Soc.* **2016**, *138* (51), 16639–16644.

(128) Listorti, A.; O'Regan, B.; Durrant, J. R. Electron Transfer Dynamics in Dye-Sensitized Solar Cells. *Chem. Mater.* **2011**, *23* (15), 3381–3399.

(129) Marcus, R. A.; Sutin, N. Electron Transfers in Chemistry and Biology. *Biochim. Biophys. Acta* **1985**, *811*, 265–322.

(130) Marcus, R. A. On the Theory of Oxidation-Reduction Reactions Involving Electron Transfer. I. *J. Chem. Phys.* **1956**, *24* (5), 966–978.

(131) Marcus, R. A. On the Theory of Electron-Transfer Reactions. VI. Unified Treatment for Homogeneous and Electrode Reactions. *J. Chem. Phys.* **1965**, *43* (2), 679–701.

(132) Sutin, N. Nuclear, Electronic, and Frequency Factors in Electron Transfer Reactions. *Acc. Chem. Res.* **1982**, *15* (9), 275–282.

(133) Piechota, E. J.; Meyer, G. J. Introduction to Electron Transfer: Theoretical Foundations and Pedagogical Examples. *J. Chem. Educ.* **2019**, *96* (11), 2450–2466.

(134) Barbara, P. F.; Meyer, T. J.; Ratner, M. A. Contemporary Issues in Electron Transfer Research. *J. Phys. Chem.* **1996**, *100* (31), 13148–13168.

(135) Libby, W. F. Electron Exchange Reactions in Aqueous Solution. *Electron Exch. React. Aqueous Solut.* **1952**, *56*, 863–868.

(136) Fawcett, R. W. *Liquids, Solutions, and Interfaces: From Classical Macroscopic Descriptions to Modern Microscopic Details*, 1st ed.; Oxford University Press: New York,

2004.

(137) Closs, G. L.; Miller, J. R. Intramolecular Long-Distance Electron Transfer in Organic Molecules. *Science.* **1988**, *240* (4851), 440–447.

(138) Yonemoto, E. H.; Riley, R. L.; Kim, Y. Il; Atherton, S. J.; Schmehl, R. H.; Mallouk, T. E. Photoinduced Electron Transfer in Covalently Linked Ruthenium Tris(Bipyridyl)-Viologen Molecules: Observation of Back Electron Transfer in the Marcus Inverted Region. *J. Am. Chem. Soc.* **1992**, *114* (21), 8081–8087.

(139) Fox, L. S.; Kozik, M.; Winkler, J. R.; Gray, H. B. Gaussian Free-Energy Dependence of Electron-Transfer Rates in Iridium Complexes. *Science.* **1990**, *247* (4946), 1069–1071.

(140) Nelson, J.; Haque, S. A.; Klug, D. R.; Durrant, J. R. Trap-Limited Recombination in Dye-Sensitized Nanocrystalline Metal Oxide Electrodes. *Phys. Rev. B - Condens. Matter Mater. Phys.* **2001**, *63*, 205321.

(141) Haque, S. A.; Tachibana, Y.; Willis, R. L.; Moser, J. E.; Gra, M.; Klug, D. R.; Durrant, J. R. Parameters Influencing Charge Recombination Kinetics in Dye-Sensitized Nanocrystalline Titanium Dioxide Films. *J. Phys. Chem. B* **2000**, *104* (3), 538–547.

(142) Kuciauskas, D.; Freund, M. S.; Gray, H. B.; Winkler, J. R.; Lewis, N. S. Electron Transfer Dynamics in Nanocrystalline Titanium Dioxide Solar Cells Sensitized with Ruthenium or Osmium Polypyridyl Complexes. *J. Phys. Chem. B* **2001**, *105* (2), 392–403.

(143) Gaal, D. A.; McGarrah, J. E.; Liu, F.; Cook, J. E.; Hupp, J. T. Nonadiabatic Electron Transfer at the Nanoscale Tin-Oxide Semiconductor/Aqueous Solution Interface. *Photochem. Photobiol. Sci.* **2004**, *3* (3), 240–245.

(144) Yan, S. G.; Hupp, J. T. Semiconductor-Based Interfacial Electron-Transfer Reactivity: Decoupling Kinetics from PH-Dependent Band Energetics in a Dye-Sensitized Titanium Dioxide/Aqueous Solution System. *J. Phys. Chem.* **1996**, *100* (17), 6867–6870.

(145) Barzykin, A. V; Tachiya, M. Mechanism of Charge Recombination in Dye-Sensitized Nanocrystalline Semiconductors: Random Flight Model. *J. Phys. Chem. B* **2002**, *106* (17), 4356–4363.

(146) Martini, I.; Hodak, J.; Hartland, G. V.; Kamat, P. V. Ultrafast Study of Interfacial Electron Transfer between 9-Anthracene-Carboxylate and TiO_2 Semiconductor Particles. *J. Chem. Phys.* **1997**, *107* (19), 8064–8072.

(147) Marcus, R. A. Chemical and Electrochemical Electron-Transfer Theory. *Annu. Rev. Phys. Chem.* **1964**, *15*, 155–196.

(148) Newton, M. D.; Sutin, N. Electron Transfer Reactions in Condensed Phases. *Annu. Rev. Phys. Chem.* **1984**, *35*, 437–480.

(149) Hush, N. S. Homogeneous and Heterogeneous Optical and Thermal Electron Transfer. *Electrochim. Acta* **1968**, *13*, 1005–1023.

(150) Gerischer, H. Electrochemical Techniques for the Study of Photosensitization. *Photochem. Photobiol.* **1972**, *16* (4), 243–260.

(151) Levich, V. G. Present State of the Theory of Oxidation-Reduction in Solution (Bulk and Electrode Reactions). In *Advances in Electrochemistry and Electrochemical Engineering*; Delahay, P., Ed.; Interscience Publishers: New York, 1966; pp 249–371.

(152) Royea, W. J.; Fajardo, A. M.; Lewis, N. S. Fermi Golden Rule Approach to Evaluating Outer-Sphere Electron-Transfer Rate Constants at Semiconductor/Liquid Interfaces. *J. Phys. Chem. B* **1997**, *101* (51), 11152–11159.

(153) Liu, Y. P.; Newton, M. D. Reorganization Energy for Electron Transfer at Film-Modified Electrode Surfaces: A Dielectric Continuum Model. *J. Phys. Chem.* **1994**, *98* (29), 7162–7169.

(154) Chidsey, C. E. Free Energy and Temperature Dependence of Electron Transfer at the Metal-Electrolyte Interface. *Science.* **1991**, *251* (4996), 919–922.

(155) Finklea, H. O.; Hanshew, D. D. Electron-Transfer Kinetics in Organized Thiol Monolayers with Attached Pentaammine(Pyridine)Ruthenium Redox Centers. *J. Am. Chem. Soc.* **1992**, *114* (9), 3173–3181.

(156) Smalley, J. F.; Feldberg, S. W.; Chidsey, C. E. D.; Linford, M. R.; Newton, M. D.; Liu, Y.-P. The Kinetics of Electron Transfer through Ferrocene-Terminated Alkanethiol Monolayers on Gold. *J. Phys. Chem.* **1995**, *99*, 13141–13149.

(157) Miller, C.; Gratzel, M. Electrochemistry at ω-Hydroxy Thiol Coated Electrodes. 2. Measurement of the Density of Electronic States Distributions for Several Outer-Sphere Redox Couples. *J. Phys. Chem.* **1991**, *95* (13), 5225–5233.

(158) Weaver, M. J. Dynamical Solvent Effects on Activated Electron-Transfer Reactions: Principles, Pitfalls, and Progress. *Chem. Rev* **1992**, *92*, 480.

(159) Gochev, A.; McManis, G. E.; Weaver, M. J. Solvent Dynamical Effects in Electron Transfer: Predicted Influences of Electronic Coupling upon the Rate-Dielectric Friction Dependence. *J. Chem. Phys.* **1989**, *91* (2), 906–916.

(160) Sumi, H.; Marcus, R. A. Dynamical Effects in Electron Transfer Reactions. *J. Chem. Phys.* **1986**, *84* (9), 4894–4914.

(161) Rips, I.; Jortner, J. Dynamic Solvent Effects on Outer-Sphere Electron Transfer. *J. Chem. Phys.* **1987**, *87* (4), 2090–2104.

(162) Jortner, J.; Bixon, M. Intramolecular Vibrational Excitations Accompanying Solvent-Controlled Electron Transfer Reactions. *J. Chem. Phys.* **1988**, *88* (1), 167–170.

(163) Hush, N. S. Adiabatic Theory of Outer Sphere Electron-Transfer Reactions in Solution. *Trans. Faraday Soc.* **1961**, *57*, 557–580.

(164) Zusman, L. D. Outer-Sphere Electron Transfer in Polar Solvents. *Chem. Phys.* **1980**, *49*, 295–304.

(165) Maroncelli, M. The Dynamics of Solvation in Polar Liquids. *J. Mol. Liq.* **1993**, *57* (C), 1–37.

(166) Barbara, P. F.; Walker, G. C.; Smith, T. P. Vibrational Modes of the Dynamic Solvent Effect in Electron and Proton Transfer. *Science.* **1992**, *256* (5059), 975–981.

(167) Matyushov, D. V. Potential-Step Transient Response of an Electrochemical System. *J. Electroanal. Chem.* **1994**, *367*, 1–6.

(168) Gorodyskii, A. V.; Karasevskii, A. I.; Matyushov, D. V. Adiabatic Outer Sphere Electron Transfer through the Metal-Electrolyte Interface. *J. Electroanal. Chem.* **1991**, *315*, 9–28.

(169) Schmickler, W. A Theory of Adiabatic Electron-Transfer Reactions. *J. Electroanal. Chem.* **1986**, *204*, 31–43.

(170) Smith, B. B.; Hynes, J. T. Electronic Friction and Electron Transfer Rates at Metallic Electrodes. *J. Chem. Phys.* **1993**, *99* (9), 6517–6530.

(171) Kuznetsov, A. M. A Unified Model of the Adiabatic Reactions of Electron Transfer at Metal Electrodes. *J. Electroanal. Chem.* **1988**, *241*, 45–56.

(172) Dogonadze, R. R.; Kuzntesov, A. M.; Vorotentsev, M. A. The Kinetics of Adiabatic and Nonadiabatic Reactions at the Metal and Semiconductor Electrodes. *Croat. Chem. Acta* **1972**, *44*, 257–273.

(173) Feldberg, S. W.; Sutin, N. Distance Dependence of Heterogeneous Electron Transfer through the Nonadiabatic and Adiabatic Regimes. *Chem. Phys.* **2006**, *324*, 216–225.

(174) Zusman, L. D. Outer-Sphere Electron Transfer Reactions at an Electrode. *Chem. Phys.* **1987**, *112* (1), 53–59.

(175) Iwasita, T.; Schmickler, W.; Schultze, J. W. The Influence of the Metal on the Kinetics of Outer Sphere Redox Reactions. *Berichte der Bunsengesellschaft für Phys. Chemie* **1985**, *89* (2), 138–142.

(176) Fawcett, W. R.; Opallo, M. The Kinetics of Heterogeneous Electron Transfer Reaction

in Polar Solvents. *Angew. Chemie Int. Ed.* **1994**, *33* (21), 2131–2143.

(177) Winkler, K.; McKnight, N.; Fawcett, W. R. Electron Transfer Kinetics of Tris(1,10-Phenanthroline)Ruthenium(II) Electrooxidation in Aprotic Solvents. *J. Phys. Chem. B* **2000**, *104* (15), 3575–3580.

(178) Pyati, R.; Murray, R. W. Solvent Dynamics Effects on Heterogeneous Electron Transfer Rate Constants of Cobalt Tris(Bipyridine). *J. Am. Chem. Soc.* **1996**, *118* (7), 1743–1749.

(179) Iwasita, T.; Schmickler, W.; Schultze, J. W. The Influence of Metal Adatoms Deposited at Underpotential on the Kinetics of an Outer-Sphere Redox Reaction. *J. Electroanal. Chem.* **1985**, *194* (2), 355–359.

(180) Smalley, J. F.; Finklea, H. O.; Chidsey, C. E. D.; Linford, M. R.; Creager, S. E.; Ferraris, J. P.; Chalfant, K.; Zawodzinsk, T.; Feldberg, S. W.; Newton, M. D. Heterogeneous Electron-Transfer Kinetics for Ruthenium and Ferrocene Redox Moieties through Alkanethiol Monolayers on Gold. *J. Am. Chem. Soc.* **2003**, *125* (7), 2004–2013.

(181) Khoshtariya, D. E.; Dolidze, T. D.; Zusman, L. D.; Waldeck, D. H. Observation of the Turnover between the Solvent Friction (Overdamped) and Tunneling (Nonadiabatic) Charge-Transfer Mechanisms for a Au/$Fe(CN)_6^{3-/4-}$Electrode Process and Evidence for a Freezing Out of the Marcus Barrier. *J. Phys. Chem. A* **2001**, *105* (10), 1818–1829.

CHAPTER 2: SURFACE GRAFTING OF RU(II) DIAZONIUM-BASED SENSITIZERS ON METAL OXIDES ENHANCES ALKALINE STABILITY FOR SOLAR ENERGY CONVERSION[1]

2.1 Introduction

Wide band gap metal oxide (MOx) semiconductor materials have applications in batteries, optoelectronics, electrocatalysis, and solar energy conversion.[1–5] Of specific importance to this Dissertation, mesoporous nanocrystalline MOx thin films serve as photoanodes or photocathodes for solar energy conversion in dye-sensitized solar cells (DSSC) and dye-sensitized photoelectrosynthesis cells (DSPECs).[4,5] In DSPECs, a photosensitizer, anchored to the photoanode (often TiO_2, SnO_2, or a $SnO_2|TiO_2$ core|shell material) is excited by sunlight, which causes electron injection into the MOx acceptor states. The oxidized sensitizer is regenerated by electron transfer from a water oxidation catalyst present either in solution or co-adsorbed to the MOx photoanode. This process is repeated several times to generate the active catalyst and enable water oxidation to molecular dioxygen and protons. The protons then diffuse through an exchange membrane to reach the photocathode (usually NiO) where they are converted into molecular dihydrogen.[5,6] Water oxidation with molecular catalysts is most rapid under alkaline conditions in the presence of a buffer base. Unfortunately, these conditions also result in significant sensitizer and catalyst desorption with the most common carboxylic acid and phosphonate surface binding

[1]This chapter previously appeared as an article in the journal *American Chemical Society Applied Materials & Interfaces*. The original citation is: Bangle, R.E.; Sampaio, R.N.; Troian-Gautier, L.; Meyer, G.J. *ACS Appl. Mater. Interfaces*. **2018**, 10 *(3)*, 3121-3132.

groups.[7–11] Thus binding motifs that are stable under alkaline conditions are critically needed for practical application of DSPECs and the realization of solar fuels.

Pioneering work since the 80's has placed ruthenium chromophores at the forefront of MOx sensitizers to visible light. Early reports used mostly ruthenium sensitizers in solution or immobilized in membranes, but the anchoring of said sensitizers to the MOx surface rapidly developed, leading to greater stability and increased charge injection.[12–19] Classical anchoring groups were carboxylic acids and cyanoacrylic derivatives.[9] Several other anchoring groups, including phosphonic acid,[7–10] silatrane,[7–9] hydroxamate,[9,20] acetyl acetonate,[9,21] boronic acid,[9] silane,[9,22,23] and pyridine derivatives[9,24] have been developed since to remediate stability issues or desorption in selected conditions. For instance, carboxylic acids, for which a pKa of around 4.7 is usually accepted, are only stable at pH values smaller than their pKa.[7] This becomes limiting when developing DSPEC devices in aqueous solution for water oxidation. Phosphonic acid derivatives were later introduced to improve aqueous stability and extend the range of pH in which a DSPEC or DSSC can be operated. Indeed, with their higher pKa, sensitizers containing phosphonic acid are more stable in neutral water. Nonetheless, the sensitizers containing phosphonic acid are not stable at pH greater than 7, a clear mismatch to the alkaline conditions ideal for implementation of water oxidation catalysts.[7]

In this Chapter, we have examined the grafting of diazonium-based ruthenium sensitizers to MOx surfaces (Fig. 2.1) in order to investigate their stability at alkaline pHs. Surface functionalization through diazonium grafting is a widely-used technique for covalent binding of organic compounds on all forms of carbon, metallic surfaces, and polymers.[25–35] A few recent studies have also shown diazonium grafting to be possible on MOx nanoparticles,

but to our knowledge neither the stability nor the functionality of these surfaces have been established.[27,36–40] In this Chapter, the electrochemical grafting of a ruthenium terpyridine sensitizer was achieved on mesoporous MOxs (TiO_2, SnO_2, ZrO_2, ZnO, indium-doped tin oxide (In_2O_3:Sn)) thin films deposited on fluorine-doped tin oxide (FTO) glass. Structurally analogous ruthenium chromophores bearing carboxylic acid or phosphonic acid groups were used to assess the comparative stability and surface coverage as well as the excited state injection properties. Despite lower injection yields, the diazonium grafted compounds displayed photostability under 100 mW/cm^{-2} illumination in pH 12 aqueous solutions for as long as 24 hours, which greatly outperformed the carboxylic and phosphonate analogues. Furthermore, the pH 12 stability under ambient light was observed for several months. The alkaline stability of diazonium-grafted sensitizers on oxide surfaces presents an opportunity to advance DSPEC applications, while the generality of the process described allows for potential applications to a wide range of technologies that utilize MOx surfaces with molecular components.

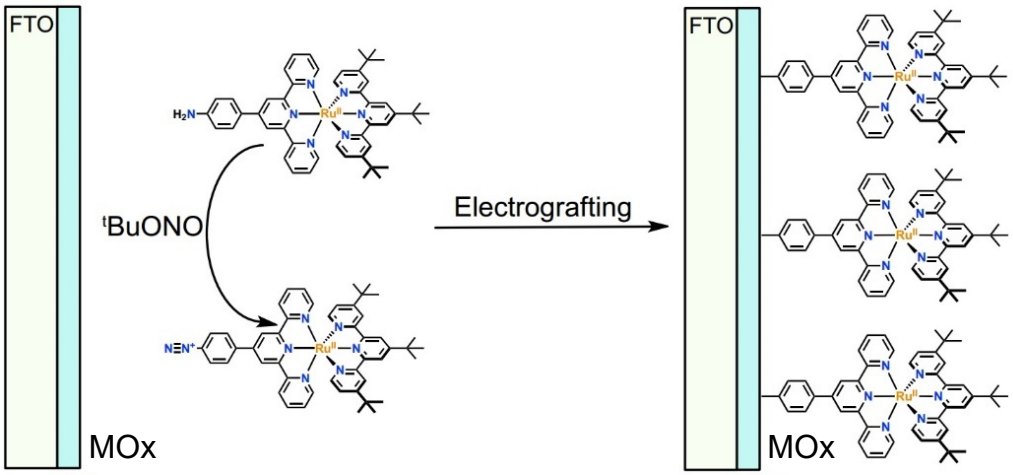

Figure 2.1. The general strategy developed for electrografting diazonium-substituted sensitizer molecules on metal oxide (MOx) surfaces. The surfaces studied here were mesoporous thin films of metal oxide nanocrystals. The reactive diazonium substituent was generated *in situ* from the reaction between the amine precursor and *tert*-butylnitrite (^{t}BuONO).

2.2 Experimental

2.2.1 Materials

The following reagents and substrates were used as received: acetonitrile (CH_3CN, Burdick & Jackson, spectrophotometric grade, 99.9%); lithium perchlorate ($LiClO_4$, Aldrich, 99.99%), sodium perchlorate ($NaClO_4$, Aldrich, ≥98.0%); tetra-n-butylammonium perchlorate ($TBAClO_4$, Alfa Aesar, electrochemical grade); titanium(IV) chloride ($TiCl_4$, Aldrich, 99.9%) ; sodium acetate (CH_3COONa, Aldrich, ≥99%); tert-butyl nitrite ($(CH_3)_3CNO_2$, Alfa Aesar, 90%); sodium nitrite ($NaNO_2$, Aldrich, ≥97%); sodium hydroxide (NaOH, Fisher, NF/FCC pellets); perchloric acid ($HClO_4$, Alfa Aesar, 70%); hydrochloric acid (HCl, Fisher, certified ACS Plus); glacial acetic acid (CH_3COOH, Fisher, certified ACS); nitric acid (HNO_3, Fisher, 70%); poly(ethylene oxide) (Aldrich); poly(ethylene glycol) (Aldrich); terpineol (Aldrich); hydroxypropyl cellulose (HPC, Aldrich); polyethylene glycol copolymer (carbowax, Aldrich); titanium(IV) isopropoxide (Aldrich, 97%); zirconium(IV) isopropoxide (99.9%, Aldrich); zinc oxide nanoparticles (40 wt% in ethanol, <130 nm diameter, Aldrich); tin(IV) dioxide nanoparticles (15 wt% in H_2O, 15 nm diameter, Alfa Aesar); In_2O_3 :Sn nanoparticles (TC8 DE, 20 wt% in ethanol, Evonik Industries) ; fluorine-doped tin oxide-coated glass (FTO, Hartford Glass Co., Inc., 2.3 mm thick, 15Ω/□). Ruthenium trichloride hydrate (Oakwood Chemicals, 97%) and 4,4’,4’’-tri-*tert*-butyl-2,2’:6’,2’’-terpyridine “ttt” (Sigma-Aldrich) were used as received. NMR solvents were purchased from Cambridge Isotope Laboratories, Inc. Ruthenium 4,4’,4’’-tri-*tert*-butyl-2,2’:6’,2’’-terpyridine trichloride, [Ru(ttt)Cl_3], tpy-C_6H_4-COOH, tpy-C_6H_4-PO_3Et_2 and tpy-C_6H_4-NH_2 were synthesized according to literature procedures.[41–44]

2.2.2 Synthesis of $[Ru(ttt)(tpy\text{-}C_6H_4\text{-}COOH)]^{2+}.2PF_6^-$

$[Ru(ttt)Cl_3]$ (52 mg, 0.085 mmol) and $tpy\text{-}C_6H_4\text{-}COOH$ (31 mg, 0.088 mmol) were place in a microwave tube. Ethanol (10 mL) and N-ethylmorpholine (0.5 mL) were added. The microwave tube was then sealed and heated under microwave irradiation at 120°C for 2 hours. After reaction, 10 mL of water and 2 mL of a saturated NH_4PF_6 aqueous solution were added. The ethanol was removed under reduced pressure and the resulting solid was recovered by filtration and washed with water, small amounts of ethanol, and diethylether. The product, termed Ru-**COOH**, was obtained as a red powder (73 mg, 75%). This compound has been previously reported using a different procedure.[45]

^1H NMR (400 MHz, ∂-CD_3CN) δ 9.02 (s, 2H), 8.78 (s, 2H), 8.64 (d, J = 8.1 Hz, 2H), 8.51 (d, J = 2.1 Hz, 2H), 8.36 (d, J = 8.4 Hz, 2H), 8.30 (d, J = 8.4 Hz, 2H), 8.04 – 7.86 (m, 2H), 7.36 (d, J = 5.5 Hz, 2H), 7.29 – 7.17 (m, 4H), 7.12 (dd, J = 6.0, 2.1 Hz, 2H), 1.75 (s, 9H), 1.31 (s, 18H). HRMS (ESI-MS) m/z: $[M\text{-}(PF_6)]^+$ Calculated for $C_{49}H_{50}F_6N_6O_2PRu$ 1001.2680; Found 1001.2609.

2.2.3 Synthesis of $[Ru(ttt)(tpy\text{-}C_6H_4\text{-}PO_3Et_2)]^{2+}.2PF_6^-$

$[Ru(ttt)Cl_3]$ (156 mg, 0.256 mmol) and $tpy\text{-}C_6H_4\text{-}PO_3Et_2$ (114 mg, 0.256 mmol) were place in a microwave tube. Ethanol (18 mL) and N-ethylmorpholine (1.5 mL) were added. The microwave tube was then sealed and heated under microwave irradiation at 120°C for 2 hours. After reaction, 10 mL of water and 2 mL of a saturated NH_4PF_6 aqueous solution were added. The ethanol was removed under reduced pressure and the resulting solid was recovered by filtration and washed with water, small amounts of ethanol, and diethylether. The product, termed Ru-**PO_3Et_2** was obtained as a red powder (280 mg, 88%).

^{1}H NMR (400 MHz, ∂-CD_3CN) δ 9.00 (s, 2H), 8.78 (s, 2H), 8.64 (d, *J* = 8.1 Hz, 2H), 8.51 (d, *J* = 2.0 Hz, 2H), 8.36 – 8.27 (m, 2H), 8.12 (dd, *J* = 12.8, 8.3 Hz, 2H), 7.95 (td, *J* = 7.8, 1.5 Hz, 2H), 7.36 (d, *J* = 5.0 Hz, 2H), 7.28 – 7.17 (m, 4H), 7.12 (dd, *J* = 6.0, 2.1 Hz, 2H), 4.19 (ddd, *J* = 8.2, 7.1, 2.8 Hz, 4H), 1.75 (s, 9H), 1.38 (d, *J* = 7.0 Hz, 6H), 1.31 (s, 18H). HRMS (ESI-MS) m/z: : $[M\text{-}PF_6]^+$ Calculated for $C_{52}H_{59}F_6N_6O_3P_2Ru$ 1093.3071; Found 1093.3017.

2.2.4 Synthesis of $[Ru(ttt)(tpy\text{-}C_6H_4\text{-}PO_3H_2)]^{2+}.2PF_6^-$

Ru-**PO_3Et_2** (330 mg, 0.266 mmol) was dissolved in 25 mL of CH_3CN. Trimethylsilyl bromide TMSBr (180 µL, 1.34 mmol) was added and the mixture was stirred at 70°C under an argon atmosphere for 24 hours. After reaction, the mixture was brought to room temperature, and 5 mL of methanol was added. The resulting solution was stirred for 30 minutes and evaporated to dryness under reduced pressure. The residue was washed with small amounts of cold CH_3CN and diethylether to obtain the title compound, termed Ru-**PO_3H_2**, as a red powder (297 mg, 94 %).

^{1}H NMR (400 MHz, ∂-CD_3OD) δ 9.31 (s, 2H), 9.08 (s, 2H), 8.90 (d, *J* = 8.1 Hz, 2H), 8.79 (d, *J* = 2.0 Hz, 2H), 8.42 (dd, *J* = 8.0, 3.1 Hz, 2H), 8.16 (dd, *J* = 13.1, 8.0 Hz, 2H), 8.01 (td, *J* = 7.9, 1.5 Hz, 2H), 7.50 – 7.42 (m, 2H), 7.37 (d, *J* = 6.0 Hz, 2H), 7.32 – 7.22 (m, 4H), 1.81 (s, 9H), 1.35 (s, 18H). HRMS (ESI-MS) m/z: : $[M\text{-}(PF_6)_2]^{2+}$ Calculated for $C_{48}H_{51}N_6O_3P_1Ru$ 446.1402; Found 446.1389.

2.2.5 Synthesis of $[Ru(ttt)(tpy\text{-}C_6H_4\text{-}NH_2)]^{2+}.2PF_6^-$

$[Ru(ttt)Cl_3]$ (156 mg, 0.256 mmol) and $tpy\text{-}C_6H_4\text{-}NH_2$ (87 mg, 0.268 mmol) were placed in a microwave tube. Ethanol (18 mL) and N-ethylmorpholine (1.5 mL) were added. The microwave tube was then sealed and heated under microwave irradiation at 120°C for 2 hours. If the chloride salt was desired, the solution was evaporated to dryness and the residue

was washed with cold ethanol and diethyl ether. If the PF_6^- compound was desired, after reaction, 10 mL of water and 2 mL of a saturated NH_4PF_6 aqueous solution were added. The ethanol was removed under reduced pressure and the resulting solid was recovered by filtration and washed with water, small amounts of ethanol and diethylether. The product, termed Ru-**NH_2**, was obtained as a red powder (225 mg, 78%). This compound has been previously reported using a different procedure.[46]

^{1}H NMR (400 MHz, ∂-CD_3CN) δ 8.89 (s, 2H), 8.77 (s, 2H), 8.60 (d, *J* = 8.2 Hz, 2H), 8.50 (d, *J* = 2.1 Hz, 2H), 8.00 (d, *J* = 8.5 Hz, 2H), 7.91 (td, *J* = 7.9, 1.6 Hz, 2H), 7.31 (d, *J* = 5.4 Hz, 2H), 7.27 (d, *J* = 5.9 Hz, 2H), 7.20 – 7.15 (m, 2H), 7.13 (dt, *J* = 6.0, 3.3 Hz, 2H), 6.95 (d, *J* = 8.5 Hz, 2H), 4.77 (s, 2H), 1.74 (s, 9H), 1.31 (s, 18H). $[M\text{-}PF_6]^+$ Calculatedd for $C_{48}H_{51}F_6N_7PRu$ 972.2891; Found 972.2800.

2.2.6 Synthesis of $[Ru(ttt)(tpy\text{-}C_6H_4\text{-}N_2^+)]^{3+}.3PF_6^-$

The procedure for synthesis of this compound, termed Ru-**N_2^+**, was inspired by a report in literature.[47] Ru-**NH_2** (75 mg, 0.084 mmol) was dissolved in 12 mL of 0.5 M HCl and brought to 0°C using an ice bath. $NaNO_2$ (15 mg, 0.217 mmol), dissolved in 1 mL of 0.5 M HCl was then added in one portion. The mixture was stirred at 0°C for 3 hours. After reaction, 2 mL of a saturated KPF_6 aqueous solution was added to precipitate the complex. The title compound was isolated as a dark-red powder by filtration and was washed with water, cold ethanol, and diethylether and used without further purification. IR (neat) ν_{max} (cm^{-1}): 3320, 3105, 2960, 2910, 2870, 2266, 1610, 1585, 1475, and 1425.

2.2.7 Characterization of Synthesized Compounds

Characteristic nuclear magnetic resonance (NMR) spectra were obtained at room temperature on a Bruker Avance III 400 MHz spectrometer. Solvent residual peaks were

used as internal standards for ^{1}H (δ =1.95 ppm for CD_3CN, 3.31 ppm for CD_3OD) and ^{13}C (δ = 77.16 ppm for $CDCl_3$, 39.52 ppm for DMSO) chemical shift referencing. NMR spectra were processed using MNOVA.

Samples were further analyzed with a hybrid LTQ FT (ICR 7T) (ThermoFisher, Bremen, Germany) mass spectrometer. Samples were introduced via a micro-electrospray source at a flow rate of 3 μL/min. Xcalibur (ThermoFisher, Breman, Germany) was used to analyze the data. Each mass spectrum was averaged over 200 time domains. Electrospray source conditions were set as: spray voltage 4.7 kV, sheath gas (nitrogen) 3 arb, auxiliary gas (nitrogen) 0 arb, sweep gas (nitrogen) 0 arb, capillary temperature 275ºC, capillary voltage 35 V and tube lens voltage 110 V. The mass range was set to 150-2000 m/z. All measurements were recorded at a resolution setting of 100,000. Solutions were analyzed at 0.1 mg/mL or less based on responsiveness to the ESI mechanism. Low-resolution mass spectrometry (linear ion trap) provided independent verification of molecular weight distributions.

UV−vis absorption spectra were recorded on a Varian Cary 60 or Cary 50 UV−vis spectrophotometer with a resolution of 1 nm. The molar absorption coefficients were determined by diluting a stock solution of the desired complex and represent averages of at least three independent measurements.

Square wave and cyclic voltammetry were performed with a BASi Epsilon potentiostat in a standard three electrode cell in CH_3CN or aqueous electrolytes. The cells consisted of a FTO/MOx working electrode and a platinum gauze counter-electrode. A non-aqueous silver/silver chloride electrode (Pine) was used as a reference electrode that was referenced to an internal ferrocene (Fc) standard (630 mV vs. NHE).

2.2.8 Synthesis and Sensitization of Metal Oxide Thin Films

Nanocrystalline anatase TiO_2 (~15 nm diameter) and ZrO_2 (~10 nm diameter) nanoparticles were prepared by acid hydrolysis of Ti(*i*-OPr)$_4$ or Zr(*i*-OPr)$_4$ as described previously.[48] SnO_2 (15 nm diameter) and In_2O_3 :Sn (~15 nm diameter) nanoparticles were prepared from colloidal nanoparticle suspensions, as described previously.[49,50] ZnO nanoparticles (<130 nm diameter) were prepared from a ZnO colloidal suspension by an adjusted previously described procedure.[51] Briefly, 15 g ZnO nanoparticle suspension was stirred and heated to 40˚C while 5% by mass hydroxypropyl cellulose was added. Following overnight stirring, 10 wt% terpineol was added followed by 5 min pulsed horn sonication.

Thin MOx (TiO_2, SnO_2, ZrO_2, ZnO, In_2O_3:Sn) nanoparticle films of approximately 4 μm were prepared by doctor blading onto transparent FTO using ~3.5 μm cellophane tape (3M) as a spacer, followed by sintering for 30 min at 450˚C under oxygen flow and storage at 80˚C. Film thickness and area were determined using a profilometer (Bruker DektatXT Profilometer). Tunneling Electron Microscopy (TEM) was used to capture images of the nanoparticles scraped from the films to measure particle size and gauge film density (See Associated Content section, Fig. 2.11).

MOx films were sensitized with Ru-$\mathbf{PO_3H_2}$ and Ru-**COOH** by at least 24 hour reaction with a concentrated solution of Ru-$\mathbf{PO_3H_2}$ and Ru-**COOH** in CH_3CN. Films were sensitized with Ru-$\mathbf{N_2^+}$ by electrografting with *in situ* generation of Ru-$\mathbf{N_2^+}$ from Ru-$\mathbf{NH_2}$.$2PF_6^-$ by reaction with tert-butyl nitrite. To do so, a 2 mM solution of Ru-$\mathbf{NH_2}$ in 100 mM $TBAClO_4$ CH_3CN electrolyte in a 3 mL cuvette was cooled to 0°C using an ice bath and sparged with argon for 30 min. After this, *tert*-butyl nitrite (20 μL, 0.15 mmol) was added and the mixture was allowed to react for 10 minutes. An immediate color change from red to

purple was noticed. After reaction, a standard three electrode electrochemical setup was introduced, in which the MOx film served as working electrode and a platinum gauze served as counter electrode. Remaining under an argon atmosphere and in an ice bath, TiO_2 films were held at a potential ranging from +100 mV to -100 mV vs. NHE for 30 min. Other metal oxides reached maximal grafting at different applied potentials, as will be addressed in the Results and Discussion sections of this Chapter. Sensitized slides were then removed, rinsed with CH_3CN to wash away unreacted material, and immersed in CH_3CN for at least 30 minutes prior to further use.

Alternatively, an aqueous electrografting method was also developed. A similar procedure was used using Ru-$\mathbf{NH_2}$.$2Cl^-$. The complex was dissolved in 3mL of aqueous 0.5 M HCl solution kept at 0°C and sparged with argon for 30 minutes before reaction with $NaNO_2$ (20 μL of a 1 M $NaNO_2$ solution, 0.02 mmol in total). A ~50 mV vs. NHE potential was applied for 30 min. The grafted surface was then washed with water and CH_3CN and soaked in CH_3CN. The aqueous electrografting gave similar absorbance results as the CH_3CN electrografting.

2.2.9 Sensitized Thin Film Characterization

Fourier transform infrared spectroscopy (FTIR) measurements were acquired on both powder and thin film samples using a Bruker model Alpha FTIR spectrophotometer equipped with an Alpha-P attenuated total reflectance (ATR) attachment. 36 spectra with a 2 cm^{-1} resolution were averaged to create the spectra with FTO subtracted as a baseline. X-ray photoelectron spectroscopy (XPS) was performed using a Kratos Axis Ultra-DLD spectrometer (Kratos Analytical Ltd., Manchester, UK) with a base pressure of 5 x 10^{-9} Torr equipped with a monochromatic Al K alpha source and a charge neutralizer. Survey and

high-resolution spectra were taken with pass energies of 80 eV and 20 eV, respectively. Binding energies (BE) were found using BE = 284.6 eV for C1s as a reference.

Sensitized film stability was determined at various pHs in the dark and under illumination. Non-illuminated film stability was determined by soaking the sensitized films in water adjusted to the desired pH. The films were immersed for a specified amount of time and were then rinsed with water adjusted to the same pH prior to UV-vis measurement at the MLCT. Fresh soaking solutions were used for each time point at which significant desorption occurred. When little desorption occurred, slides were analyzed in a single solution. Alternatively, films were placed in water adjusted to the desired pH and constantly illuminated with a 455 nm LED (Thor labs, 100 mW cm^{-2}) while periodic UV-vis measurements at the MLCT were made to determine photostability.

Ru(III/II) reduction potentials of the sensitizers were measured on In_2O_3:Sn thin films by spectroelectrochemistry. Spectra were monitored by an Avantes AvaLight DHc light source and an Avantes StarLine AvaSpec-2048 UV/visible spectrophotometer, while potentials were applied by a Pine Research Instrumentation (PRI) Wavenow potentiostat controlled by Aftermath software (PRI). In_2O_3:Sn on a FTO thin film served as the working electrode with a platinum gauze counter electrode, and a Ag/AgCl saturated KCl reference electrode was employed. Sensitized thin films were submerged in argon-purged, pH-adjusted aqueous solutions.

Photocurrents over extended time periods were examined with a home-built H cell using TiO_2 and SnO_2 thin films as working electrodes and platinum gauze as counter electrode. Electrodes were submerged in a nitrogen-saturated aqueous solution of 0.1 M acetate buffer and 0.5 M $NaClO_4$ adjusted to pH 5 or 12. The working and counter electrodes

were separated by a Nafion proton-exchange membrane, with 50 mM sacrificial electron donor on the working electrode side (hydroquinone for pH 5 solutions, triethanolamine for pH 12 solutions). An overpotential of 400 mV vs NHE was applied, and the cell was illuminated at 1 Sun using a Cole-Parmer Illuminator (41720 series) equipped with a 400 nm low-pass filter (Thor labs).

2.3 Results

Three ruthenium sensitizers (Fig. 2.2) were obtained by reaction of the precursor ruthenium 4,4',4''-tri-*tert*-butyl-2,2':6',2''-terpyridine trichloride, [Ru(ttt)Cl_3] with the corresponding terpyridine ligand in ethanol in the presence of N-ethyl-morpholine. With regard to Ru-$\mathbf{N_2^+}$, it was either isolated by reaction of the parent amino compound (Ru-$\mathbf{NH_2}$) with $NaNO_2$, or generated *in situ* with *tert*-butyl nitrite (^{t}BuONO).

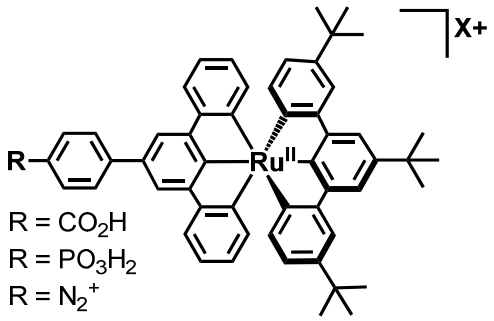

Figure 2.2. Ruthenium sensitizers used in this study that differ only by their anchoring group (Ru-**COOH,** Ru-$\mathbf{PO_3H_2}$ or Ru-$\mathbf{N_2^+}$). In the case of Ru-**COOH** and Ru-$\mathbf{PO_3H_2}$, the overall charge is 2+ whereas in the case of Ru-$\mathbf{N_2^+}$, the overall charge is 3+.

These ruthenium sensitizers differed only by their anchoring group, i.e. carboxylic acid (Ru-**COOH**), phosphonic acid (Ru-$\mathbf{PO_3H_2}$), or diazonium (Ru-$\mathbf{N_2^+}$). The electron donating tri-*tert*-butyl moieties were introduced to the uppermost terpyridine to increase excited state localization on the ligand nearest the surface to favor charge injection. The bulkiness of these groups might also prevent polymerization side-reactions that have been

previously reported for grafting of diazonium salts.[26,28,36]Meosporous oxide thin films were sensitized with Ru-**COOH** or Ru-$\mathbf{PO_3H_2}$ by overnight reactions in concentrated CH_3CN solutions (dyeing solutions). Functionalization by Ru-$\mathbf{N_2^+}$ was achieved by an electrografting procedure developed herein and described below.

2.3.1 Diazonium Electrografting

The electrografting of Ru-$\mathbf{N_2^+}$ was first optimized for TiO_2 and was then adjusted for SnO_2, ZnO, ZrO_2, and In_2O_3:Sn. A 2 mM solution of Ru-$\mathbf{NH_2}$ was reacted with an excess of *tert*-butyl-nitrite in 100 mM $TBAClO_4$ CH_3CN for 10 minutes at 0°C under argon to yield the desired Ru-$\mathbf{N_2^+}$. A constant potential ranging from +100 mV to -100 mV vs. NHE was applied for 30 min to the mesoporous nanocrystalline (anatase)TiO_2 thin film. The same procedure achieved grafting on the other MOx slides, but the applied potential that gave the highest surface coverage (termed here "optimal potential") was dependent on the identity of the MOx. Optimal potentials are presented over a 200 mV range for each MOx to account for small variations observed between samples (Table 2.1). The electrografting was nearly insensitive to whether $TBAClO_4$ or $LiClO_4$ electrolyte solutions were used. Both the period of time for which that potential was applied (from 5 to 60 minutes) and the sensitizer concentration (from 0.5 mM to 4 mM) were found to affect the sensitizer surface coverage, but increases in surface coverage were limited beyond the time and sensitizer concentration used herein, *i.e.* 30 minutes and 2 mM.

The sensitizer surface coverage, Γ, was calculated with Eq. 2.1, where ε is the sensitizer extinction coefficient (Associated Content, Fig. 2.12), A_{max} is the maximum absorbance value attained on each MOx thin film, and 1000 is a factor to convert from L to cm^3.[52]

$$\Gamma = \frac{A_{max}}{\varepsilon \times 1000} \quad (2.1)$$

The Ru-$\mathbf{N_2}^+$ data corresponds to grafting for 30 min from a 2 mM Ru-$\mathbf{N_2}^+$ solution. Surface coverage calculations were complicated by the large spectral shift observed between Ru-$\mathbf{N_2}^+$ in solution and the sensitizers grafted on the surface (Associated Content, Fig. 2.12). This means that the extinction coefficient measured for Ru-$\mathbf{N_2}^+$ gave no information about the surface coverage. To approximate surface coverage in this case, the value 17,000 M^{-1} cm^{-1} was used, assuming Ru-$\mathbf{N_2}^+$ on the surface to have a similar extinction coefficient as Ru-$\mathbf{PO_3H_2}$ and Ru-**COOH**, 17500 M^{-1} cm^{-1} and 20900 M^{-1} cm^{-1} respectively. Functionalization with Ru-$\mathbf{PO_3H_2}$ resulted in surface coverages very similar to those measured for Ru-$\mathbf{N_2}^+$ grafting, and functionalization with Ru-**COOH** consistently resulted in lower surface coverages.

Table 2.1. Surface Coverage and Absorption Maxima of the Sensitized MOx Surfaces

	Ru-$\mathbf{N_2}^+$			Ru-$\mathbf{PO_3H_2}$		Ru-**COOH**	
	Surface Coverage (mol cm^{-2} x 10^{-8})	MLCT Absorption Max (nm)	App. Potential (V vs NHE) [2]	Surface Coverage (mol cm^{-2} x 10^{-8})	MLCT Absorption Max (nm)	Surface Coverage (mol cm^{-2} x 10^{-8})	MLCT Absorption Max (nm)
TiO_2	8.8	492	0.1 – -0.1	10.5	486	2.9	486
SnO_2	5.3	492	0.225 – 0.025	3.8	486	1.7	488
ZnO	10.6	491	0.3 – 0.1	3.8	485	2.3	486
ZrO_2	4.7	490	-1.1 – -1.3	4.3	486	2.3	487
In_2O_3:Sn	10.0	491	0.1 – -0.1	7.2	485	- [3]	- [3]

The amount of grafted sensitizer was found to increase rapidly as more reducing potentials were applied (Fig. 2.3). The "turn on" potential for grafting on TiO_2, SnO_2, and ZnO was significantly more positive than the potential at which reduction of the oxide thin

[2]The range of applied potentials found to induce maximum surface coverage.

[3]Surface functionalization did not occur to an appreciable degree on In_2O_3:Sn.

films could be spectroscopically or electrochemically detected (Fig. 2.3). This behavior, however, differed for ZrO_2 and In_2O_3:Sn, for which the grafting was concurrent with current onset. At applied potentials more negative than the "turn on" potential, the surface coverages decreased in what is termed a "turn off." It should be noted that the ZrO_2 grafting did not occur until a potential more negative than the potential "turn off" for the other MOx. Interestingly, no grafting was observed when TiO_2 films were first reduced electrochemically at -1.0 V (as indicated by color change in the film) and then exposed to Ru-$\mathbf{N_2}^+$; the dark coloration associated with TiO_2 reduction was unchanged with no evidence for sensitization. Additionally, when the FTO generally exposed in mesopores was coated and blocked with $TiCl_4$ (described previously) prior to doctor-blading TiO_2, the TiO_2 films grafted Ru-$\mathbf{N_2}^+$ in the same way as films on untreated FTO.[53] Despite these curious phenomena, electrochemical grafting was successfully optimized for TiO_2, SnO_2, ZnO, ZrO_2, and In_2O_3:Sn (Table 2.1).

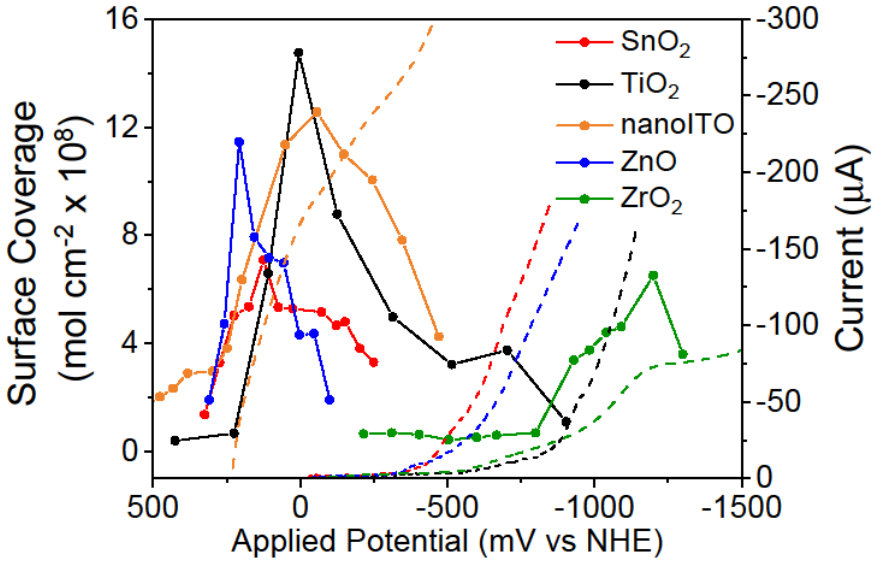

Figure 2.3. The left hand side shows the surface coverage (solid) as a function of applied potential for TiO_2 (black), SnO_2 (red), ZnO (blue), ZrO_2 (green), and In_2O_3:Sn (orange). Each data point represents a new MOx thin film, and the solid lines are present to guide the eye. The surface grafting was performed in 2 mM Ru-$\mathbf{N_2}^+$ in 100 mM $TBAClO_4$ CH_3CN for 30 min. The right-hand side shows linear voltammetry data (dashed) for each undyed MOx film. The voltammetry experiments were performed on undyed films in 100 mM $TBAClO_4$ CH_3CN.

Solution studies were performed to gain insight into chemistry in the sensitizer solutions that might account for the inability to graft at more negative applied potentials. In a typical experiment, TiO_2 thin films were submerged in relatively dilute (~0.9 mM) Ar-purged, 0˚C Ru-$\mathbf{N_2}^+$ solutions and held at potentials either more or less reducing than the ideal electrografting potential for TiO_2 (70 mV and -530 mV vs NHE) for 30 minutes, then the electrodes were removed. The UV-vis spectra of the solution before and after potential application show a significant change after the more negative potential was applied (Fig. 2.4). Similar changes occurred, albeit to a much smaller extent, at open circuit or when a less negative potential was applied. The spectrum measured after reduction bared a marked resemblance to Ru-$\mathbf{NH_2}$ or other ruthenium-bisterpyridine sensitizers (Fig. 2.4).

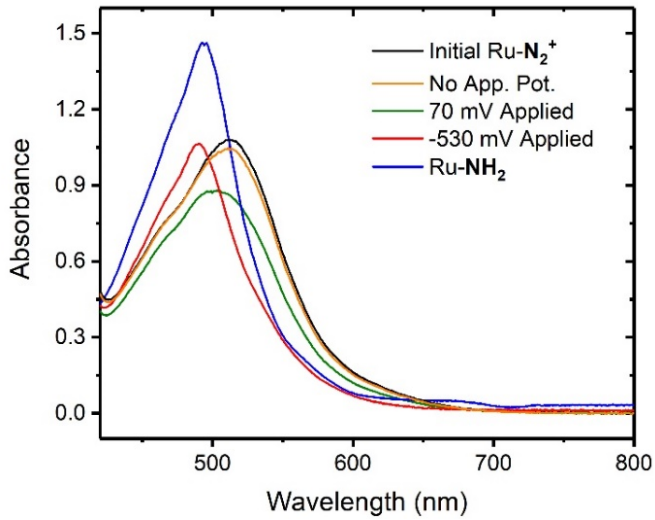

Figure 2.4. The visible absorption spectra of Ru-$\mathbf{N_2}^+$ sensitizer solutions before (black) and after 30 min of standing in solution at 0°C (orange), after applying 70 mV vs NHE (green), or after -530 mV vs NHE (red) in comparison to an equal-concentration solution of Ru-$\mathbf{NH_2}$ (blue).

Figure 2.5 shows the absorbance spectra of the sensitizers in solution and on a representative MOx surface (TiO_2). The absorption was characteristic of metal-to-ligand charge-transfer (MLCT) transitions. The MLCT maximum shifted with the nature of the binding group and was independent of MOx surface, as can be seen in Table 2.1 and Fig. 2.13 in the Associated Content section. As compared to Ru-$\mathbf{PO_3H_2}$ and Ru-**COOH**, the Ru-$\mathbf{N_2}^+$ grafted thin films displayed an MLCT absorbance that was broader and slightly red-shifted (~5 nm). It should be noted that though these absorbance values are normalized, maximum attainable surface coverages depended on the nature of the MOx and the binding group. Representative spectra illustrating surface coverages of each sensitizer on each surface are shown in the Associated Content (Fig. 2.13).

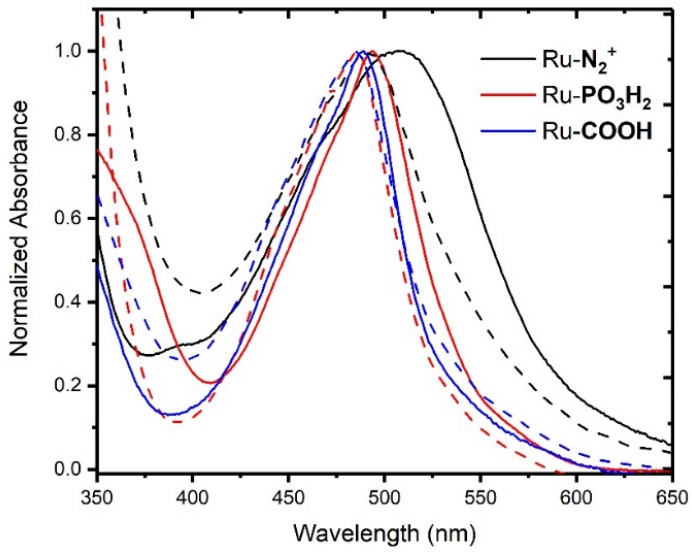

Figure 2.5. Normalized UV-vis absorbance spectra of Ru-$\mathbf{N_2}^+$ (black), Ru-$\mathbf{PO_3H_2}$ (red), and Ru-**COOH** (blue) in CH_3CN solution (solid) and anchored to TiO_2 (dashed).

2.3.2 Surface Characterization

The nature of the bonds between Ru-$\mathbf{N_2}^+$, Ru-$\mathbf{PO_3H_2}$, and Ru-**COOH** and the surfaces were analyzed by FTIR spectroscopy as solid samples and on all the MOx except In_2O_3:Sn due to its lack of transmittance between 1500 and 4000 cm^{-1}.[54,55] Solid samples of the sensitizers exhibited three characteristic peaks between 2850 and 2970 cm^{-1} corresponding to stretches of the three sensitizer *tert*-butyl groups, a C=C stretching peak at 1610 cm^{-1}, and many shared peaks in the fingerprint region that were independent of the binding group, (Fig. 2.6). Several of these peaks were also present on the sensitized MOx surfaces, but were not present in spectra of unsensitized MOx films, i.e. vibrations at 2960, 2910, 2870, 1610, and 1400 cm^{-1}. These peaks were common to all grafted MOx surfaces. The majority of the peaks are sharp and clear in the solid ruthenium sensitizers, however, they are significantly broadened and decreased in intensity on the MOx surfaces. Individual peaks are difficult to assign in the 1750-1500 cm^{-1} region for the different metal oxides. However, the broad and sharp absorbance peaks in this region that are metal oxide

independent likely correspond to sensitization. In addition to peaks shared between ruthenium sensitizers regardless of binding group, sharp peaks were observed in solid Ru-$\mathbf{N_2}^+$ at 2266 and 3320 cm^{-1} that were not present when Ru-$\mathbf{N_2}^+$ was grafted to any MOx surface. Ru-**COOH** sensitized MOx films displayed usually sharp C=O stretching peaks at 1730 cm^{-1}, but this peak was notably broader on TiO_2. Additionally, a peak at 1544 cm^{-1} was present on all MOx surfaces grafted with Ru-$\mathbf{N_2}^+$ that did not appear in the solid sample or on surfaces functionalized with Ru-$\mathbf{PO_3H_2}$ or Ru-**COOH.**

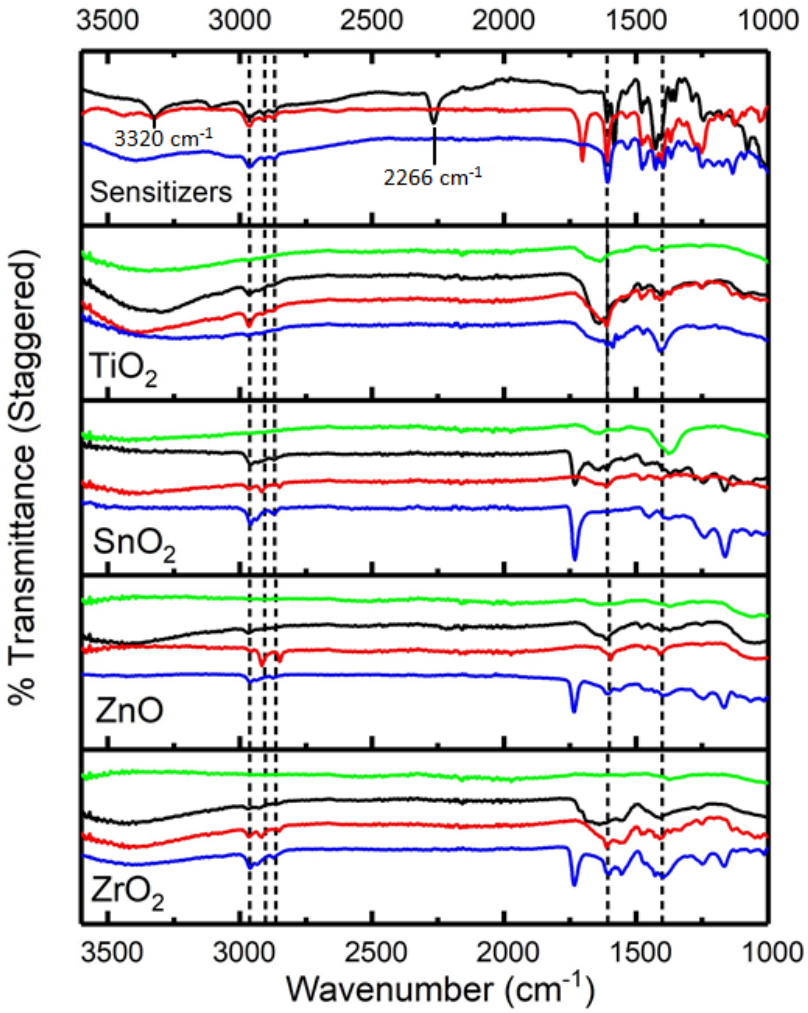

Figure 2.6. FTIR spectra of the ruthenium sensitizers before (top) and after sensitization of a metal oxide surface. Unsensitized films (green) are compared to Ru-$\mathbf{N_2}^+$ (black), Ru-$\mathbf{PO_3H_2}$ (red), and Ru-**COOH** (blue) on each examined MOx. Common peaks between the surfaces are marked by dashed lines (2960, 2910, 2870, 1610, and 1400 cm^{-1}).

The XPS spectra of Ru-$\mathbf{N_2}^+$ grafted to TiO_2 (Fig. 2.7) showed the presence of a peak at 285.0 eV that has been attributed to Ru 3d as well as the absence of a diazonium peak at 403.8 eV.[28,56] Titanium peaks in the XPS spectra were standard for TiO_2, with no peak present that would be indicative of Ti(III) or a Ti-C bond (455 eV).[36,56,57] A peak at 531.6 eV representing a Ti-O-C bond was present on TiO_2 films sensitized with Ru-$\mathbf{N_2}^+$ that was absent on unsensitized TiO_2 films and TiO_2 films sensitized with Ru-$\mathbf{PO_3H_2}$ and Ru-**COOH**.[58–61] XPS spectra of SnO_2, ZnO, and ZrO_2 (Associated Content, Fig. 2.14) also show no detectable change in oxidation state of the metal in the film, the presence of a Ru 3d peak, and the absence of diazonium peak. These features all indicate similar binding on all MOx.[62]

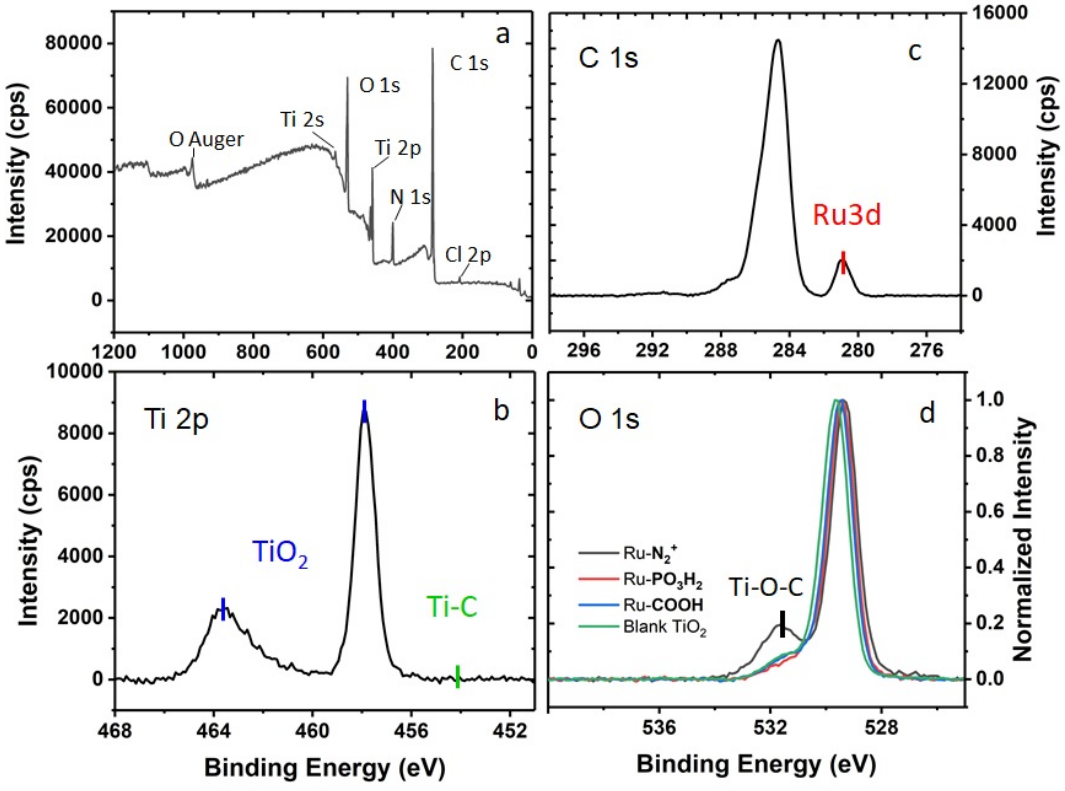

Figure 2.7. The XPS spectra of Ru-$\mathbf{N_2}^+$ sensitized TiO_2. a) Spectra from 0 to 1200 eV. b) High resolution Ti 2p region with characteristic TiO_2 peaks marked in blue and absent Ti-C peak marked in green. c) High resolution C 1s region of the spectra with characteristic Ru 3d peak marked in red. d) High resolution O 1s region with overlaid spectra (intensity normalized) for Ru-$\mathbf{N_2}^+$ (black), Ru-$\mathbf{PO_3H_2}$ (red), Ru-**COOH** (blue) and blank TiO_2 (green) with characteristic peak for Ti-O-C marked in black.

The Ru(III/II) reduction potentials of both Ru-$\mathbf{PO_3H_2}$ and the electrografted Ru-$\mathbf{N_2^+}$ on MOx surfaces were measured by spectroelectrochemistry on In_2O_3:Sn at pH 1, 5, and 10 in aqueous solution and found to be $E_{1/2} = 1.07 \pm 0.02$ mV vs. NHE. Note that desorption of Ru-$\mathbf{PO_3H_2}$ was observed while performing measurements at alkaline pHs.

2.3.3 Surface Stability

Figure 2.8 shows the relative stability of Ru-$\mathbf{N_2^+}$ and Ru-$\mathbf{PO_3H_2}$ grafted on TiO_2 in aqueous solutions of pH= 7, 10, and 12. Once bound to the surface, the diazonium sensitizers were remarkably stable. Even when immersed in saturated NaOH solution for several days, no notable desorption of diazonium-grafted sensitizers was observed. In short time scale experiments (up to 6 hours) in the dark, Ru-$\mathbf{N_2^+}$ stability on TiO_2 was monitored up to pH 12. Ru-$\mathbf{N_2^+}$ remained stable on the surface under all examined conditions, while Ru-$\mathbf{PO_3H_2}$ at pH 7 desorbed by more than 50% in less than one minute as measured at the MLCT absorbance (Fig. 2.8a). In an analogous fashion, Ru-**COOH** desorbed immediately at pHs greater than 5 (not shown). Under constant illumination (455 nm light, 100 mW/cm^2) for 24 hours at pH 12, Ru-$\mathbf{N_2^+}$ maintained >97% surface coverage as measured by the MLCT absorbance and displayed no spectral shifts (Fig. 2.8b). Full spectra over 24 hours under illumination are shown in Associated Content, Fig. 2.15.

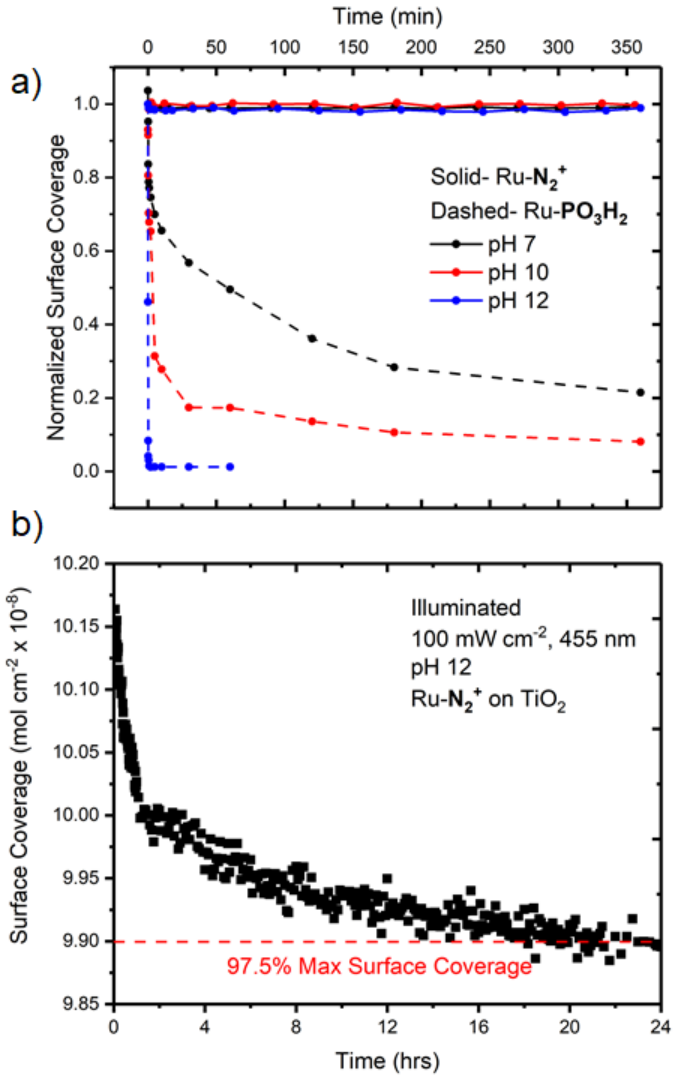

Figure 2.8. Surface coverage as monitored at the respective MLCT absorbances versus time for a) non-illuminated and b) illuminated sensitized TiO_2. In a) Ru-$\mathbf{N_2}^+$ (solid) was compared to Ru-$\mathbf{PO_3H_2}$ (dashed) while immersed at pH 7 (black), pH 10 (red), and pH 12 (blue) aqueous solutions over 6 hours. In b) Ru-$\mathbf{N_2}^+$ was illuminated with 455 nm, 100 mW/cm^2 light over 24 hours while immersed in pH 12 solution.

2.3.4 Sensitized Thin Film Photocurrents

Photocurrents produced by the sensitizer MOx were measured under 1 Sun illumination with 200 mV applied potential in the presence of 50 mM electron donor (hydroquinone at pH 5 and triethanolamine at pH 12). Small photocurrents were measured on TiO_2 with either Ru-$\mathbf{N_2}^+$ or Ru-$\mathbf{PO_3H_2}$. To enhance the photocurrent amplitude, SnO_2, with a

conduction band ~500 mV more positive than TiO_2, was used. With sensitized SnO_2, significantly larger photocurrents were attained despite lower surface coverage. The sensitized SnO_2 photocurrents were thus considered further. Though photocurrents measured in alkaline conditions were small, at pH 12 the Ru-$\mathbf{N_2^+}$ grafted SnO_2 films produced and maintained photocurrents for >4 hours with little loss (<25%) (Fig. 2.9). It should be noted that in Figure 2.9, the initial peak as the light was turned on was reproducible. It is a commonly-seen feature in sensitized interfaces in aqueous solution and has been attributed to electrode polarization.[63–66] UV-Visible absorption data clearly show that this initial photocurrent signature does not result from sensitizer desorption. At pH 5, photocurrents were measured for both TiO_2 and SnO_2. Both Ru-$\mathbf{N_2^+}$ and Ru-$\mathbf{PO_3H_2}$ were stable on the surface on the time-scales employed. Photocurrent densities were normalized for the sensitizer surface coverages. Surprisingly, Ru-$\mathbf{PO_3H_2}$ produced 7x the current of Ru-$\mathbf{N_2^+}$ on SnO_2 and almost 30x the current of Ru-$\mathbf{N_2^+}$ on TiO_2 (Fig. 2.9). This stark binding group-dependence was replicable across all pH values at which Ru-$\mathbf{PO_3H_2}$ was reasonably stable on the surface on the timescales of the experiments (30 min, up to pH 8). Ru-**COOH** was not included for comparison because significant desorption occurred above pH 5.

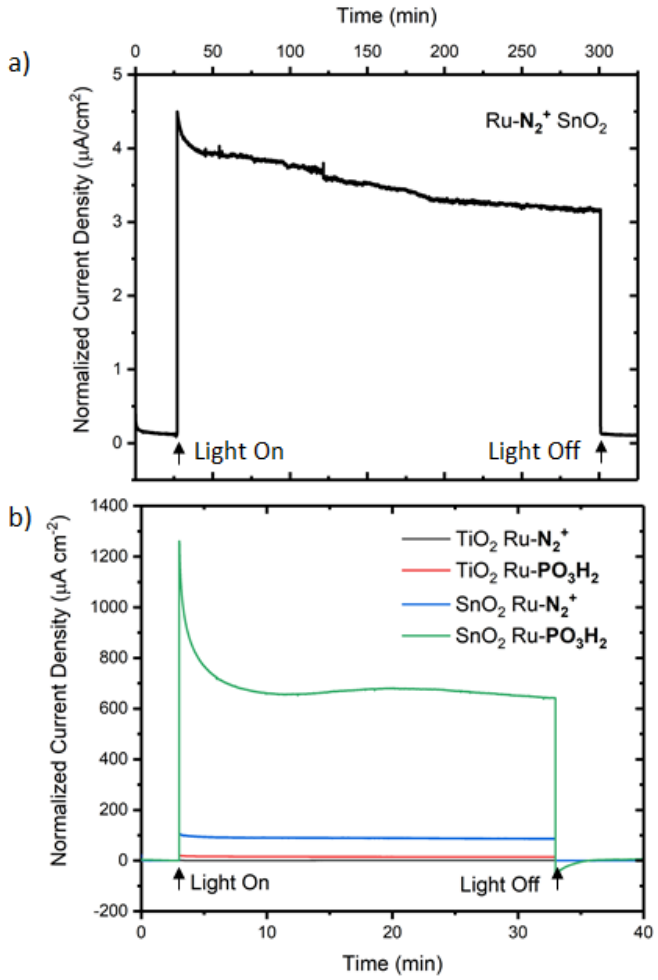

Figure 2.9. a) Sustained photocurrent density normalized for surface coverage measured at pH 12 for SnO_2 grafted with Ru-$\mathbf{N_2}^+$. b) Photocurrent densities normalized for surface coverage on TiO_2 with Ru-$\mathbf{N_2}^+$ (black), TiO_2 with Ru-$\mathbf{PO_3H_2}$ (red), SnO_2 with Ru-$\mathbf{N_2}^+$ (blue), and SnO_2 with Ru-$\mathbf{PO_3H_2}$ (green) were measured at pH 5. In both cases, photocurrent densities were measured under 1 Sun illumination in aqueous 0.1 M acetate buffer, 0.5 M $NaClO_4$, 50 mM sacrificial electron donor (hydroquinone at pH 5, triethanolamine at pH 12).

2.4 Discussion

There are very few fundamental studies that report on the grafting of diazonium-based compounds to MOx colloids or thin films.[27,36–40] For example, viologen phenyl diazonium salts have recently been grafted on TiO_2 for the development of electrochromic materials.[40] These studies have shown the grafting process to be possible, but their use in

solar devices is limited.[36] The functionality and stability of these grafted MOxs has not been, to our knowledge, previously examined.[27,36–40] Here, the synthesis of three structurally related ruthenium sensitizers are reported that differ only by the anchoring group; Ru-$\mathbf{N_2^+}$, Ru-$\mathbf{PO_3H_2}$, and Ru-**COOH**. The electrochemical grafting procedure reported for Ru-$\mathbf{N_2^+}$ enabled meaningful comparisons of all three sensitizers on mesoporous MOx thin films composed of TiO_2, SnO_2, ZrO_2, ZnO, and In_2O_3:Sn nanoparticles. Most notably, the diazonium-grafted MOx films were stable in highly alkaline conditions, including saturated NaOH solution. Below we describe a proposed mechanism for the diazonium electrografting and the remarkable stability toward surface hydrolysis.

Attenuated total reflectance FTIR measurements showed that the sensitized thin films that were not highly sensitive to the identity of the MOx or binding group. Some peak shifts and differences in intensity and linewidth were observed, but most clear peaks could be found in common between all MOx and binding methods. The low intensity bands measured on the MOx surface made further assignment ambiguous. Spectra of solid Ru-$\mathbf{N_2^+}$ exhibited intense peaks at 2266 and 3320 cm^{-1}, regions in which diazonium stretches are known to occur.[57,67] These peaks were absent when Ru-$\mathbf{N_2^+}$ was grafted to a MOx surface, indicating that the sensitizer grafted by removal of the $-N_2^+$ group, as seen previously in diazonium grafting of organic compounds.[26,27,36] The XPS data confirmed that grafting successfully occurred through the presence of a Ru 3d peak at 281 eV.[56] The Ti 2p peaks were in good agreement with literature values for TiO_2 (464 eV and 458 eV),[56,68] with no evidence of Ti-C bond formation that is known to give rise to a peak at 455 eV.[36] A significant band ascribed to a Ti-O-C bond was observed at 531.6 eV on films grafted with Ru-$\mathbf{N_2^+}$ that has been previously reported.[58,59,61] This band was absent in unsensitized TiO_2 thin films or those

sensitized with Ru-**PO_3H_2** and Ru-**COOH**. Taken together, this data indicates that Ru-**N_2^+** formed a M-O-C bond with terminal oxygen in the lattice of TiO_2 and other MOx, as has been reported previously.[36] Importantly, this M-O-C bond is covalent, in contrast to dative bonds that are often thought to for between phosphonic or carboxylic acids and MOx materials. This is likely responsible for the greater stability of grafted Ru-**N_2^+**.

In other instances of diazonium electrografting, azo coupling has been reported to form of multilayers of the grafted molecular species, but evidence suggests that this did not occur here.[26,28,36] Most directly, the surface coverage for Ru-**N_2^+** on electrografted MOx films reached a plateau with time with maximum attainable values similar to surface coverages measured for Ru-**PO_3H_2** sensitized films. Electrografting for times longer than ~30 min did not result in increased sensitizer surface coverage. However, FTIR and XPS evidence was inconclusive with regard to the question of azo coupling. The FTIR spectra of all MOx surfaces grafted with Ru-**N_2^+** exhibited a peak at 1544 cm^{-1} that is in the azo (1490-1550 cm^{-1}) and C=C stretching regions.[69] In the N 1s region of XPS spectra of all Ru-**N_2^+**-grafted MOx surfaces, a shoulder was present (~399 eV) that was not present for Ru-**PO_3H_2** sensitized films. This may correspond to terpyridine ligands that are not complexed to Ru on the surface, as previously reported.[25,70] Taken together this evidence precludes a definitive claim of no azo coupling in Ru-**N_2^+** grafted sensitizer layers, but the observed maximum surface coverage implies that it was either limited or absent.

Figure 2.10 displays the proposed reaction mechanism between Ru-**N_2^+** and the MOx surface, which is supported by previous work.[36] Electrochemical diazonium grafting is proposed to occur when the $-N_2^+$ group was removed by one electron reduction (1 in Fig. 2.10) to generate an aryl radical that subsequently abstracted a hydrogen atom from the MOx

surface (2 in Fig. 2.10). The newly formed surface oxygen radical is then proposed to react with a second aryl radical in solution to form a MOx-O-aryl-Ru bond (3 in Fig. 2.10). Though we propose here that two diazonium sensitizers are involved in this reaction, we cannot exclude the possibility that steps 2 and 3 in Fig. 2.10 might occur in a single concerted step involving a solvent molecule.

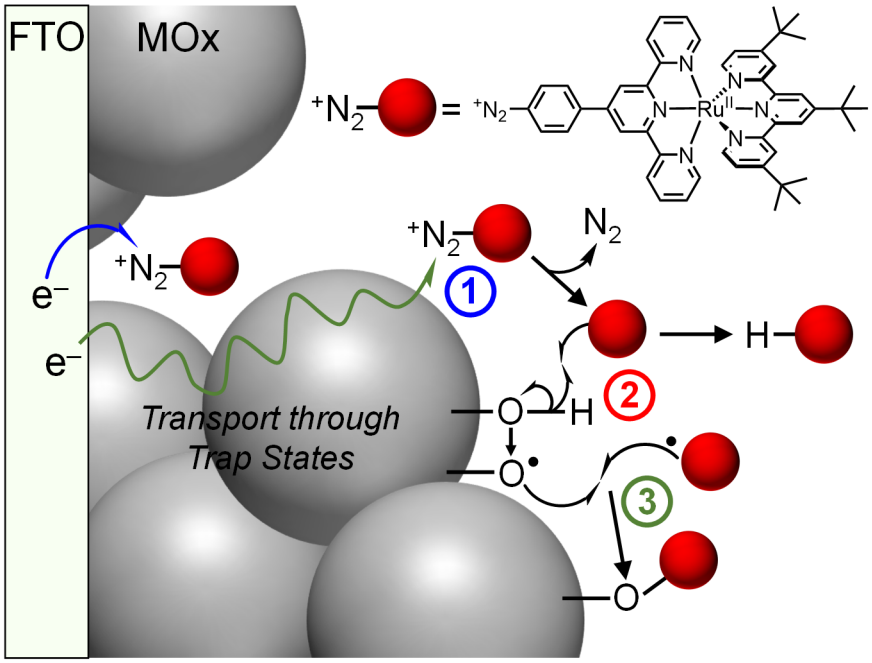

Figure 2.10. Proposed electrografting mechanism for Ru-$\mathbf{N_2^+}$ with a FTO-MOx surface. The grafting occurs at the FTO (blue arrow) or by electrons in trap states (green arrow). Upon reduction of Ru-$\mathbf{N_2^+}$ (step 1), N_2 gas is released and an aryl radical is formed that abstracts a hydrogen atom from a surface hydroxyl group to yield an unreactive ruthenium sensitizer and an M-O$^{\bullet}$ radical (step 2). The oxygen radical then reacts with another aryl radical generated by surface reduction (step 1) to form the covalent M-O-C(aryl) bond (step 3). The possibility that steps 2 and 3 occur in one concerted step cannot be ruled out, nor can the possibility of CH_3CN as a H atom source.

The observation of an MOx dependent "optimal potential" range for maximum surface coverage provided additional insights into the grafting mechanism. For TiO_2, SnO_2, and ZnO, Ru-$\mathbf{N_2^+}$ grafting was initiated at potentials significantly more positive than the potential at which reduction of the MOx thin films was observed by electrochemical or spectroscopic means. Electrografting was then absent at more negative potentials. To

rationalize this “turn on” potential, it is hypothesized that a few electrons in deep trap states initiate the grafting reaction chemistry. This is consistent with grafting dependent on the MOx identity, as the onset potentials were correlated with the onset of MOx reduction as measured by linear voltammetry. Diazonium reduction could occur at the FTO substrate (Fig. 2.10), but limited numbers of radicals could be produced in this way as the exposed FTO surface area is small. It was shown that initiation did not solely occur at the FTO, as FTO substrates that had been treated with $TiCl_4$ to block FTO exposure were sensitized through Ru-$\mathbf{N_2}^+$ electrografting to the same extent as untreated slides.

To better understand the “turn off” potential, unsensitized TiO_2 films were reduced at a potential of ~-1 V vs NHE. The black coloration of the films was maintained as the applied potential was removed and an argon purged Ru-$\mathbf{N_2}^+$ solution was introduced. No evidence for sensitization to the surface was observed. This indicates that electrons within the TiO_2 films were not sufficient to complete the electrografting reaction and may have inhibited the productive reactions observed when only a few electrons were present. While speculative, it may be that the electrons present in the reduced MOx thin films rapidly react with the surface radicals generated in steps 2 and/or 3 in Fig. 2.10, thereby inhibiting formation of the O-C bonds. It is also possible that the increased numbers of electrons in the films at more reducing potentials increase the Ru-$\mathbf{N_2}^+$ degradation reaction rates. This possibility is supported by the spectral change in Ru-$\mathbf{N_2}^+$ solutions observed upon application of a potential more negative than the “turn off” potential. This is also consistent with the “turn off” dependence on the MOx identity, especially the much more reducing potential required to both “turn on” and “turn off” grafting in the insulating ZrO_2. This is consistent with the

relative density of states for each material and the necessity of available redox-active states to provide electrons for Ru-$\mathbf{N_2}^+$ electrografting.

The Ru-$\mathbf{N_2}^+$ grafted MOx thin films were remarkably stable in alkaline solution, with no observed desorption of sensitizers during storage in aqueous pH 12 solution for months. Films left for several days in saturated NaOH were still highly colored, yet complete desorption of Ru-$\mathbf{PO_3H_2}$ and Ru-$\mathbf{CO_2H}$ was apparent. Under 100 mW/cm^2 irradiation for 24 hours at pH 12, >97% of the initial Ru-$\mathbf{N_2}^+$ grafted TiO_2 surface coverage was maintained. Photocurrents also displayed high stability. Sustained photocurrents were measured for Ru-$\mathbf{N_2}^+$ on SnO_2 for >4 hours at pH 12. With more acidic conditions, comparative studies with Ru-$\mathbf{PO_3H_2}$ were possible, and the photocurrent were found to be significantly larger for Ru-$\mathbf{PO_3H_2}$ than those for Ru-$\mathbf{N_2}^+$. This may arise from weaker electronic coupling to the Ti sites resulting in fewer injected electrons. It may also result from stronger electronic coupling from the covalent bonds resulting in fast back electron transfer and a net decrease in photocurrent. If diazonium electrografting and the excellent alkaline stability that it instantiates is to be leveraged for DSPEC applications, either photo-initiated injection yields on nanosecond time-scales must be understood and optimized.

2.5 Conclusions

In conclusion, electrografting of a diazonium-substituted sensitizer was successfully performed on a range of MOx surfaces (TiO_2, SnO_2, ZnO, ZrO_2, and In_2O_3:Sn). The observed stability in alkaline conditions represents a substantial advance from the state-of-the-art. Indeed, comparative studies with equivalent sensitizers with -COOH and -PO_3H_2 anchoring groups were found to be only stable up to pH 4 and pH 7, respectively. Though

recent explorations of hydroxamic acid and silatrane anchoring groups have suggested they may be stable in alkaline conditions, they may not be optimal for all DSPEC applications.[7] Films sensitized with Ru-$\mathbf{N_2}^+$ studied in this Chapter show remarkable stability at pH 12 and beyond. The stability that diazonium-grafted Ru-based sensitizers offer in alkali conditions allows for MOx sensitization and anchoring of water oxidation catalysts in conditions at which water splitting is most thermodynamically accessible. In addition, the versatility of this electrografting technique to many oxide interfaces presents an opportunity for applications outside of solar energy conversion.

2.6 Acknowledgements

This material is based upon work solely supported as part of the UNC EFRC: Center for Solar Fuels, an Energy Frontier Research Center funded by the U.S. Department of Energy, Office of Science, Office of Basic Energy Sciences under Award Number DE-SC0001011. The authors thank the University of North Carolina Department of Chemistry Mass Spectrometry Core Laboratory and Dr. B. Ehrmann for assistance with mass spectrometry analysis. This work was performed in part at the Chapel Hill Analytical and Nanofabrication Laboratory, CHANL, a member of the North Carolina Research Triangle Nanotechnology Network, RTNN, which is supported by the National Science Foundation, Grant ECCS-1542015, as part of the National Nanotechnology Coordinated Infrastructure, NNCI.

2.7 Associated Content

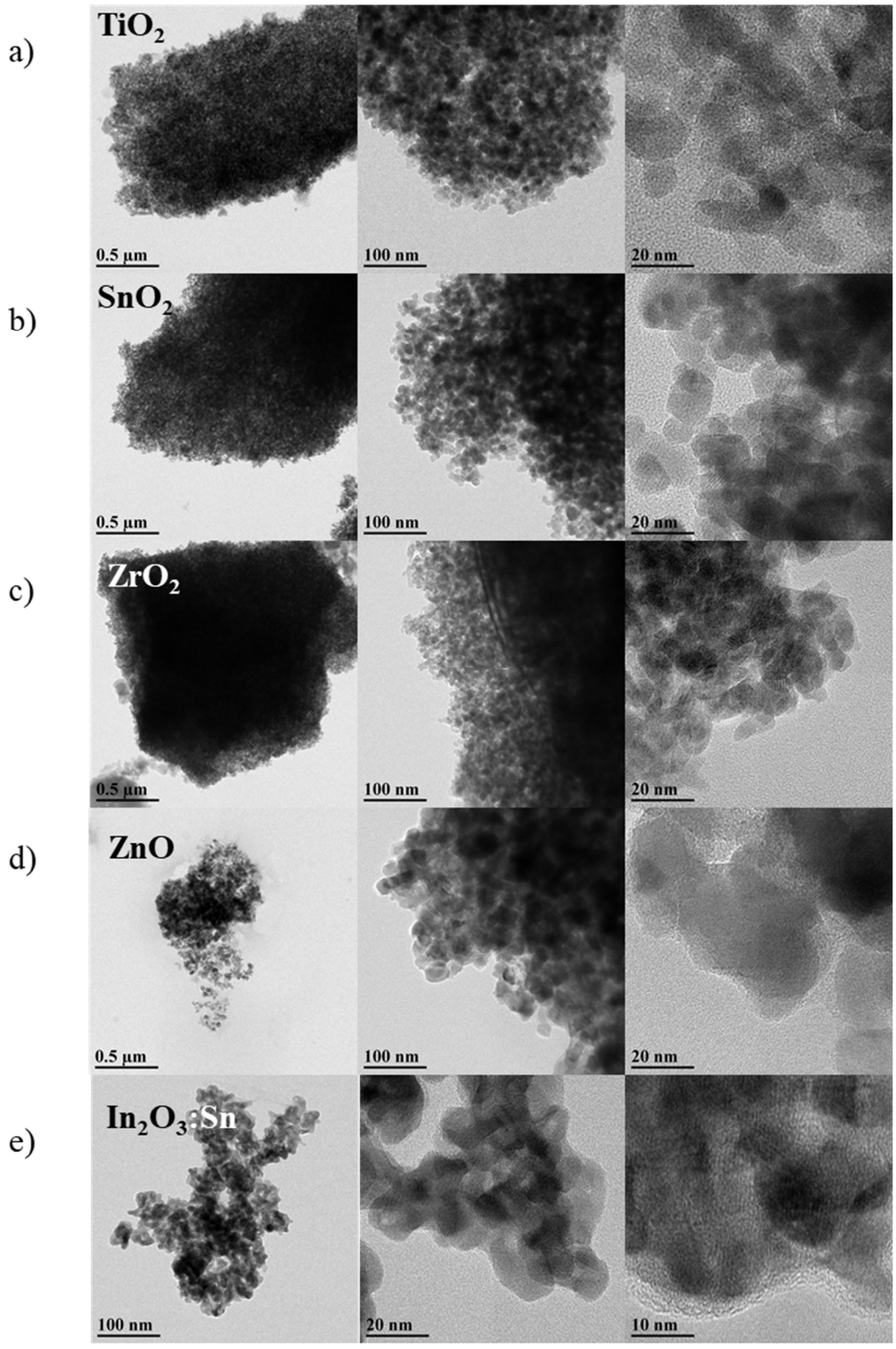

Figure 2.11. TEM images of MOx nanoparticles scraped from thin films. Types of MOx are separated as a) TiO_2, b) SnO_2, c) ZrO_2, d) ZnO, and e) In_2O_3:Sn.

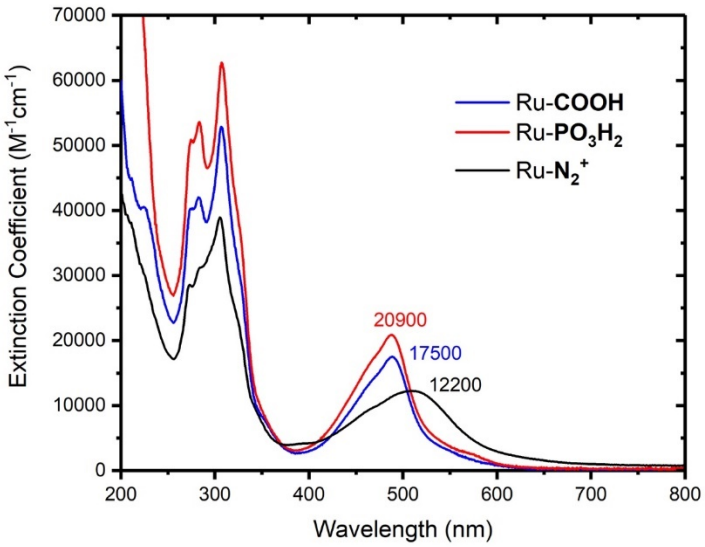

Figure 2.12. Extinction coefficients of Ru-$\mathbf{N_2}^+$ (black), Ru-$\mathbf{PO_3H_2}$ (red), and Ru-**COOH** (blue) dissolved in CH_3CN.

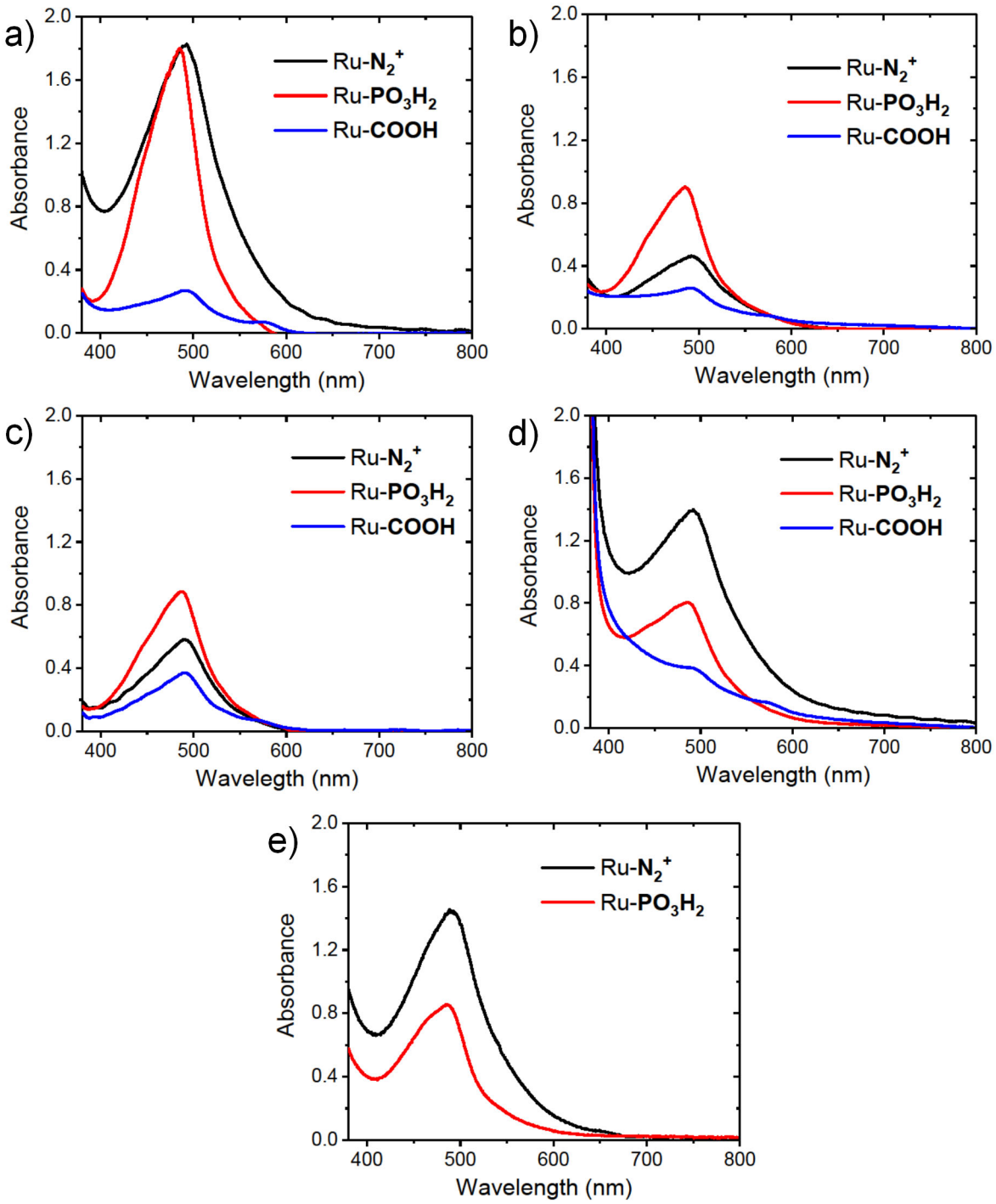

Figure 2.13. UV-Vis absorbance spectra of sensitized MOx surfaces showing relative absorbance intensity. Ru-$\mathbf{N_2}^+$ (black), Ru-$\mathbf{PO_3H_2}$ (red), and Ru-**COOH** (blue) are shown for a) TiO_2, b) SnO_2, c) ZrO_2, d) ZnO, and e) In_2O_3:Sn. Ru-$\mathbf{N_2}^+$ grafted films were made by electrografting at held potentials given in Table 2.1 using a 2 mM Ru-$\mathbf{N_2}^+$ solution in 100 mM $TBAClO_4$ CH_3CN for 30 min. Ru-$\mathbf{PO_3H_2}$ and Ru-**COOH** were adsorbed by soaking films in concentrated solutions in CH_3CN.

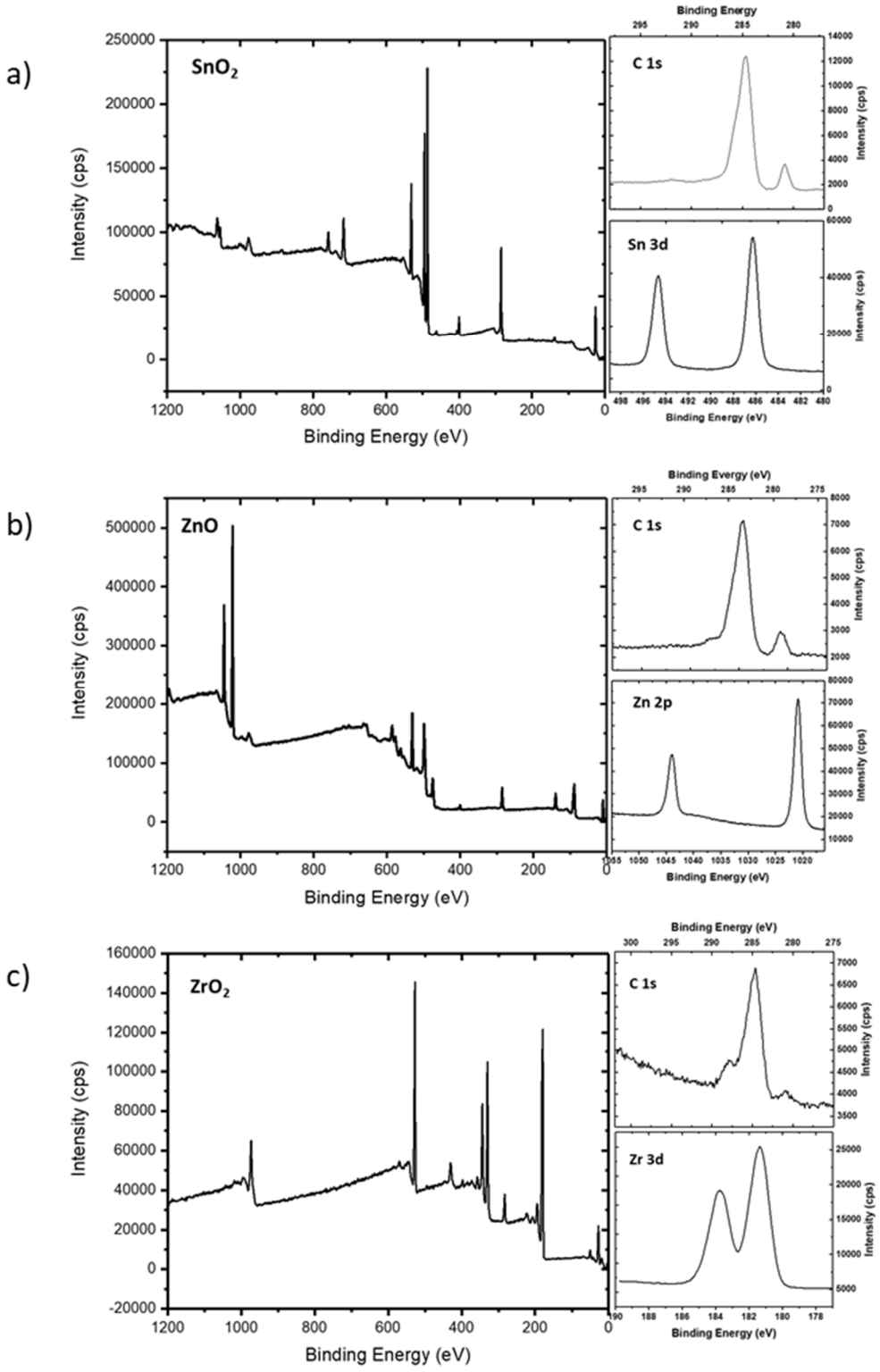

Figure 2.14. XPS spectra of a) SnO_2, b) ZnO, and c) ZrO_2 films sensitized with Ru-$\mathbf{N_2}^+$. High-definition spectral regions verify the presence of the sensitizer through the presence of a Ru 3d peak (C1s) and show no detectable change in oxidation state of the metal.

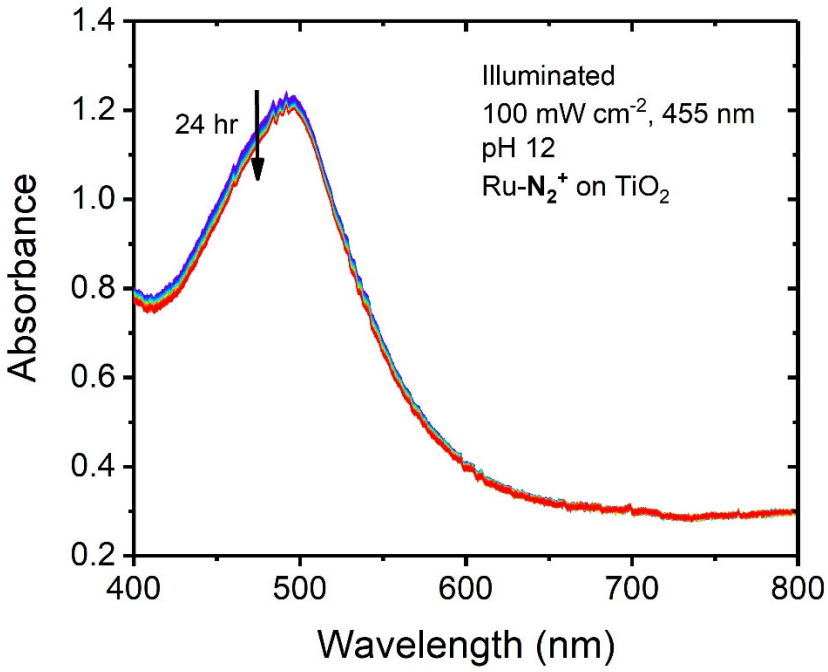

Figure 2.15. UV-visible spectra of Ru-$\mathbf{N_2}^+$ sensitized TiO_2 in pH 12 aqueous solution as it is illuminated with 455 nm, 100 mW cm^{-2} light over 24 hrs. No spectral shift is observed, and little change in absorbance occurs.

REFERENCES

(1) Desilvestro, J.; Haas, O. Metal Oxide Cathode Materials for Electrochemical Energy Storage: A Review. *J. Electrochem. Soc.* **1990**, *137*, 5C–22C.

(2) Ohta, H.; Hosono, H. Transparent Oxide Optoelectronics. *Mater. Today* **2004**, 42–51.

(3) Kolmakov, A.; Moskovits, M. Chemical Sensing and Catalysis by One-Dimensional Metal-Oxide Nanostructures. *Annu. Rev. Mater. Res.* **2004**, *34*, 151–180.

(4) Hagfeldt, A.; Boschloo, G.; Sun, L.; Kloo, L.; Pettersson, H. Dye-Sensitized Solar Cells. *Chem. Rev.* **2010**, *110*, 6595–6663.

(5) Alibabaei, L.; Luo, H.; House, R. L.; Hoertz, P. G.; Lopez, R.; Meyer, T. J. Applications of Metal Oxide Materials in Dye Sensitized Photoelectrosynthesis Cells for Making Solar Fuels: Let the Molecules Do the Work. *J. Mater. Chem. A* **2013**, *1*, 4133–4145.

(6) Brennaman, M. K.; Dillon, R. J.; Alibabaei, L.; Gish, M. K.; Dares, C. J.; Ashford, D. L.; House, R. L.; Meyer, G. J.; Papanikolas, J. M.; Meyer, T. J. Finding the Way to Solar Fuels with Dye-Sensitized Photoelectrosynthesis Cells. *J. Am. Chem. Soc.* **2016**, *138*, 13085–13102.

(7) Materna, K. L.; Crabtree, R. H.; Brudvig, G. W. Anchoring Groups for Photocatalytic Water Oxidation on Metal Oxide Surfaces. *Chem. Soc. Rev.* **2017**, *46*, 6099–6110.

(8) Brennan, B. J.; Llansola Portolés, M. J.; Liddell, P. A.; Moore, T. A.; Moore, A. L.; Gust, D. Comparison of Silatrane, Phosphonic Acid, and Carboxylic Acid Functional Groups for Attachment of Porphyrin Sensitizers to TiO_2 in Photoelectrochemical Cells. *Phys. Chem. Chem. Phys.* **2013**, *15*, 16605–16614.

(9) Zhang, L.; Cole, J. M. Anchoring Groups for Dye-Sensitized Solar Cells. *ACS Appl. Mater. Interfaces* **2015**, *7*, 3427–3455.

(10) Hanson, K.; Brennaman, M. K.; Luo, H.; Glasson, C. R. K.; Concepcion, J. J.; Song, W.; Meyer, T. J. Photostability of Phosphonate-Derivatized, Ru^{II} Polypyridyl Complexes on Metal Oxide Surfaces. *ACS Appl. Mater. Interfaces* **2012**, *4*, 1462–1469.

(11) Hyde, J. T.; Hanson, K.; Vannucci, A. K.; Lapides, A. M.; Alibabaei, L.; Norris, M. R.; Meyer, T. J.; Harrison, D. P. Electrochemical Instability of Phosphonate-Derivatized, Ruthenium(III) Polypyridyl Complexes on Metal Oxide Surfaces. *ACS Appl. Mater. Interfaces* **2015**, *7*, 9554–9562.

(12) O'Regan, B.; Grätzel, M. A Low-Cost, High-Efficiency Solar Cell Based on Dye-Sensitized Colloidal TiO_2 Films. *Nature* **1991**, *353*, 737–740.

(13) Clark, W. D. K.; Sutin, N. Spectral Sensitization of N-Type TiO_2 Electrodes by Polypyridineruthenium(II) Complexes. *J. Am. Chem. Socitey* **1977**, *99*, 4676–4682.

(14) Sprintschnik, G.; Sprintschnik, H. W.; Kirsch, P. P.; Whitten, D. G. Preparation and Photochemical Reactivity of Surfactant Ruthenium(II) Complexes in Monolayer Assemblies and at Water-Solid Interfaces. *J. Am. Chem. Soc.* **1977**, *99*, 4947–4954.

(15) Kirsch-De Mesmaeker, A.; Nasielski, J.; Willem, R. Photoelectrochemistry of $Ru(bpy)_3^{2+}$ in Basic Medium at SnO_2 and Metal Electrodes. *Bull. Soc. Chim. Belg.* **1982**, *91*, 731–742.

(16) Memming, R.; Schröppel, F. Electron Transfer Reactions of Excited Ruthenium(II) Complexes in Monolayer Assemblies at the SnO_2-Water Interface. *Chem. Phys. Lett.* **1979**, *62*, 207–210.

(17) Goodenough, J. B.; Hamnett, A.; Dare-Edwards, M. P.; Campet, G.; Wright, R. D. Inorganic Materials for Photoelectrolysis. *Surf. Sci.* **1980**, *101*, 531–540.

(18) Garcia, C. G.; Iha, M. Y. N.; Argazzi, R.; Bignozzi, C. A. 4-Phenylpyridine as Ancillary Ligand in Ruthenium(II) Polypyridyl Complexes for Sensitization of N-Type TiO_2 Electrodes. *J. Photochem. Photobiol. A Chem.* **1998**, *115*, 239–242.

(19) Hamnet, A.; Dare-Edwards, M. P.; Wright, R. D.; Seddon, K. R.; Goodenough, J. B. Photosensitization of Titanium(IV) Oxide with Tris(2,2'-bipyridine)ruthenium(II) Chloride. Surface States of Titanium(IV) Oxide. *J. Phys. Chem.* **1979**, *83*, 3280–3290.

(20) Brewster, T. P.; Konezny, S. J.; Sheehan, S. W.; Martini, L. A.; Schmuttenmaer, C. A.; Batista, V. S.; Crabtree, R. H. Hydroxamate Anchors for Improved Photoconversion in Dye-Sensitized Solar Cells. *Inorg. Chem.* **2013**, *52*, 6752–6764.

(21) Warnan, J.; Guerin, V. M.; Anne, F. B.; Pellegrin, Y.; Blart, E.; Jacquemin, D.; Pauporté, T.; Odobel, F. Ruthenium Sensitizer Functionalized by Acetylacetone Anchoring Groups for Dye-Sensitized Solar Cells. *J. Phys. Chem. C* **2013**, *117*, 8652–8660.

(22) Gou, F.; Jiang, X.; Li, B.; Jing, H.; Zhu, Z. Salicylic Acid as a Tridentate Anchoring Group for Azo -Bridged Zinc Porphyrin in Dye-Sensitized Solar Cells. *ACS Appl. Mater. Interfaces* **2013**, *5*, 12631–12637.

(23) Szpakolski, K.; Latham, K.; Rix, C.; Rani, R. A.; Kalantar-Zadeh, K. Silane: A New Linker for Chromophores in Dye-Sensitised Solar Cells. *Polyhedron* **2013**, *52*, 719–732.

(24) Takijiri, K.; Morita, K.; Nakazono, T.; Sakai, K.; Ozawa, H. Highly Stable Chemisorption of Dyes with Pyridyl Anchors over TiO_2: Application in Dye-Sensitized Photoelectrochemical Water Reduction in Aqueous Media. *Chem. Commun.* **2017**, *53*, 3042–3045.

(25) Mahmoud, A. M.; Bergren, A. J.; McCreery, R. L. Derivatization of Optically Transparent Materials with Diazonium Reagents for Spectroscopy of Buried Interfaces. *Anal. Chem.* **2009**, *81*, 6972–6980.

(26) Pinson, J.; Podvorica, F. Attachment of Organic Layers to Conductive or Semiconductive Surfaces by Reduction of Diazonium Salts. *Chem. Soc. Rev.* **2005**, *34*, 429–439.

(27) Brymora, K.; Fouineau, J.; Eddarir, A.; Chau, F.; Yaacoub, N.; Grenèche, J. M.; Pinson, J.; Ammar, S.; Calvayrac, F. Grafting of Diazonium Salts on Oxides Surface: Formation of Aryl-O Bonds on Iron Oxide Nanoparticles. *J. Nanoparticle Res.* **2015**, *17*, 438.

(28) Troian-Gautier, L.; Martínez-Tong, D. E.; Hubert, J.; Reniers, F.; Sferrazza, M.; Mattiuzzi, A.; Lagrost, C.; Jabin, I. Controlled Modification of Polymer Surfaces through Grafting of Calix[4]arene-Tetradiazoate Salts. *J. Phys. Chem. C* **2016**, *120*, 22936–22945.

(29) Garrett, D. J.; Jenkins, P.; Polson, M. I. J.; Leech, D.; Baronian, K. H. R.; Downard, A. J. Diazonium Salt Derivatives of Osmium Bipyridine Complexes: Electrochemical Grafting and Characterisation of Modified Surfaces. *Electrochim. Acta* **2011**, *56*, 2213–2220.

(30) Troian-Gautier, L.; Valkenier, H.; Mattiuzzi, A.; Jabin, I.; Van Den Brande, N.; Van Mele, B.; Hubert, J.; Reniers, F.; Bruylants, G.; Lagrost, C.; Leroux, Y. Extremely Robust and Post-Functionalizable Gold Nanoparticles Coated with calix[4]arenes via Metal–carbon Bonds. *Chem. Commun.* **2016**, *52*, 10493–10496.

(31) Sayed, S. Y.; Bayat, A.; Kondratenko, M.; Leroux, Y.; Hapiot, P.; McCreery, R. L. Bilayer Molecular Electronics: All-Carbon Electronic Junctions Containing Molecular Bilayers Made with "Click" Chemistry. *J. Am. Chem. Soc.* **2013**, *135*, 12972–12975.

(32) Leroux, Y. R.; Hapiot, P. Nanostructured Monolayers on Carbon Substrates Prepared by Electrografting of Protected Aryldiazonium Salts. *Chem. Mater.* **2013**, *25*, 489–495.

(33) Leroux, Y. R.; Fei, H.; Noël, J. M.; Roux, C.; Hapiot, P. Efficient Covalent Modification of a Carbon Surface: Use of a Silyl Protecting Group to Form an Active Monolayer. *J. Am. Chem. Soc.* **2010**, *132*, 14039–14041.

(34) Santos, L.; Mattiuzzi, A.; Jabin, I.; Vandencasteele, N.; Reniers, F.; Reinaud, O.; Hapiot, P.; Lhenry, S.; Leroux, Y.; Lagrost, C. One-Pot Electrografting of Mixed Monolayers with Controlled Composition. *J. Phys. Chem. C* **2014**, *118*, 15919–15928.

(35) Mattiuzzi, A.; Jabin, I.; Mangeney, C.; Roux, C.; Reinaud, O.; Santos, L.; Bergamini, J.-F.; Hapiot, P.; Lagrost, C. Electrografting of Calix[4]arenediazonium Salts to Form Versatile Robust Platforms for Spatially Controlled Surface Functionalization. *Nat. Commun.* **2012**, *3*, 1–8.

(36) Lund, T.; Nguyen, P. T.; Ruhland, T. Electrochemical Grafting of TiO_2-Based Photo-Anodes and Its Effect in Dye-Sensitized Solar Cells. *J. Electroanal. Chem.* **2015**, *758*, 85–92.

(37) Merson, A.; Dittrich, Th.; Zidon, Y.; Rappich, J.; Shapira, Y. Charge Transfer from TiO_2 into Adsorbed Benzene Diazonium Compounds. *Appl. Phys. Lett.* **2004**, *85*, 1075–1076.

(38) Xiong, W.; Yu, L.; Shi, H.; Phillips, D. L.; Chan, W. K. Study of Photoinduced Electron Transfer Process in Ruthenium Complex Modified Zinc Oxide Nanoparticles by Ultrafast Time-Resolved Transient Absorption Spectroscopy. *J. Inorg. Organomet. Polym. Mater.* **2017**, *27*, 39–47.

(39) Bell, K. J.; Brooksby, P. A.; Polson, M. I. J.; Downard, A. J. Evidence for Covalent Bonding of Aryl Groups to MnO_2 Nanorods from Diazonium-Based Grafting. *Chem. Commun.* **2014**, *50*, 13687–13690.

(40) Cao, L.; Fang, G.; Wang, Y. Electroreduction of Viologen Phenyl Diazonium Salts as a Strategy to Control Viologen Coverage on Electrodes. *Langmuir* **2017**, *33*, 980–987.

(41) Spampinato, V.; Tuccitto, N.; Quici, S.; Calabrese, V.; Marletta, G.; Torrisi, A.; Licciardello, A. Functionalization of Oxide Surfaces by Terpyridine Phosphonate Ligands: Surface Reactions and Anchoring Geometry. *Langmuir* **2010**, *26*, 8400–8406.

(42) Ashford, D. L.; Song, W.; Concepcion, J. J.; Glasson, C. R. K.; Brennaman, M. K.; Norris, M. R.; Fang, Z.; Templeton, J. L.; Meyer, T. J. Photoinduced Electron Transfer in a Chromophore-Catalyst Assembly Anchored to TiO_2. *J. Am. Chem. Soc.* **2012**, *134*, 19189–19198.

(43) Lainé, P.; Bedioui, F.; Ochsenbein, P.; Marvaud, V.; Bonin, M.; Amouyal, E. A New Class of Functionalized Terpyridyl Ligands as Building Blocks for Photosensitized Supramolecular Architectures. Synthesis, Structural, and Electronic Characterizations. *J. Am. Chem. Soc.* **2002**, *124*, 1364–1377.

(44) Ben Hadda, T.; Le Bozec, H. Preparation and Characterization of Ruthenium Complexes with the New 4,4′,4″-Tri-Tert-Butylterpyridine Ligand and with 4,4′-Di-Tert-Butylbipyridine. *Polyhedron* **1988**, *7*, 575–577.

(45) Preiß, J.; Jäger, M.; Rau, S.; Dietzek, B.; Popp, J.; Martínez, T.; Presselt, M. How Does Peripheral Functionalization of Ruthenium(II)-Terpyridine Complexes Affect Spatial Charge Redistribution after Photoexcitation at the Franck-Condon Point? *ChemPhysChem* **2015**, *16*, 1395–1404.

(46) Spettel, K. E.; Damrauer, N. H. Synthesis, Electrochemical Characterization, and Photophysical Studies of Structurally Tuned Aryl-Substituted Terpyridyl Ruthenium(II) Complexes. *J. Phys. Chem. A* **2014**, *118*, 10649–10662.

(47) Matheu, R.; Francàs, L.; Chernev, P.; Ertem, M. Z.; Batista, V.; Haumann, M.; Sala, X.; Llobet, A. Behavior of the Ru-Bda Water Oxidation Catalyst Covalently Anchored on Glassy Carbon Electrodes. *ACS Catal.* **2015**, *5*, 3422–3429.

(48) Heimer, T. A.; D'Arcangelis, S. T.; Farzad, F.; Stipkala, J. M.; Meyer, G. J. An Acetylacetonate-Based Semiconductor−Sensitizer Linkage. *Inorg. Chem.* **1996**, *35*, 5319–5324.

(49) Barr, T. J.; Sampaio, R. N.; DiMarco, B. N.; James, E. M.; Meyer, G. J. Phantom Electrons in Mesoporous Nanocrystalline SnO_2 Thin Films with Cation-Dependent Reduction Onsets. *Chem. Mater.* **2017**, *29*, 3919–3927.

(50) Farnum, B. H.; Morseth, Z. A.; Brennaman, M. K.; Papanikolas, J. M.; Meyer, T. J. Application of Degenerately Doped Metal Oxides in the Study of Photoinduced Interfacial Electron Transfer. *J. Phys. Chem. B* **2015**, *119*, 7698–7711.

(51) Tiwana, P.; Docampo, P.; Johnston, M. B.; Snaith, H. J.; Herz, L. M. Electron Mobility and Injection Dynamics in Mesoporous ZnO, SnO_2, and TiO_2 Films Used in Dye-Sensitized Solar Cells. *ACS Nano* **2011**, *5*, 5158–5166.

(52) DiMarco, B. N.; Motley, T. C.; Balok, R. S.; Li, G.; Siegler, M. A.; O 'Donnell, R. M.; Hu, K.; Meyer, G. J. A Distance Dependence to Lateral Self-Exchange across Nanocrystalline TiO_2. A Comparative Study of Three Homologous Ru III/II Polypyridyl Compounds. *J Phys Chem C* **2016**, *120*, 14226–14235.

(53) Sedghi, A.; Miankushki, H.N. Influence of $TiCl_4$ Treatment on Structure and Performance of Dye-Sensitized Solar Cells. *Jpn. J. Appl. Phys* **2013**, *52*, 75002.

(54) Henry, J.; Livingstone, J. ITO Film Analyses by FTIR. *Infrared Phys. Technol.* **1995**, *36*, 779–784.

(55) Naghavi, N.; Marcel, C.; Dupont, L.; Rougier, A.; Leriche, J.; Guêry, C. Structural and Physical Characterisation of Transparent Conducting Pulsed Laser Deposited In_2O_3±ZnO Thin Films. *J. Mater. Chem.* **2000**, *10*, 2315–2319.

(56) Moulder, J. F.; Stickle, W. F.; Sobol, P. E.; Bomben, K. D. *Handbook of XPS*; Chastain, J., King, R. C., Eds.; Physical Electronics, Inc: Eden Prairie, Minnesota, 1992.

(57) Wagner, C. D.; Gale, L. H.; Raymond, R. H. Two-Dimensional Chemical State Plots: A Standardized Data Set for Use in Identifying Chemical States by X-Ray Photoelectron Spectroscopy. *Anal. Chem.* **1979**, *51*, 466–482.

(58) Wang, W. S.; Wang, D. H.; Qu, W. G.; Lu, L. Q.; Xu, A. W. Large Ultrathin Anatase TiO_2 Nanosheets with Exposed {001} Facets on Graphene for Enhanced Visible Light Photocatalytic Activity. *J. Phys. Chem. C* **2012**, *116*, 19893–19901.

(59) Bajestani, Z. G.; Yürüm, A.; Yürüm, Y. Significant Improvement in the Hydrogen Storage Capacity of a Reduced Graphene oxide/TiO_2 Nanocomposite by Chemical Bonding of Ti–O–C. *RSC Adv.* **2016**, *6*, 32831–32838.

(60) Zheng, T.; Feng, E.; Wang, Z.; Gong, X.; Tian, Y. Mechanism of Surface-Enhanced Raman Scattering Based on 3D Graphene–TiO_2 Nanocomposites and Application to Real-Time Monitoring of Telomerase Activity in Differentiation of Stem Cells. *ACS Appl. Mater. Interfaces* **2017**, *9*, 36596–36605.

(61) Babelon, P.; Dequiedt, A. S.; Mostéfa-Sba, H.; Bourgeois, S.; Sibillot, P.; Sacilotti, M. SEM and XPS Studies of Titanium Dioxide Thin Films Grown by MOCVD. *Thin Solid Films* **1998**, *322*, 63–67.

(62) Stranick, M. A.; Moskwa, A. SnO_2 by XPS. *Surf. Sci. Spectra* **1993**, *2*, 50–54.

(63) Alibabaei, L.; Sherman, B. D.; Norris, M. R.; Brennaman, M. K.; Meyer, T. J. Visible Photoelectrochemical Water Splitting into H_2 and O_2 in a Dye-Sensitized Photoelectrosynthesis Cell. *Proc. Nat. Acad. Sci. USA* **2015**, *112*, 5899–5902.

(64) Alibabaei, L.; Brennaman, M. K.; Norris, M. R.; Kalanyan, B.; Song, W.; Losego, M. D.; Concepcion, J. J.; Binstead, R. A.; Parsons, G. N.; Meyer, T. J. Solar Water Splitting in a Molecular Photoelectrochemical Cell. *Proc. Nat. Acad. Sci. USA* **2013**, *110*, 20008–20013.

(65) Michaux, K. E.; Gambardella, A. A.; Alibabaei, L.; Ashford, D. L.; Sherman, B. D.; Binstead, R. A.; Meyer, T. J.; Murray, R. W. Visible Photoelectrochemical Water Splitting Based on a Ru(II) Polypyridyl Chromophore and Iridium Oxide Nanoparticle Catalyst. *J. Phys. Chem. C* **2015**, *119*, 17023–17027.

(66) Sheridan, M. V.; Sherman, B. D.; Coppo, R. L.; Wang, D.; Marquard, S. L.; Wee, K.; Murakami Iha, N. Y.; Meyer, T. J. Evaluation of Chromophore and Assembly Design in Light-Driven Water Splitting with a Molecular Water Oxidation Catalyst. *ACS Energy Lett.* **2016**, *1*, 231–236.

(67) Pan, Y.; Tong, B.; Shi, J.; Zhao, W.; Shen, J.; Zhi, J.; Dong, Y. Fabrication, Characterization, and Optoelectronic Properties of Layer-by-Layer Films Based on Terpyridine-Modified MWCNTs and Ruthenium(III) Ions. *J. Phys. Chem. C* **2010**, *114*, 8040–8047.

(68) Diebold, U. The Surface Science of Titanium Dioxide. *Surf. Sci. Rep.* **2003**, *48*, 53–229.

(69) Ahmed, F.; Dewani, R.; Pervez, M. K.; Mahboob, S. J.; Soomro, S. A. Non-Destructive FT-IR Analysis of Mono Azo Dyes. *Bulg. Chem. Commun.* **2016**, *48*, 71–77.

(70) Agnès, C.; Arnault, J.; Omnès, F.; Jousselme, B.; Billon, M.; Bidan, G.; Mailley, P. XPS Study of Ruthenium Tris-Bipyridine Electrografted from Diazonium Salt Derivative on Microcrystalline Boron Doped Diamond. *Phys. Chem. Chem. Phys.* **2009**, *11*, 11647–11654.

CHAPTER 3: TUNNELING AND THERMALLY-ACTIVATED ELECTRON TRANSFER IN DYE-SENSITIZED $SNO_2|TIO_2$ CORE|SHELL NANOSTRUCTURES[4]

3.1 Introduction

Metal oxide nanostructures, which are composed of a core of one metal oxide and a shell of another, are promising materials for applications in sensitized photoelectrodes,[1–3] gas sensors,[4] batteries,[5,6] and perovskite solar cells.[7] A particularly promising core|shell material for solar energy conversion applications is a SnO_2 core with a TiO_2 shell generated by atomic layer deposition (ALD), abbreviated $SnO_2|TiO_2$.[8–13] In regenerative dye-sensitized solar cells, mesoporous thin films of $SnO_2|TiO_2$ have higher efficiencies than do films of SnO_2 alone.[8,11,13] For dye-sensitized water oxidation, the $SnO_2|TiO_2$ materials are superior to either TiO_2 or SnO_2.[9,10] The improved performance is generally attributed to inhibited recombination of the injected electrons ($MO_2(e^-)$) with the oxidized sensitizer or catalyst (S^+), Eq. 3.1.

$$MO_2(e^-)|\text{-}S^+ \rightarrow MO_2|\text{-}S \qquad (3.1)$$

The origins of the slowed charge recombination, however, remain uncertain.[1,12,14–17] Previous researchers have proposed a band edge offset model to rationalize the slow interfacial electron transfer (ET) in $SnO_2|TiO_2$, referring to the disparate band edge minima of the two oxides— the conduction band edge minimum of rutile SnO_2 is ~ 0.5 eV more

[4]This chapter previously appeared as an article in the *Journal of Physical Chemistry C*. The original citation is: Bangle, R.E.; Mortelliti, M.J.; Troian-Gautier, L.; Dempsey, J.L.; Meyer, G.J. *J. Phys. Chem. C*. **2020**, 124 *(45)*, 25148-25159.

positive than that of rutile TiO_2. Hence, in this model, an electron in the SnO_2 core must move through or over a 0.5 eV barrier to undergo ET to molecular acceptors.[15] Because of the difficulty of overcoming such a large barrier, ET has been proposed by several researchers to occur through tunneling, an assignment generally supported by an exponential dependence of the ET rate constant on the shell thicknesses.[12,14–17] Importantly, all of these studies, and the few which invoke a thermally activated mechanism,[12,14,16] were performed at a single temperature, so the mechanistic assignments remain speculative. Further, the band edge offset model relies on band edge positions of crystalline materials measured in aqueous solution and ignores the large spread (~ 1 V) of reported flat band potentials[18–20] as well as the possibility of a mixed oxide phase at the $SnO_2|TiO_2$ interface.[21–23]

In this Chapter, we quantify the electron transfer described in Eq. 3.1 over a 70 °C temperature range for mesoporous thin films of rutile SnO_2, rutile TiO_2, anatase TiO_2, $ZrO_2|TiO_2$, and $SnO_2|TiO_2$ sensitized to visible light with [Ru(2,2′-bipyridine)$_2$(4,4′-bis(phosphonic acid)-2,2′-bipyridine)]$^{2+}$ (RuP) which is thermally competent to drive water oxidation. The temperature dependent kinetic studies reported here enable direct assignment of the underlying electron transfer mechanism(s) as activated or tunneling. Comparative studies with rutile SnO_2 and both the anatase and rutile polymorphs of TiO_2 show an ~ six-fold smaller barrier for ET from SnO_2, which undoubtedly underlies the reported efficiency improvements of TiO_2-based dye-sensitized solar cells.[24,25] In sensitized $SnO_2|TiO_2$, Arrhenius and Eyring analysis as a function of shell thickness and post-deposition heat treatment provide the detailed mechanistic insights necessary to propose a predictive model for interfacial ET. This model is supported by temperature-dependent kinetics observed in sensitized $ZrO_2|TiO_2$, where the insulator ZrO_2 precludes electron transport to the core.

3.2 Experimental

3.2.1 Electrode Materials and Fabrication

A paste of ~10 nm rutile SnO_2 nanocrystals was prepared as described previously.[26] Glacial acetic acid was added dropwise to a SnO_2 colloid solution (Alfa Aesar, 15 wt/v%, ~15 nm diameter). The solution was stirred at room temperature for 36 hours before acid digestion at 240 °C for 80 hours. The resulting clumpy solution was sonicated using a Branson ultrasonic horn, and hydroxypropylcellulose (Sigma-Aldrich, M_w ~80,000 Da, M_n ~ 10,000, powder, 20 mesh particle size) was added slowly to 5 wt% while vigorously stirring. The resulting paste was stirred at room temperature for 2 weeks prior to use.

ZrO_2 paste was synthesized by modifying a reported procedure.[27] 17 mL of 70 wt% zirconium(IV) propoxide in 1-propanol (Sigma-Aldrich) was added dropwise at 0.5 mL/min to a stirring 100 mL aqueous solution of 0.1 M HNO_3. The solution of white particulate was heated at 100 °C until concentrated to 33 mL (6-8 hours). The resulting solution was subjected to acid digestion at 190 °C for 15 hours (45 min ramp-up and 1 hr ramp-down). The suspension was sonicated in an ice bath for 20 minutes then vigorously stirred as 9 wt% of hydroxypropylcellulose (Sigma- Aldrich, M_w ~80,000 Da, M_n ~ 10,000, powder, 20 mesh particle size) was added over the course of an hour. The resulting paste was stirred for 2 days prior to use. High-resolution transmission electron microscopy of the paste revealed quasi-spherical ZrO_2 nanocrystals with a diameter of 14.3 ± 6.3 nm averaged over 150 measurements.

Sol-gel pastes of anatase TiO_2 (*a*-TiO_2) and *r*-TiO_2 were prepared as previously described.[26–28] For *a*-TiO_2, 15 nm nanocrystals were synthesized by dropwise addition of 10 mL titanium(IV) isopropoxide (Aldrich, 97%) to a solution of 0.42 mL 70% HNO_3 in 60 mL

deionized water, which was then concentrated at 95 °C to a total volume of 20 mL and subjected to acid digestion for 12 hours at 200 °C. After allowing the paste to cool, 1 g finely ground carbowax (polyethyleneglycol Bisphenol A Epichlorohydrin Copolymer 15,000-20,000 Da; Aldrich) was added. The paste was stirred for 5 days prior to use. For *r*-TiO_2, ~75 nm nanorods were synthesized by dropwise addition of $TiCl_4$ (Sigma-Aldrich, 99.9%) to deionized water to create a 2M solution. The solution was rapidly diluted to 0.5 M $TiCl_4$ and stirred for 5 days at room temperature in the dark. The milky white solution was sonicated in an ice bath for 50 minutes, and the liquid was decanted from the solid after settling for 3 hours. The powder was suspended in ethanol and centrifuged (5500 rpm). After supernatant removal and resuspension in ethanol, the solution underwent 3 cycles of sonication in an ice bath followed by rotary evaporation and resuspension in ethanol. Following the third cycle, the solid was suspended in Milli-Q water to create a ~15 wt% *r*-TiO_2 solution. Hydroxypropylcellulose was added slowly to 7 wt%, and the paste was stirred for two days prior to use.

Thin films were fabricated by doctor-blading a metal oxide paste onto clean fluorine-doped tin oxide glass plates (FTO, Hartford Glass, 15 Ω/sq) or glass microscope slides, using a layer of Scotch tape as a spacer. After doctor blading the pastes onto FTO-coated glass and drying in air 30 min, the films were heat treated. SnO_2 films were heated at 450 °C for 1 hour. To avoid cracking, the ZrO_2 films were first heated at 100 °C for 10 minutes, followed by heating at 450 °C for 1 hour. The *a*-TiO_2 films were heated at 450 °C for 30 minutes under O_2 flow. The *r*-TiO_2 films were heated at 100 °C for 10 minutes, and subsequently heated at 500 °C for 1 hour. The films then immediately underwent either atomic layer deposition or sensitization. Films thicknesses were measured by a Bruker Optics DektakXT

stylus profilometer as follows: SnO_2 was 4-6 μm, ZrO_2 was 5-7 μm, *a*-TiO_2 was 4 μm, and *r*-TiO_2 was 5-6 μm.

3.2.2 Atomic Layer Deposition (ALD) of TiO_2 Shells

Atomic layer deposited coatings were fabricated using an Ultratech/Cambridge NanoTech Savannah S200 reactor system. Tetrakisdimethylamidotitanium(IV) (TDMA-Ti) (Sigma-Aldrich, 99.999%) and ultrapure DI water served as the reactant and co-reactant for the deposition of TiO_2, each equilibrated at 75 °C for 1 hour prior to deposition. Ultrahigh purity N_2 (Airgas, 99.999%) served as the carrier gas. The empty ALD chamber was pre-treated with 50 cycles of TiO_2 deposited at 150 °C to ensure a consistent sticking coefficient to the reactor walls. Metal oxide films annealed on FTO were aligned parallel to the inlet and outlet ports, and the chamber was placed under dynamic vacuum for 10 minutes with a carrier gas flow rate of 20 sccm. Prior to precursor exposure, the chamber was isolated from dynamic vacuum, which was resumed during the purge steps. One ALD cycle consisted of a 0.5 sec dose of TDMA-Ti, 20 sec exposure, 30 sec purge, 0.02 sec dose of H_2O, 20 sec exposure, and 30 sec purge. The flow rate was reduced to 5 sccm prior to precursor doses and increased to 400 sccm during purges. The thickness of the shell was controlled by the number of applied ALD cycles. After ALD, the core|shell films were immediately heat treated for 30 min (225 °C/hr ramp-up, 450 °C/hr ramp-down). Core|shell films termed “unannealed” were treated at 200 °C, and films termed “annealed” were heated at 450 °C.

Herein, shell thicknesses are described in terms of the number of ALD cycles of TiO_2 rather than a geometric thickness to avoid mischaracterizing inhomogeneous shells. For the sake of comparison, the TiO_2 ALD in this study has been estimated from transmission

electron microscopy to deposit 0.66 Å per cycle, similar to the per-cycle deposition previously measured by ellipsometry on planar silicon wafers.[14,21]

3.2.3 Sensitization

Metal oxide materials were sensitized to the maximum attainable surface coverage by reaction with 6 mM [Ru(2,2′-bipyridine)$_2$(4,4′-bis(phosphonic acid)-2,2′-bipyridine)]$^{2+}$, abbreviated RuP, in methanol for 24 hours. The synthesis of RuP has been discussed previously.[29]

3.2.4 Film Characterization

Raman spectra were acquired using a Renishaw inVia Raman spectrophotometer equipped with a Leica microscope. The 633 nm excitation source was generated by a RenishawRL633 HeNe laser. The Raman shift was calibrated to the silicon F_{1g} peak (520.2 ± 0.2 cm^{-1}). 20 accumulative measurements were performed for each sample in the dark using a 1800 I/mm (vis) grating, a CCD camera detector, and a 10 second exposure time.

High resolution transmission electron microscopy (HRTEM) imaging was performed using a FEI Talos F200X transmission electron microscope which applied an accelerating voltage of 200 kV. Samples were stripped from glass microscope slides using an electron microscopy razor blade, and the powder was sonicated for 20 minutes in ethanol. The resulting dispersions were drop-cast onto 400 mesh lacey carbon grids and dried under vacuum. All images were analyzed in ImageJ software. Lattice space (d-space) values were quantified by averaging at least 10 measurements obtained from the fast-Fourier transform (FFT) of a selected area of the image. If necessary, for some samples a circular mask was applied to two diffraction points and d-space values were obtained from the inverse FFT.

UV–visible absorbance spectra were obtained on an Agilent Cary 60 UV–vis spectrophotometer. The films were immersed in N_2-sparged 0.1 M $HClO_4$ aqueous solutions and held at 45° relative to the incident light.

3.2.5 Transient Absorption Spectroscopy

Transient absorption spectroscopy in N_2-sparged 0.1 M aqueous $HClO_4$ was performed using a previously described apparatus.[30] Pulsed light excitation was enacted with a Q-switched, pulsed Nd:YAG laser doubled to 532 nm (Quantel, U.S.A., Brilliant B, 5-6 nm FWHM). Samples were excited at 1 Hz with laser fluence at the sample of ~ 3 mJ/pulse. Absorption changes were probed by a 150 W xenon arc lamp aligned perpendicular to the pulse beam. The probe lamp was pulsed to 70 V at 1 Hz for time scales < 100 μs. Light detection was accomplished with a SPEX 1702/04 monochromator optically coupled to a photomultiplier tube (Hamamatsu R928) connected to a digital oscilloscope (LeCroy 9450, Dual 330 MHz). The overall instrument response time was ~ 10 ns. Single wavelength kinetics are presented as an average of 90-150 laser pulses. Transient absorption spectroscopy was performed as a function of sample temperature, 10 °C to 80 °C, which was controlled with a CoolSpek cryostat (Unisoku).

3.3 Results

3.3.1 Characterization of SnO_2|TiO_2 Core|Shell Films

Mesoporous thin films of rutile SnO_2 nanocrystals, which are quasi-spherical and ~ 10 nm in diameter, form mesoporous films that have been characterized previously.[26] Atomic layer deposition (ALD) of TDMA-Ti onto this SnO_2 enabled fabrication of SnO_2|$XTiO_2$ core|shell materials, where X is the number of ALD cycles. After TiO_2 deposition,

$SnO_2|XTiO_2$ materials termed 'unannealed' were heated to 200 °C for 30 minutes, while $SnO_2|XTiO_2$ termed 'annealed' were heated to 450 °C. As shown in HRTEM images (Figs. 3.1 and 3.13-14 in the Associated Content section), deposition of 10 cycles of TiO_2 results in films nearly indistinguishable from bare SnO_2, while deposition of 20, 30, or 50 cycles of TiO_2 results in smooth shells that progressively thicken with X. As observed previously, application of 50 ALD cycles of TiO_2 partially fills the mesoporous void spaces in the SnO_2.[14,21,26,31–33] In both annealed and unannealed materials, rutile SnO_2 cores are identifiable in HRTEM images (Fig 3.1) by lattice fringes with 0.330 nm and 0.260 nm d-space value, which are characteristic of the SnO_2 (110) and (101) crystalline planes, respectively. Unannealed TiO_2 shells exhibit no discernable lattice fringes (Fig 3.1a-d), while annealed TiO_2 shells exhibit lattice fringes with 0.320 nm, 0.250 nm, 0.220 nm, and/or 0.170 nm d-space values. The TiO_2 matrix for $SnO_2|50TiO_2$, which partially fills the SnO_2 pores, was highly polycrystalline, which increased the uncertainty of d-space measurements, with standard deviations from ±0.010 nm to ±0.017 nm. Nevertheless, these lattice spacings in the annealed materials are characteristic of rutile TiO_2 (*r*-TiO_2) (110), (101), (111), and (211) crystalline planes, respectively (Fig 3.1e-h).

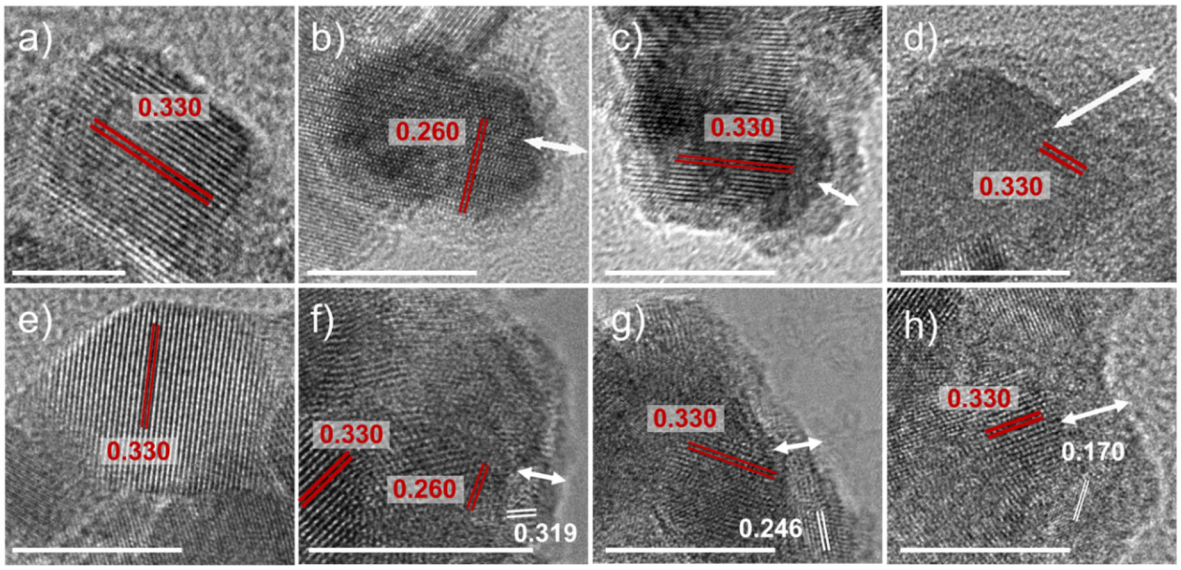

Figure 3.1. HRTEM images of unannealed a) $SnO_2|10TiO_2$, b) $SnO_2|20TiO_2$, c) $SnO_2|30TiO_2$, and d) $SnO_2|50TiO_2$ and annealed e) $SnO_2|10TiO_2$, f) $SnO_2|20TiO_2$, g) $SnO_2|30TiO_2$, and h) $SnO_2|50TiO_2$. White bars at the bottom of each image represent a 10 nm scale. Annealed materials were treated at 450 °C after ALD, while unannealed materials were treated at 200 °C. Each ALD cycle indicated as X in $SnO_2|XTiO_2$ is estimated to deposit ~ 0.66 Å TiO_2. White arrows denote the TiO_2 shells, red lines represent the lattice fringe measurements characteristic of SnO_2, and white lines represent the lattice fringe measurements characteristic of *r*-TiO_2. These magnified images are portions of Figs. 3.13 and 3.14 in the Associated Content section.

Annealed and unannealed $SnO_2|XTiO_2$ materials also exhibit distinctive Raman spectra (Fig. 3.2). Rutile SnO_2 displays prominent E_g and A_{1g} phonon modes at 476 and 633 cm^{-1} respectively, a broad band centered at 560 cm^{-1} (labeled S_1) ascribed to a non-stoichiometric SnO_x species, and small features at 245 and 310 cm^{-1} attributable to infrared-active phonon modes with E_u symmetry.[26,34–40] In unannealed $SnO_2|XTiO_2$ materials, addition of TiO_2 layers progressively depresses the S_1 band, enhances the A_{1g} and E_u modes, and generally broadens features, but no clear new bands arise. In contrast, addition of annealed TiO_2 results in progressive growth of a small spectral feature at 245 cm^{-1} and broad peaks centered at 430 and 603 cm^{-1}. These peaks are not visible in $SnO_2|10TiO_2$ and are unclear in $SnO_2|20TiO_2$, but are easily distinguished in annealed $SnO_2|30TiO_2$ and

$SnO_2|50TiO_2$. The peak positions are consistent with the reported Raman spectrum of *r*-TiO_2 multi-phonon, A_{1g}, and E_g modes, respectively.[41,42]

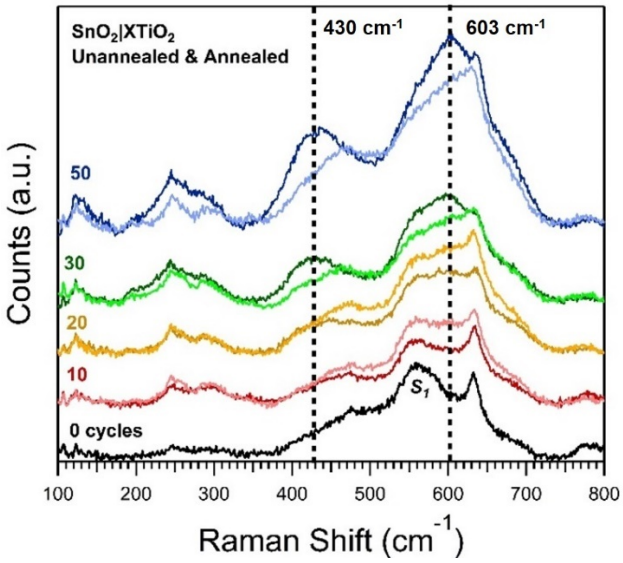

Figure 3.2. Raman spectra of unannealed (light) and annealed (dark) $SnO_2|XTiO_2$ where X is the number of cycles of TiO_2 deposited, indicated on the left. Each ALD cycle is estimated to deposit ~ 0.66 Å TiO_2.

Previous reports have established that ALD-generated TiO_2 coatings are amorphous when deposited at temperatures below 150-250° C, while exposure to higher temperatures leads to either anatase TiO_2 (*a*-TiO_2,150-400 °C) or *r*-TiO_2 (> 300 °C).[43–45] Growth of *r*-TiO_2 has been reported at lower temperatures, however, on SnO_2 and other rutile substrates.[46,47] This literature precedence is in line with HRTEM and Raman evidence for *r*-TiO_2 in annealed shells, heated to 450 °C, and the lack of evidence for crystalline TiO_2 in unannealed shells, heated to 200 °C. In total HRTEM images, Raman spectra, and previous literature are consistent with the assignment of TiO_2 shells in 'annealed' $SnO_2|XTiO_2$ as rutile and in 'unannealed' $SnO_2|XTiO_2$ as amorphous.

3.3.2 Characterization of ZrO_2|TiO_2 Core|Shell Films

Nanocrystals of ZrO_2 form mesoporous films analogous to the SnO_2 materials. Analysis of this ZrO_2 by HRTEM reveals quasi-spherical nanocrystals with an average size of 14 ± 6 nm. A small population of larger nanocrystals possess a more rod-like morphology (Fig. 3.15 in the Associated Content section). Atomic layer deposition of TiO_2 onto ZrO_2 nanocrystalline films results in ZrO_2|XTiO_2 materials, which are heat treated for 30 minutes at either 200 °C (unannealed) or 450 °C (annealed). As for SnO_2|10TiO_2, HRTEM images of unannealed and annealed ZrO_2|10TiO_2 are nearly indistinguishable from ZrO_2 alone (Figs. 3.16-3.17 in Associated Content). A smooth shell without discernable lattice fringes is observed for 20, 30, and 50 unannealed TiO_2 cycles (Fig. 3.16). Annealed ZrO_2|XTiO_2 samples with at least 20 ALD cycles of TiO_2 have visible shells that appear to have continuous lattice fringes extending to the edges of the nanocrystals (Fig. 3.17).

Raman spectra of ZrO_2 materials (Fig. 3.18 in Associated Content) display peaks indicative of monoclinic and tetragonal ZrO_2 phases, assignments supported by the observed x-ray diffraction pattern (Fig. 3.19 in Associated Section).[48] Deposition of 10 ALD cycles of TiO_2 results in Raman spectra nearly indistinguishable from that of ZrO_2, regardless of post-deposition heat treatment. Raman spectra of unannealed ZrO_2|20TiO_2 and ZrO_2|30TiO_2 weakly exhibit additional peaks at 150 and 421 cm^{-1} which become prominent in unannealed ZrO_2|50TiO_2 (Fig. 3.18a). Occurrence of these features is accompanied by a shift of ZrO_2 x-ray diffraction peaks to larger 2θ values (Fig. 3.19). Upon annealing, the Raman peaks at 150 and 421 cm^{-1} are enhanced and an additional peak at 531 cm^{-1} arises for ZrO_2|30TiO_2 and ZrO_2|50TiO_2 (Fig. 3.18). The sharp peak at 150 cm^{-1} is consistent with the E_g phonon mode

of anatase TiO_2 (*a*-TiO_2), while the peaks at 421 cm^{-1} and 531 cm^{-1} most closely resemble prominent modes of $ZrTiO_4$.[42,49–54]

Raman and HRTEM evidence thus suggest that shells in annealed $ZrO_2|XTiO_2$ consist of *a*-TiO_2 with $ZrTiO_4$ species at the interface. For unannealed $ZrO_2|XTiO_2$, despite lack of evidence for crystallinity in HRTEM, Raman spectra indicate that some portions of the thickest TiO_2 shells are anatase. However, interposition of thin ALD layers of amorphous Al_2O_3 between the SnO_2 and unannealed TiO_2 shells removes the 150 and 421 cm^{-1} Raman peaks, suggesting shells in these materials remain amorphous. Annealing these $SnO_2|Al_2O_3|TiO_2$ materials returns the sharp Raman peak indicative of *a*-TiO_2 at 150 cm^{-1}, but no features characteristic of $ZrTiO_4$ (Fig. 3.20 in the Associated Content).[49–54]

3.3.3 Sensitization with RuP

Mesoporous, nanocrystalline thin films of SnO_2 and ZrO_2 are nearly transparent to visible light (Fig. 3.3a and Fig. 3.21a in Associated Content). Addition of ALD TiO_2 generates progressively more opaque films that both scatter more light and exhibit lower energy fundamental absorbance features, consistent with previous literature.[21] Films were sensitized to visible light with surface-anchored RuP, as indicated by the characteristic RuP metal-to-ligand charge transfer (MLCT) absorption peak (Fig. 3.3b and Fig. 3.21b). Surface coverages of RuP, Γ, were calculated from the MLCT absorbance using Eq. 3.2 (Table 3.1), where A_{max} is the maximum MLCT absorption, and ε_{max} is the molar absorption coefficient of RuP at the same wavelength (13,300 M^{-1} cm^{-1}, 460 nm).[55]

$$\Gamma = \frac{A_{max}}{1000 \times \varepsilon_{max}} \tag{3.2}$$

Deposition of TiO_2 lowers the attainable Γ as pore filling results in smaller available surface areas. Additionally, Γ values are generally larger for unannealed over annealed core|shell materials and for $ZrO_2|TiO_2$ over $SnO_2|TiO_2$.

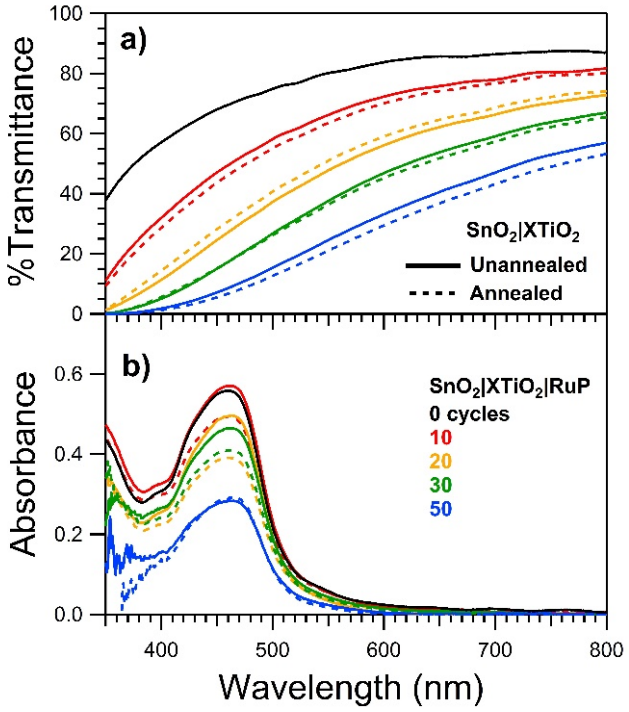

Figure 3.3. UV-Visible spectra acquired in aqueous 0.1 M $HClO_4$ for a) unsensitized and b) RuP-sensitized $SnO_2|XTiO_2$ materials, where X is the number of ALD cycles. Each ALD cycle is estimated to deposit ~ 0.66 Å TiO_2. Solid lines represent unannealed films, while dashed lines represent annealed. Spectra in b) were generated by subtraction of the spectra of the unsensitized materials from spectra of RuP-sensitized films.

Table 3.1. RuP Surface Coverage, Γ, in Sensitized Core|Shell Materials

	Γ (x 10^{-8} mol cm^{-2})			
	$SnO_2|XTiO_2$		**$ZrO_2|XTiO_2$**	
X	**Annealed**	**Unannealed**	**Annealed**	**Unannealed**
10	3.7	4.3	4.1	4.5
20	2.9	3.7	4.2	4.5
30	3.1	3.5	4.3	5.2
50	2.2	2.1	2.3	2.4

3.3.4 Temperature Dependence of Interfacial Electron Transfer

Transient absorption spectroscopy in N_2-sparged aqueous 0.1 M $HClO_4$ solution was employed to quantify interfacial electron transfer (ET) pseudo-rate constants for annealed and unannealed $SnO_2|XTiO_2$. As shown in Fig. 3.4, pulsed 532 nm light generates a RuP excited state which rapidly transfers an electron into poorly-defined acceptor states in the core|shell material. Within the 10 ns instrument response time, this forms an oxidized RuP molecule—signified by a long-lived decrease in the RuP MLCT absorbance (ΔA) spanning ~ 385–500 nm—and an excess electron in the $SnO_2|TiO_2$. The core|shell electron then recombines through interfacial ET with the oxidized sensitizer (Eq. 3.1, Fig. 3.4), and the RuP transient spectral change returns to the initial absorbance. The ET was monitored at 402 nm, which is an isosbestic point of the RuP excited state transient absorption spectrum, as a function of temperature from 10 to 80 °C for both annealed and unannealed RuP-sensitized $SnO_2|TiO_2$ materials with shells of variable thicknesses (Fig. 3.5, Figs. 3.22-3.23 in Associated Content). In all cases, initial absorption magnitudes are recovered within 5 ms, indicating no net photochemistry occurs. Small sample-to-sample adjustments to the laser fluence ensured nearly constant initial ΔA.[56] For the majority of $SnO_2|XTiO_2$ variations, ET accelerates at high temperatures, with the exception of unannealed $SnO_2|50TiO_2$ for which ET kinetics are temperature independent.

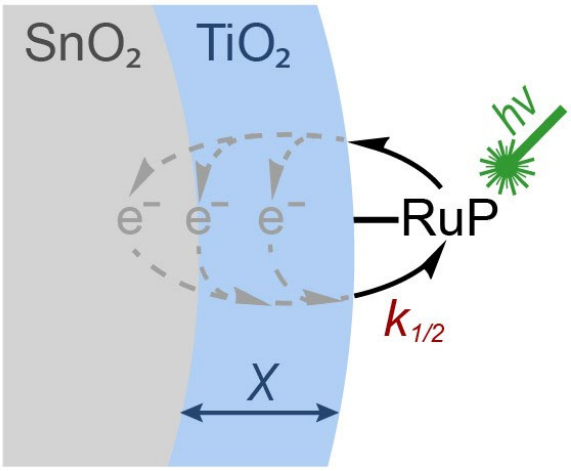

Figure 3.4. A SnO_2 nanoparticle core is coated with a TiO_2 shell through ALD. The number of applied ALD cycles (X) controls the shell thickness. Materials are sensitized with RuP, which is excited with pulsed 532 nm light to initiate electron transfer from the RuP excited state into the material. The acceptor states in the core/shell are poorly defined and could exist in the core, shell, or interface (gray arrows). Electrons in the material then recombine with the photo-oxidized RuP through interfacial ET with rate constant $k_{1/2}$, as reflected in the observed transient spectral changes.

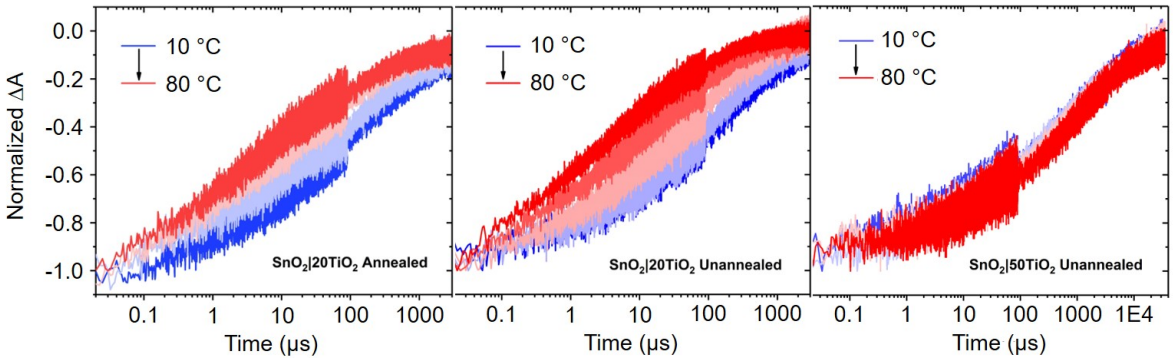

Figure 3.5. Transient absorption changes (ΔA) monitored in aqueous 0.1 M $HClO_4$ at 402 nm over the indicated temperature ranges following pulsed 532 nm light excitation of RuP-sensitized $SnO_2|XTiO_2$ films, where X is the number of ALD TiO_2 cycles. Each ALD cycle is estimated to deposit ~ 0.66 Å TiO_2. Shells were either annealed (heated to 450 °C) or unannealed (heated to 200 °C) post deposition as indicated.

As frequently reported in mesoporous metal oxide materials, interfacial ET kinetics were non-exponential.[57,58] As such, interfacial ET pseudo-rate constants, $k_{1/2}$, were approximated as the inverse of the time required for ΔA at 20 ns to decay by half. Arrhenius plots (Fig. 3.6a) show that core|shell materials annealed at 450 °C post TiO_2 deposition

manifest exclusively linear temperature dependence of ln($k_{1/2}$) values from 10 to 80 °C. In contrast, unannealed $SnO_2|10TiO_2$, $SnO|20TiO_2$, and $SnO_2|30TiO_2$, each heated to 200 °C post TiO_2 deposition, exhibit non-linear Arrhenius plots (Fig. 3.6b). Values of ln($k_{1/2}$) are nearly temperature-independent below ~ 40 °C, but increase linearly (and remarkably steeply for $SnO_2|20TiO_2$ and $SnO_2|30TiO_2$) at higher temperatures. Temperature-independent ET is observed across the entire probed range for unannealed $SnO_2|50TiO_2$.

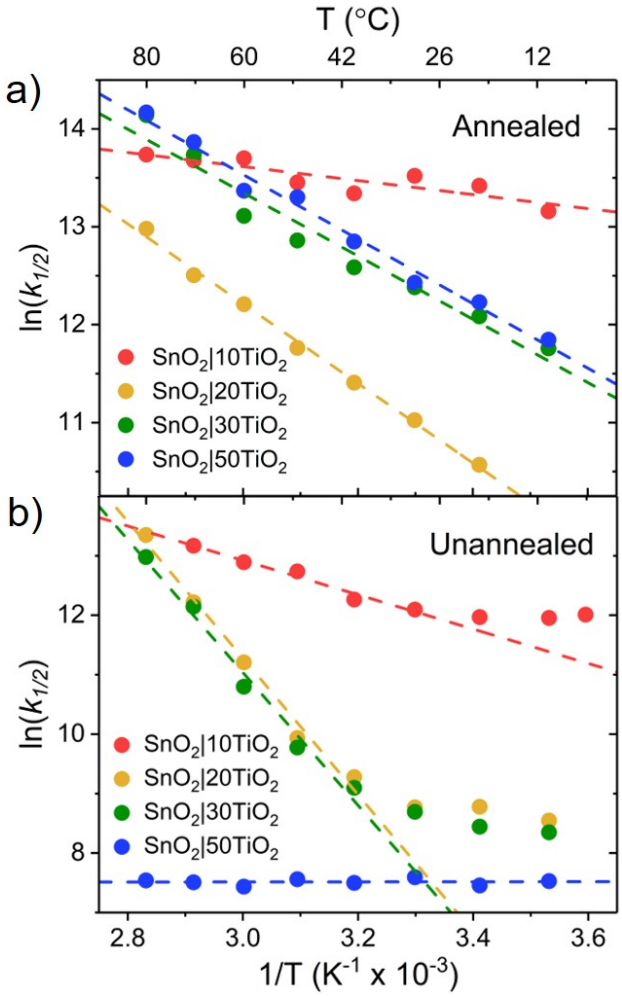

Figure 3.6. Arrhenius analysis of interfacial electron transfer following 532 nm pulsed light excitation in aqueous 0.1 M $HClO_4$ for RuP-sensitized $SnO_2|XTiO_2$ films, where X in the number of ALD TiO_2 cycles. Each ALD cycle is estimated to deposit ~ 0.66 Å TiO_2. Materials were heated post TiO_2 deposition for 30 min to either a) 450 °C (annealed) or b) 200 °C (unannealed). Dashed lines represent fits of the linear portions of the data to Eq. 3.3.

Analogous reference studies were performed for RuP-sensitized rutile SnO_2, *r*-TiO_2, and *a*-TiO_2 mesoporous thin films. Transient spectral changes for SnO_2 and *a*-TiO_2 were measured at 402 nm after 532 nm pulsed light excitation as a function of temperature (Fig. 3.24 in Associated Content). The fundamental absorbance of *r*-TiO_2 prevented spectroscopic detection at 402 nm, so spectral changes were instead monitored at 460 nm. Pseudo-rate constants of ET for both *r*-TiO_2 and *a*-TiO_2 increase with temperature to a similar degree, while for SnO_2, ET pseudo-rate constants increase only slightly with temperature (Fig. 3.7).

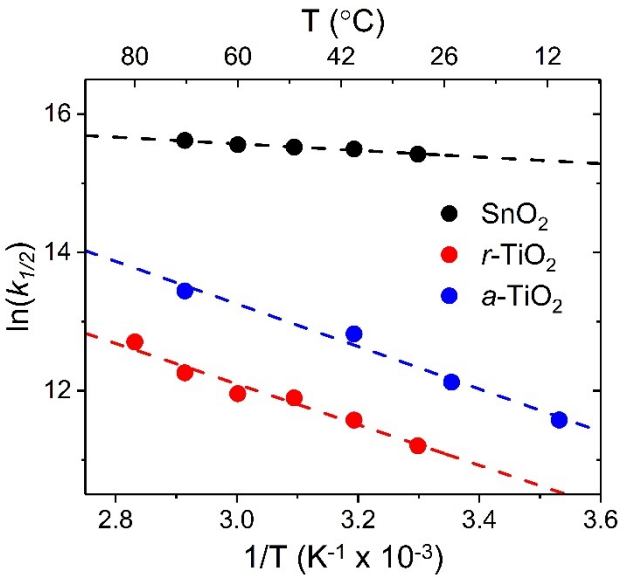

Figure 3.7. Arrhenius analysis of interfacial electron transfer following 532 nm pulsed light excitation in aqueous 0.1 M $HClO_4$ for RuP-sensitized SnO_2, rutile TiO_2 (*r*-TiO_2), and anatase TiO_2 (*a*-TiO_2). Dashed lines represent fits to Eq. 3.3.

Interfacial ET pseudo rate constants were also quantified as a function of temperature from transient spectral changes for RuP-sensitized ZrO_2|XTiO_2 materials (Figs. 3.25-3.26 in Associated Content). Insulating ZrO_2 cores possess high-energy acceptor states which are thought to be inaccessible to the RuP excited state, forcing injected electrons to reside exclusively in the TiO_2 shell.[14,17] Here, the kinetic response to temperature was insensitive to the post-deposition heat treatment (Fig. 3.8). For annealed and unannealed ZrO_2|10TiO_2, $k_{1/2}$

increases only slightly with temperature. For all other $ZrO_2|XTiO_2$ materials, Arrhenius plots display similar slopes, greater than that of $ZrO_2|10TiO_2$. Kinetics were within error the same when a thin layer of amorphous Al_2O_3 was deposited onto the ZrO_2 prior to TiO_2 deposition to form unannealed $ZrO_2|Al_2O_3|50TiO_2$ (Fig. 3.27 in Associated Content).[59]

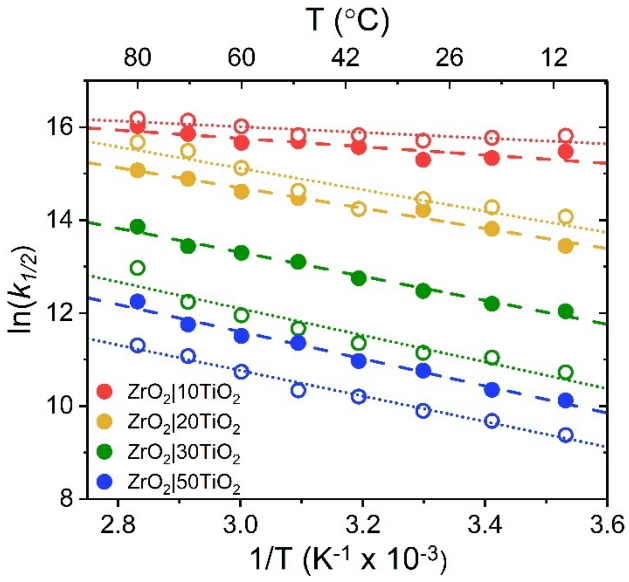

Figure 3.8. Arrhenius plots of interfacial electron transfer following 532 nm pulsed light excitation in aqueous 0.1 M $HClO_4$ for RuP-sensitized $ZrO_2|XTiO_2$ films, where X in the number of ALD TiO_2 cycles, that were either annealed (solid circles, dashed lines) or unannealed (open circle, dotted lines) post TiO_2 deposition. Each ALD cycle is estimated to deposit ~ 0.66 Å TiO_2. Dashed lines represent fits to Eq. 3.3.

3.3.5 Arrhenius and Eyring Analysis

The Arrhenius equation states that thermally-activated electron transfer rate constants are defined by a pre-exponential frequency factor A, the temperature T, and an activation energy E_a (Eq. 3.3).

$$\ln k_{1/2} = \left(\frac{E_a}{R}\right)\frac{1}{T} + \ln A \qquad (3.3)$$

Under conditions in which interfacial ET rate constants depend exponentially on temperature, E_a vales were quantified from Arrhenius plots (Fig. 3.6-3.8) using Eq. 3 (Table 3.2, Fig. 3.9).

For SnO_2, E_a is small— ~ 4 kJ mol^{-1}, and *a*- and *r*-TiO_2 display equal E_a values—24 kJ mol^{-1}. In annealed $SnO_2|TiO_2$ films, E_a is ~ 6 kJ mol^{-1} for $SnO_2|10TiO_2$, but ~ 30 kJ mol^{-1} for materials with thicker shells.[60] The same is true for both annealed and unannealed $ZrO_2|XTiO_2$. In unannealed $SnO_2|XTiO_2$, significantly larger E_a values are observed— ~ 25 kJ mol^{-1} for $SnO_2|10TiO_2$ and ~ 95 kJ mol^{-1} for $SnO_2|20TiO_2$ and $SnO_2|30TiO_2$.

Table 3.2. Activation Energies, E_a, for Interfacial Electron Transfer

	E_a (kJ mol^{-1})	
	Annealed[5]	**Unannealed**[6]
SnO_2	4 ± 1	
***r*-TiO_2**	24 ± 4	
***a*-TiO_2**	24 ± 2	
$SnO_2|10TiO_2$	6 ± 3	25 ± 3
$SnO_2|20TiO_2$	34 ± 4	96 ± 10
$SnO_2|30TiO_2$	27 ± 3	93 ± 11
$SnO_2|50TiO_2$	27 ± 3	-
$ZrO_2|10TiO_2$	7 ± 2	5 ± 1
$ZrO_2|20TiO_2$	18 ± 1	19 ± 5
$ZrO_2|30TiO_2$	22 ± 3	24 ± 2
$ZrO_2|50TiO_2$	24 ± 1	23 ± 3

[5]Heated to 450 °C for 30 min in air after TiO_2 deposition.

[6]Heated to 200 °C for 30 min in air after TiO_2 deposition.

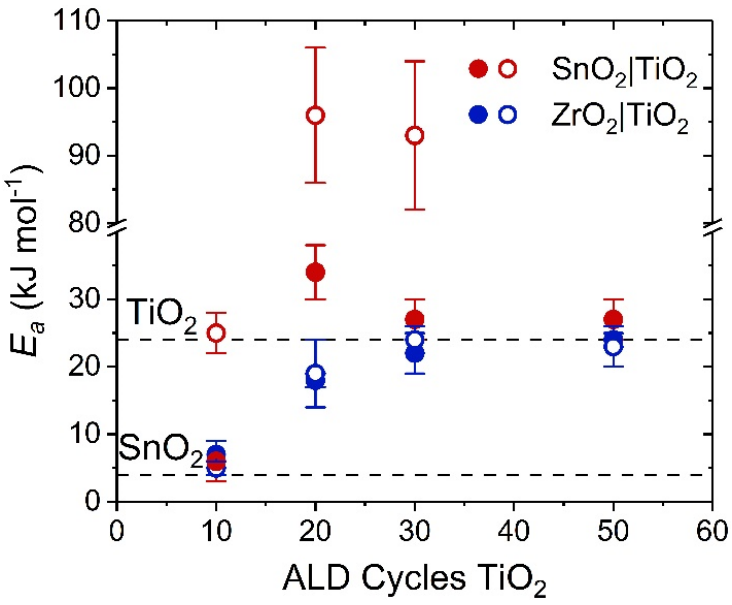

Figure 3.9. Activation energies, E_a, for temperature-dependent interfacial electron transfer on core|shell films in aqueous 0.1 M $HClO_4$ as a function of shell thickness, represented by the number of ALD cycles of TiO_2. Each ALD cycle is estimated to deposit ~ 0.66 Å TiO_2. Annealed shells are represented as solid circles, while unannealed shells are represented as open circles. $SnO_2|TiO_2$ films are shown in red, and $ZrO_2|TiO_2$ films are shown in blue. Reference E_a values for SnO_2 and TiO_2 are shown as dashed lines. Equal values of E_a were obtained for *a*-TiO_2 and *r*-TiO_2.

Similarly, the Eyring equation, Eq. 3.4, describes thermally-activated ET rate constants in terms of the enthalpy, $\Delta H^{\ddagger}$, and entropy, $\Delta S^{\ddagger}$, of activation, which allow calculation of the Gibbs free energy of activation, $\Delta G^{\ddagger}$ (Table 3.3, Fig. 3.28 in Associated Content).

$$\ln\left(\frac{k}{T}\right) = \frac{-\Delta H^{\ddagger}}{R}\frac{1}{T} + \ln\left(\frac{k_b}{h}\right) + \frac{\Delta S^{\ddagger}}{R} \qquad (3.4)$$

It should be noted that $\Delta S^{\ddagger}$ and $\Delta G^{\ddagger}$ depend on the absolute values of the ET rate constants, while in this study $k_{1/2}$ pseudo-rate constants serve as proxies. As such, the internal comparisons of $\Delta S^{\ddagger}$ and $\Delta G^{\ddagger}$ are more meaningful than absolute values.

Table 3.3. Enthalpies, $\Delta H^{\ddagger}$, Entropies, $\Delta S^{\ddagger}$, and Gibbs Free Energies, $\Delta G^{\ddagger}$, of Activation

	Annealed[7]			Unannealed[8]		
	$\Delta H^{\ddagger}$ (kJ mol^{-1})	$\Delta S^{\ddagger}$ (J mol^{-1} K^{-1})	$\Delta G^{\ddagger}$ [c] (kJ mol^{-1})	$\Delta H^{\ddagger}$ (kJ mol^{-1})	$\Delta S^{\ddagger}$ (J mol^{-1} K^{-1})	$\Delta G^{\ddagger}$[9] (kJ mol^{-1})
SnO_2|10TiO_2	3 ± 1	-123 ± 3	44 ± 2	21 ± 2	-74 ± 5	46 ± 3
SnO_2|20TiO_2	31 ± 1	-51 ± 2	48 ± 1	93 ± 5	130 ± 15	51 ± 9
SnO_2|30TiO_2	24 ± 2	-62 ± 6	45 ± 4	90 ± 6	120 ± 15	51 ± 10
SnO_2|50TiO_2	25 ± 1	-59 ± 3	44 ± 2	-	-	-
ZrO_2|10TiO_2	10 ± 1	12 ± 4	6 ± 3	8 ± 1	7 ± 4	5 ± 2
ZrO_2|20TiO_2	21 ± 1	35 ± 3	9 ± 2	22 ± 3	44 ± 7	7 ± 5
ZrO_2|30TiO_2	24 ± 1	34 ± 3	13 ± 2	26 ± 2	27 ± 7	18 ± 4
ZrO_2|50TiO_2	27 ± 1	28 ± 3	18 ± 2	25 ± 1	17 ± 3	20 ± 2

Values of $\Delta H^{\ddagger}$ are analogous to E_a values quantified through Arrhenius analysis, and display the same trends with core identity, shell thickness, and post-deposition heat treatment. Values of $\Delta S^{\ddagger}$, however, provide new insights (Fig. 3.10).[61] For ZrO_2|$XTiO_2$, values of $\Delta S^{\ddagger}$ are insensitive to post-deposition heat treatment and are near 0 J mol^{-1} K^{-1}. Annealed SnO_2|$XTiO_2$ and unannealed SnO_2|10TiO_2 undergo ET with large negative $\Delta S^{\ddagger}$, between –50 and –120 J mol^{-1} K^{-1}. In stark contrast, unannealed SnO_2|20TiO_2 and SnO_2|30TiO_2 undergo ET with $\Delta S^{\ddagger} \approx +125$ J mol^{-1} K^{-1}. Values of $\Delta H^{\ddagger}$ and $\Delta S^{\ddagger}$ were used to calculate $\Delta G^{\ddagger}$ at 60 °C (Table 3.3), a temperature at which ET is temperature dependent in all materials except unannealed SnO_2|50TiO_2. For ZrO_2|$XTiO_2$, $\Delta G^{\ddagger}$ increased linearly with shell thickness. Interestingly, however, in SnO_2|$XTiO_2$, the interplay of $\Delta H^{\ddagger}$ and $\Delta S^{\ddagger}$ result in nearly equal $\Delta G^{\ddagger}$ for all samples, 47 ± 3 kJ mol^{-1}. For both ZrO_2|$XTiO_2$ and SnO_2|$XTiO_2$, $\Delta G^{\ddagger}$ values predict the observed $k_{1/2}$ remarkably well (Fig. 3.11).

[7]Heated to 450 °C after TiO_2 deposition.

[8]Heated to 200 °C after TiO_2 deposition.

[9]Calculated as $\Delta G^{\ddagger} = \Delta H^{\ddagger} - T\Delta S^{\ddagger}$ for 60 °C.

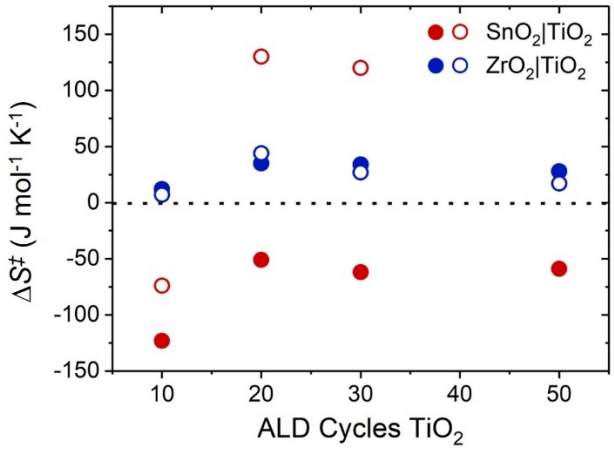

Figure 3.10. Values of $\Delta S^{\ddagger}$ for thermally-activated interfacial electron transfer on RuP-sensitized core|shell films in aqueous 0.1 M $HClO_4$. Each ALD cycle is estimated to deposit 0.66 Å TiO_2. Annealed materials, heated to 450 °C post TiO_2 deposition, are shown as solid circles, while unannealed materials, heated to only 200 °C, are shown as open circles. $SnO_2|TiO_2$ films are shown in red, while $ZrO_2|TiO_2$ films are shown in blue.

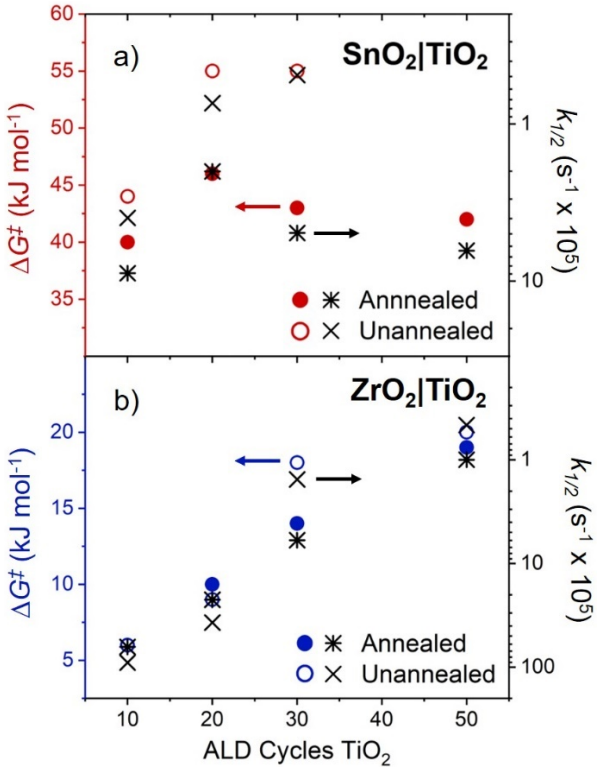

Figure 3.11. Comparative values of $\Delta G^{\ddagger}$ (linear scale, red or blue circles) and $k_{1/2}$ (log scale, black crosses and asterisks) for temperature-dependent interfacial ET in 0.1 M $HClO_4$ for RuP-sensitized a) $SnO_2|XTiO_2$ and b) $ZrO_2|XTiO_2$. Values observed at 60 °C are given, but similar agreement holds at all temperatures at which ET is thermally activated. Annealed materials are represented by closed circles ($\Delta G^{\ddagger}$) and asterisks ($k_{1/2}$). Unannealed materials are represented by open circles ($\Delta G^{\ddagger}$) and crosses ($k_{1/2}$).

3.4 Discussion

Interfacial electron transfer pseudo-rate constants $k_{1/2}$ were quantified as a function of temperature for RuP-sensitized mesoporous thin films of rutile SnO_2, anatase TiO_2 (*a*-TiO_2), rutile TiO_2 (*r*-TiO_2), $ZrO_2|XTiO_2$, and $SnO_2|XTiO_2$ (where X is the number of applied ALD cycles). For $SnO_2|XTiO_2$, the kinetic response varied dramatically between materials that were heated to 200 °C post TiO_2 deposition, termed 'unannealed', and materials that were heated to 450 °C, termed 'annealed'. While $k_{1/2}$ for annealed films increased exponentially with temperature, unannealed films exhibited $k_{1/2}$ values that were temperature-independent from 10 to 40 °C and increased exponentially at higher temperatures. For the thickest unannealed shells, $SnO_2|50TiO_2$, $k_{1/2}$ values were within experimental error equal across the entire probed temperature range, 10 to 80 °C.

Raman and HRTEM analysis indicate that, for $SnO_2|XTiO_2$, unannealed TiO_2 shells are likely amorphous, while annealed shells exhibit lattice fringes and Raman spectra consistent with the rutile polymorph, *r*-TiO_2. Because this morphology change appears to be associated with stark differences in ET kinetics, these $SnO_2|XTiO_2$ materials lend an opportunity to develop a structure–function relationship between the crystallinity and the mechanism of interfacial electron transfer.

The temperature dependence of electron transfer kinetics differentiates thermally-activated and tunneling reactions.[62–64] For thermally-activated ET, rate constants are predicted to increase exponentially with temperature, as described by Eq. 3.3 and 3.4. Conversely, tunneling rate constants are predicted to be temperature independent, as described by Eq. 3.5, where $k°$ is the inherent electron transfer rate constant, β is the tunneling decay parameter, and D is the ET distance.

$$k = k^{\circ} e^{-\beta D} \quad (3.5)$$

As such, an exponential temperature dependence of pseudo rate constants in this study indicates thermally-activated interfacial ET, while temperature independence denotes tunneling.

3.4.1 Thin TiO_2 Shells

Annealed and unannealed $ZrO_2|10TiO_2$ and $SnO_2|10TiO_2$ exhibit behavior distinct from materials of the same composition with thicker shells. Because these thin shells are not discernable in HRTEM images or Raman spectra, definitive morphology assignment is not possible. As such, meaningful structure function relationships cannot be unambiguously determined.

The kinetic results do reveal, however, that these thin-shell materials undergo faster ET than do materials with thicker shells. For annealed $SnO_2|10TiO_2$ and both annealed and unannealed $ZrO_2|10TiO_2$, values of $k_{1/2}$ increase exponentially with temperature, which indicates a thermally-activated ET. Unannealed $SnO_2|10TiO_2$, however, undergoes thermally-activated ET only at temperatures above ~ 40 °C, while at lower temperatures, ET occurs through tunneling. The fast ET kinetics in all thin-shell samples are consistent with small ET barriers signified by low E_a values. Additionally, they exhibit anomalously low (*i.e.* more negative) values of $\Delta S^{\ddagger}$, indicating transition states more entropically penalized than those in thicker shells. Annealed $SnO_2|10TiO_2$ exhibits an E_a within experimental error equal to both annealed and unannealed $ZrO_2|10TiO_2$ and SnO_2. This suggests annealed $SnO_2|10TiO_2$ may have a common ET rate determining step (RDS) with one or more of these materials, but evidence is inconclusive.

3.4.2 Annealed $SnO_2|XTiO_2$

Raman spectra and HRTEM images of annealed $SnO_2|XTiO_2$, where X is 20, 30, and 50, suggest that the TiO_2 shells have a rutile morphology. In these crystalline materials, values of $k_{1/2}$ increase exponentially with temperature from 10 to 80 °C, which shows that the RDS is exclusively thermally activated, with an activation energy of 30 ± 3 kJ mol^{-1} regardless of shell thickness. Importantly, this activation energy is only slightly larger than the E_a quantified for *r*-TiO_2 and annealed $ZrO_2|XTiO_2$, $E_a \approx 24$ kJ mol^{-1}. In $ZrO_2|XTiO_2$, the high energy acceptor states of the ZrO_2 core are inaccessible to electrons transferred from the RuP excited state. As such, annealed $ZrO_2|XTiO_2$ serves as a proxy for the behavior of the TiO_2 shell alone, albeit an imperfect one due to its anatase crystallinity.[14] The discrepancy should be minimal, however, as equal E_a values were quantified for *a*- and *r*-TiO_2. The near parity of E_a between annealed $SnO_2|XTiO_2$, annealed $ZrO_2|XTiO_2$, and *r*-TiO_2 suggests a shared interfacial ET RDS.

The study of interfacial ET in dye-sensitized mesoporous TiO_2 materials has a long history,[65–67] much of which is concerned with determining the RDS and the physical source of the non-exponential kinetics.[57,68–70] Though far from conclusive,[71–73] under many experimental conditions, the observed rate constants report on transport of the injected electron to the oxidized sensitizer,[69,70,74] suggesting interfacial ET in TiO_2 to be rate limited by small polaron transport between $Ti^{III/IV}$ sites.[75] As such, the RDS for interfacial ET in annealed $SnO_2|XTiO_2$ is herein proposed to be electron $Ti^{III/IV}$ hopping, as shown in Fig. 3.12. This is consistent with both the nearly equivalent E_a measured for annealed $SnO_2|XTiO_2$, annealed $ZrO_2|XTiO_2$, and *r*-TiO_2 and the lack of shell thickness dependence for E_a in annealed $SnO_2|XTiO_2$. It also does not preclude the possibility that electrons move

between the SnO_2 and TiO_2 phases, as transport through SnO_2 is faster than that through TiO_2.[75]

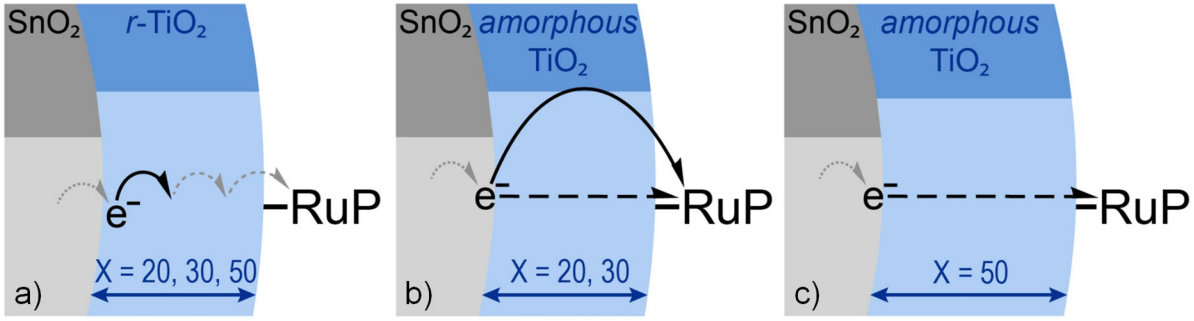

Figure 3.12. Proposed interfacial electron transfer mechanisms in a) annealed and b-c) unannealed $SnO_2|XTiO_2$ in which X is the number of applied ALD cycles is X. Black arrows represent rate determining steps (RDS)—solid arrows are thermally activated and dashed are tunneling. Dashed gray arrows represent fast steps after an RDS, and gray dotted arrows indicate fast steps that may occur before the RDS. a) In annealed $SnO_2|XTiO_2$, HRTEM and Raman evidence suggest shells are rutile (*r*-TiO_2). Temperature-dependent kinetics are consistent with the RDS being thermally-activated $Ti^{III/IV}$ hopping through the shell. b-c) In unannealed $SnO_2|XTiO_2$, HRTEM and Raman evidence suggest shells are amorphous. b) When X = 20 and 30, temperature-dependent kinetics are consistent with tunneling from the core or interface to the RuP at low temperatures and activation into a conduction band-like transition state at high temperatures. c) When X = 50, temperature-independent kinetics are consistent with tunneling from the interface or core to the RuP.

Annealed $SnO_2|XTiO_2$ materials do, however, exhibit ET E_a values slightly larger than $ZrO_2|XTiO_2$ and *r*-TiO_2. Additionally, Eyring analysis reveals that $\Delta S^{\ddagger}$ for ET in annealed $SnO_2|XTiO_2$ is more negative than that of $ZrO_2|XTiO_2$, indicating a significant entropic penalty upon entering the transition state. Though the physical origin of this difference is not well-understood, it may reflect the chemical environment of the donor Ti^{III} in the $Ti^{III/IV}$ hop. If the donor Ti^{III} in the RDS is in or near the SnO_2/TiO_2 interface, lattice distortions may lead to a disordered reagent state, and thus the observed entropic cost in the transition state.

3.4.3 Unannealed $SnO_2|XTiO_2$

Unannealed $SnO_2|XTiO_2$ materials exhibit starkly different temperature-dependent kinetics than do their annealed counterparts. Raman spectra and HRTEM images of unannealed $SnO_2|XTiO_2$, where X is 20, 30, and 50, suggest the TiO_2 shells to be amorphous. For the thickest unannealed shells, $SnO_2|50TiO_2$, temperature-independent $k_{1/2}$ values from 10 to 80 °C indicate that interfacial ET occurs exclusively through tunneling. Tunneling is also indicated in unannealed $SnO_2|20TiO_2$ and $SnO_2|30TiO_2$ at temperatures below 40 °C. At higher temperatures, however, the $k_{1/2}$ values accelerate rapidly with temperature as a thermally-activated ET mechanism with a remarkably large barrier, $E_a \approx 95$ kJ mol^{-1}, eclipses the tunneling reaction.

These data reveal that, for $SnO_2|XTiO_2$ materials, the post-deposition heat treatment and resulting shell morphology determine the operative interfacial ET mechanism. The amorphous TiO_2 shell alone, however, is not sufficient to account for the tunneling and large ET barriers in unannealed $SnO_2|XTiO_2$. Though Raman and HRTEM evidence suggest that unannealed $ZrO_2|20/30TiO_2$ and $ZrO_2|Al_2O_3|50TiO_2$ have amorphous shells, these materials undergo exclusively thermally-activated ET, unlike the $SnO_2|XTiO_2$ materials. In fact, for ZrO_2 with amorphous TiO_2 shells, $k_{1/2}$ and E_a values were within experimental error equal to those of annealed $ZrO_2|XTiO_2$ with anatase shells, a surprising finding which suggests TiO_2 crystallinity may not significantly impact ET under these conditions. The $ZrO_2|XTiO_2$ ET barrier $E_a \approx 24$ kJ mol^{-1} is in stark contrast to unannealed $SnO_2|20/30TiO_2$, where an incredibly large barrier exists that cannot be overcome at low temperatures. As such, the RDS for interfacial ET in unannealed $SnO_2|XTiO_2$ cannot be $Ti^{III/IV}$ hopping, nor is it easily

rationalized by any mechanism that invokes only the amorphous TiO_2 shell. The RDS must instead involve either the SnO_2 core or the SnO_2/TiO_2 interface.

The RDS of thermally-activated ET in unannealed $SnO_2|XTiO_2$ is highly entropically favored, with $\Delta S^{\ddagger} \approx 125$ J mol^{-1} K^{-1}. This large positive $\Delta S^{\ddagger}$ value indicates the transition state to be significantly more disordered than the reactant state. A highly energetic and highly disordered transition state is consistent with activation into or near the delocalized TiO_2 conduction band. It is plausible that this activation results in ET into the amorphous TiO_2, and the electron then undergoes comparatively fast $Ti^{III/IV}$ hopping to the $Ru^{III}P$ acceptor. This mechanism, however, is inconsistent with the changeover from large-barrier thermally-activated ET in unannealed $SnO_2|20/30TiO_2$ to tunneling at all temperatures in unannealed $SnO_2|50TiO_2$. Instead, it is proposed that thermally-activated interfacial ET in unannealed $SnO_2|20/30TiO_2$ occurs in one step—an electron moves directly from the core or interface to the $Ru^{III}P$ through a conduction-band like transition state.

In total, this data suggests a physical picture of interfacial ET in unannealed $SnO_2|XTiO_2$ (Fig. 3.12) in which electron movement from the core or interface into the amorphous TiO_2 is associated with a prohibitively large energetic barrier. This is consistent with recent findings that electron transport in a $SnO_2|XTiO_2$-based dye-sensitized solar cell occurs through TiO_2 when the material is annealed but SnO_2 when the material is unannealed.[21] At low temperatures, electrons in unannealed $SnO_2|XTiO_2$ tunnel from either the core or core/shell interface to the $Ru^{III}P$ sensitizer. At higher temperatures, the rate constant for thermally-activated ET from the core or interface to the $Ru^{III}P$ becomes faster than the tunneling process and thus predominates. This mechanistic change is able to occur at a relatively low temperature, ~ 40 °C, despite a massive activation barrier due to the entropic

favorability of a delocalized conduction band-like transition state. In materials with very thick amorphous shells (SnO_2|50TiO_2), however, the distance between the core or interface and the $Ru^{III}P$ is too great to cover in a single activated step, and ET occurs exclusively through tunneling.

3.4.4. Informing a Predictive Model

Here, the thickness and morphology of the TiO_2 shell in a SnO_2|TiO_2 core|shell nanostructure was found to determine the mechanism by which the material underwent interfacial electron transfer with a surface-anchored molecule. Control of the shell thickness and morphology should thus allow predictable control of the interfacial ET rate constant and help realize the specific goal of slowing undesirable charge recombination in core|shell nanostructures utilized for solar energy conversion.

In both annealed and unannealed SnO_2|XTiO_2, interfacial ET was observed to be thermally activated under at least some conditions. Despite that thermally-activated ET in annealed and unannealed SnO_2|XTiO_2 seem to have different RDSs, the reactions occur with similar Gibbs activation energies. In unannealed SnO_2|XTiO_2, the interplay of large enthalpic barriers and significant entropic incentives results in $\Delta G^{\ddagger}$ values only slightly larger than those of the annealed SnO_2|XTiO_2. This similarity in $\Delta G^{\ddagger}$ results in unannealed SnO_2|20/30TiO_2 manifesting interfacial ET $k_{1/2}$ values less than an order of magnitude smaller than those of the annealed materials (Fig. 3.11).

The smallest attainable $k_{1/2}$ values are instead achieved by promoting a tunneling mechanism, especially at the elevated temperatures at which terrestrial solar energy conversion devices operate. The structure/function relationship between the shell morphology and the ET mechanism thus becomes instructive. To create a system in which

electrons will reliably tunnel, shells must be amorphous and sufficiently thick to disallow a thermally-activated direct electron transfer from the core or interface to the molecular acceptor.

The kinetic data in this study suggest that electron transfer between a crystalline core or the nearby core|shell interface and an amorphous shell may be prohibitively difficult. The physical reason, however is not readily apparent from these results. Electron transfer between rutile SnO_2 and amorphous TiO_2 could be constrained by the difficulty of increasing the effective mass of the electron, of a large polaron becoming a small polaron, or of moving from an s to a d orbital between which coupling is poor. Currently, however, the acceptor states of $SnO_2|XTiO_2$ materials are not well characterized. A better understanding of the electron dynamics within $SnO_2|TiO_2$ and other core|shell nanostructures is necessary to clarify the details of their interfacial electron transfer mechanisms.

3.5 Conclusions

This Chapter represents a significant step forward in elucidating detailed mechanistic information on interfacial electron transfer in $SnO_2|TiO_2$ core|shell nanostructures to molecular acceptors at the TiO_2 shell surface. Temperature dependent kinetic studies have definitively shown that both tunneling and thermally-activated electron transfer are operative in sensitized $SnO_2|TiO_2$ materials. Most notably, the mechanism of interfacial electron transfer depends critically on the temperature to which the $SnO_2|TiO_2$ is heated after TiO_2 deposition. High annealing temperatures result in rutile TiO_2 shells and thermally-activated electron transfer proposed herein to be rate limited by $Ti^{III/IV}$ hopping in the shell. Low annealing temperatures result in amorphous TiO_2 shells and a kinetic competition between

tunneling and thermally-activated interfacial electron transfer. Here, remarkably large activation energies are offset by entropically favorable transition states. Ultimately, the interplay of entropic and enthalpic barriers reliably predicts the interfacial electron transfer pseudo-rate constants of each sensitized material. The slowest interfacial electron transfer is achieved in thick amorphous shells and occurs by a tunneling mechanism.

3.6 Acknowledgements

The authors would like to thank Dr. Erica M. James for thoughtful conversations. This material is based upon work solely supported by the Alliance for Molecular PhotoElectrode Design for Solar Fuels (AMPED), an Energy Frontier Research Center (EFRC) funded by the U.S. Department of Energy, Office of Science, Office of Basic Energy Sciences under Award Number DE-SC0001011. REB acknowledges the National Science Foundation for an individual Graduate Research Fellowship under Grant No. DGE-1650116. This work was performed in part using instrumentation at the Chapel Hill Analytical and Nanofabrication Laboratory, CHANL, a member of the North Carolina Research Triangle Nanotechnology Network, RTNN, which is supported by the National Science Foundation, Grant ECCS- 1542015, as part of the National Nanotechnology Coordinated Infrastructure, NNCI. This work was performed in part at the Analytical Instrumentation Facility (AIF) at North Carolina State University, which is supported by the State of North Carolina and the National Science Foundation (award number ECCS-1542015). This work made use of instrumentation at AIF acquired with support from the National Science Foundation (DMR-1726294). The AIF is a member of the North Carolina Research Triangle Nanotechnology Network (RTNN), a site in the National Nanotechnology Coordinated Infrastructure (NNCI).

3.7 Associated Content

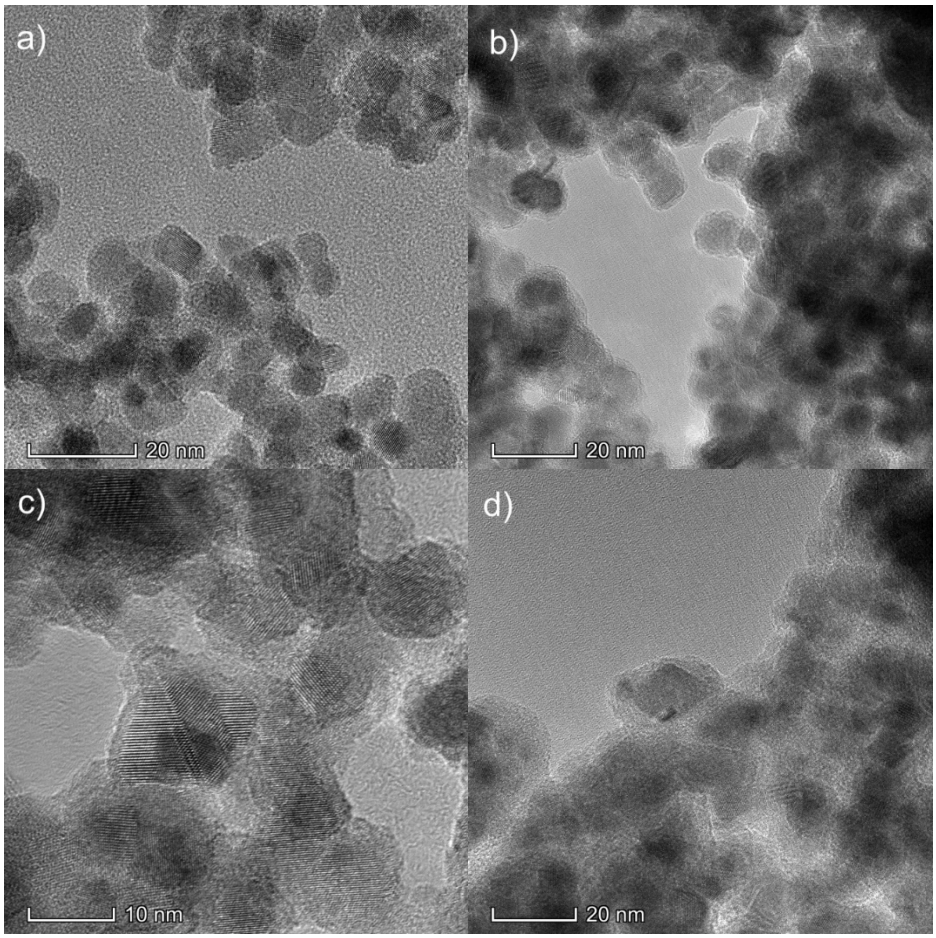

Figure 3.13. HRTEM images of unannealed a) $SnO_2|10TiO_2$, b) $SnO_2|20TiO_2$, c) $SnO_2|30TiO_2$, and d) $SnO_2|50TiO_2$. After ALD, materials were heated to 200 °C for 30 min in air. Each ALD cycle is estimated to deposit ~ 0.66 Å TiO_2.

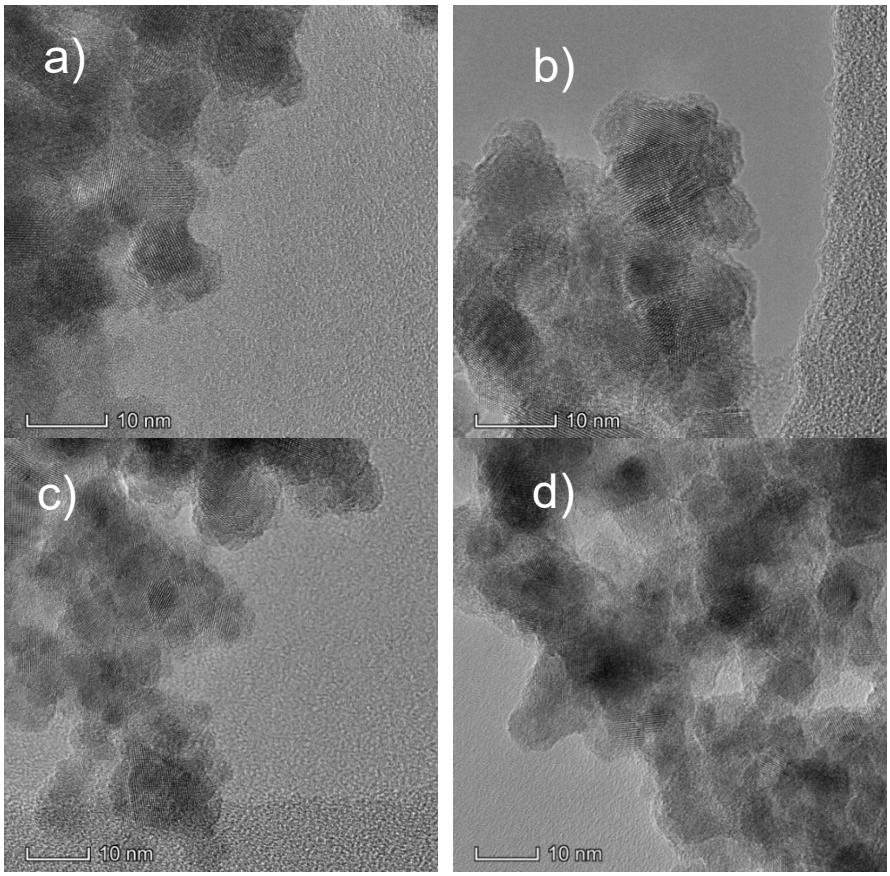

Figure 3.14. HRTEM images of annealed a) $SnO_2|10TiO_2$, b) $SnO_2|20TiO_2$, c) $SnO_2|30TiO_2$, and d) $SnO_2|50TiO_2$. Annealing was performed by heating at 450 °C for 30 min in air. Each ALD cycle is estimated to deposit ~ 0.66 Å TiO_2.

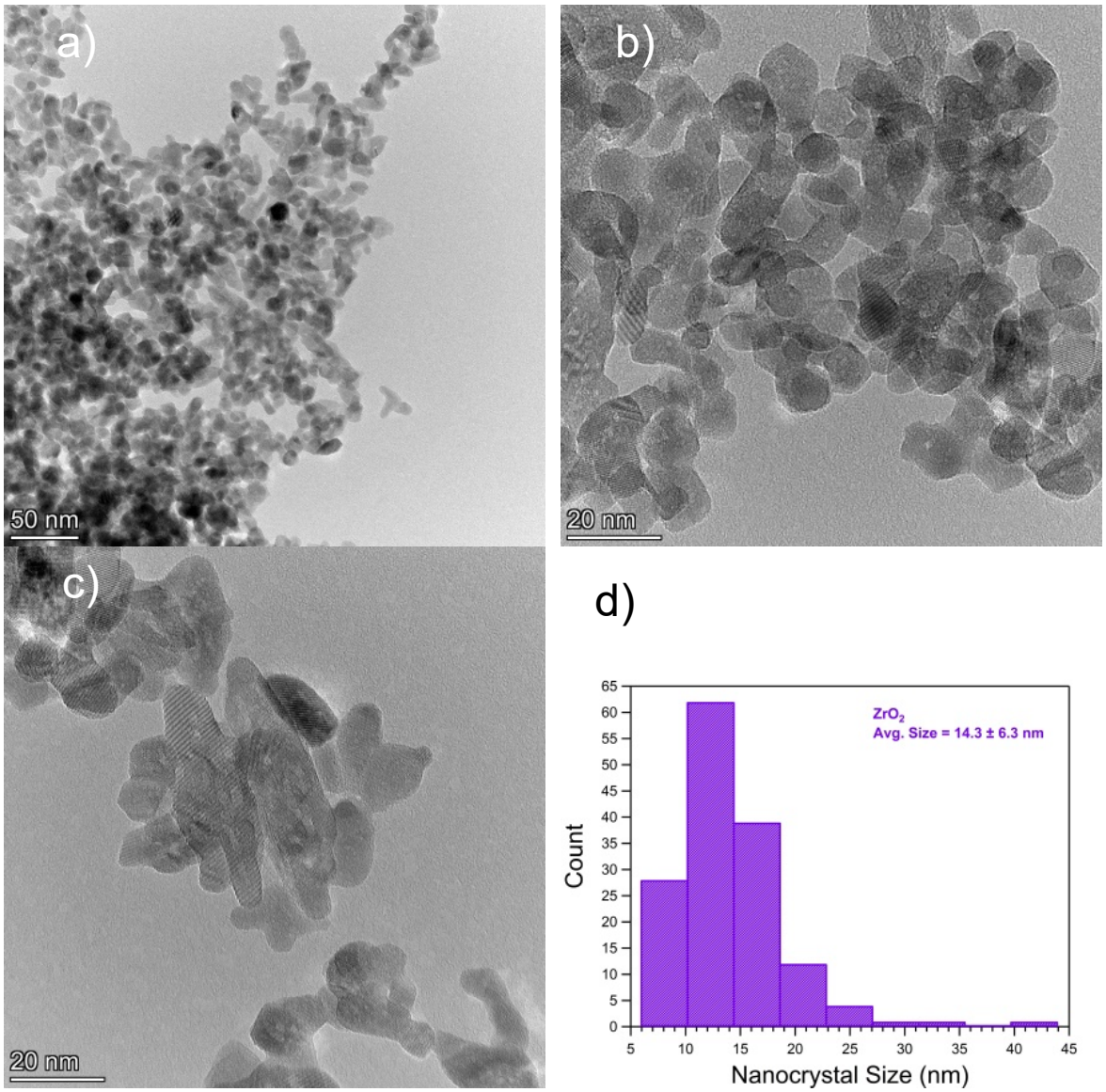

Figure 3.15. HRTEM images of a-c) ZrO_2 nanocrystals and d) their size distribution (14 ± 6 nm). Lattice fringes are visible when images are magnified.

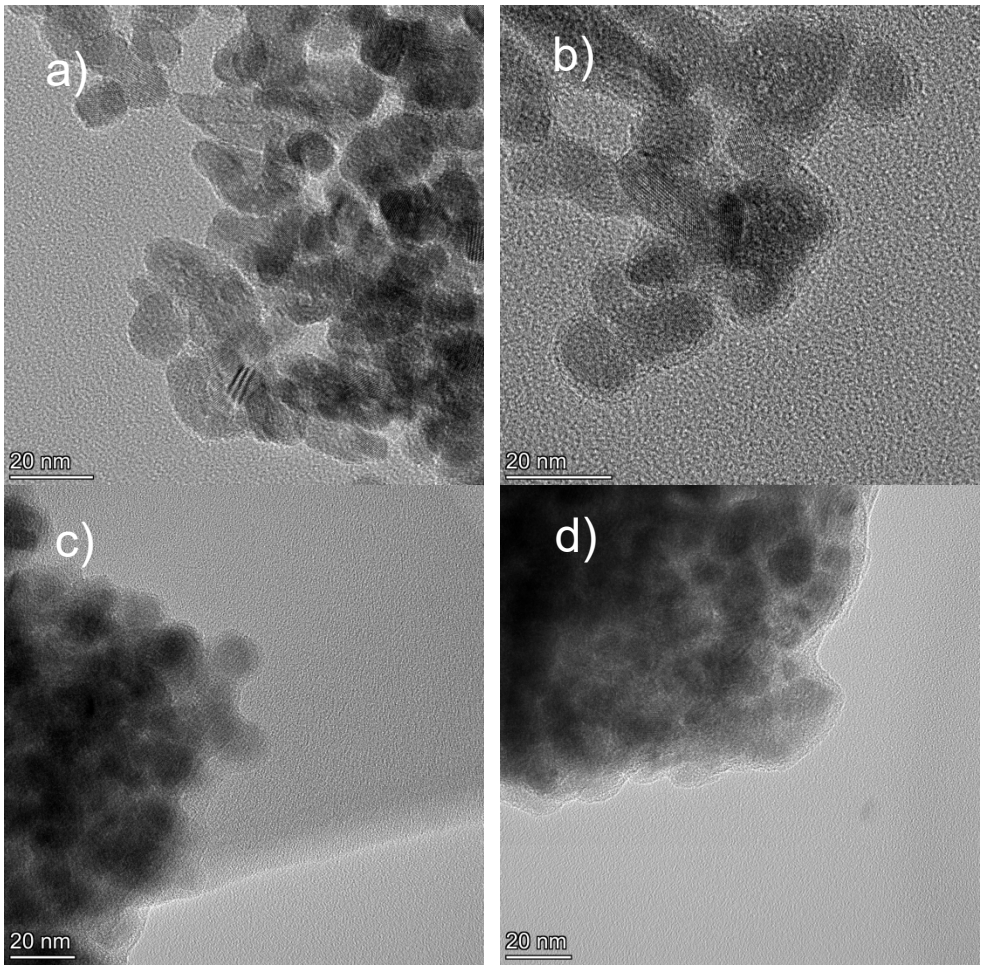

Figure 3.16. HRTEM images of unannealed a) $ZrO_2|10TiO_2$, b) $ZrO_2|20TiO_2$, c) $ZrO_2|30TiO_2$, and d) $ZrO_2|50TiO_2$. Materials were heat treated for 30 minutes at 200 °C post TiO_2 deposition. Each ALD cycle is estimated to deposit ~ 0.66 Å TiO_2.

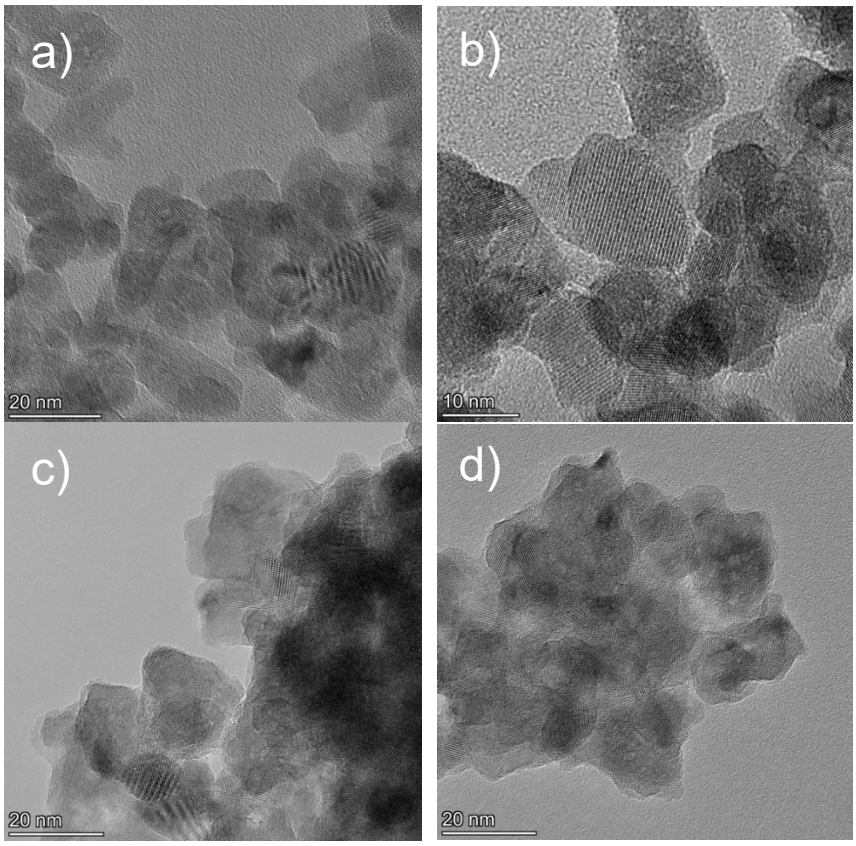

Figure 3.17. HRTEM images of annealed a) $ZrO_2|10TiO_2$, b) $ZrO_2|20TiO_2$, c) $ZrO_2|30TiO_2$, and d) $ZrO_2|50TiO_2$. Annealing was performed at 450 °C for 30 min in air. Each ALD cycle is estimated to deposit ~ 0.66 Å TiO_2.

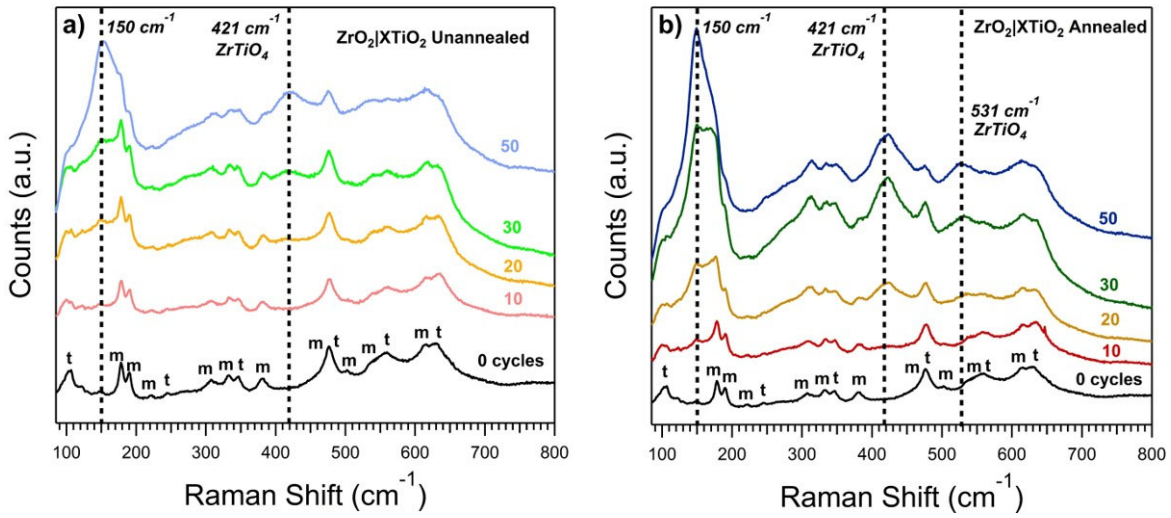

Figure 3.18. Raman spectra for a) unannealed and b) annealed $ZrO_2|XTiO_2$ where X is the number of cycles of TiO_2 deposited. The labels "m" and "t" represent the monoclinic and tetragonal phonon modes, respectively, for ZrO_2. Each ALD cycle is estimated to deposit 0.66 Å TiO_2.

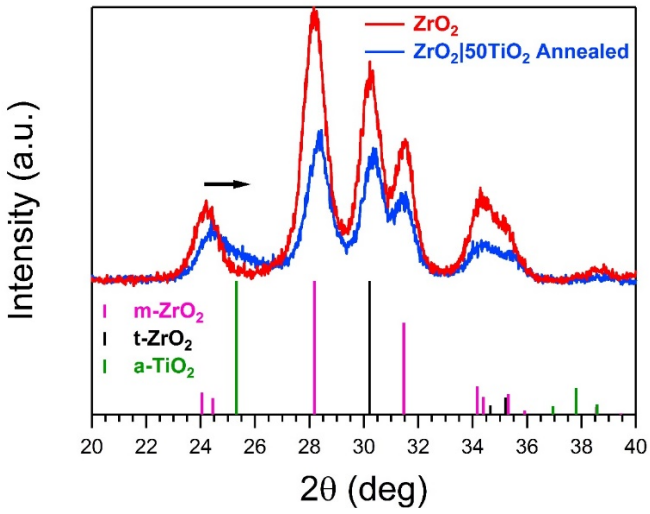

Figure 3.19. Grazing incidence angle XRD of ZrO_2 (red) and annealed $ZrO_2|50TiO_2$ (blue). Grazing incidence angle X-ray diffraction was performed using a Rigaku SmartLab diffractometer with a 3 kW Cu tube Kα X-ray source (λ = 1.5406 Å) and a HyPix-3000 high-energy-resolution multi-dimensional detector operated in 0D mode. Measurements were performed at a fixed incidence angle of 1.000 degree with a step of 0.020 degrees at a speed of 1.000 degree per minute. Diffraction patterns were analyzed and assigned in Rigaku's PDXL2 software. Here, films were doctor-bladed onto microscope slides to avoid FTO diffraction. ICSD data for monoclinic ZrO_2 (m-ZrO_2, pink, PDF card No. 01-086-1450), tetragonal ZrO_2 (t-ZrO_2, black, PDF card No. 01-075-9645), and tetragonal anatase TiO_2 (a-TiO_2, green, PDF card No. 01-084-1285) are presented as vertical lines at the bottom of the graph. After annealing $ZrO_2|50TiO_2$, the m-ZrO_2 (011) at 24.05 deg, (110) at 24.45 deg, and (-111) at 28.18 dg, and the t-ZrO_2 (101) at 30.21 all shift toward higher 2θ values. Annealing was performed at 450 °C for 30 min in air. Each ALD cycle is estimated to deposit 0.66 Å TiO_2.

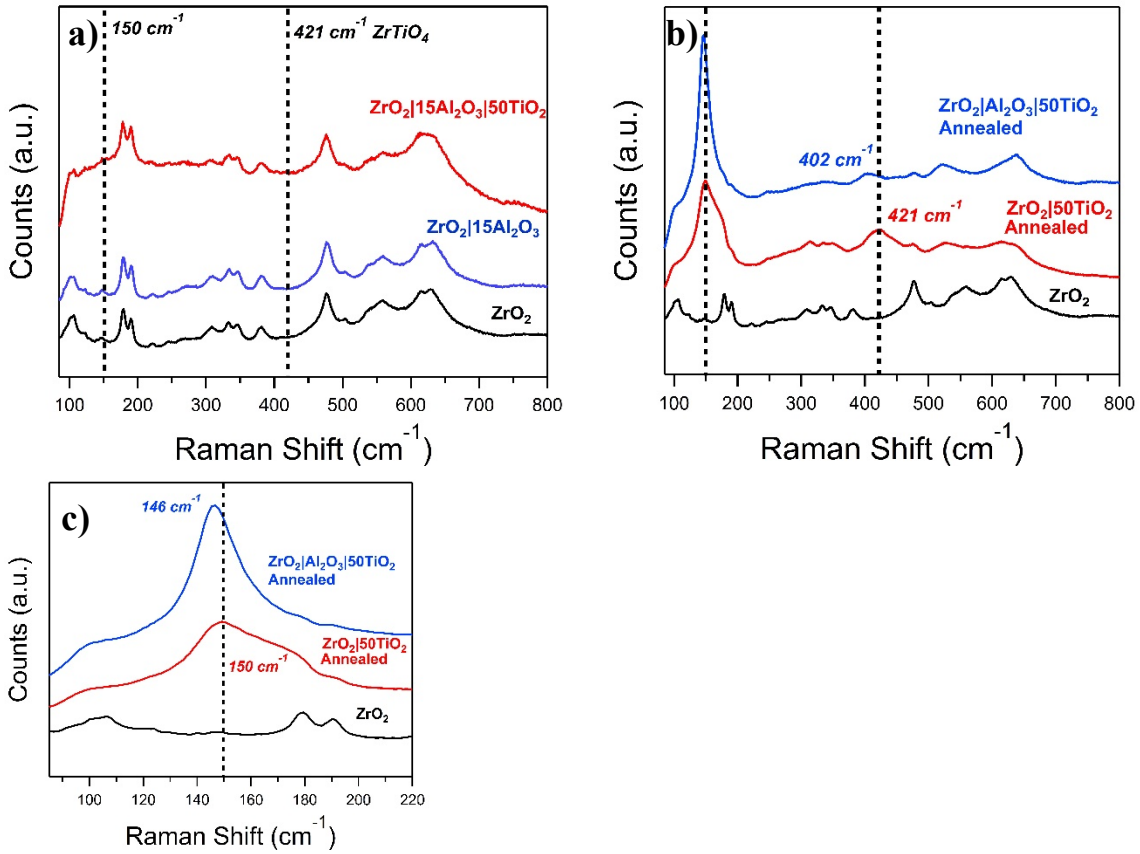

Figure 3.20. a) Raman spectra of ZrO_2 (bottom, black), $ZrO_2|15Al_2O_3$ (middle, blue) and, $ZrO_2|15Al_2O_3|50TiO_2$ (top, red). Minimal changes are observed among the samples, demonstrating that the insulating amorphous alumina inner layer prevented crystallization of the TiO_2 shell. To create the alumina inner layer, 50 ALD cycles of alumina was first deposited at 130 °C to pre-treat the *empty* reactor chamber using Trimethylaluminum (TMA, Sigma-Aldrich, 97%) and ultrapure DI water at 130 °C. Both water and TMA precursor reservoirs were held at room temperature. 15 cycles of Al_2O_3 was subsequently deposited on six freshly prepared ZrO_2 slides at 130 °C using a 0.02 sec pulse of TMA, 20 sec exposure, 30 sec purge, 0.02 sec pulse of H_2O, 20 sec exposure, 30 sec purge. The nitrogen flow rate during exposures was 5 sccm, and the flow rate for the purges was 20 sccm. After 15 cycles of Al_2O_3 was deposited on ZrO_2, the films were heated in air at 200 °C for 30 min to remove adventitious carbon. The 50 cycles of TiO_2 was deposited using the recipe detailed in the experimental section. b) Raman spectra comparing ZrO_2 with annealed $ZrO_2|50TiO_2$ and $ZrO_2|15Al_2O_3|50TiO_2$. Characteristic anatase $E_{g(1)}$, $B_{1g(1)}$, $B_{1g(2)}$, and $E_{g(2)}$ phonon modes are observed at 146, 402, 519, and 639 cm^{-1} for annealed $ZrO_2|15Al_2O_3|50TiO_2$. c) Magnification on the lower wavenumber region displaying a 4 cm^{-1} red-shift in peak maxima from annealed $ZrO_2|50TiO_2$ to $ZrO_2|15Al_2O_3|50TiO_2$.

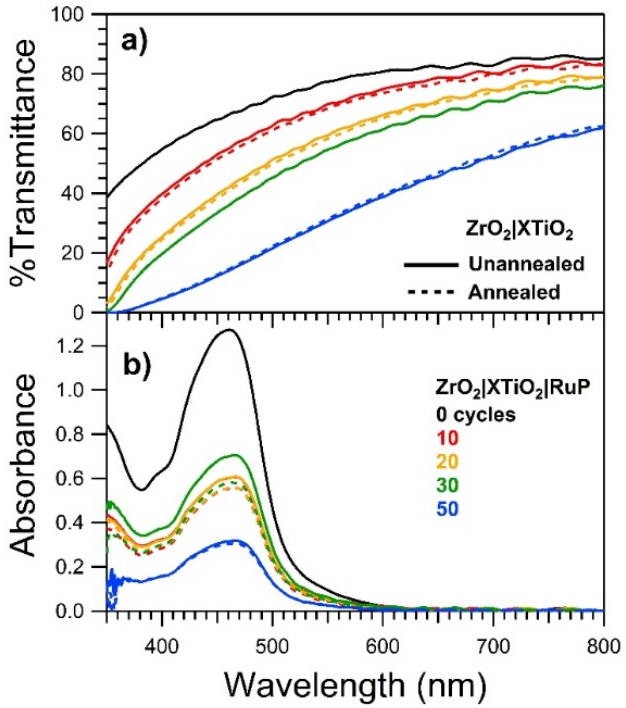

Figure 3.21. UV-vis spectra of a) bare $ZrO_2|XTiO_2$ (reported as %transmittance) and b) RuP-sensitized $ZrO_2|XTiO_2$ in N_2-sparged pH 1 $HClO_4$, where X is the number of ALD cycles of TiO_2. Each ALD cycle is estimated to deposit 0.66 Å TiO_2. The high degree of scatter by the films obscures the true fundamental absorption onset of the metal oxide material. To account for increasing scatter with increasing TiO_2 shell thickness, the spectra of the bare films were subtracted from the spectra of the dye-sensitized films to generate spectra in (b). The wavy patterns at higher wavelengths in the spectra are due to thin film interference.

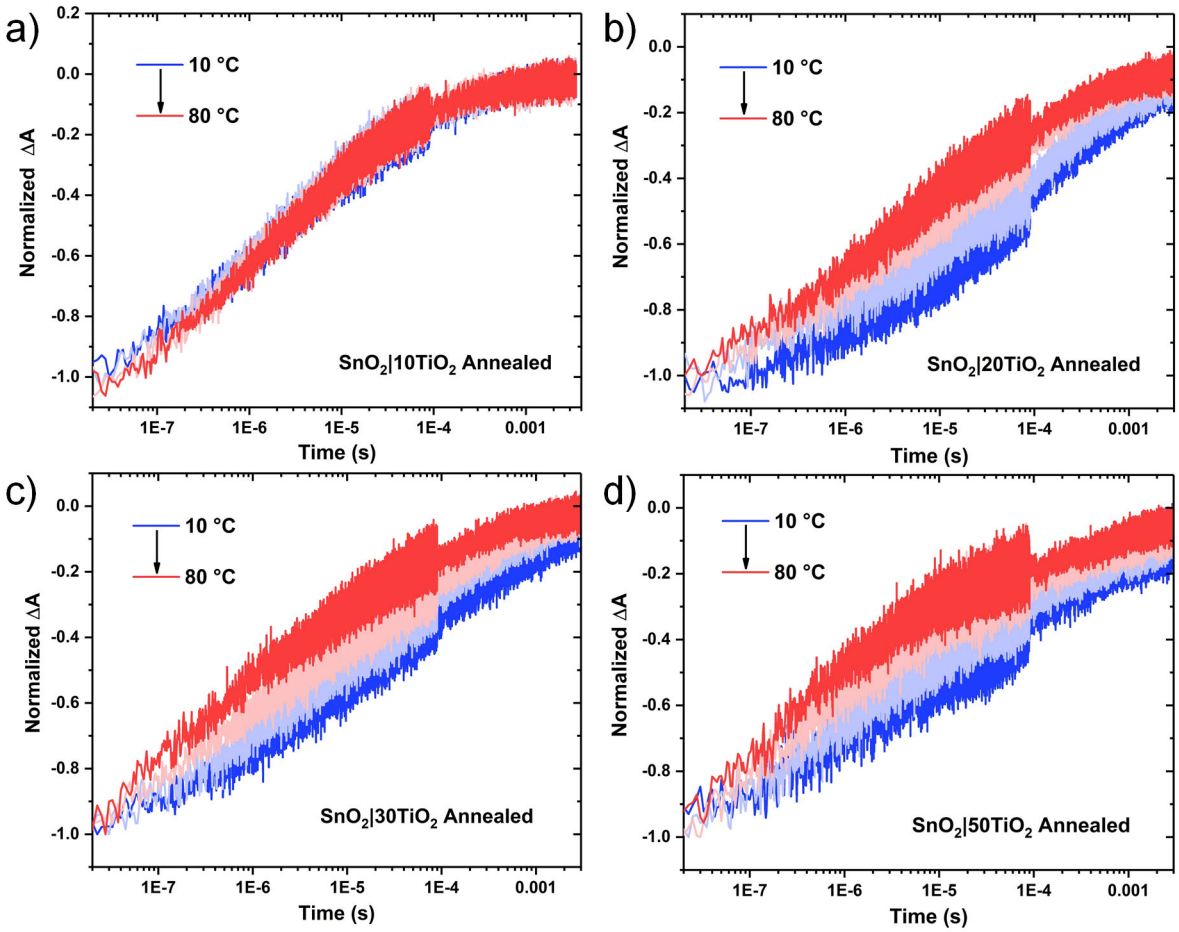

Figure 3.22. Absorption changes measured at 402 nm after pulsed 532 nm light excitation in aqueous 0.1 M $HClO_4$ over the indicated temperature range for RuP-sensitized annealed $SnO_2|XTiO_2$ films where X is the number of ALD cycles of TiO_2. Each ALD cycle is estimated to deposit 0.66 Å TiO_2.

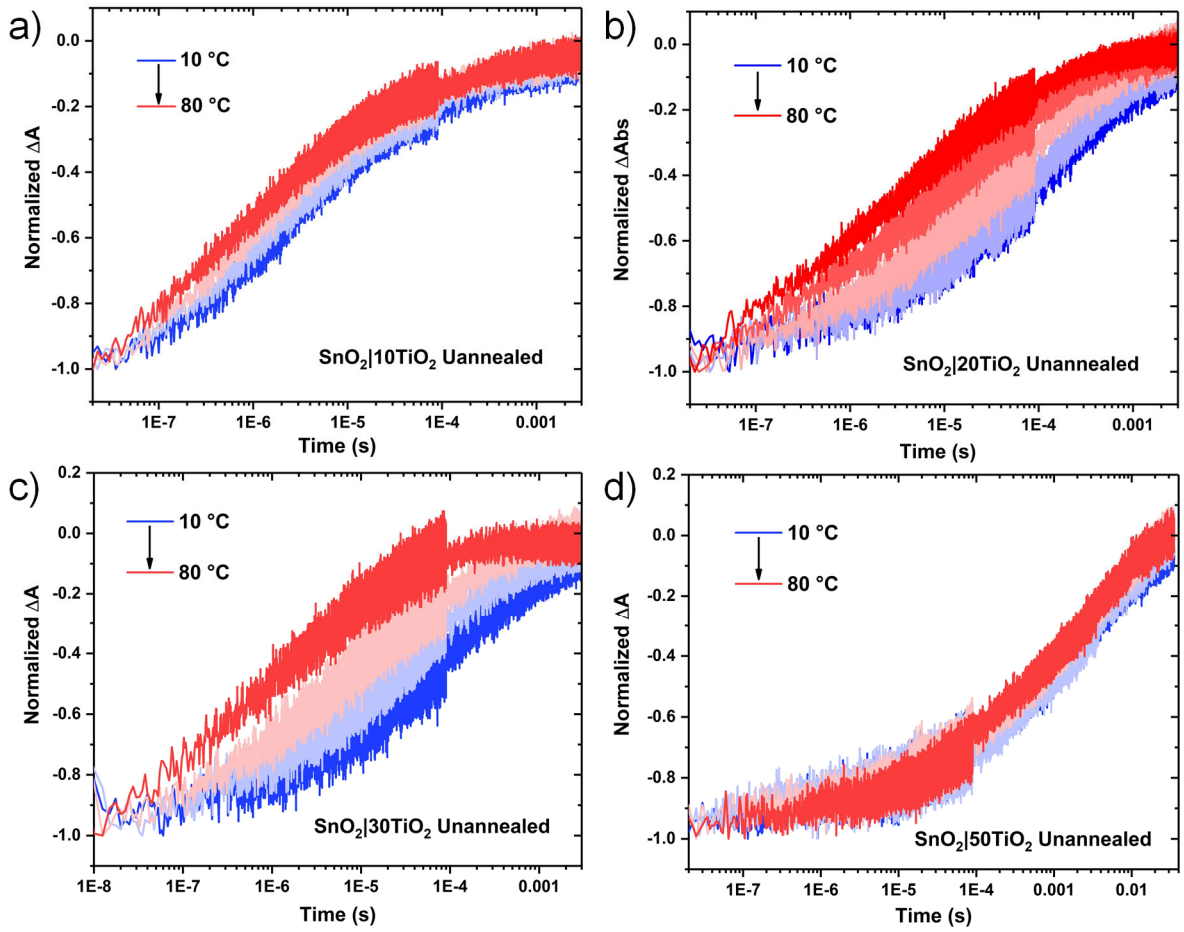

Figure 3.23. Absorption changes measured at 402 nm after pulsed 532 nm light excitation in aqueous 0.1 M $HClO_4$ over the indicated temperature range for RuP-sensitized unannealed $SnO_2|XTiO_2$ materials where X is the number of ALD cycles of TiO_2. Each ALD cycle is estimated to deposit 0.66 Å TiO_2.

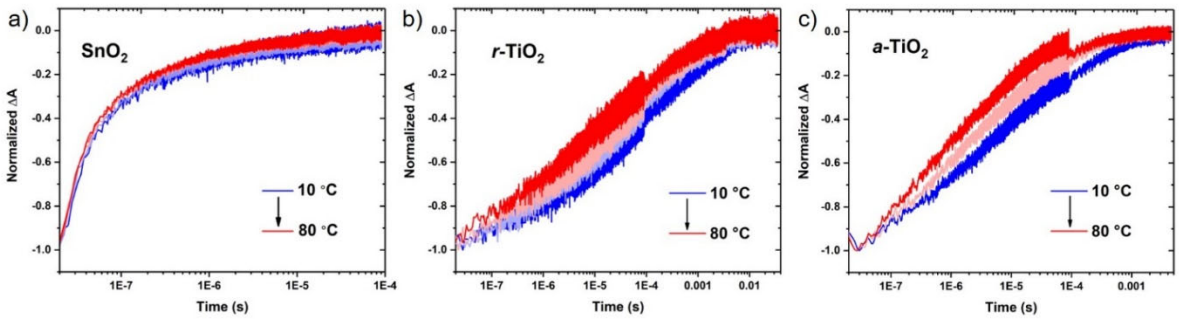

Figure 3.24. Absorption changes measured at 402 nm (a and c) or 460 nm (b) after pulsed 532 nm light excitation in aqueous 0.1 M $HClO_4$ over the indicated temperature range for RuP-sensitized mesoporous nanocrystalline thin films a) rutile SnO_2, b) rutile TiO_2, and c) anatase TiO_2.

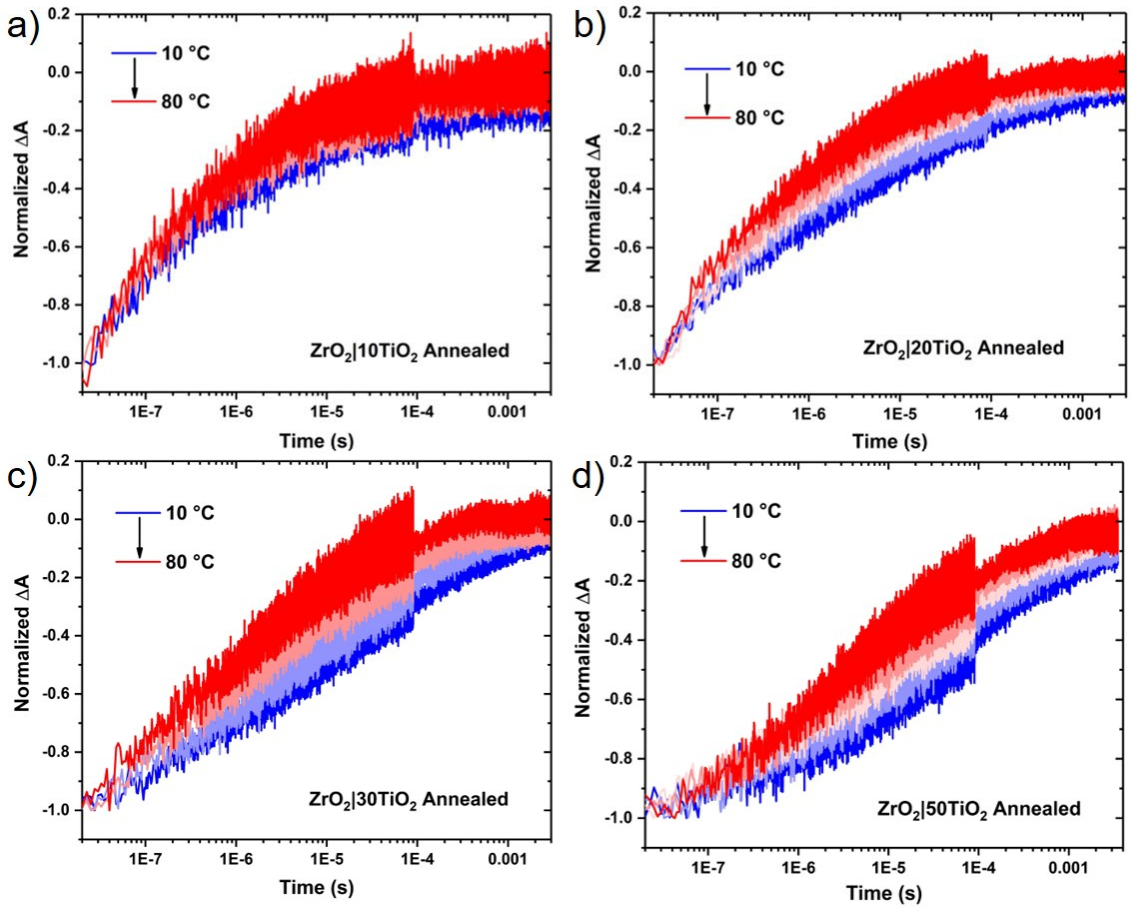

Figure 3.25. Absorption changes measured at 402 nm after pulsed 532 nm light excitation in aqueous 0.1 M $HClO_4$ over the indicated temperature range for RuP-sensitized annealed $ZrO_2|XTiO_2$ films where X is the number of ALD cycles of TiO_2. Each ALD cycle is estimated to deposit 0.66 Å TiO_2.

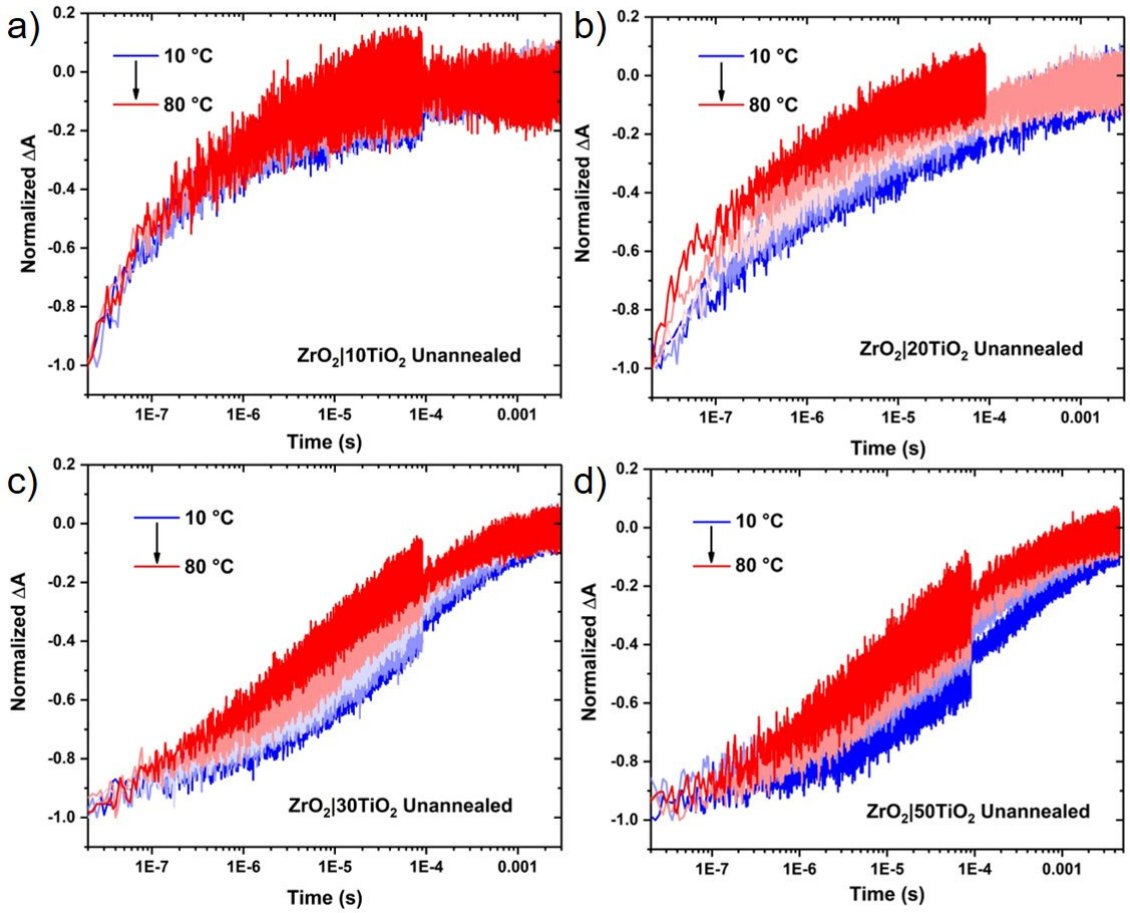

Figure 3.26. Absorption changes measured at 402 nm after pulsed 532 nm light excitation in aqueous 0.1 M $HClO_4$ over the indicated temperature range for RuP-sensitized unannealed $ZrO_2|XTiO_2$ films where X is the number of ALD cycles of TiO_2. Each ALD cycle is estimated to deposit 0.66 Å TiO_2.

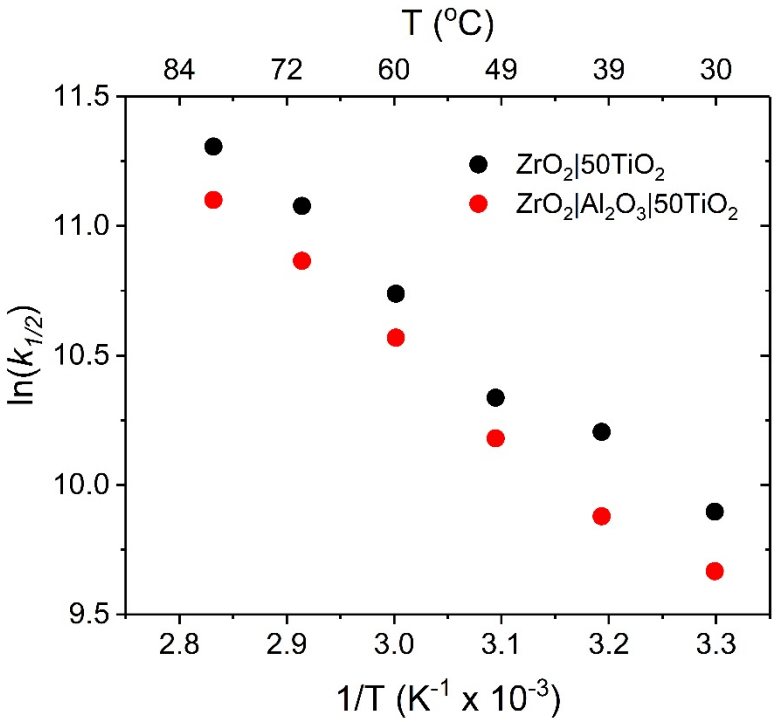

Figure 3.27. Arrhenius plots of interfacial electron transfer following 532 nm pulsed light excitation in aqueous 0.1 M $HClO_4$ for RuP-sensitized unannealed $ZrO_2|50TiO_2$ (black) and $ZrO_2|Al_2O_3|50TiO_2$ (red) films, both treated at 200 °C after TiO_2 deposition. Each ALD cycle is estimated to deposit ~ 0.66 Å TiO_2.

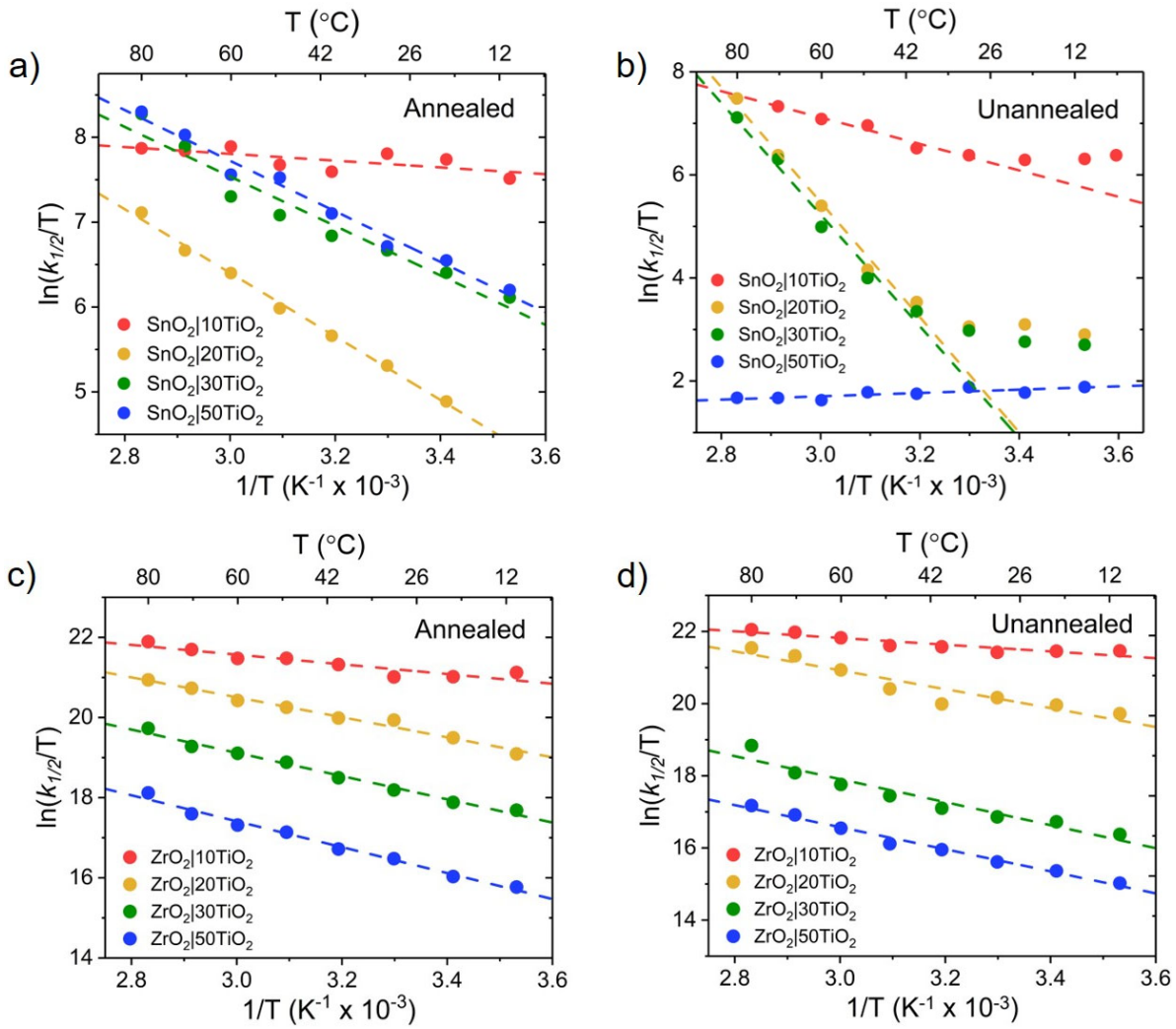

Figure 3.28. Eyring analysis of interfacial electron transfer following 532 nm pulsed light excitation in aqueous 0.1 M $HClO_4$ for RuP-sensitized core|XTiO_2 materials, where X in the number of ALD TiO_2 cycles. Films were a) annealed $SnO_2|TiO_2$, b) unannealed $SnO_2|TiO_2$, c) annealed $ZrO_2|TiO_2$, and d) unannealed $ZrO_2|TiO_2$. Dashed lines represent fits of the linear portions of the data to the Eyring equation, Eq. 3.4.

REFERENCES

(1) Li, W.; Elzatahry, A.; Aldhayan, D.; Zhao, D. Core-Shell Structured Titanium Dioxide Nanomaterials for Solar Energy Utilization. *Chem. Soc. Rev.* **2018**, *47* (22), 8203–8237.

(2) Brennaman, M. K.; Dillon, R. J.; Alibabaei, L.; Gish, M. K.; Dares, C. J.; Ashford, D. L.; House, R. L.; Meyer, G. J.; Papanikolas, J. M.; Meyer, T. J. Finding the Way to Solar Fuels with Dye-Sensitized Photoelectrosynthesis Cells. *J. Am. Chem. Soc.* **2016**, *138*, 13085–13102.

(3) Prasittichai, C.; Hupp, J. T. Surface Modification of SnO_2 Photoelectrodes in Dye Sensitized Solar Cells: Significant Improvements in Photovoltage via Al_2O_3 Atomic Layer Deposition. *J. Phys. Chem. Lett.* **2010**, *1* (10), 1611–1615.

(4) Miller, D. R.; Akbar, S. A.; Morris, P. A. Nanoscale Metal Oxide-Based Heterojunctions for Gas Sensing: A Review. *Sensors Actuators, B Chem.* **2014**, *204*, 250–272.

(5) Idota, Y.; Kubota, T.; Matsufuji, A.; Maekawa, Y.; Miyasaka, T. Tin-Based Amorphous Oxide: A High-Capacity Lithium-Ion-Storage Material. *Science.* **1997**, *276* (5317), 1395–1397.

(6) Su, L.; Jing, Y.; Zhou, Z. Li Ion Battery Materials with Core-Shell Nanostructures. *Nanoscale* **2011**, *3* (10), 3967–3983.

(7) Liu, P.; Wang, C.; Zhou, D.; Yuan, Q.; Wang, Y.; Hu, Y.; Han, D.; Feng, L. WO_x@PEDOT Core-Shell Nanorods: Hybrid Hole-Transporting Materials for Efficient and Stable Perovskite Solar Cells. *ACS Appl. Energy Mater.* **2018**, *1* (4), 1742–1752.

(8) Pang, A.; Sun, X.; Ruan, H.; Li, Y.; Dai, S.; Wei, M. Highly Efficient Dye-Sensitized Solar Cells Composed of TiO_2@SnO_2 Core-Shell Microspheres. *Nano Energy* **2014**, *5*, 82–90.

(9) Wee, K. R.; Sherman, B. D.; Brennaman, M. K.; Sheridan, M. V.; Nayak, A.; Alibabaei, L.; Meyer, T. J. An Aqueous, Organic Dye Derivatized SnO_2/TiO_2 Core/Shell Photoanode. *J. Mater. Chem. A* **2016**, *4* (8), 2969–2975.

(10) Wang, D.; Wang, L.; Brady, M. D.; Dares, C. J.; Meyer, G. J.; Meyer, T. J.; Concepcion, J. J. Self-Assembled Chromophore−Catalyst Bilayer for Water Oxidation in a Dye-Sensitized Photoelectrosynthesis Cell. *J. Phys. Chem. C* **2019**, *123*, 30039–30045.

(11) Karlsson, M.; Jõgi, I.; Eriksson, S. K.; Rensmo, H.; Boman, M.; Boschloo, G.; Hagfeldt, A. Dye-Sensitized Solar Cells Employing a SnO_2-TiO_2 Core-Shell Structure Made by Atomic Layer Deposition. *Chimia (Aarau).* **2013**, *67* (3), 142–148.

(12) Alibabaei, L.; Farnum, B. H.; Kalanyan, B.; Brennaman, M. K.; Losego, M. D.;

Parsons, G. N.; Meyer, T. J. Atomic Layer Deposition of TiO_2 on Mesoporous NanoITO: Conductive Core-Shell Photoanodes for Dye-Sensitized Solar Cells. *Nano Lett* **2014**, *14*, 3255–3261.

(13) Sherman, B. D.; Ashford, D. L.; Lapides, A. M.; Sheridan, M. V; Wee, K.-R.; Meyer, T. J. Light-Driven Water Splitting with a Molecular Electroassembly-Based Core/Shell Photoanode. *J. Phys. Chem. Lett* **2015**, *6*, 3213–3217.

(14) Knauf, R. R.; Kalanyan, B.; Parsons, G. N.; Dempsey, J. L. Charge Recombination Dynamics in Sensitized SnO_2/TiO_2 Core/Shell Photoanodes. *J. Phys. Chem. C* **2015**, *119*, 28353–28360.

(15) Prasittichai, C.; Avila, J. R.; Farha, O. K.; Hupp, J. T. Systematic Modulation of Quantum (Electron) Tunneling Behavior by Atomic Layer Deposition on Nanoparticulate SnO_2 and TiO_2 Photoanodes. *J. Am. Chem. Soc.* **2013**, *135* (44), 16328–16331.

(16) Avila, J. R.; Katz, M. J.; Farha, O. K.; Hupp, J. T. Barrier-Layer-Mediated Electron Transfer from Semiconductor Electrodes to Molecules in Solution: Sensitivity of Mechanism to Barrier-Layer Thickness. *J. Phys. Chem. C* **2016**, *120* (1), 20922–20928.

(17) Gish, M. K.; Lapides, A. M.; Brennaman, M. K.; Templeton, J. L.; Meyer, T. J.; Papanikolas, J. M. Ultrafast Recombination Dynamics in Dye-Sensitized SnO_2/TiO_2 Core/Shell Films. *J. Phys. Chem. Lett.* **2016**, *7* (24), 5297–5301.

(18) Cao, F.; Oskam, G.; Searson, P. C.; Stipkala, J. M.; Heimer, T. A.; Farzad, F.; Meyer, . J. Electrical and Optical Properties of Porous Nanocrystalline TiO_2 Films. *J. Phys. Chem.* **1995**, *99* (31), 11974–11980.

(19) Moehl, T.; Suh, J.; Sévery, L.; Wick-Joliat, R.; Tilley, S. D. Investigation of (Leaky) ALD TiO_2 Protection Layers for Water-Splitting Photoelectrodes. *ACS Appl. Mater. Interfaces* **2017**, *9* (50), 43614–43622.

(20) Castillo-Lora, J.; Mitsuhashi, R.; Mayer, J. M. Revealing the Relative Electronic Landscape of Colloidal ZnO and TiO_2 Nanoparticles via Equilibration Studies. *J. Phys. Chem. C* **2019**, *123* (16), 10262–10271.

(21) James, E. M.; Bennett, M. T.; Bangle, R. E.; Meyer, G. J. Electron Localization and Transport in SnO_2/TiO_2 Mesoporous Thin Films: Evidence for a $SnO_2/Sn_xTi_{1-x}O_2/TiO_2$ Structure. *Langmuir* **2019**, *35* (39), 12694–12703.

(22) James, E. M.; Barr, T. J.; Meyer, G. J. Evidence for an Electronic State at the Interface between the SnO_2 Core and the TiO_2 Shell in Mesoporous SnO_2/TiO_2 Thin Films. *ACS Appl. Energy Mater.* **2018**, *1* (2), 859–867.

(23) Trotochaud, L.; Boettcher, S. W. Synthesis of Rutile-Phase $Sn_xTi_{1-x}O_2$ Solid-Solution and $(SnO_2)_x/(TiO_2)_{1-x}$ Core/Shell Nanoparticles with Tunable Lattice Constants and

Controlled Morphologies. *Chem. Mater.* **2011**, *23* (22), 4920–4930.

(24) Green, A. N. M.; Palomares, E.; Haque, S. A.; Kroon, J. M.; Durrant, J. R. Charge Transport versus Recombination in Dye-Sensitized Solar Cells Employing Nanocrystalline TiO_2 and SnO_2 Films. *J. Phys. Chem. B* **2005**, *109*, 12525–12533.

(25) Mathew, S.; Yella, A.; Gao, P.; Humphry-Baker, R.; E Curchod, B. F.; Ashari-Astani, N.; Tavernelli, I.; Rothlisberger, U.; Khaja Nazeeruddin, M.; Grätzel, M. Dye-Sensitized Solar Cells with 13% Efficiency Achieved through the Molecular Engineering of Porphyrin Sensitizers. *Nat. Chem.* **2014**, *6*, 242–247.

(26) Mortelliti, M. J.; Wang, A. N.; Dempsey, J. L. Atomic Layer Deposition of SnO_x onto Mesoporous, Nanocrsytalline TiO_2 and SnO_2 Thin Films. *Polyhedron* **2019**, *171*, 433–437.

(27) Heimer, T. A.; D'Arcangelis, S. T.; Farzad, F.; Stipkala, J. M.; Meyer, G. J. An Acetylacetonate-Based Semiconductor−Sensitizer Linkage. *Inorg. Chem.* **1996**, *35* (18), 5319–5324.

(28) Swierk, J. R.; Regan, K. P.; Jiang, J.; Brudvig, G. W.; Schmuttenmaer, C. A. Rutile TiO_2 as an Anode Material for Water-Splitting Dye-Sensitized Photoelectrochemical Cells. *ACS Energy Lett.* **2016**, *1* (3), 603–606.

(29) Norris, M. R.; Concepcion, J. J.; Glasson, C. R. K.; Fang, Z.; Lapides, A. M.; Ashford, D. L.; Templeton, J. L.; Meyer, T. J. Synthesis of Phosphonic Acid Derivatized Bipyridine Ligands and Their Ruthenium Complexes. *Inorg. Chem.* **2013**, *52* (21), 12492–12501.

(30) Argazzi, R.; Bignozzi, C. A.; Heimer, T. A.; Castellano, F. N.; Meyer, G. J. Enhanced Spectral Sensitivity from Ruthenium(II) Polypyridyl Based Photovoltaic Devices. *Inorg. Chem.* **1994**, *33*, 5741–5749.

(31) Dendooven, J.; Goris, B.; Devloo-Casier, K.; Levrau, E.; Biermans, E.; Baklanov, M. R.; Ludwig, K. F.; Voort, P. Van Der; Bals, S.; Detavernier, C. Tuning the Pore Size of Ink-Bottle Mesopores by Atomic Layer Deposition. *Chem. Mater.* **2012**, *24* (11), 1992–1994.

(32) Dendooven, J.; Devloo-Casier, K.; Ide, M.; Grandfield, K.; Kurttepeli, M.; Ludwig, K. F.; Bals, S.; Van Der Voort, P.; Detavernier, C. Atomic Layer Deposition-Based Tuning of the Pore Size in Mesoporous Thin Films Studied by in Situ Grazing Incidence Small Angle X-Ray Scattering. *Nanoscale* **2014**, *6* (24), 14991–14998.

(33) Dendooven, J.; Pulinthanathu Sree, S.; De Keyser, K.; Deduytsche, D.; Martens, J. A.; Ludwig, K. F.; Detavernier, C. In Situ X-Ray Fluorescence Measurements during Atomic Layer Deposition: Nucleation and Growth of TiO_2 on Planar Substrates and in Nanoporous Films. *J. Phys. Chem. C* **2011**, *115* (14), 6605–6610.

(34) Liu, L. Z.; Xu, J. Q.; Wu, X. L.; Li, T. H.; Shen, J. C.; Chu, P. K. Optical Identification of Oxygen Vacancy Types in SnO_2 Nanocrystals. *Appl. Phys. Lett.* **2013**, *102*

(3), 1–5.

(35) Zuo, J.; Xu, C.; Liu, X.; Wang, C.; Wang, C.; Hu, Y.; Qian, Y. Study of the Raman Spectrum of Nanometer SnO_2. *J. Appl. Phys.* **1994**, *75* (3), 1835–1836.

(36) Abello, L.; Bochu, B.; Gaskov, A.; Koudryavtseva, S.; Lucazeau, G.; Roumyantseva, M. Structural Characterization of Nanocrystalline SnO_2 by X-Ray and Raman Spectroscopy. *J. Solid State Chem.* **1998**, *135* (1), 78–85.

(37) Diéguez, A.; Romano-Rodríguez, A.; Vilà, A.; Morante, J. R. The Complete Raman Spectrum of Nanometric SnO_2 Particles. *J. Appl. Phys.* **2001**, *90* (3), 1550–1557.

(38) Song, M.; Wu, Y.; Zhao, Y.; Du, C.; Su, Y. Structural Insight on Defect-Rich Tin Oxide for Smart Band Alignment Engineering and Tunable Visible-Light-Driven Hydrogen Evolution. *Inorg. Chem.*

(39) Batzill, M.; Diebold, U. The Surface and Materials Science of Tin Oxide. *Prog. Surf. Sci.* **2005**, *79* (2–4), 47–154.

(40) Geurts, J.; Rau, S.; Richter, W.; Schmitte, F. J. SnO Films and Their Oxidation to SnO_2: Raman Scattering, IR Reflectivity and X-Ray Diffraction Studies. *Thin Solid Films* **1984**, *121* (3), 217–225.

(41) Ma, H. L.; Yang, J. Y.; Dai, Y.; Zhang, Y. B.; Lu, B.; Ma, G. H. Raman Study of Phase Transformation of TiO_2 Rutile Single Crystal Irradiated by Infrared Femtosecond Laser. *Appl. Surf. Sci.* **2007**, *253* (18), 7497–7500.

(42) Frank, O.; Zukalova, M.; Laskova, B.; Kürti, J.; Koltai, J.; Kavan, L. Raman Spectra of Titanium Dioxide (Anatase, Rutile) with Identified Oxygen Isotopes (16, 17, 18). *Phys. Chem. Chem. Phys.* **2012**, *14* (42), 14567–14572.

(43) Lee, W.-J.; Hon, M.-H. Space-Limited Crystal Growth Mechanism of TiO_2 Films by Atomic Layer Deposition. *J. Phys. Chem. C* **2010**, *114*, 6917–6921.

(44) Aarik, J.; Aidla, A.; Uustare, T.; Sammelselg, V. Morphology and Structure of TiO2 Thin Films Grown by Atomic Layer Deposition. *J. Cryst. Growth* **1995**, *148* (3), 268–275.

(45) Miikkulainen, V.; Leskelä, M.; Ritala, M.; Puurunen, R. L. Crystallinity of Inorganic Films Grown by Atomic Layer Deposition: Overview and General Trends. *J. Appl. Phys.* **2013**, *113* (2).

(46) Nie, A.; Liu, J.; Li, Q.; Cheng, Y.; Dong, C.; Zhou, W.; Wang, P.; Wang, Q.; Yang, Y.; Zhu, Y.; Zeng, Y.; Wang, H. Epitaxial TiO_2/SnO_2 Core-Shell Heterostructure by Atomic Layer Deposition. *J. Mater. Chem.* **2012**, *22* (21), 10665–10671.

(47) Wang, H.; Xu, S.; Gordon, R. G. Low Temperature Epitaxial Growth of High

Permittivity Rutile TiO_2 on SnO_2. *Electrochem. Solid-State Lett.* **2010**, *13* (9), G75–G78.

(48) Pezzotti, G.; Porporati, A. A. Raman Spectroscopic Analysis of Phase-Transformation and Stress Patterns in Zirconia Hip Joints. *J. Biomed. Opt.* **2004**, *9* (2), 372–384.

(49) Naumenko, A.; Gnatiuk, I.; Smirnova, N.; Eremenko, A. Characterization of Sol–Gel Derived TiO_2/ZrO_2 Films and Powders by Raman Spectroscopy. *Thin Solid Films* **2012**, *520*, 4541–4546.

(50) Azough, F.; Freer, R.; Petzelt, J. A Raman Spectral Characterization of Ceramics in the System ZrO_2-TiO_2. *J. Mater. Sci.* **1993**, *28*, 2273–2276.

(51) Krebs, M. A.; Condrate Sr, R. A. A Raman Spectral Characterization of Various Crystalline Mixtures in the ZrO_2-TiO_2 and HfO_2-TiO_2 Systems. *J. Mater. Sci. Lett.* **1988**, *7*, 1327–1330.

(52) George, A.; Solomon, S.; Thomas, J. K.; John, A. Characterizations and Electrical Properties of $ZrTiO_4$ Ceramic. *Mater. Res. Bull.* **2012**, *47*, 3141–3147.

(53) Lucena, P. R. De; Leite, E. R.; Pontes, F. M.; Longo, E.; Pizani, P. S.; Varela, J. A. Photoluminescence: A Probe for Short, Medium and Long-Range Self-Organization Order in $ZrTiO_4$ Oxide. *J. Solid State Chem.* **2006**, *179*, 3997–4002.

(54) Kim, Y. K.; Jang, H. M. Raman Line-Shape Analysis of Nano-Structural Evolution in Cation-Ordered $ZrTiO_4$-Based Dielectrics. *Solid State Commun.* **2003**, *127*, 433–437.

(55) Brady, M. D.; Troian-Gautier, L.; Sampaio, R. N.; Motley, T. C.; Meyer, G. J. Optimization of Photocatalyst Excited- and Ground-State Reduction Potentials for Dye-Sensitized HBr Splitting. *ACS Appl. Mater. Interfaces* **2018**, *10* (37), 31312–31323.

(56) Knauf, R. R.; Brennaman, M. K.; Alibabaei, L.; Norris, M. R.; Dempsey, J. L. Revealing the Relationship between Semiconductor Electronic Structure and Electron Transfer Dynamics at Metal Oxide-Chromophore Interfaces. *J. Phys. Chem. C* **2013**, *117*, 25259–25268.

(57) Nelson, J.; Chandler, R. E. Random Walk Models of Charge Transfer and Transport in Dye Sensitized Systems. *Coord. Chem. Rev.* **2004**, *248*, 1181–1194.

(58) Haque, S. A.; Tachibana, Y.; Willis, R. L.; Moser, J. E.; Grätzel, M.; Klug, D. R.; Durrant, J. R. Parameters Influencing Charge Recombination Kinetics in Dye-Sensitized Nanocrystalline Titanium Dioxide Films. *J. Phys. Chem. B* **2000**, *104*, 538–547.

(59) Jakschik, S.; Schroeder, U.; Hecht, T.; Bartha, J. W.; Gutsche, M.; Seidl, H. Crystallization Behavior of Thin ALD-Al_2O_3 Films. *Thin Solid Films* **2003**, *425*, 216–220.

(60) Troian-Gautier, L.; Sampaio, R. N.; Piechota, E. J.; Brady, M. D.; Meyer, G. J.

Barriers for Interfacial Back-Electron Transfer: A Comparison between TiO_2 and SnO_2/TiO_2 Core/Shell Structures. *J. Chem. Phys.* **2019**, *150*, 041719.

(61) Troian-Gautier, L.; DiMarco, B. N.; Sampaio, R. N.; Marquard, S. L.; Meyer, G. J. Evidence That $\Delta S^{\ddagger}$ Controls Interfacial Electron Transfer Dynamics from Anatase TiO_2 to Molecular Acceptors. *J. Am. Chem. Soc.* **2018**, *140* (8), 3019–3029.

(62) Hines, T.; Diez-Perez, I.; Hihath, J.; Liu, H.; Wang, Z.-S.; Zhao, J.; Zhou, G.; Müllen, K.; Tao, N. Transition from Tunneling to Hopping in Single Molecular Junctions by Measuring Length and Temperature Dependence. *J. Am. Chem. Soc.* **2010**, *132* (33), 11658–11664.

(63) Weiss, E. A.; Tauber, M. J.; Kelley, R. F.; Ahrens, M. J.; Ratner, M. A.; Wasielewski, M. R. Conformationally Gated Switching between Superexchange and Hopping within Oligo-p-Phenylene-Based Molecular Wires. *J. Am. Chem. Soc.* **2005**, *127*, 11842–11850.

(64) Katoh, R.; Furube, A. Tunneling-Type Charge Recombination in Nanocrystalline TiO_2 Films at Low Temperature. *J. Phys. Chem. Lett.* **2011**, *2* (15), 1888–1891.

(65) Huang, S. Y.; Schlichtho, G.; Nozik, A. J.; Gratzel, M.; Frank, A. J. Charge Recombination in Dye-Sensitized Nanocrystalline TiO_2 Solar Cells. *J. Phys. Chem. B* **1997**, *101* (14), 2576–2582.

(66) Hagfeldt, A.; Boschloo, G.; Sun, L.; Kloo, L.; Pettersson, H. Dye-Sensitized Solar Cells. *Chem. Rev.* **2010**, *110*, 6595–6663.

(67) Ardo, S.; Meyer, G. J. Photodriven Heterogeneous Charge Transfer with Transition-Metal Compounds Anchored to TiO_2 Semiconductor Surfaces. *Chem. Soc. Rev.* **2009**, *38* (1), 115–164.

(68) Ghosh, H. N.; Asbury, J. B.; Weng, Y.; Lian, T. Interfacial Electron Transfer between $Fe(II)(CN)_6^{4-}$ and TiO_2 Nanoparticles: Direct Electron Injection and Nonexponential Recombination. *J. Phys. Chem. B* **1998**, *102* (50), 10208–10215.

(69) Nelson, J.; Haque, S. A.; Klug, D. R.; Durrant, J. R. Trap-Limited Recombination in Dye-Sensitized Nanocrystalline Metal Oxide Electrodes. *Phys. Rev. V* **2001**, *63* (20), 205321.

(70) Haque, S. A.; Tachibana, Y.; Willis, R. L.; Moser, J. E.; Gra, M.; Klug, D. R.; Durrant, J. R. Parameters Influencing Charge Recombination Kinetics in Dye-Sensitized Nanocrystalline Titanium Dioxide Films. *J. Phys. Chem. B* **2000**, *104* (3), 538–547.

(71) Sampaio, R. N.; Dimarco, B. N.; Meyer, G. J. Activation Energies for Electron Transfer from TiO_2 to Oxidized Dyes: A Surface Coverage Dependence Correlated with Lateral Hole Hopping. *ACS Energy Lett.* **2017**, *2* (10), 2402–2407.

(72) Boschloo, G.; Hagfeldt, A. Activation Energy of Electron Transport in Dye-Sensitized

TiO_2 Solar Cells. *J. Phys. Chem. B* **2005**, *109* (24), 12093–12098.

(73) Kopidakis, N.; Benkstein, K. D.; Van De Lagemaat, J.; Frank, A. J.; Yuan, Q.; Schiff, E. A. Temperature Dependence of the Electron Diffusion Coefficient in Electrolyte-Filled TiO_2 Nanoparticle Films: Evidence against Multiple Trapping in Exponential Conduction-Band Tails. *Phys. Rev. B* **2006**, *73* (4), 045326.

(74) Brigham, E. C.; Meyer, G. J. Ostwald Isolation to Determine the Reaction Order for $TiO_2(e^-)|S^+ \leftrightarrow TiO_2|S$ Charge Recombination at Sensitized TiO_2 Interfaces. *J. Phys. Chem. C* **2014**, *118*, 7886–7893.

(75) Tsuda, N.; Nasu, K.; Fujimori, A.; Siratori, K. *Electronic Conduction in Oxides* , 2nd ed.; Cardona, M., Fulde, P., von Klitzing, K., Queisser, H.-J., Merlin, R., Stormer, H., Eds.; Springer: New York, 2000.

CHAPTER 4: FACTORS THAT CONTROL THE DIRECTION OF EXCITED STATE ELECTRON TRANSFER AT DYE-SENSITIZED OXIDE INTERFACES[10]

4.1 Introduction

Mesoporous thin films of nanocrystalline TiO_2 sensitized to visible light with molecular sensitizers, such as Ru-polypyridyl complexes, porphyrins, or donor-π-acceptor organic dyes, have been widely utilized for solar energy conversion.[1–4] Absorption of a photon by the sensitizer results in electron transfer from the excited state to the TiO_2 acceptor states in a process often called electron injection[5–9] that drives electrical power generation in dye-sensitized solar cells. Thus, efficient injection is vital to high-performance dye-sensitized solar cells. Although less well optimized, the use of p-type metal oxides allows for electron transfer in the opposite direction: electron transfer from the metal oxide to the sensitizer excited state, a process that is often termed hole transfer.[10,11] This Chapter reports the use of dye-sensitized *conductive* oxide materials where the direction of electron transfer can be controlled through external potential application and through the oxide-sensitizer electronic coupling.

The efficiency of these interfacial electron transfer reactions is predicted to depend on the energetic overlap and electronic coupling between the excited state sensitizer and the redox active states within the metal oxide.[8,12–17] Substantial literature precedent exists for tuning the excited state injection yield through molecular-level modification of the

[10]This chapter previously appeared as an article in the *Journal of Physical Chemistry C*. The original citation is: Bangle, R.E.; Meyer, G.J. *J. Phys. Chem. C*. **2019**, 123 *(42)*, 25967-25976.

sensitizers, the electrolyte composition, or surface functionalization of the oxide.[5,12,25,26,17–24] Of particular note to this Chapter, injection into both TiO_2 and SnO_2 has been reported to decrease under negative applied potentials.[5,12,17,19,21,27,28] Studies comparing injection into metal oxide nanocrystallites, however, have to date only systematically examined *semiconducting* metal oxides[16,25,29] and have not considered transparent *conducting* oxides (TCOs), which have vastly different electronic structures and behaviors.

In contrast to conventional semiconducting oxides, TCOs have high electrical conductivity that results from the high doping levels.[30–32] This high conductivity paired with optical transparency in the visible region make TCOs a promising candidate for new classes of photoelectrodes and a tool for the elucidation of fundamental charge transfer reactions. Such high doping precludes the generation of a large open circuit photovoltage through dye-sensitization, yet are potentially useful for applications in solar fuel production under short circuit conditions.[33–38] Tin-doped indium oxide (ITO) is a prominent TCO where Sn doping raises the Fermi level to within the conduction band to generate free carriers. This leads to ITO having metallic properties such as high conductivity and plasmon absorption features, while still being transparent in the visible region.[30–32,39–42] This is in contrast to TiO_2 and SnO_2 where the Fermi level is within the forbidden bandgap and free carriers are absent.

The use of ITO as a photoelectrode has historically had limited success.[36,43] Injection from sensitizer excited states has been observed,[34,39,42,44] but is followed by rapid detrimental recombination of the injected electron with the oxidized sensitizer. Recent studies have, however, successfully slowed recombination through control of the sensitizer surface orientation.[35–38,43] Furthermore, the high conductivity has enabled direct measure of the reorganization energy for interfacial electron and proton-coupled electron transfer

reactions.[39,42,45] These examples encourage the continued and increased use of ITO as a photoelectrode and prompt studies into the fundamental reactivity of dye-sensitized ITO interfaces.

In this Chapter, excited state electron transfer with ITO, TiO_2, and SnO_2 metal oxides sensitized to visible light with [Ru(2,2′-bipyridine)$_2$(4,4′-(PO_3H_2)$_2$-2,2′-bipyridine)]Br_2 (RuP) and [Ru(2,2′-bipyrazine)$_2$(4,4′-(PO_3H_2)$_2$-2,2′-bipyridine)]Br_2 (Ru(bpz)) (Fig. 4.1), were examined in a conventional three electrode photoelectrochemical cell. The direction of excited state electron transfer was found to be dependent on the electronic structure of the metal oxide, the applied potential, and the sensitizer-oxide electronic coupling. In particular, ITO was shown to both accept and donate electrons to molecular excited states, and the efficiency of each reaction was determined by the energetic position of the Fermi level and the electronic coupling between the oxide and the redox active Ru metal center and diimine ligands. These factors represent important consideration for applications of TCOs in solar energy conversion.

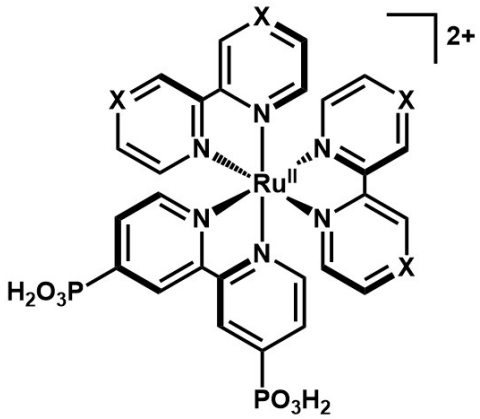

Figure 4.1. Structure of sensitizers employed in this study, abbreviated RuP (X = C) and Ru(bpz) (X = N).

4.2 Experimental

4.2.1 Materials

The following materials were purchased from the indicated supplier and used without further purification: acetonitrile (CH_3CN, Brudick and Jackson, Spectrochemical grade), lithium perchlorate ($LiClO_4$, Aldrich, 99.99%), argon (Airgas, 99.999%), titanium(IV) isopropoxide (Aldrich, 97%), zirconium(IV) isopropoxide (Aldrich, 99.9%), tin(IV) dioxide nanoparticles (15 wt% in H_2O, 15 nm diameter, Alfa Aesar); In_2O_3:Sn (ITO) nanoparticles (TC8 DE, 20 wt% in ethanol, Evonik Industries); fluorine-doped tin(IV) oxide-coated glass (FTO, Hartford Glass Co., Inc., 2.3 mm thick, 15Ω/sq). The following compounds were synthesized as previously described: $[Ru(2,2'\text{-bpy})_2(4,4'\text{-}(PO_3H_2)_2\text{-}2,2'\text{-bpy})]Br_2$ (RuP)[46] and $[Ru(2,2'\text{-bpz})_2(4,4'\text{-}(PO_3H_2)_2\text{-}2,2'\text{-bpy})]Br_2$ (Ru(bpz))[47] where bpy is 2,2'-bipyridine, and bpz is 2,2'-bipyrazine (Fig. 4.1).

4.2.2 Thin Film Preparation

Nanocrystalline (~15nm diameter) suspensions of TiO_2 and ZrO_2 were prepared using a previously described sol-gel method[48] by acid hydrolysis of titanium(IV) isopropoxide and zirconium(IV) isopropoxide. Sol-gel pastes of SnO_2 and ITO were prepared from colloidal nanoparticle suspensions by addition of polymeric porosity developers (poly(ethylene oxide) and poly(ethylene glycol) or hydroxypropyl cellulose, respectively) as described previously.[39,49] Nanoparticle pastes were doctor-bladed onto conductive FTO-coated glass, dried in air for ~30 minutes, and sintered for 30 minutes at 450 ˚C under O_2. The resulting mesoporous nanocrystalline thin films were 3-4 μm thick as measured by a Bruker DektatXT profilometer. Films were stored at 80 ˚C until used further. Sensitizers were adsorbed to

saturation surface coverage to the mesoporous films by ~24 hour soaking in aqueous pH 1 $HClO_4$ solutions of the sensitizer.

4.2.3. Electrochemistry and Spectro-electrochemistry

For all experiments in which a potential was applied, a standard three electrode cell was employed. The working electrode was the metal oxide film on conductive FTO-coated glass; the counter electrode was Pt mesh; and the reference electrode was a silver wire in 100 mM $LiClO_4$ CH_3CN. Reference electrodes were calibrated by measurement of the ferrocene reduction potential ($Fc^{+/0}$ $E_{1/2}$) in 100 mM *tert*-butyl ammonium perchlorate CH_3CN, and all values were reported as values versus the normal hydrogen electrode (NHE) after conversion using $Fc^{+/0}$ $E_{1/2}$ = +630 mV vs NHE. Solutions were sparged with argon for at least 20 minutes prior to electrochemical experiments. Transient absorption spectroscopy and steady-state and time-resolved photoluminescence experiments with an applied potential were performed using a BASi Epsilon potentiostat to hold an applied potential for the duration of the experiment.

Double potential step chronoamperometry (DPSCA) and steady state spectroelectrochemistry experiments were performed with potentials applied by a Pine Research Instrumentation Wavenow potentiostat controlled by Aftermath software (PRI). DPSCA experiments were performed by stepping between subsequent positive (+0.9 V vs NHE, 10 seconds), negative (varied, 30-45 seconds), then positive (+0.9 V, 30-45 seconds) potentials while measuring the resulting current. The negative potential charged the films, and the resulting charge was extracted upon switching to the positive potential. The measured current of the charge extraction was integrated to find the charge in a film at a given applied potential, which was then converted to number of electrons per cm^3.

Spectro-electrochemistry experiments were performed by measuring the UV-visible spectrum of a film using an Avantes AvaLight DHc light source and an Avantes StarLine AvaSpec-2048 UV/visible spectrophotometer with varied applied potentials. A modified Nernst equation was used to model the mole fraction of $Ru(bpz)^{2+}$, $Ru(bpz)^{+}$, or $Ru(bpz)^{3+}$ at each applied potential, Eq. 4.1 where χ is the mole fraction of the complex, E_{app} is the applied potential, $E^{o\prime}$ is the formal reduction potential, and α is a non-ideality factor.

$$\chi = \frac{1}{1+10^{(Eapp-E^{o\prime})/(59.2\alpha)}} \quad (4.1)$$

The potential at which the mole fractions of $Ru(bpz)^{+}$ and $Ru(bpz)^{2+}$ were equal was taken to be the formal reduction potential, $E^{o\prime\,2+/+}$ = -0.52 V vs NHE. Similarly, the potential at which the mole fractions of $Ru(bpz)^{3+}$ and $Ru(bpz)^{2+}$ were equal was $E^{o\prime\,3+/2+}$ = +2.05 V vs NHE.

4.2.4. Photoluminescence and Transient Absorption Spectroscopy

Steady-state photoluminescence (PL) spectra were obtained using a Horiba Fluorolog 3 spectrofluorometer with a 450 W Xe arc lamp as the excitation source. Samples were excited at 460 nm, near the MLCT peak for RuP. PL spectra were detected from a front facing orientation to limit the effects of scatter from the metal oxide nanocrystallites and FTO substrates.

Time-resolved PL experiments were performed with a nitrogen dye laser. A PTI GL-3300 nitrogen laser pumped a Photon Technology International GL-301 dye laser pulsed centered at 445 nm performed excitation. Signal was detected by a Hamamatsu R928 PMT optically coupled to a ScienceTech model 9010 monochromator and a LeCroy Waverunner LT322 oscilloscope. Measurements were averaged over 180 laser pulses.

Transient absorption spectroscopy with nanosecond time resolution was performed using an apparatus described previously.[50] Pulsed excitation was accomplished using a Q-switched, pulsed Nd:YAG laser (Quantel U.S.A.(Big Sky) Brilliant B, 5-6 ns FWHM) doubled to 532 nm. The laser fluence at the samples was 1-3 mJ/pulse at 1 Hz unless otherwise noted. A 150 W xenon arc lamp aligned perpendicular to the laser served as the probe beam. For measurements of time < 100 μs, the probe lamp was pulsed with 70 V at 1 Hz. Signal was detected with a monochromator (SPEX 1702/04) optically coupled to a Hamamatsu R928 PMT connected to a computer-interfaced digital oscilloscope (LeCroy 9450, Dual 330 MHz). Overall instrument response time was ~10 ns. Single wavelength kinetic experiments were averages of 90-150 laser pulses. Transient spectra were generated by averaging 30 laser pulses at each wavelength (10 nm steps) over a range of 370-800 nm. Transient spectra were modelled using Mathematica 11 (Wolfram) by a sum of the independently measured delta spectra between the species present before and after the laser pulse (S*, S^+, and S^-) optimized by linear least squares regression.

4.3 Results

In this study, light-initiated interfacial electron transfer between Ru-polypyridyl sensitizers and metal oxide nanocrystalline films were characterized in a three electrode photoelectrochemical cell in 0.1 M $LiClO_4$ CH_3CN at open circuit and with an applied potential (E_{app}). The visible absorption spectra of the sensitizers anchored to each metal oxide and the unsensitized metal oxides are shown in Fig. 4.2. The ground state $Ru^{3+/2+}$ and $Ru^{2+/+}$ reduction potentials ($E°'$) were determined by spectro-electrochemistry for the sensitizers anchored to ITO. The absorption spectra of the 1-electron oxidized and reduced sensitizers

are given in Fig. 4.10 in the Associated Content section. The 1-electron reduced sensitizers absorbed light centered at ~510 nm, and the 1-electron oxidized sensitizers displayed bleach from 380-550 nm. The equilibrium potential where the two redox states were in equal concentration was taken as the formal reduction potential (Fig. 4.11 in Associated Content and Table 4.1).[20,39] The excited state reduction potentials ($E°'$ $Ru^{3+/2+*}$ and $E°'$ $Ru^{2+*/+}$) were determined through thermodynamic cycles with the ground state potentials, and the free energy stored in the excited state as has been previously described.[22] From this data it is clear that RuP is a potent photoreductant while Ru(bpz) is a strong photooxidant.

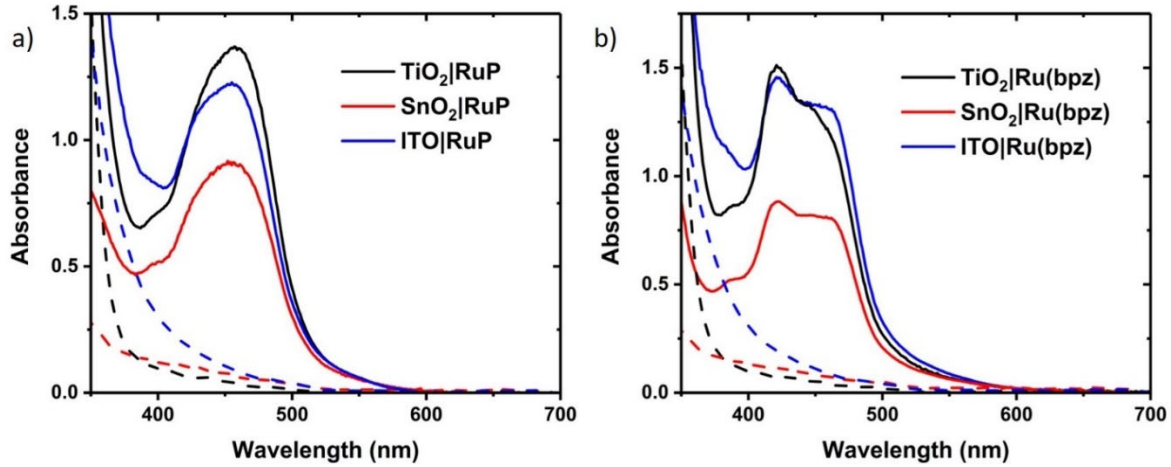

Figure 4.2. The visible absorbance spectra for the sensitizers a) RuP and b) Ru(bpz) anchored at saturation surface coverage to TiO_2 (black), SnO_2 (red), and ITO (blue) in 0.1 M $LiClO_4$ CH_3CN. The dashed spectra of represent unsensitized metal oxide films.

Table 4.1: Reduction potentials of the sensitizers anchored to ITO

	$E°'$ $Ru^{3+/2+}$ (V vs NHE)	$E°'$ $Ru^{3+/2+*}$ (V vs NHE)	$E°'$ $Ru^{2+/+}$ (V vs NHE)	$E°'$ $Ru^{2+*/+}$ (V vs NHE)
ITO|RuP	+1.54 [11]	-0.62 [11]	-1.26 [11]	+0.88 [11]
ITO|Ru(bpz)	+2.05	-0.05	-0.52	+1.58

The sensitized metal oxide thin films were characterized by double potential step chronoamperometry (DPSCA). In these experiments, the potential was held at a sufficiently

[11]Taken from Ref. 39.

negative potential to partially reduce the oxide. The potential was then rapidly switched to a more positive value and integration of the current provided the charge within the film that was then divided by the film volume to provide the electron density. This procedure was repeated at a series of reducing potentials which allowed the density of states as a function of potential to be determined. The densities of states acquired in this way were insensitive to whether RuP or Ru(bpz) were employed. The densities of states were found to be dependent on the nature of the oxide material (Fig. 4.3) and were well modelled by an exponential function for TiO_2 and ITO and a sigmoidal function for SnO_2. The largest electron density change was observed for ITO. TiO_2 had a greater electron density than SnO_2 at $E_{app} < -0.5$ V, but this was reversed at $E_{app} > -0.5$ V. For TiO_2 and SnO_2, this represents an absolute electron density, as essentially all of the charge was removed at the positive potential. For ITO, however, significant electron density was present at the positive potential and the data should be viewed as a change in electron density.

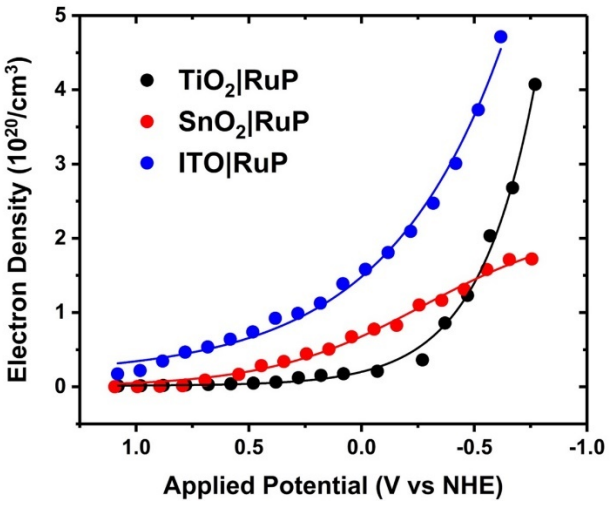

Figure 4.3. Charge extraction quantified by double potential step chronoamperometry for the indicated dye-sensitized metal oxide in a 0.1 M $LiClO_4$ CH_3CN electrolyte. Overlaid as solid lines are fits to an exponential function for TiO_2 and ITO and a sigmoidal function for SnO_2.

4.3.1. Photoluminescence

Photoluminescence (PL) was observed from RuP and Ru(bpz) and the PL spectra were measured as a function of E_{app} (Fig. 4.4 inset). For TiO_2|RuP and SnO_2|RuP, the PL spectra displayed a maximum at 16,000 cm^{-1} that was insensitive to the applied potential. The PL maximum measured for ITO|RuP red shifted by ~1000 cm^{-1} with application of positive potentials. The PL spectra of Ru(bpz) displayed a maximum at 15,500 cm^{-1} that was insensitive to the applied potential when anchored to TiO_2, SnO_2, or ITO.

The PL intensity was dependent on the applied potential, the sensitizer, and the metal oxide. For TiO_2|RuP and SnO_2|RuP, the PL intensity was very small at open circuit (not shown) and at positive applied potentials, but increased with more negative applied potentials (Fig. 4.4a,b). The opposite behavior was observed for ITO|RuP (Fig. 4.4c) and ITO|Ru(bpz) (Fig. 4.4f), for which the PL intensity was large at positive potentials and decreased at negative potentials. The PL spectra of TiO_2|Ru(bpz) and SnO_2|Ru(bpz) showed little or no dependence on E_{app} with positive applied potentials, +1.4 V $\geq E_{app} \geq$ +0.2 V, but the PL intensity decreased with $E_{app} \leq 0$ V (Fig. 4.4d,e).

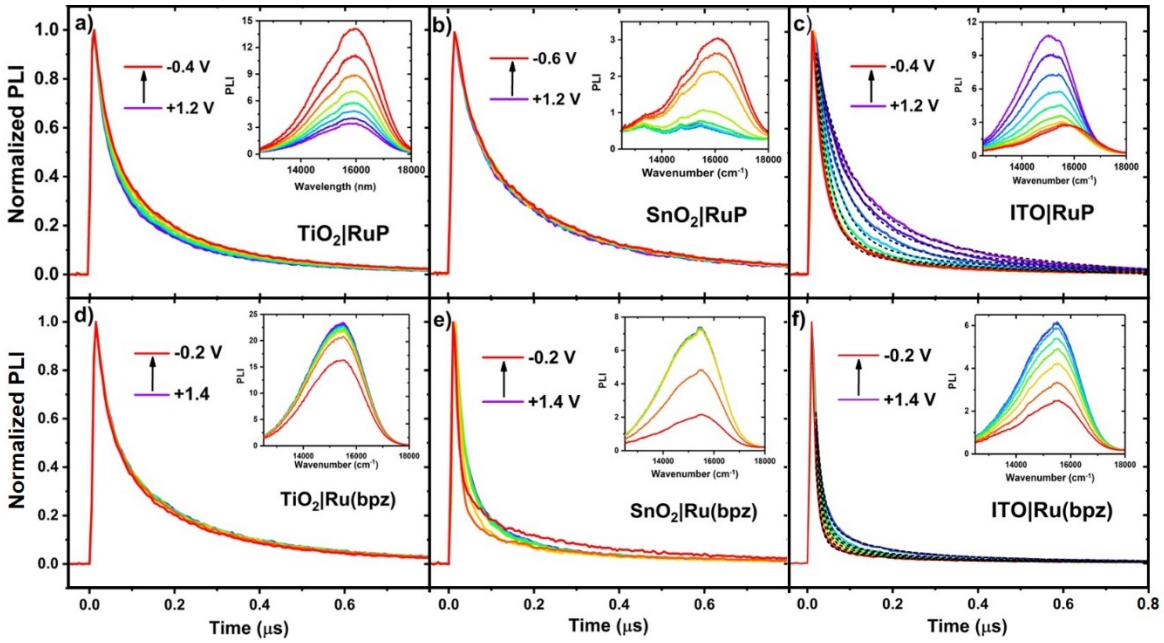

Figure 4.4. Time resolved PL decays measured at 650 nm after pulsed 445 nm excitation of the indicated dye-sensitized metal oxide in 0.1 M $LiClO_4$ CH_3CN over the applied potential ranges given. Insets provide the PL spectra under the same conditions. Average rate constants extracted from this data are given as k_{pl} in Table 4.2. Overlaid for ITO|S are fits to Eq. 4.5.

Pulsed light excitation of the sensitized oxide materials provided PL decays that were non-exponential under all conditions investigated.[6,8] Average rate constants, k_{pl}, were extracted by taking the inverse of the time required for the PL to decay to 1/e of the initial value and are compiled in Table 4.2. At applied potentials where the PL intensity was a maximum, so too was the average excited state lifetime. Negative applied potentials resulted in longer lived excited states for TiO_2|RuP* and SnO_2|RuP* and shorter for ITO|RuP*. More rapid excited state decay was observed at negative applied potentials for ITO|Ru(bpz)*. Excited state relaxation for TiO_2|Ru(bpz)* and SnO_2|Ru(bpz)* were insensitive to the applied potential over the range +1.4 V $\geq E_{app} \geq$ 0 V and decreased when E_{app} was less than 0 V. Overlaid fits for ITO|S* to Eq. 4.5 (discussed below, Fig. 4.12 in the Associated Content section) are provided in Fig. 4.4.

4.3.2 Transient Absorption Spectroscopy

Interfacial electron transfer was directly quantified by nanosecond transient absorption spectroscopy. Visible light excitation of either sensitizer resulted in the characteristic absorption features of a metal-to-ligand charge transfer (MLCT) excited state: an absorption band with a maximum in the ultraviolet region and a bleach centered at ~460 nm (Fig. 4.10 in Associated Content). A ground/excited state isosbestic point was identified at 402 nm.

Regardless of the underlying metal oxide, pulsed light excitation of RuP yielded a long-lived bleach across the visible region consistent with formation of the oxidized sensitizer (Fig. 4.10). This feature was most pronounced with positive applied potentials while at negative potentials the spectra was predominated by the RuP* spectrum (Fig. 4.13 in Associated Content). The transient absorbance spectra present upon pulsed light excitation of Ru(bpz) anchored to the metal oxides held at a given applied potential are shown in Fig. 4.5. The transient absorption data at observation times < 0.5 μs was predominately due to the MLCT excited state (Fig. 4.10). For TiO_2|Ru(bpz) regardless of E_{app}, the excited state was observed exclusively (Fig. 4.5a). The spectra were well-modelled by the spectrum of Ru(bpz)* anchored to the insulator ZrO_2 with no evidence of interfacial electron transfer. In contrast, transient absorption spectra of SnO_2|Ru(bpz) and ITO|Ru(bpz) with negative E_{app} displayed a growth in absorption centered at 510 nm at observation times > 0.5 μs (Fig. 4.5b,c). The transient absorbance spectra at all observation times were well-modelled by a sum of the spectral changes associated with the MLCT excited state and the reduced Ru(bpz) complex. Though the positive absorption growth of SnO_2|RuP was small, there was a

systematic difference from the excited state spectrum in the 470 – 530 nm region where reduced Ru(bpz) has a characteristic absorption (Fig. 4.5b, inset).

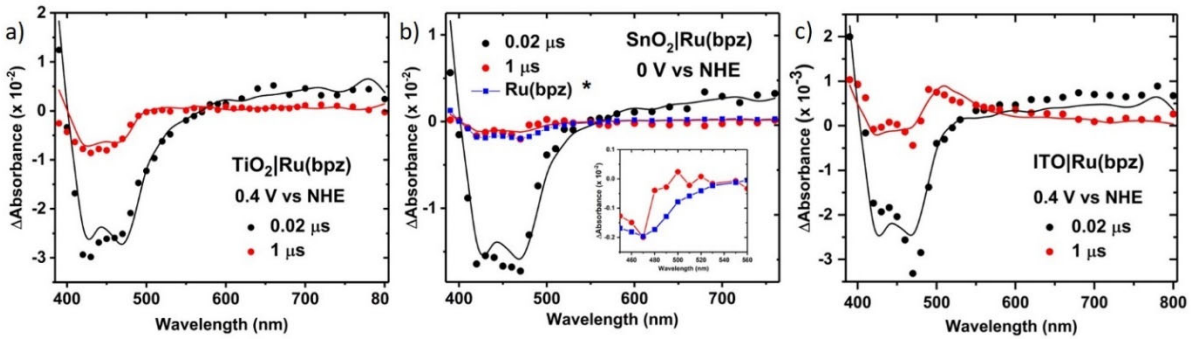

Figure 4.5. Transient absorption spectra of Ru(bpz) anchored to (a) TiO_2, (b) SnO_2, and (c) ITO in 0.1 M $LiClO_4$ CH_3CN recorded 0.02 μs (black) and 1 μs (red) after pulsed 532 nm laser excitation. Overlaid are simulations generated by linear least squares regression with the Ru(bpz)* spectrum (a) or a sum of the Ru(bpz)* and reduced Ru(bpz) spectra (b and c). In b) the excited state difference spectrum of ZrO_2|Ru(bpz)* (blue) is included. The inset is a view of the spectra that emphasizes the systematic difference between the spectra measured for SnO_2|Ru(bpz) and ZrO_2|Ru(bpz)*.

The transient absorbance change monitored at 500 nm upon pulsed light excitation for Ru(bpz) anchored to the metal oxides as a function of the applied potential is given in Fig. 4.6. For TiO_2|Ru(bpz), an absorbance bleach was observed that returned to the ground state absorbance with kinetics that were independent of applied potential when +1.4 V ≥ E_{app} ≥ 0 V (Fig. 4.6a). When E_{app} < 0 V, the bleach amplitude was smaller and relaxation to the ground state was enhanced. A similar bleach was observed for SnO_2|Ru(bpz) when +1.4 V ≥ E_{app} ≥ +0.6 V with kinetics that were independent of the applied potential (Fig. 4.6b). Application of a more negative potential, +0.4 V ≥ E_{app} ≥ +0.2 V, resulted in a diminished bleach that relaxed more quickly to the ground state. With E_{app} ≤ 0 V, a positive transient absorbance signal was observed. Pulsed excitation of ITO|Ru(bpz) yielded a short-lived bleach followed by a long-lived positive absorbance. The amplitude of the bleach decreased

with negative applied potentials, while the amplitude of the positive feature increased, (Fig. 4.6c).

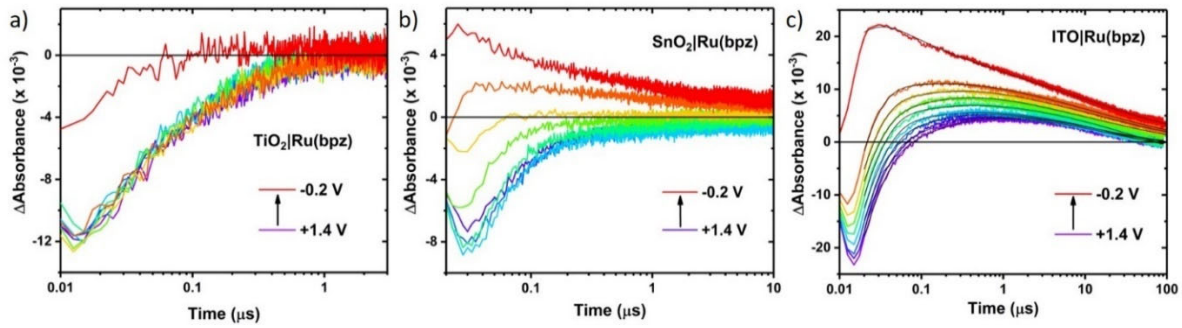

Figure 4.6. Absorbance change monitored at 500 nm with the indicated applied potentials vs NHE after pulsed 532 nm light excitation of Ru(bpz) anchored to a) TiO_2, b) SnO_2, or c) ITO. Overlaid in c) are fits to Eq. 4.4, and the rate constants extracted are given in Table 4.2.

The transient absorption and photoluminescence kinetic data were used to determine the rate constants for excited state relaxation, injection, and hole transfer that are summarized in Table 4.2. The average rate constants for excited state relaxation in the absence of interfacial electron transfer processes were measured with the sensitizers anchored to ZrO_2. The excited state relaxation was non-exponential, but was well described by the Kohlrausch-Williams Watts (KWW) function from which an average rate constant, k_{es}, was extracted, Eq. 4.2 and 4.3. Here β is inversely related to a Levy distribution of rate constants with $0 < \beta \leq 1$.[51]

$$\mathrm{A}(t) = \mathrm{A}_0 \mathrm{e}^{-(kt)^{\beta}} \tag{4.2}$$

$$k_{es} = \frac{k\beta}{\Gamma\left(\frac{1}{\beta}\right)} \tag{4.3}$$

Excited state relaxation rate constants were found to be 2.5 x 10^6 and 14 x 10^6 s^{-1} for RuP* and Ru(bpz)*, respectively. The average rate constants for PL decay of the sensitizers anchored to the other oxides, k_{pl}, were larger when interfacial electron transfer occurred

(Table 4.2). Excited state injection for RuP* could not be time-resolved, consistent with $k_{inj} > 10^8$ s^{-1}. There was no evidence for excited state injection by Ru(bpz)*.

Table 4.2. Average Rate Constants for Excited State Decay, Injection, and Hole Transfer

	E_{app} (V vs NHE)	k_{pl} (x 10^7 s^{-1})[12]	k_{inj} (x 10^7 s^{-1})[13]	k_{ht} (x 10^7 s^{-1})[14]
TiO_2|RuP	+1 V	1.3	> 10	-
	0 V	1.1	> 10	-
SnO_2|RuP	+1 V	0.7	> 10	-
	0 V	0.6	> 10	-
ITO|RuP	+1 V	1.0	> 10	1.5
	0 V	2.2	> 10	3.3
TiO_2|Ru(bpz)	+1 V	0.9	-	-
	0 V	1.0	-	-
SnO_2|Ru(bpz)	+1 V	1.7	-	-
	0 V	3.1	-	> 10
ITO|Ru(bpz)	+1 V	3.4	-	6.5
	0 V	4.7	-	8.9

Transient absorption kinetics shown in Fig. 4.6c were non-exponential and consisted of contributions from both Ru(bpz)* decay and formation of the reduced sensitizer by interfacial hole transfer. The hole transfer rate constants, k_{ht}, were obtained with Eq. 4.4.

$$A(t) = A_1 e^{-(k_{es}t)^{\beta}} + A_2 e^{-k_{ht}t} + A_3 e^{-(k_{rec}t)^{\beta'}} \quad (4.4)$$

Here the first term corresponded to excited state decay, the second to hole transfer and the third for recombination of the reduced sensitizer with a hole in the oxide. The first term was fixed to values measured by transient absorbance on ZrO_2. While the second two terms in Eq. 4.4 represent a five-parameter fit, hole transfer produced a long-lived interfacial charge separated state that was kinetically well separated in time. This allowed for discrete

[12]Average excited state decay rates quantified by time-resolved photoluminescence.

[13]Excited state injection could not be time-resolved with the apparatus utilized.

[14]Average excited state hole transfer rate constants measured directly by transient absorption for ITO|(Ru(bpz)) and inferred from potential dependent photoluminescence decays for ITO|RuP.

quantification. The hole transfer rate constants increased with negative applied potentials (Table 4.2 and Fig. 4.12 in Associated Content).

The time resolved photoluminescence decays for ITO|Ru(bpz)* in Fig. 4.4f were modelled by Eq. 4.5, where the values of k_{es}, k_{ht}, and β were determined from transient absorbance data.

$$PLI(t) = PLI_1 e^{-(k_{es}t)^{\beta}} + PLI_2 e^{-k_{ht}t} \quad (4.5)$$

Hole transfer products were not directly observed for ITO|RuP and were instead inferred from the potential dependent PL decays in Fig. 4.4c that were modelled with Eq. 4.5 to estimate k_{ht} values.

The transient concentrations of oxidized RuP were quantified at the ground-excited state isosbestic point (402 nm) as the applied potential was tuned (Fig. 4.14 in Associated Content). The signal amplitude at 20 ns (A_0) divided by the amplitude at the most positive applied potential for each metal oxide ($A_{0,max}$), $A_0/A_{0,max}$, provided information on the injection yield as a function of E_{app} (Fig. 4.7). For TiO_2|RuP, the injection yield was the same for $E_{app} \geq 0$ V, but injection yields decreased sharply at more negative applied potentials. A similar trend was observed for SnO_2|RuP with little change in injection when $E_{app} \geq 0.4$ V and decreased injection yields when $E_{app} < 0.4$ V. For ITO|RuP, a decrease in the injection yield occurred even at the most positive applied potentials. Regardless of metal oxide, injection became undetectably small as the applied potential approached the excited-state reduction potential of RuP ($E^{o\,3+/2+}$* = -0.62 V).[39]

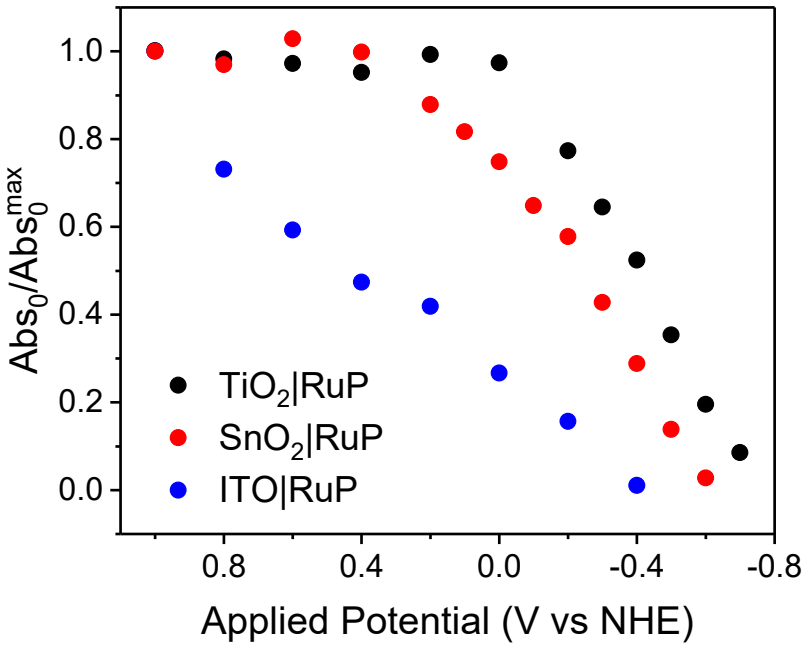

Figure 4.7. The amplitude of the absorption change measured 20 ns (A_0) after pulsed 532 nm excitation divided by the largest amplitude measured at positive applied potential ($A_{0,max}$) as a function of the applied potential for the indicated RuP sensitized oxide in 0.1 M $LiClO_4$ CH_3CN.

4.4 Discussion

Excited state interfacial electron transfer was quantified with three nanocrystalline metal oxides, the *conducting* ITO and the *semiconducting* TiO_2 and SnO_2. Electron transfer from the excited state sensitizer to the metal oxide, injection, and electron transfer from the metal oxide to the excited state, hole transfer, were quantified. In agreement with Marcus-Gerischer electron transfer theory, the key factors that determined the direction of light-driven electron flow were determined to be the oxide electronic structure and the electronic coupling between the sensitizer and the oxide surface.[39,52–56] These two factors are discussed below with the context for the relevant literature and applications in solar energy conversion.

4.4.1 Oxide Electronic Structure

A key difference between the semiconducting and conducting oxides was the electron density at positive applied potentials. For the semiconducting TiO_2 and SnO_2 there was no evidence for excess electrons consistent with the presence of the forbidden band gap.[1–3,57] For the conductive oxide ITO, electrons were present at all the potentials studied, behavior expected for the metal-like nature of this oxide.[31,58] The electron density magnitude was quantified in the dark by a double potential step, charge extraction technique. The best fits of the charge extraction data are replotted in Fig. 4.8 where $\rho(E)$ represents the oxide density of states. Note that the onset potential for SnO_2 was more positive than that of TiO_2, indicative of a more positive flat band potential. As previously reported, the TiO_2 density of states was much larger at more negative potentials, behavior consistent with the lower dielectric constant of SnO_2.[49] The density of states of the ITO were largest at all applied potentials and increased exponentially as the Fermi level was raised toward the vacuum level. It is important to note that a significant electron density existed at the positive potential used to extract the charge, so the $\rho(E)$ for ITO is best thought of a difference in density of states and not an absolute value as was the case for TiO_2 and SnO_2.

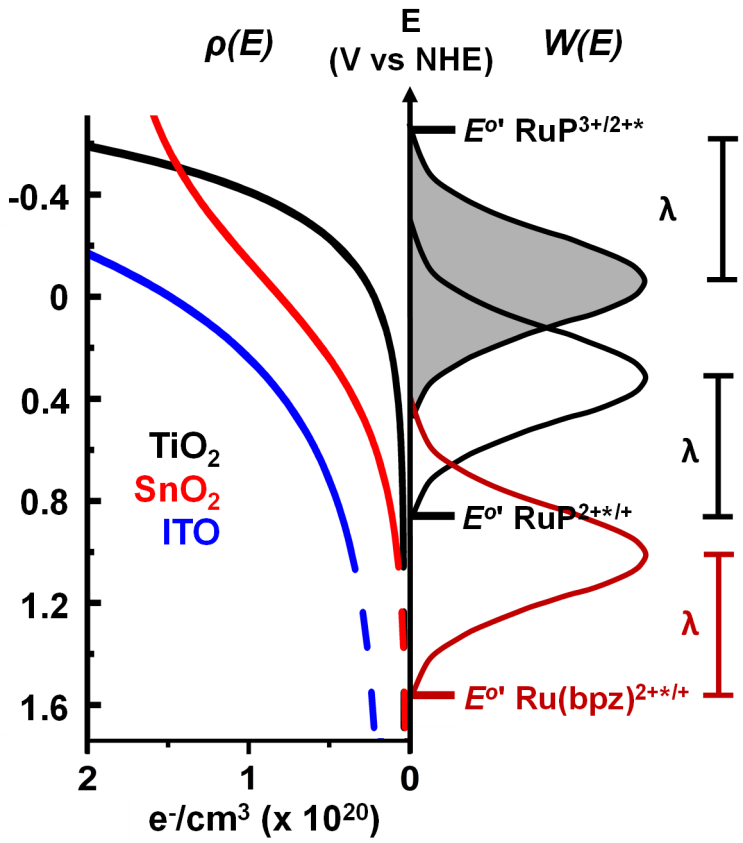

Figure 4.8. The density of states, *ρ(E)*, of the metal oxides with the free energy distributions, *W(E)*, for the indicated redox states of RuP (black) and Ru(bpz) (red). Dashed lines are extrapolations of these fits beyond the experimental range. Gaussian distributions for the sensitizers are shown for hole transfer (unshaded) and injection (shaded).

Also indicated in Fig. 4.8 are Gaussian distributions *W(E)* of the sensitizer electronic states calculated by Eq. 4.6. The width of the Gaussian distribution is defined as 2λ, where λ is the total reorganization energy for electron transfer.[12,39,52] A value of λ = 0.6 eV was utilized here based on the reported value for ITO|$RuP^{3+/2+}$.[39] It was tacitly assumed that the reorganization energy for the two sensitizers was the same and independent of which states participated in the redox chemistry. These distributions and the oxide density of states provide a means to predict the electron transfer kinetics in the framework of Marcus-Gerischer electron transfer theory.[6,39,62,52–56,59–61]

$$W(E) = \frac{1}{\sqrt{4\pi\lambda k_B T}} \exp\left(\frac{-(\Delta G^o(E)+\lambda)^2}{4\lambda k_B T}\right) \quad (4.6)$$

In Marcus-Gerischer theory, interfacial electron transfer occurs with a distribution of activation energies (*W(E)*) between discrete isoenergetic states of the sensitizer and the oxide (*ρ(E)*).[12,39,52] The rate constant for interfacial electron transfer, k_{IET}, is determined by the electrode/molecule coupling matrix (H_{ab}) and the degree of energetic overlap between *ρ(E)* and *W(E)*, Eq. 4.7.

$$k_{IET} = \frac{2\pi}{\hbar}\int_{-\infty}^{\infty}\rho(E)f(E,E_F)|H_{ab}(E)|^2W(E)\,dE \qquad (4.7)$$

For injection, the shaded excited state donor distribution of $RuP^{3+/2+*}$ have good overlap with the unfilled states of all the oxides, consistent with the rapid injection measured here, $k_{inj} > 10^8$ s^{-1}.[12,39,63] As the applied potential, E_{app}, was raised, the injection yields decreased. For TiO_2|RuP and SnO_2|RuP, the applied potential where injection began to measurably decrease aligned well with potentials at which occupation of the metal oxide acceptor states resulted in a smaller overlap with the excited state sensitizer.

For ITO|RuP, the injection yields as a function of the applied potential could not be explained by overlap of the excited state donor with the oxide acceptor states. With the reasonable assumption that the applied potential defines the ITO Fermi level, $eE_{app} \approx E_F$, the injection yields decreased when E_F was several hundred millivolts more positive on an electrochemical scale than $E^{o\prime}$ $RuP^{3+/2+*}$ and the related Gaussian distribution *W(E)*. This behavior was attributed to competitive hole transfer. The donor states in the ITO have significant overlap with the excited state acceptor distribution, *W(E)* $RuP^{2+*/+}$. While the PL intensity supported this explanation, the RuP^{+} product of hole transfer was not observed spectroscopically. Since the reduced sensitizer is a very potent reductant, $E^{o\prime}$ $RuP^{2+/+}$ = -1.26 V, it has quantitative overlap with the ITO acceptor states. It is expected to rapidly transfer an electron to the ITO thermally, thereby precluding its detection.

The unshaded Gaussian distributions *W(E)* in Fig. 4.8 represent the energetic range over which the sensitizer excited states can be reduced, relevant to hole transfer. Due to its conductive character, ITO has a significant density of redox active states that overlap fully with the empty states of $Ru(bpz)^{2+*/+}$ and $RuP^{2+*/+}$. This allows hole transfer within the Marcus-Gerischer framework. For ITO|Ru(bpz), hole transfer was directly observed spectroscopically. Furthermore, the rate constant for hole transfer was found to increase markedly as the Fermi level was raised toward the vacuum level, in good agreement with theory. Contrarily, SnO_2 and TiO_2 have small overlap with the sensitizer acceptor states, so hole transfer was not expected under most conditions. At an applied bias of 0 V there was evidence for hole transfer for $SnO_2|Ru(bpz)^{2+*/+}$, but not $TiO_2|Ru(bpz)^{2+*/+}$. This occurs because SnO_2 has a larger density of low energy donor states under these conditions. The observation of hole transfer in SnO_2, but not in TiO_2, provides an alternative explanation for why SnO_2 is an inferior oxide material for applications in dye-sensitized solar cells.

While the integrated overlap of the oxide electronic states and the excited state sensitizer shown in Fig. 4.8 explains most of the experimental results, it does not fully explain all the data. For example, why was excited state injection absent for ITO|Ru(bpz)* even when the Fermi level was held at very positive potentials with quantitative overlap? Why was there no evidence for hole transfer for TiO_2, even at the most negative applied potentials where considerable overlap was evident? Finally, if the reduced RuP^+ was not observed on ITO due to a subsequent fast thermal electron transfer to the oxide, why didn't the same occur for $Ru(bpz)^+$? To address these questions, the electronic coupling matric element, H_{ab}, in the Marcus-Gerischer equation must be explicitly considered.

4.4.2 Electronic Coupling

A significant difference between the two sensitizers employed is the location of the excited state electron. In RuP*, the excited state is localized on the phosphonated bipyridine ligand that links the sensitizer to the oxide. In Ru(bpz)*, the excited state is localized on a bipyrazine ligand.[20] In other words, the excited state is localized on a ligand adjacent to the oxide in RuP* and remote from the oxide in Ru(bpz)* (Fig. 4.9). While the presence of a common surface anchoring ligand might reasonably be expected to provide the same electronic coupling for the two sensitizers, the electronic coupling to the redox active ligand is quite different as a result of the inherent asymmetry of these charge-transfer excited states.

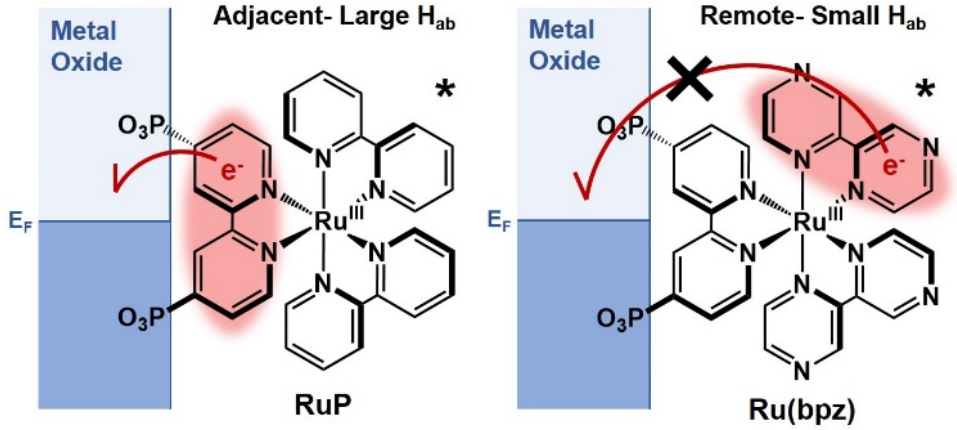

Figure 4.9. Excited state localization adjacent to the metal oxide for RuP* provides larger electronic coupling than does excited state localization on the remote ligand for Ru(bpz)*.

Localization of the excited state on the surface anchoring ligand is believed optimal for excited state injection in dye-sensitized solar cells.[1,2] In contrast, a remote excited state has weaker electronic coupling which enhances the probability that excited state relaxation will compete with electron injection. The absence of excited state injection for ITO|Ru(bpz)* at potentials as positive as +1.4 V indicates that electronic coupling at dye-sensitized electrode interfaces is even more important than previously thought.

Formally, hole transfer involves electron transfer from the oxide to the Ru^{III} center. The localization shown in Fig. 4.9 is most ideal for hole transfer to Ru(bpz)* as the electron has a pathway to tunnel through the surface anchoring ligand to Ru^{III}.[35] In contrast, electron transfer to Ru^{III} may be impeded by the excited state localized on the adjacent ligand. Indeed, Coulombic repulsion may shift the local electron density away from the surface resulting in weaker electronic coupling. This likely explains the inability to directly observe hole transfer for ITO|RuP and the smaller hole transfer rate constants that were inferred from the time resolved PL data (Table 4.2). In principle, hole transfer to RuP* could occur by a charge-shift type mechanism,[64] but no evidence for this was observed experimentally.

In the above discussion, it was assumed that $eE_{app} \approx E_F$ for the conductive metal oxide ITO. It should be noted, however, that a potential drop across the mesoporous thin film or imperfect contact between with the fluorine doped tin oxide (FTO) substrate may result in some deviations.[65] This assumption however, provides good agreement with the experimental data and suggests minimal discrepancies between E_{app} and the ITO Fermi level. Further, the applied potential dependence of both hole transfer rate constants and injection yields requires that the Fermi energy be tuned relative to the sensitizer excited state reduction potentials even at very negative applied potentials where the TiO_2 and SnO_2 are highly reduced. Such conditions can lead to Fermi level pinning (sometimes called band edge unpinning), but there was no evidence for this suggesting that the interface behaves ideally.[1,2]

4.5 Conclusions

Two key factors were identified that control the direction of electron flow at dye-sensitized oxide surfaces: the density of redox active states and the electronic coupling. The

transparent conducting oxide ITO underwent efficient hole transfer to an excited state sensitizer. The same reactivity was only achieved under narrow conditions for the semiconductor SnO_2. For ITO|RuP, hole transfer occurred in competition with excited state injection leading to decreased injection yields. Because ITO has a large density of electronic states at energies within the bandgap of TiO_2 and SnO_2, it was capable of efficient hole transfer reactivity when excited state electronic coupling to the metal center was optimized and to the reduced ligand was minimized. Though hole transfer may be detrimental to the performance of ITO as a photoanode, it opens up the possibility of using ITO as a photocathode.

4.6 Acknowledgements

The authors thank Dr. Jenny Schneider and Dr. Ludovic Troian-Gautier for helpful discussions and suggestions. This material is based upon work solely supported by the Alliance for Molecular PhotoElectrode Design for Solar Fuels (AMPED), an Energy Frontier Research Center (EFRC) funded by the U.S. Department of Energy, Office of Science, Office of Basic Energy Sciences under Award Number DE-SC0001011. R.E.B. acknowledges the National Science Foundation for an individual Graduate Research Fellowship under Grant No. DGE-1650116.

4.7 Associated Content

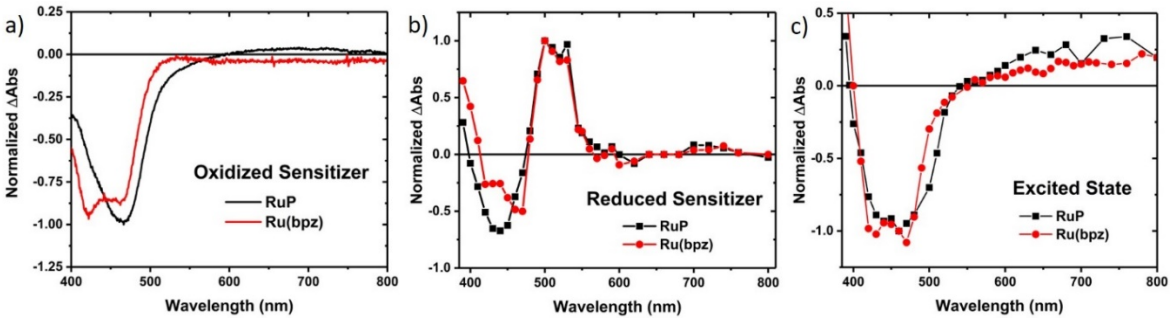

Figure 4.10. The delta absorbance spectra from the ITO|Ru(II) state to the (a) oxidized and (b) reduced forms of ITO|RuP (black) and ITO|Ru(bpz) (red). The spectra of the oxidized sensitizers were generated by spectroelectrochemistry in a 3 electrode photoelectrochemical cell with a 0.1 M $LiClO_4$ CH_3CN electrolyte. Complete oxidation was distinguished by cessation of spectral change upon positive applied potential shifts. The absorption spectra of the reduced sensitizers were generated by transient absorption changes upon pulsed laser excitation of the sensitizers solvated in CH_3CN with 10 mM concentrations of a tri-*p*-tolylamine donor. c) Transient absorption changes that occurred upon excited state formation were measured by pulsed laser excitation of the sensitizers anchored to the insulator ZrO_2.

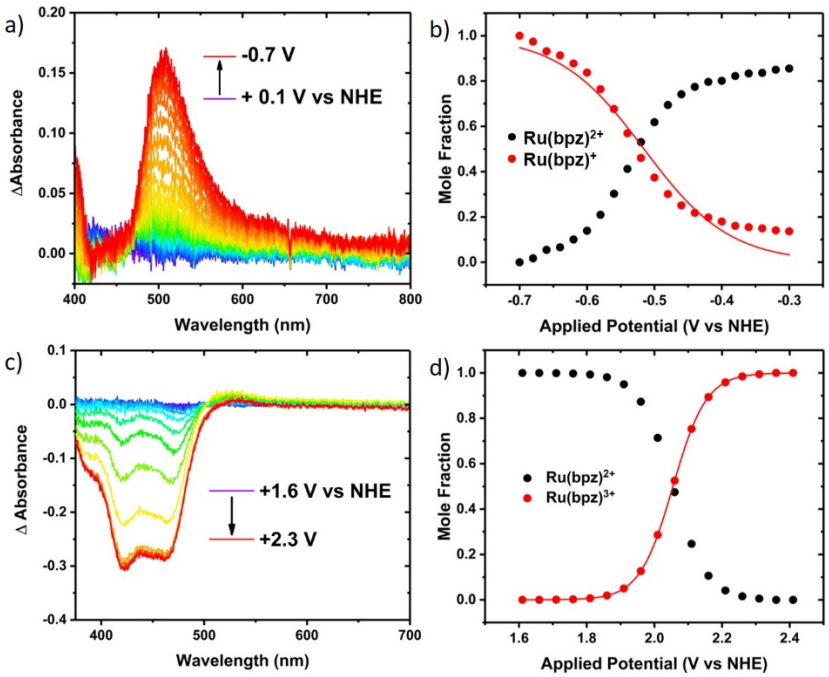

Figure 4.11. a) Reductive and c) oxidative spectroelectrochemistry of ITO|Ru(bpz) to determine $E^{o\prime}$ $Ru^{2+/+}$ and $E^{o\prime}$ $Ru^{3+2/+}$ in 0.1 M $LiClO_4$ CH_3CN. Mole fractions of $Ru(bpz)^{2+}$ and b) $Ru(bpz)^{+}$ or d) $Ru(bpz)^{3+}$ as a function of the applied potential with overlaid fits to the modified Nernst equation

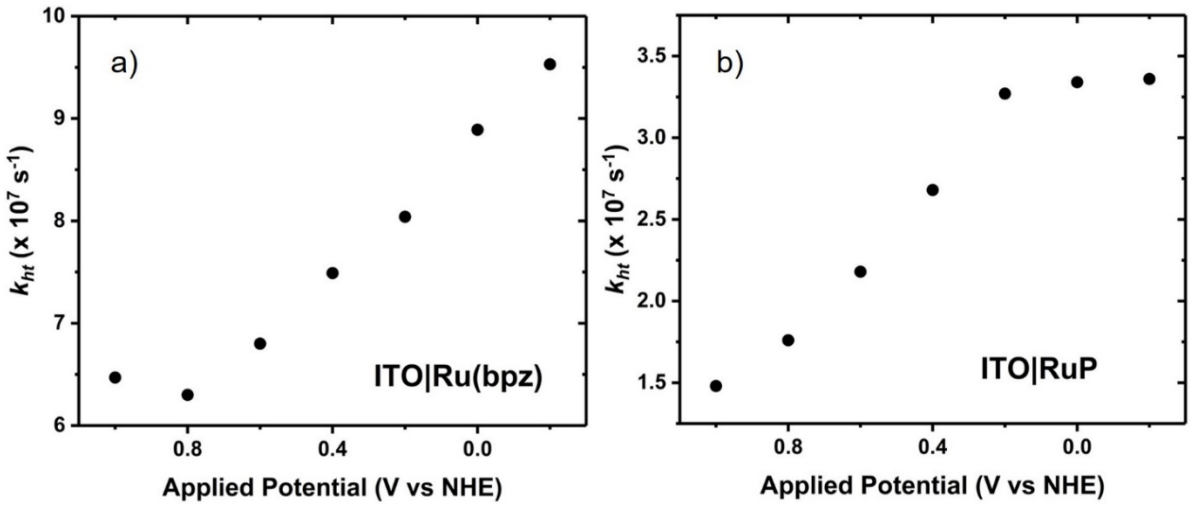

Figure 4.12 Hole transfer rate constants k_{ht} extracted from transient absorption changes measured at 500 nm upon pulsed 532 nm light excitation in 0.1 M $LiClO_4$ CH_3CN for ITO|Ru(bpz) (a) or from photoluminescence decay kinetics measured at 650 nm upon pulsed 455 nm light excitation in 0.1 M $LiClO_4$ CH_3CN for ITO|RuP (b).

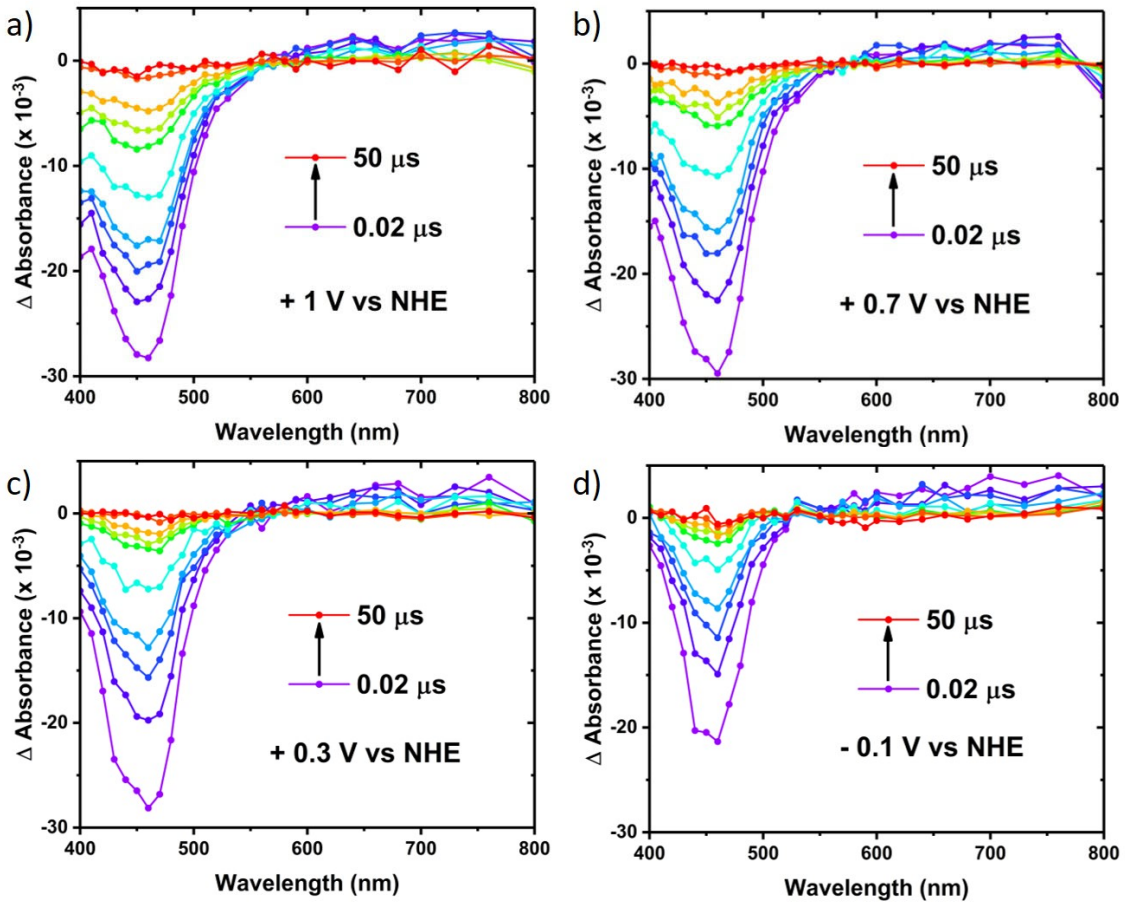

Figure 4.13. Transient absorbance spectra measured at the indicated delay time after pulsed 532 nm excitation of ITO|RuP (lines added to guide the eye) in 0.1 M $LiClO_4$ CH_3CN at the indicated applied potentials.

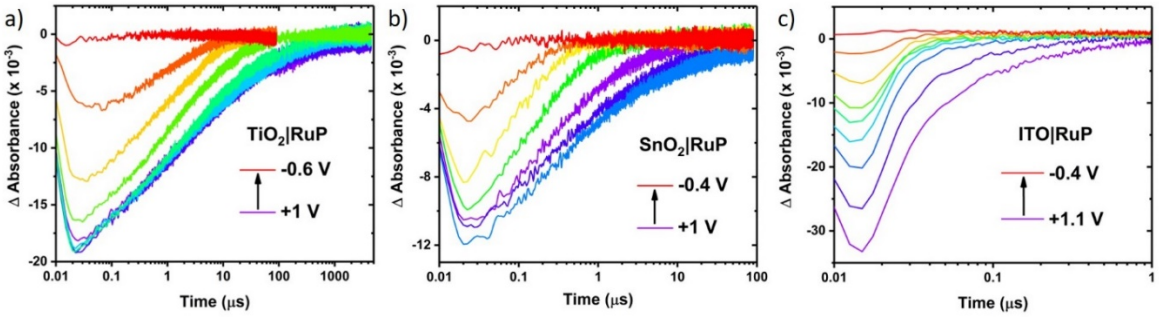

Figure 4.14. Transient absorbance changes monitored at 402 nm after pulsed 532 nm excitation of RuP anchored to a) TiO_2, b) SnO_2, and c) ITO in 0.1 M $LiClO_4$ CH_3CN over the indicated applied potential range.

REFERENCES

(1) Hagfeldt, A.; Boschloo, G.; Sun, L.; Kloo, L.; Pettersson, H. Dye-Sensitized Solar Cells. *Chem. Rev.* **2010**, *110*, 6595–6663.

(2) Ardo, S.; Meyer, G. J. Photodriven Heterogeneous Charge Transfer with Transition-Metal Compounds Anchored to TiO_2 Semiconductor Surfaces. *Chem. Soc. Rev.* **2009**, *38*, 115–164.

(3) Grätzel, M. Dye-Sensitized Solar Cells. *J. Photochem. Photobiol. C Photochem. Rev.* **2003**, *4*, 145–153.

(4) Materna, K. L.; Crabtree, R. H.; Brudvig, G. W. Anchoring Groups for Photocatalytic Water Oxidation on Metal Oxide Surfaces. *Chem. Soc. Rev.* **2017**, *46*, 6099–6110.

(5) Kelly, C. A.; Meyer, G. J. Excited State Processes at Sensitized Nanocrystalline Thin Film Semiconductor Interfaces. *Coord. Chem. Rev.* **2001**, *211*, 295–315.

(6) Anderson, N. A.; Lian, T. Ultrafast Electron Transfer at the Molecule-Semiconductor Nanoparticle Interface. *Annu. Rev. Phys. Chem.* **2005**, *56*, 491–519.

(7) Duncan, W. R.; Prezhdo, O. V. Theoretical Studies of Photoinduced Electron Transfer in Dye-Sensitized TiO_2. *Annu. Rev. Phys. Chem.* **2007**, *58*, 143–184.

(8) Rao, V. G.; Lu, H. P. Inhomogeneous and Complex Interfacial Electron-Transfer Dynamics: A Single-Molecule Perspective. *ACS Energy Lett.* **2016**, *1*, 773–791.

(9) Bedja, I.; Hotchandani, S.; Kamat, P. V. Preparation and Photoelectrochemical Characterization of Thin SnO_2 Nanocrystalline Semiconductor Films and Their Sensitization with Bis(2,2'-Bipyridine) (2,2'-Bipyridine-4,4'-Dicarboxylic Acid)Ruthenium(II) Complex. *J. Phys. Chem.* **1994**, *98*, 4133–4140.

(10) Odobel, F.; Pellegrin, Y.; Gibson, E. A.; Hagfeldt, A.; Smeigh, A. L.; Hammarström, L. Recent Advances and Future Directions to Optimize the Performances of P-Type Dye-Sensitized Solar Cells. *Coord. Chem. Rev.* **2012**, *256*, 2414–2423.

(11) He, J.; Lindstrom, H.; Hagfeldt, A.; Lindquist, S.-E. Dye-Sensitized Nanostructured p-Type Nickel Oxide Film as a Photocathode for a Solar Cell. *J. Phys. Chem. B* **1999**, *103*, 8940–8943.

(12) Watson, D. F.; Meyer, G. J. Electron Injection at Dye-Sensitized Semiconductor Electrodes. *Annu. Rev. Phys. Chem.* **2005**, *56*, 119–156.

(13) Rao, V. G.; Dhital, B.; Peter Lu, H. Single-Molecule Interfacial Electron Transfer Dynamics of Porphyrin on TiO_2 Nanoparticles: Dissecting the Interfacial Electric Field and Electron Accepting State Density Dependent Dynamics. *Chem. Commun.* **2015**, *51*, 16821–

16824.

(14) Rao, V. G.; Dhital, B.; He, Y.; Lu, H. P. Single-Molecule Interfacial Electron Transfer Dynamics of Porphyrin on TiO_2 Nanoparticles: Dissecting the Complex Electronic Coupling Dependent Dynamics. *J. Phys. Chem. C* **2014**, *118*, 20209–20221.

(15) Tachibana, Y.; Rubtsov, I. V; Montanari, I.; Yoshihara, K.; Klug, D. R.; Durrant, J. R. Transient Luminescence Studies of Electron Injection in Dye Sensitised Nanocrystalline TiO_2 Films. *J. Photochem. Photobiol. A Chem.* **2001**, *142*, 215–220.

(16) Stockwell, D.; Yang, Y.; Huang, J.; Anfuso, C.; Huang, Z.; Lian, T. Comparison of Electron-Transfer Dynamics from Coumarin 343 to TiO_2, SnO_2, and ZnO Nanocrystalline Thin Films: Role of Interface-Bound Charge-Separated Pairs. *J. Phys. Chem. C* **2010**, *114*, 6560–6566.

(17) Tachibana, Y.; Haque, S. A.; Mercer, I. P.; Moser, J. E.; Klug, D. R.; Durrant, J. R. Modulation of the Rate of Electron Injection in Dye-Sensitized Nanocrystalline TiO_2 Films by Externally Applied Bias. *J. Phys. Chem. B* **2001**, *105*, 7424–7431.

(18) Kelly, C. A.; Farzad, F.; Thompson, D. W.; Stipkala, J. M.; Meyer, G. J. Cation-Controlled Interfacial Charge Injection in Sensitized Nanocrystalline TiO_2. *Langmuir* **1999**, *15*, 7047–7054.

(19) Koops, S. E.; O'Regan, B. C.; Barnes, P. R. F.; Durrant, J. R. Parameters Influencing the Efficiency of Electron Injection in Dye-Sensitized Solar Cells. *J. Am. Chem. Soc.* **2009**, *131*, 4808–4818.

(20) Brady, M. D.; Troian-Gautier, L.; Sampaio, R. N.; Motley, T. C.; Meyer, G. J. Optimization of Photocatalyst Excited- and Ground-State Reduction Potentials for Dye-Sensitized HBr Splitting. *ACS Appl. Mater. Interfaces* **2018**, *10*, 31312–31323.

(21) Farzad, F.; Thompson, D. W.; Kelly, C. A.; Meyer, G. J. Competitive Intermolecular Energy Transfer and Electron Injection at Sensitized Semiconductor Interfaces. *J. Am. Chem. Soc* **1999**, *121*, 5577–5578.

(22) Koops, S. E.; Durrant, J. R. Transient Emission Studies of Electron Injection in Dye Sensitised Solar Cells. *Inorganica Chim. Acta* **2008**, *361*, 663–670.

(23) Kuciauskas, D.; Monat, J. E.; Villahermosa, R.; Gray, H. B.; Lewis, N. S.; McCusker, J. K. Transient Absorption Spectroscopy of Ruthenium and Osmium Polypyridyl Complexes Adsorbed onto Nanocrystalline TiO_2 Photoelectrodes. *J. Phys. Chem. B* **2002**, *106*, 9347–9358.

(24) Watson, D. F.; Marton, A.; Stux, A. M.; Meyer, G. J. Influence of Surface Protonation on the Sensitization Efficiency of Porphyrin-Derivatized TiO_2. *J. Phys. Chem. B* **2004**, *108*, 11680–11688.

(25) She, C.; Guo, J.; Irle, S.; Morokuma, K.; Mohler, D. L.; Zabri, H.; Odobel, F.; Youm, K.-T.; Liu, F.; Hupp, J. T.; Lian, T. Comparison of Interfacial Electron Transfer through Carboxylate and Phosphonate Anchoring Groups. *J. Phys. Chem. A* **2007**, *111*, 6832–6842.

(26) Flynn, C. J.; Mccullough, S. M.; Oh, E.; Li, L.; Mercado, C. C.; Farnum, B. H.; Li, W.; Donley, C. L.; You, W.; Nozik, A. J.; Mcbride, J. R.; Meyer, T. J.; Kanai, Y.; Cahoon, J. F. Site-Selective Passivation of Defects in NiO Solar Photocathodes by Targeted Atomic Deposition. *ACS Appl. Mater. Interfaces* **2016**, *8*, 4754–4761.

(27) O'Regan, B.; Moser, J.; Anderson, M.; Gratzel, M. Vectorial Electron Injection into Transparent Semiconductor Membranes and Electric Field Effects on the Dynamics of Light-Induced Charge Separation. *J. Phys. Chem.* **1990**, *94*, 8720–8726.

(28) Kamat, P. V.; Bedja, I.; Hotchandani, S.; Patterson, L. K. Photosensitization of Nanocrystalline Semiconductor Films. Modulation of Electron Transfer between Excited Ruthenium Complex and SnO_2 Nanocrystallites with an Externally Applied Bias. *J. Phys. Chem.* **1996**, *100*, 4900–4908.

(29) Fessenden, R. W.; Kamat, P. V. Rate Constants for Charge Injection from Excited Sensitizer into SnO_2, ZnO, and TiO_2 Semiconductor Nanocrystallites. *J. Phys. Chem.* **1995**, *99*, 12902–12906.

(30) Edwards, P. P.; Porch, A.; Jones, M. O.; Morgan, D. V.; Perks, R. M. Basic Materials Physics of Transparent Conducting Oxides. *Dalt. Trans.* **2004**, *0*, 2995.

(31) Klein, A. Transparent Conducting Oxides: Electronic Structure-Property Relationship from Photoelectron Spectroscopy with in Situ Sample Preparation. *J. Am. Ceram. Soc.* **2012**, *96*, 331–345.

(32) Klein, A.; Körber, C.; Wachau, A.; Säuberlich, F.; Gassenbauer, Y.; Harvey, S. P.; Proffit, D. E.; Mason, T. O. Transparent Conducting Oxides for Photovoltaics: Manipulation of Fermi Level, Work Function and Energy Band Alignment. *Materials (Basel).* **2010**, *3*, 4892–4914.

(33) Hoertz, P. G.; Chen, Z.; Kent, C. A.; Meyer, T. J. Application of High Surface Area Tin-Doped Indium Oxide Nanoparticle Films as Transparent Conducting Electrodes. *Inorg. Chem.* **2010**, *49*, 8179–8181.

(34) Farnum, B. H.; Morseth, Z. A.; Lapides, A. M.; Rieth, A. J.; Hoertz, P. G.; Brennaman, M. K.; Papanikolas, J. M.; Meyer, T. J. Photoinduced Interfacial Electron Transfer within a Mesoporous Transparent Conducting Oxide Film. *J. Am. Chem. Soc.* **2014**, *136*, 2208–2211.

(35) Huang, Z.; He, M.; Yu, M.; Click, K.; Beauchamp, D.; Wu, Y. Dye-Controlled Interfacial Electron Transfer for High-Current Indium Tin Oxide Photocathodes. *Angew. Chemie Int. Ed.* **2015**, *54*, 6857–6861.

(36) Sampaio, R. N.; Troian-Gautier, L.; Meyer, G. J. A Charge-Separated State That Lives for Almost a Second at a Conductive Metal Oxide Interface. *Angew. Chemie* **2018**, *130*, 15616–15620.

(37) Shan, B.; Das, A. K.; Marquard, S.; Farnum, B. H.; Wang, D.; Bullock, R. M.; Meyer, T. J. Photogeneration of Hydrogen from Water by a Robust Dye-Sensitized Photocathode. *Energy Environ. Sci.* **2016**, *9*, 3693–3697.

(38) Leem, G.; Black, H. T.; Shan, B.; Bantang, J. P. O.; Meyer, T. J.; Reynolds, J. R.; Schanze, K. S. Photocathode Chromophore–Catalyst Assembly via Layer-By-Layer Deposition of a Low Band-Gap Isoindigo Conjugated Polyelectrolyte. *ACS Appl. Energy Mater.* **2018**, *1*, 62–67.

(39) Farnum, B. H.; Morseth, Z. A.; Brennaman, M. K.; Papanikolas, J. M.; Meyer, T. J. Application of Degenerately Doped Metal Oxides in the Study of Photoinduced Interfacial Electron Transfer. *J. Phys. Chem. B* **2015**, *119*, 7698–7711.

(40) Garcia, G.; Buonsanti, R.; Runnerstrom, E. L.; Mendelsberg, R. J.; Llordes, A.; Anders, A.; Richardson, T. J.; Milliron, D. J. Dynamically Modulating the Surface Plasmon Resonance of Doped Semiconductor Nanocrystals. *Nano Lett.* **2011**, *11*, 4415–4420.

(41) Frank, G.; Kostlin, H. Electrical Properties and Defect Model of Tin-Doped Indium Oxide Layers. *Appl. Phys. A Solids Surfaces* **1982**, *27*, 197–206.

(42) Farnum, B. H.; Morseth, Z. A.; Brennaman, M. K.; Papanikolas, J. M.; Meyer, T. J. Driving Force Dependent, Photoinduced Electron Transfer at Degenerately Doped, Optically Transparent Semiconductor Nanoparticle Interfaces. *J. Am. Chem. Soc.* **2014**, *136*, 15869–15872.

(43) Farnum, B. H.; Wee, K.-R.; Meyer, T. J. Self-Assembled Molecular p/n Junctions for Applications in Dye-Sensitized Solar Energy Conversion. *Nat. Chem.* **2016**, *8*, 845–852.

(44) Lu, P. H.; Xie, X. S. Single-Molecule Kinetics of Interfacial Electron Transfer. *J. Phys. Chem. B* **1997**, *101*, 2753–2757.

(45) Schneider, J.; Bangle, R. E.; Swords, W. B.; Troian-Gautier, L.; Meyer, G. J. Determination of Proton-Coupled Electron Transfer Reorganization Energies with Application to Water Oxidation Catalysts. *J. Am. Chem. Soc.* **2019**, *141*, 9758–9763.

(46) Norris, M. R.; Concepcion, J. J.; Glasson, C. R. K.; Fang, Z.; Lapides, A. M.; Ashford, D. L.; Templeton, J. L.; Meyer, T. J. Synthesis of Phosphonic Acid Derivatized Bipyridine Ligands and Their Ruthenium Complexes. *Inorg. Chem.* **2013**, *52*, 12492–12501.

(47) Raber, M. M.; Brady, M. D.; Troian-Gautier, L.; Dickenson, J. C.; Marquard, S. L.; Hyde, J. T.; Lopez, S. J.; Meyer, G. J.; Meyer, T. J.; Harrison, D. P. Fundamental Factors Impacting the Stability of Phosphonate-Derivatized Ruthenium Polypyridyl Sensitizers

Adsorbed on Metal Oxide Surfaces. *ACS Appl. Mater. Interfaces* **2018**, *10*, 22821–22833.

(48) Heimer, T. A.; D'Arcangelis, S. T.; Farzad, F.; Stipkala, J. M.; Meyer, G. J. An Acetylacetonate-Based Semiconductor−Sensitizer Linkage. *Inorg. Chem.* **1996**, *35*, 5319–5324.

(49) Barr, T. J.; Sampaio, R. N.; Dimarco, B. N.; James, E. M.; Meyer, G. J. Phantom Electrons in Mesoporous Nanocrystalline SnO_2 Thin Films with Cation-Dependent Reduction Onsets. *Chem. Mater.* **2017**, *29*, 3919–3927.

(50) Argazzi, R.; Bignozzi, C. A.; Heimer, T. A.; Castellano, F. N.; Meyer, G. J. Enhanced Spectral Sensitivity from Ruthenium(II) Polypyridyl Based Photovoltaic Devices. *Inorg. Chem.* **1994**, *33*, 5741–5749.

(51) Dimarco, B. N.; Troian-Gautier, L.; Sampaio, R. N.; Meyer, G. J. Dye-Sensitized Electron Transfer from TiO_2 to Oxidized Triphenylamines That Follows First-Order Kinetics. *Chem. Sci.* **2018**, *9*, 940–949.

(52) Bard, A. J.; Faulkner, Larry, R. Microscopic Theories of Charge Transfer. In *Electrochemical Methods: Fundamentals and Applications*; Harris, D., Swain, E., Robey, C., Aiello, E., Eds.; John Wiley & Sons, Inc: New York, 2001; pp 115–132.

(53) Marcus, R. A. On the Theory of Oxidation-Reduction Reactions Involving Electron Transfer. I. *J. Chem. Phys.* **1956**, *24*, 966–978.

(54) Marcus, R. A. Chemical and Electrochemical Electron-Transfer Theory. *Annu. Rev. Phys. Chem.* **1964**, *15*, 155–196.

(55) Gerischer, H.; Willig, F. Reactions of Excited Dye Molecules at Electroes. *Top. Curr. Chem.* **1976**, *61*, 31–84.

(56) Chidsey, C. E. Free Energy and Temperature Dependence of Electron Transfer at the Metal-Electrolyte Interface. *Science* **1991**, *251*, 919–922.

(57) Berger, T.; Monllor-Satoca, D.; Jankulovska, M.; Lana-Villarreal, T.; Gómez, R. The Electrochemistry of Nanostructured Titanium Dioxide Electrodes. *Chem. Phys. Chem.* **2012**, *13*, 2824–2875.

(58) Farnum, B. H.; Nakada, A.; Ishitani, O.; Meyer, T. J. Bias-Dependent Oxidative or Reductive Quenching of a Molecular Excited-State Assembly Bound to a Transparent Conductive Oxide. *J. Phys. Chem. C* **2015**, *119*, 25180–25187.

(59) Gerischer, H. Electrochemical Techniques for the Study of Photosensitization. *Photochem. Photobiol.* **1972**, *16*, 243–260.

(60) Hush, N. S. Adiabatic Theory of Outer Sphere Electron-Transfer Reactions in

Solution. *Trans. Faraday Soc.* **1961**, *57*, 557–580.

(61) Marcus, R. A. Exchange Reactions and Electron Transfer Reactions Including Isotopic Exchange. *Discuss. Faraday Soc.* **1960**, *29*, 21–31.

(62) Sutin, N. Nuclear, Electronic, and Frequency Factors in Electron Transfer Reactions. *Acc. Chem. Res.* **1982**, *15*, 275–282.

(63) Hale, J. M. Electrode Reactions Involving Electronically Excited States of Molecules. *J. Phys. Chem* **1969**, *73*, 3196–3201.

(64) Honda, S.; Yokoya, S.; Ohkita, H.; Benten, H.; Ito, S. Light-Harvesting Mechanism in Polymer/Fullerene/Dye Ternary Blends Studied by Transient Absorption Spectroscopy. *J. Phys. Chem. C* **2011**, *115*, 11306–11317.

(65) Zaban, A.; Meier, A.; Gregg, B. A. Electric Potential Distribution and Short-Range Screening in Nanoporous TiO_2 Electrodes. *J. Phys. Chem. B* **1997**, *101*, 7985–7990.

CHAPTER 5: DETERMINATION OF PROTON-COUPLED ELECTRON TRANSFER REORGANIZATION ENERGIES WITH APPLICATION TO WATER OXIDATION CATALYSTS[15]

5.1 Introduction

Proton-coupled electron transfer (PCET) describes reactions that involve a change in both electron and proton content between reactants and products.[1–3] Homogeneous reactions have been characterized, some of which were inspired by natural photosynthesis.[4–10] The PCET reactivity at semiconducting[11,12] and metal[13–15] interfaces has also garnered considerable interest. Like electron transfer (ET) reactions, PCET dynamics are expected to depend on the electronic coupling H_{ab}, the free energy change $-\Delta G^{o}$, and the reorganization energy λ, yet a consensus on the magnitude of λ does not exist. Babcock predicted that protein reorganization would be smaller when the H^+ and the e^- were transferred together as opposed to sequentially.[16,17] This seems intuitively reasonable, yet the limited experimental data available today suggests the opposite, $\lambda_{PCET} \geq \lambda_{ET}$.[5,18,19] It is desirable to determine λ_{PCET} directly from kinetic data measured as a function of $-\Delta G^{o}$ as described by Marcus.[20–22] Electrochemical techniques enable continuous tuning of $-\Delta G^{o}$ without the need to synthesize a family of donor–acceptor compounds.[23–25]

In this Chapter is reported a new kinetic method that utilizes the highly doped oxide material In_2O_3:Sn (ITO) whose transparent and conductive nature has been widely exploited

[15]This chapter previously appeared as an article in the *Journal of the American Chemical Society*. The original citation is: Schneider, J.; Bangle, R.E.; Swords, W.B.; Troain-Gautier, L.; Meyer, G.J. *J. Am. Chem. Soc.* **2019**, 141 *(25)*, 9758-9763.

for spectro-electrochemical characterizations.[26] Photoactive water oxidation catalysts that undergo well-defined PCET chemistry were chosen for this case study.[27–30] Pulsed light excitation of the ruthenium catalysts $[Ru^{II}(tpy)(4,4'\text{-}(PO_3H_2)_2\text{-}bpy)OH_2]^{2+}$ (Ru^{II}-OH_2), where tpy is 2,2′:6′,2″-terpyridine and bpy is 2,2′-bipyridine, resulted in rapid excited state electron transfer to the ITO yielding the oxidized catalyst and an injected electron. The subsequent recombination reaction was tuned above and below the pK_a of Ru^{III}-OH_2 to be primarily ET (pH < 1.7) or PCET (2 ≤ pH ≤ 5), noting that the latter reaction can occur either in one concerted step (CPET) or sequentially (Fig. 5.1).[29] The data revealed that reactivity at pH > 1.7 was kinetically inhibited relative to reactivity < 1.7, behavior that likely resulted from an almost 2-fold increase in the reorganization energy of PCET relative to ET. The generality of this approach was tested with a second water oxidation catalyst $[Ru^{II}(tpy)(4,4'\text{-}(CH_2\text{-}PO_3H_2)_2\text{-}bpy)OH_2]^{2+}$. These experiments provide a new method by which λ_{PCET} can be systematically quantified, and the reported PCET values in this Chapter give insights into water oxidation with molecular catalysts.

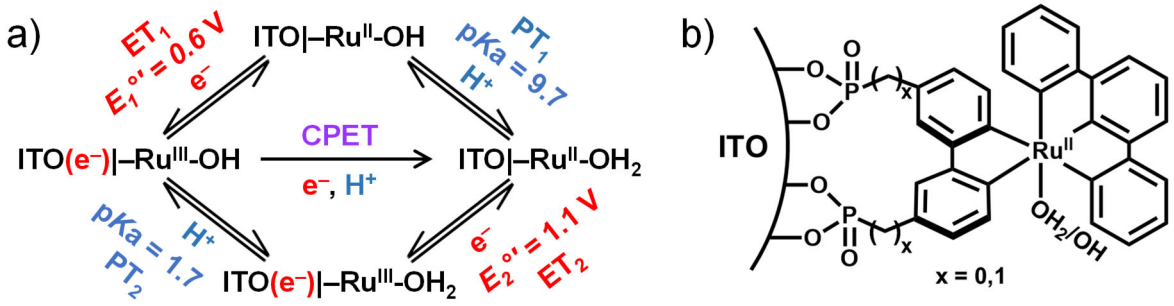

Figure 5.1. a) Interfacial PCET reaction pathways (sequential or concerted) for the ITO(e⁻) and the oxidized water oxidation catalyst. The ET reaction was characterized at pH < 1.7 (ET_2). The PCET reactivity was characterized at pH ≥ 2. b) Chemical structure of the surface-anchored catalysts without (x = 0; Ru^{II}-OH_2) and with a methylene spacer (x = 1; $[Ru^{II}(tpy)(4,4'\text{-}(CH_2\text{-}PO_3H_2)_2\text{-}bpy)OH_2]^{2+}$).

5.2 Experimental

5.2.1 ITO Thin Film Preparation

The mesoporous ITO films were prepared as previously reported[23] with a thin ZrO_2 shell deposited by atomic layer deposition for better resolution of the reaction kinetics.[31] An ITO dispersion in ethanol (20 % by weight, Evonik) was stirred overnight with an equal volume of 10 wt% solution of Hydroxypropyl Cellulose (Sigma Aldrich) in ethanol. This mixture was then used for film preparation. Thin films were deposited by doctor blade technique onto FTO substrates using one layer of scotch tape to define film thickness, in general 1 layer of scotch tape resulted in 3-4 μm thick films. To obtain mesoporous ITO films the fresh doctor bladed films were annealed in tube furnace for 30 min at 450 °C under oxygen atmosphere. Sensitization of the mesoporous ITO thin films was accomplished by overnight reaction in 5 μM aqueous catalyst solutions resulting in surface coverages of ~ 2 x 10^{-8} mol cm^{-2}, about ¼ of the saturation surface coverage, abbreviated ITO|-Ru^{II}-OH_2. The catalysts $[Ru^{II}(tpy)(4,4'\text{-}(PO_3H_2)_2\text{-}bpy)OH_2]^{2+}$ and $[Ru^{II}(tpy)(4,4'\text{-}(CH_2\text{-}PO_3H_2)_2\text{-}bpy)OH_2]^{2+}$, where bpy is 2,2′-bipyridine and tpy is 2,2′:6′,2″-terpyridine, were synthesized as previously reported.[30,32]

The surface coverage was determined using a modified Beer-Lambert law, $A = 1000\varepsilon\Gamma$, with Γ representing the surface coverage, ε the extinction coefficient. The extinction coefficient for the peak of the $[Ru^{II}(tpy)(bpy)_2(4,4'\text{-}(PO_3H_2)_2\text{-}bpy)OH_2]^{2+}$ metal-to-ligand charge transfer absorbance is 9600 M^{-1} cm^{-1}.[29] The absorbance of the ruthenium catalyst was uniform across the metal oxide thin film, i.e. the same absorbance value was measured at several different locations on the thin film, which implies that the Ru-catalyst was homogeneously distributed over the ITO electrode. The catalyst is most likely bound to the

surface via the bidentate mode of the phosphonate group, as IR spectroscopy studies suggest.[33]

5.2.2 Atomic Layer Deposition (ALD)

A Cambridge NanoTech Savannah S200 instrument was used to deposit a conformal shell of ZrO_2 on ITO as described previously[34] at a deposition temperature of 150 °C. In deposition cycles, a 0.3 s pulse of Tetrakis(dimethylamido)zirconium(IV) was followed by a 20 s exposure in the reactor and a 60 s purge.

5.2.3 Electrochemical and Spectroelectrochemical Measurements

Spectroelectrochemistry experiments were performed with an Avantes AvaLight DHc light source and an Avantes StarLine AvaSpec-2048 UV/visible spectrophotometer. Transient absorption, spectroelectrochemical, and cyclic voltammetry experiments were performed in a standard three electrode cell comprised of a Ru-catalyst sensitized ITO/FTO working electrode, a Ag/AgCl (4 M KCl, externally referenced to SCE), and a Pt mesh counter electrode. Solutions were sparged with argon for at least 20 min prior to all electrochemical experiments. A BASi Epsilon potentiostat was used to hold an applied potential for the duration of the experiment.

5.2.4 Transient Absorption Spectroscopy Measurements

Nanosecond transient absorption spectroscopy (TA) was performed using a Q-switched, pulsed Nd:YAG laser (Quantel U.S.A.(Big Sky) Brilliant B, 5-6 ns FWHM) doubled to 532 nm as the pulse beam.[35] The laser fluence at samples was 1-4 mJ/pulse at 1 Hz. A 150 W xenon arc lamp aligned orthogonal to the laser served as probe beam. For measurements of time < 100 μs, the probe lamp was pulsed with 70 V at 1 Hz. Signal was detected with a monochromator (SPEX 1702/04) optically coupled to a Hamamatsu R928

photomultiplier tube. Transient data were acquired with a computer-interfaced digital oscilloscope (LeCroy 9450, Dual 330 MHz) with an overall instrument response time of ~10 ns. Single wavelength kinetic traces consisted of 90-150 averaged laser pulses. Transient spectra were generated from single wavelength measurements over a 370-800 nm range in 10 nm steps. Typically, 30 transients were signal averaged at each monitored wavelength.

5.2.5 Kinetic Analysis

The decay dynamics were described by the rate constants $k_{1/2}$ determined from the time required for the signal ($\Delta Absobance_{490nm}$) to decay to ½ of the initial signal amplitude, $k_{1/2} = 1/t_{1/2}$.[23] Alternative analysis in which rates were represented as the time required for the signal to decay to 1/e of the initial amplitude resulted in invariant determined values of λ. The statistical error for reorganization energy for ET and PCET process was 0.5 ± 0.05 eV and 0.9 ± 0.06 eV, respectively.

5.3 Results and Discussion

The visible absorbance spectra of an ITO|-Ru^{II}-OH_2 electrode were recorded in pH = 1 and 5 aqueous $HClO_4$ solutions (Fig. 5.2). For both pH values a broad metal-to-ligand charge transfer (MLCT) absorption band centered at 490 nm was obtained. A quasi-reversible $E_{1/2}(Ru^{III/II})$ redox wave was measured by cyclic voltammetry as a function of pH (Fig. 5.6 in the Associated Content section). A Nernstian shift of 59 mV/pH was observed from pH = 5 to 1.7 indicative of a one-electron and one proton reaction (Fig. 5.2b). At pH values below 1.7, $E_{1/2}(Ru^{III/II})$ was pH independent evincing the one-electron oxidation without proton involvement. Literature values for $E_{1/2}$ $[Ru^{III/II}(OH_2/OH)(tpy)(bpy)]^{3+/2+}$ displayed a small negative potential shift (<50 mV) attributed to the absence of the electron

withdrawing phosphonate groups.[27,29] Also indicated on this plot are pK_a values of Ru^{II}-OH_2 and Ru^{III}-OH_2, the formal reduction potentials of the aquo $E°'_2(Ru^{III}/OH_2)$ and hydroxo $E°'_1$ (Ru^{III}/OH) catalysts.

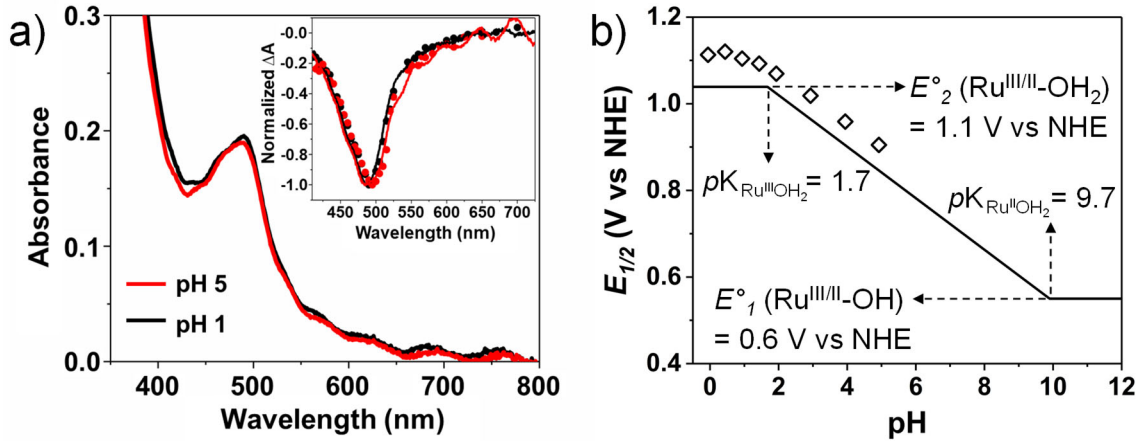

Figure 5.2. (a) Visible absorption spectra of ITO|-Ru^{II}-OH_2 recorded in a pH 1 (black) or pH 5 (red) solution. The inset shows the transient absorption spectra measured 20 ns after pulsed 532 nm excitation (4 mJ cm^{-2}) at pH 1 (black circles) and 5 (red circles) with overlaid spectro-electrochemical data as the solid lines. (b) Plots of $E_{1/2}$ as a function of pH for the $Ru^{III/II}$ redox chemistry measured on the ITO surface (diamonds) and previously reported data for the catalyst without phosphonate groups in fluid solution (solid lines).[27]

The inset of Fig. 5.2a shows transient spectra measured 20 ns after pulsed 532 nm laser excitation of ITO|-Ru^{II}-OH_2 in pH 1 and 5 solutions with overlaid Ru^{II} to Ru^{III} absorbance difference spectra obtained from spectro-electrochemistry. The prompt MLCT bleach was consistent with rapid excited-state electron transfer $k_{inj} > 10^8$ s^{-1} and the formation of an injected electron and oxidized catalyst. Transient absorption spectra alone did not report on the protonation state of the coordinated water. This was instead inferred from the kinetic data. Under all experimental conditions employed, one transient interfacial state was observed that recombined to ground-state products without evidence of permanent photochemistry.

Recombination of the injected electrons with the oxidized catalyst was measured as a function of the applied potential, E_{app}, and pH in a standard three-electrode cell. The

recombination kinetics were measured over the potential range −0.1 to +0.9 V vs NHE in 100 mV increments. Single-wavelength kinetic data on nanosecond and longer time scales at pH 1 and pH 3, respectively, show recombination is significantly faster at low pH (Fig. 5.3). The recombination reaction was tuned with pH to occur with and without proton involvement. For example, at pH 1 about 90% of the oxidized catalysts were present as $Ru^{III}OH_2$, and the primary reaction was ET. At pH 3 about 95% of the catalysts were $Ru^{III}OH$, and the primary reaction was PCET.

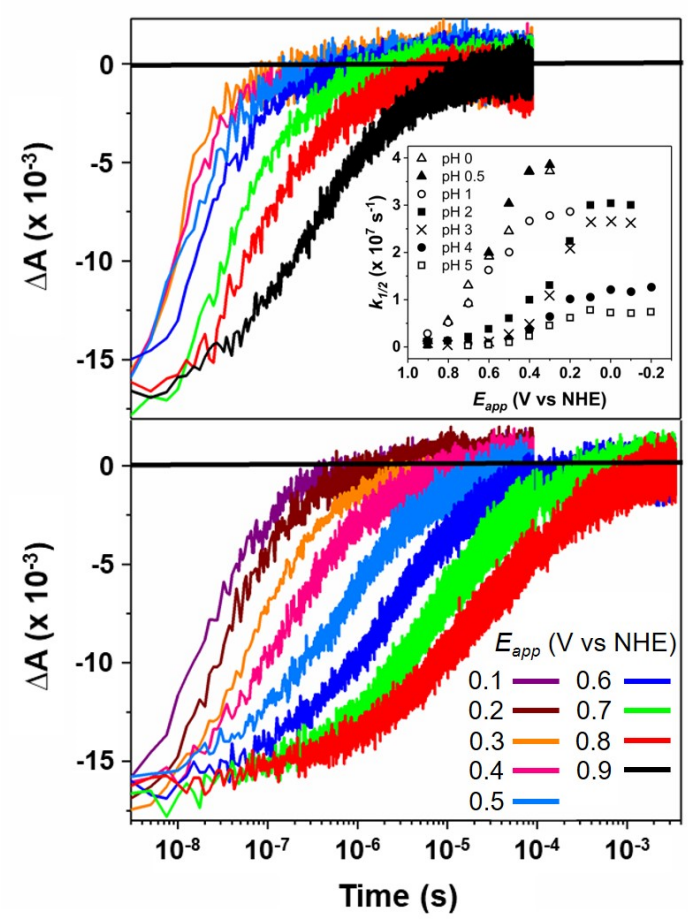

Figure 5.3. Absorption changes monitored at 490 nm after pulsed 532 nm laser excitation of ITO|-Ru^{II}-OH_2 as a function of E_{app} at pH 1 (top) and at pH 3 (bottom). The $k_{1/2}$ values obtained at different pH values are shown as a function of E_{app} in the inset.

As is commonly observed on oxide surfaces, the transient data were not well described by a first-order kinetic model, so the reciprocal of the time required for 1/2 of the

charge separated states to recombine ($k_{1/2}$) was taken as a proxy for the rate constant.[23,36,37] The $k_{1/2}$ values measured at different pH values are represented as a function of E_{app} in the inset of Fig. 5.3. The largest rate constants were measured at pH 0–1, where an ET mechanism was expected. Under conditions that promoted PCET, the rate constants were smaller. At any given pH, the rate constants saturated at large driving force ($-E_{app}$) consistent with Marcus–Gerischer theory *vida infra*. The smaller $k_{1/2}^{max}$ values at pH > 3 are not fully understood, but may be due to weaker coupling between the catalyst and the oxide as evidenced by desorption under alkaline conditions.

These kinetic experiments were repeated in D_2O to determine the kinetic isotope effect (KIE = k_H/k_D). At pH ≥ 2, a KIE = 1.12 ± 0.04 was measured, where at pH ≤ 1 there was no measurable isotope effect with a KIE = 0.99 ± 0.02 (Fig. 5.7 in the Associated Content Section). Unfortunately, the KIE values do not in themselves distinguish the PCET mechanism, as they are known to vary widely 0.5–700.[8,38–41]

The PCET reduction of Ru^{III}-OH to yield Ru^{II}-OH_2 can occur either via stepwise[15,28,35,42] or concerted[13,14] mechanisms (Fig. 5.1). In the case of stepwise PT-ET, the free energy change for proton transfer ($\Delta G_{PT}^{o} = -0.059 \cdot (pK_a(Ru^{III}OH_2/OH) - pK_a(H_3O^+/H_2O) = -0.1$ eV) is independent of E_{app}. Thus, rate limiting PT would result in potential independent rate constants, clearly contrary to the kinetic data in Fig. 5.3. The rate limiting ET with a PT pre-equilibrium is unlikely, as the observed rate constant does not follow $k_{1/2}$(pH 5) = $K_a k_{1/2}$(pH 0). Further, at constant ET driving force, the observed recombination at pH 5 was slower than at pH 1, contradictory to an ET-limited mechanism (Fig. 5.8 in the Associated Content section). Hence, a CPET mechanism is most consistent with the experimental data.

By analogy to heterogeneous ET reactions, the free energy dependence of the PCET kinetic data were analyzed with Marcus–Gerischer theory as illustrated in Fig. 5.4 with the rate constant k defined in Eq. 5.1.[43]

$$k = \frac{2\pi}{\hbar}\int_{-\infty}^{\infty}\rho(E)f(E,E_F)|H_{ab}|^2W(E)dE \quad (5.1)$$

Here, the total distribution of electronic levels in the ITO electrode is represented by $\rho(E)$, and their occupancy is controlled by E_{app} which sets the Fermi energy, E_F. The high carrier density of ITO provides metallic character, and $\rho(E)$ has been shown to vary continuously over the applied potential range utilized here. The term $f(E, E_F)$ is the Fermi–Dirac distribution, and $H_{ab}(E)$ is the electronic coupling matrix element. The catalyst acceptor states are represented by $W(E)$, a Gaussian distribution of classical activation energies (Eq. 5.2).[44]

$$W(E) = \frac{1}{\sqrt{4\pi k_B T}}\exp\left(\frac{-(\Delta G^\circ+\lambda)^2}{4\lambda k_B T}\right) \quad (5.2)$$

Here, ΔG^o is controlled by $E_F = E_{app}$. Both PCET and ET occur isoenergetically.[23] The free energy for ET $\Delta G_{ET}{}^o$ corresponds to the difference between E_F and the standard reduction potential $E_2°$ (Eq. 5.3). For PCET the free energy is equal to the sum of $\Delta G_{ET}{}^o$ and $\Delta G_{PT}{}^o$, and $\Delta G_{PT}{}^o$ is determined by the relative pK_a values of $Ru^{III}OH_2/OH$ (pK_a = 1.7) and H_3O^+/H_2O (pK_a = 0) (Eq. 5.4).[45,46]

$$\Delta G^\circ{}_{ET} = -\left(eE^\circ{}_2\left(Ru^{III/II}OH_2\right) - E_F\right) \quad (5.3)$$

$$\Delta G^\circ{}_{PCET} = \Delta G^\circ{}_{ET} + \Delta G^\circ{}_{PT} \quad (5.4)$$

$$= -\left(eE^\circ{}_2\left(Ru^{III/II}OH_2\right) - E_F\right) - 2.3RT(pK_a(Ru^{III}\,OH_2/OH) - pK_a(H_3O^+/H_2O))$$

Values of $k_{1/2}$ at each E_{app} (or $-\Delta G°$) are given in Tables 5.1 and 5.2 in the Associated Content section.

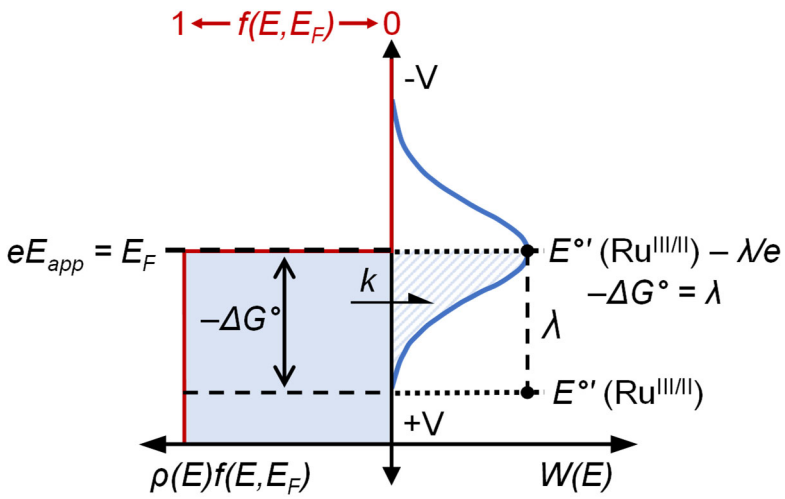

Figure 5.4. Gerischer diagram representation of energetics associated with PCET from ITO to Ru^{III}-OH to yield Ru^{II}-OH_2.

In the low-temperature limit of the Fermi–Dirac distribution and with the assumption that $\rho(E)$ and $H_{ab}(E)$ are independent of E_{app}, Eqs. 5.1 and 5.2 become Eqs. 5.5 and 5.6.

$$k = k^{max} \int_{E_F}^{\infty} \frac{1}{\sqrt{4\pi k_B T}} \exp\left(\frac{-(\Delta G^{\circ}+\lambda)^2}{4\lambda k_B T}\right) dE \tag{5.5}$$

$$\frac{k}{k^{max}} = \frac{1}{2}\left[1 - \mathrm{erf}\left(\frac{\Delta G^{\circ}+\lambda}{2\sqrt{\lambda k_B T}}\right)\right] \tag{5.6}$$

Marcus–Gerischer theory predicts increased rate constants with increasing $-\Delta G^{o}$. Because of the continuum of the electronic states in ITO, the rate constants are expected to reach a maximum when $-\Delta G^{o} > 2\lambda$. This is in contrast to the inverted region predicted by Marcus for molecular electron transfer reactions.[44] In addition, at the condition $-\Delta G^{o} = \lambda$, k is not maximized but is equal to half the value of k^{max} as indicated in Fig. 5.4.

Plots of k/k^{max} ($k = k_{1/2}$, $k^{max} = k_{1/2}{}^{max}$) as a function of driving force are shown in Fig. 5.5a for both ET (black) and PCET (blue). As expected, k increased with $-\Delta G^{o}$ until a maximum value was realized. Fits of the experimental data to Eq. 5.6 gave $\lambda_{ET} = 0.5$ eV and $\lambda_{PCET} = 0.9$ eV. The corresponding $W(E)$ functions are shown in Fig. 5.5b. To test generality, a derivative with a methylene spacer between the catalyst and the phosphonate binding group

$[Ru^{II}(tpy)(4,4'\text{-}(CH_2\text{-}PO_3H_2)_2\text{-}bpy)OH_2]^{2+}$ (Fig. 5.1) was analyzed in this manner to yield λ_{ET} of 0.4 eV and λ_{PCET} of 0.8 eV (Fig. 5.9-5.11). Prior literature reports $\lambda_{PCET} > 1$ eV in homogeneous solutions[18,28,47–49] and ~0.7 eV for heterogeneous interfaces.[14] Theoretical predictions by Hammes-Schiffer et al.[19,50] indicate an additional ~0.3 eV in reorganization for PCET relative to ET, which is in a good agreement with the experimental value of 0.4 eV found here.

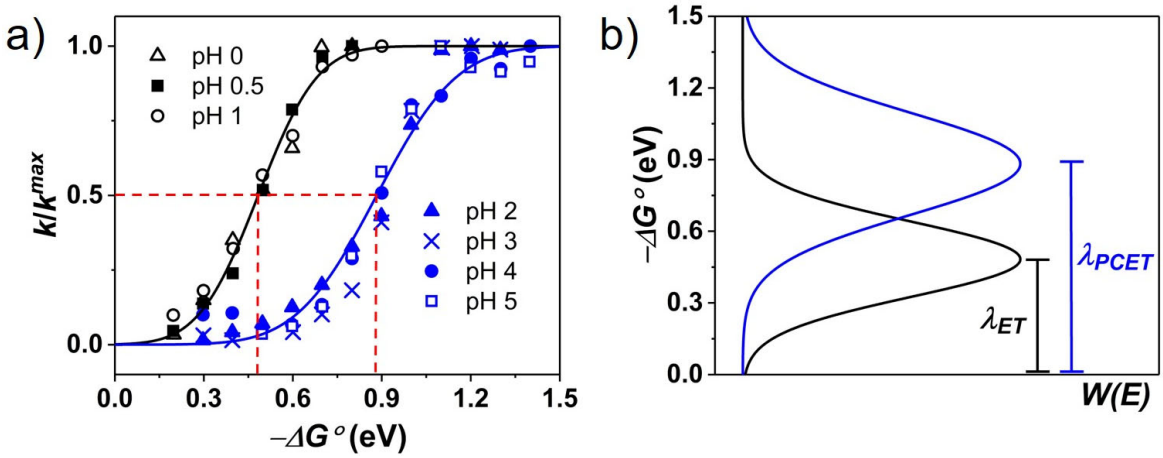

Figure 5.5. a) Normalized rate constants (symbols) and fit to Eq. 5.4 (solid lines) for ET (black) and PCET (blue). Dashed red lines represent the condition, $-\Delta G^o = \lambda$, at which $k = 1/2\ k^{max}$. (b) $W(E)$ obtained from differentiation of the fit with indicated values for $\lambda_{ET} = 0.5$ eV and $\lambda_{PCET} = 0.9$ eV.

5.4 Conclusions

This Chapter demonstrates a successful application of Marcus–Gerischer theory to quantify experimentally the reorganization energy for PCET reactions. The approach requires only a transparent conductor, a means to photo-initiate the PCET reaction, and a method to monitor the kinetic rate constant as a function of the applied potential. Future studies in which the PCET reactivity occurs to fully solvated species outside the electric double layer are expected to provide first-order kinetics[51] and a better understanding of how the oxide

interface influences reorganization energies.[52] For the reduction of Ru^{III}-OH to Ru^{II}-OH_2 reported here, a PCET pathway was identified that required 0.4 eV higher reorganization energy than did electron transfer without proton involvement. The decreased recombination rate constants to water oxidation catalysts represents an important advance as charge recombination limits the efficiency of dye-sensitized water oxidation. Hence, solar water oxidation efficiencies may be enhanced by inhibiting recombination at pH values that promote PCET.

5.5 Acknowledgements

The authors thank Prof. Jillian Dempsey and Dr. Eric J. Piechota for fruitful discussions and helpful suggestions. This material is based upon work solely supported by the Alliance for Molecular PhotoElectrode Design for Solar Fuels (AMPED), an Energy Frontier Research Center (EFRC) funded by the U.S. Department of Energy, Office of Science, Office of Basic Energy Sciences under Award Number DESC0001011. R.E.B. acknowledges the National Science Foundation for an individual Graduate Research Fellowship under Grant No. DGE-1650116. This work made use of atomic layer deposition instrumentation at the Chapel Hill Analytical and Nanofabrication Laboratory (CHANL), a member of the North Carolina Research Triangle Nanotechnology Network (RTNN), supported by the National Science Foundation (Grant ECCS-1542015) as part of the National Nanotechnology Coordinated Infrastructure (NNCI).

5.6 Associated Content

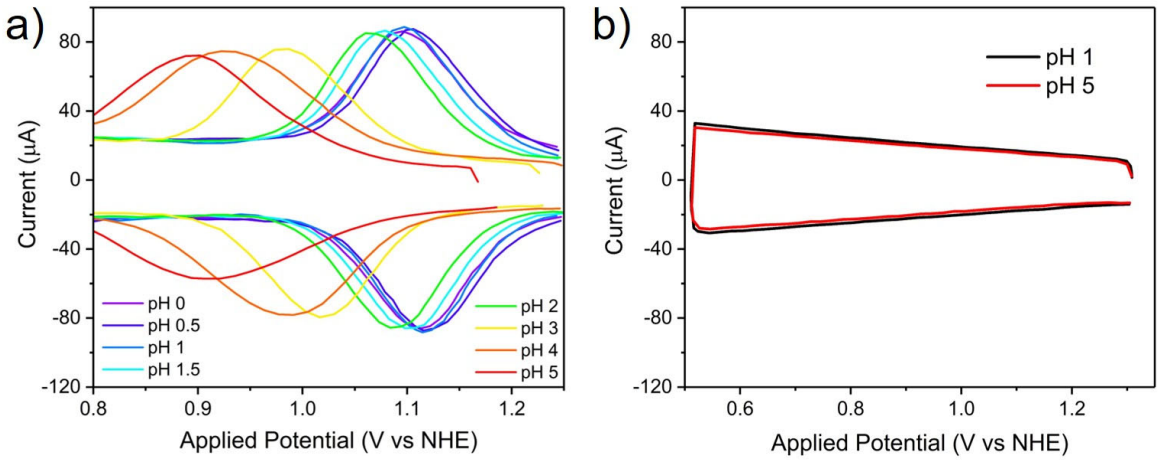

Figure 5.6. a) Cyclic voltammograms of $Ru^{III/II}$ for $[Ru^{II}(tpy)(4,4'\text{-}(PO_3H_2)_2\text{-}bpy)OH_2]^{2+}$ measured in the pH region 0-5. b) Cyclic voltammograms of ITO electrode measured at pH 1 and 5. Scan rate = 10 mV/s. The experiments in the present study have been carried out at low catalyst surface coverages to inhibit disproportionation reaction chemistry.[30]

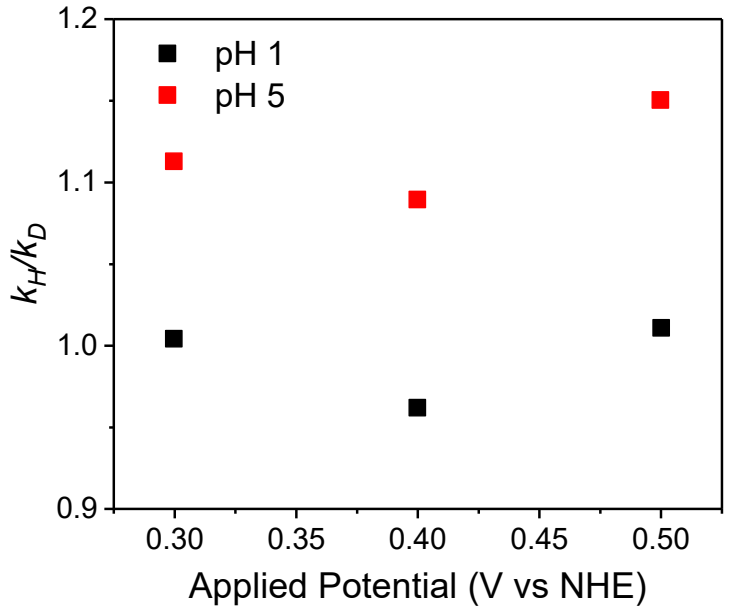

Figure 5.7. Kinetic isotope effect k_H/k_D as function of E_{app} measured at pH 1 and 5 after pulsed 532 nm laser excitation of ITO|-Ru^{II}-OH_2. Transient absorption signals used to calculate k_H/k_D were monitored at 490 nm after 532 nm laser excitation.

Table 5.1. Summary of the transient absorption kinetic data for ΔA_{490nm} obtained at pH 1 with corresponding free energy values. $-\Delta G°_{ET}$ was calculated according to Eq. 5.3, with $E_2°'$ ($Ru^{III/II}OH_2$) = 1.1 V vs NHE.

E_{app} (V vs NHE)	$-\Delta G°$ (eV)	$k_{1/2}$ (s^{-1})
0.9	0.2	2.9×10^6
0.8	0.3	5.1×10^6
0.7	0.4	9.2×10^6
0.6	0.5	1.6×10^7
0.5	0.6	2.0×10^7
0.4	0.7	2.7×10^7
0.3	0.8	2.8×10^7
0.2	0.9	2.8×10^7

Table 5.2. Summary of the transient absorption kinetic data for ΔA_{490nm} obtained at pH 2-5 with corresponding free energy values. $-\Delta G°_{PCET}$ was calculated according to Eq. 5.4, with $E_2°'$ ($Ru^{III/II}OH_2$) = 1.1 V vs NHE.

E_{app} (V vs NHE)	$-\Delta G°$ (eV)	$k_{1/2}$			
		pH 2	pH 3	pH 4	pH 5
0.8	0.4	1.3×10^6	2.6×10^5	-	-
0.7	0.5	2.2×10^6	5.1×10^5	2.1×10^5	1.5×10^5
0.6	0.6	3.7×10^6	1.2×10^6	4.7×10^5	4.1×10^5
0.5	0.7	5.9×10^6	2.5×10^6	1.5×10^6	9.5×10^5
0.4	0.8	9.9×10^6	4.8×10^6	3.4×10^6	2.2×10^6
0.3	0.9	1.3×10^7	1.1×10^7	6.3×10^6	4.4×10^6
0.2	1.0	2.2×10^7	2.1×10^7	1.0×10^7	6.1×10^6
0.1	1.1	3.0×10^7	2.6×10^7	1.0×10^7	7.7×10^6
0	1.2	3.0×10^7	2.7×10^7	1.2×10^7	7.1×10^6
-0.1	1.3	3.0×10^7	2.6×10^7	1.1×10^7	7.0×10^6

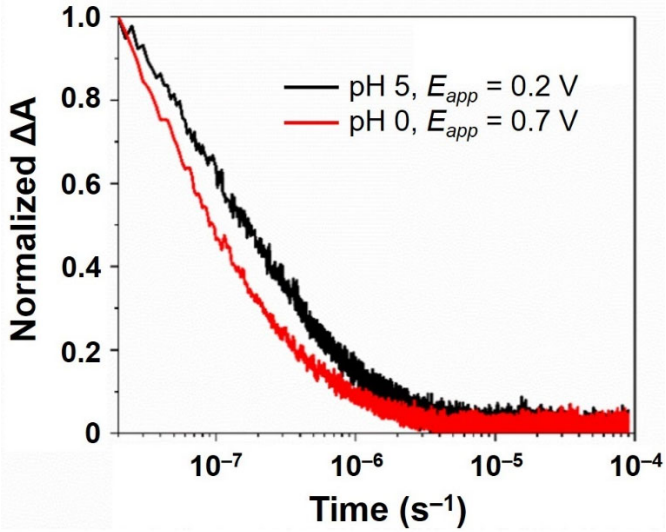

Figure 5.8. Normalized absorption change monitored at 490 nm after pulsed 532 nm laser excitation of ITO|-Ru^{II}-OH_2 at pH 0 (red) and at pH 5 (black). Note that the applied bias was controlled to assure a constant free energy change of -0.4 eV when electron transfer was the only assumed mechanism.

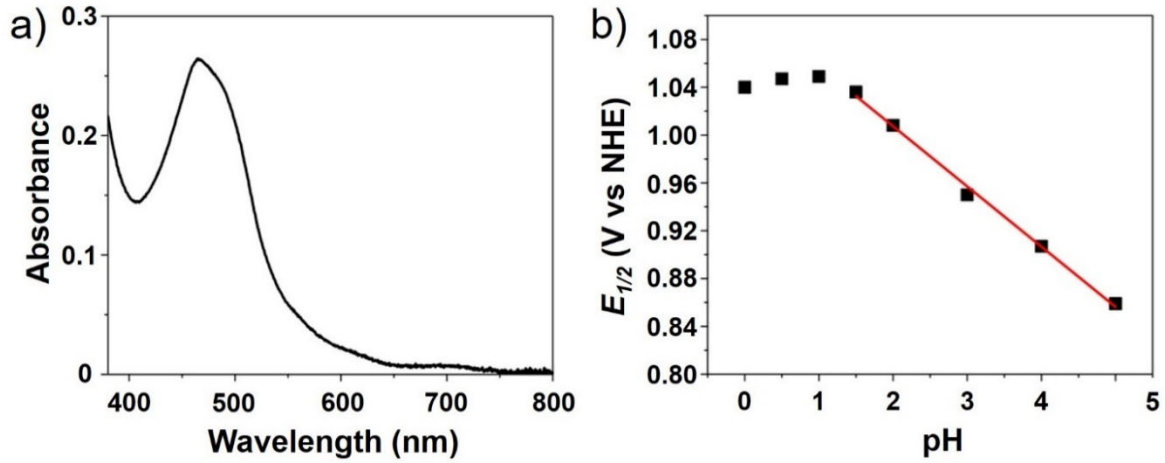

Figure 5.9. a) The visible absorption spectra of $[Ru^{II}(tpy)(4,4'\text{-}(CH_2\text{-}PO_3H_2)_2\text{-}bpy)OH_2]^{2+}$ recorded at a pH 3. b) Plots of $E_{1/2}$ as a function of pH for the $Ru^{III/II}$ redox chemistry measured on the ITO surface.

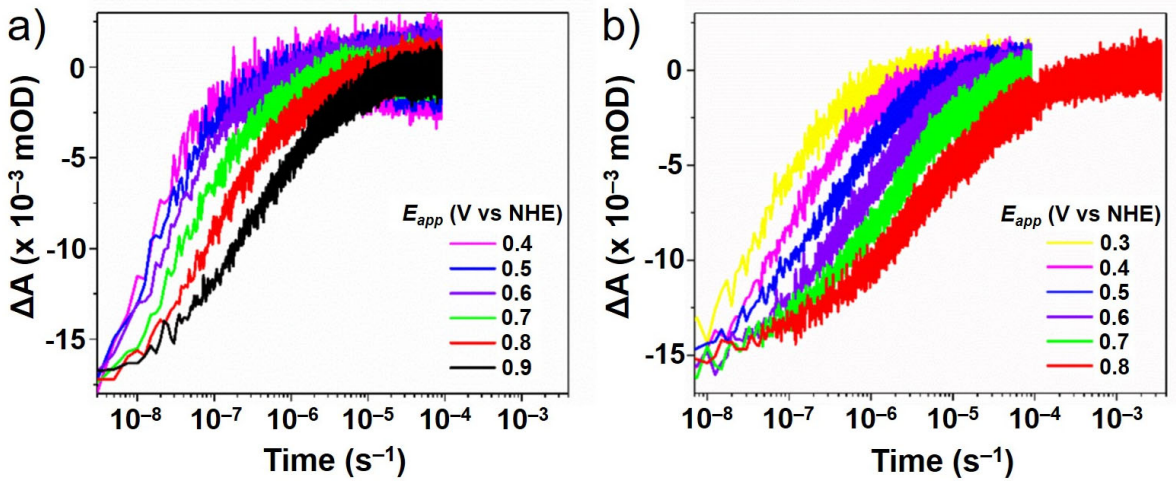

Figure 5.10. Absorption changes monitored at 490 nm after pulsed 532 nm laser excitation of ITO|-[Ru^{II}(tpy)(4,4′-(CH_2-PO_3H_2)$_2$-bpy)OH_2]$^{2+}$ as function of E_{app} at a) pH 1 and b) pH 3.

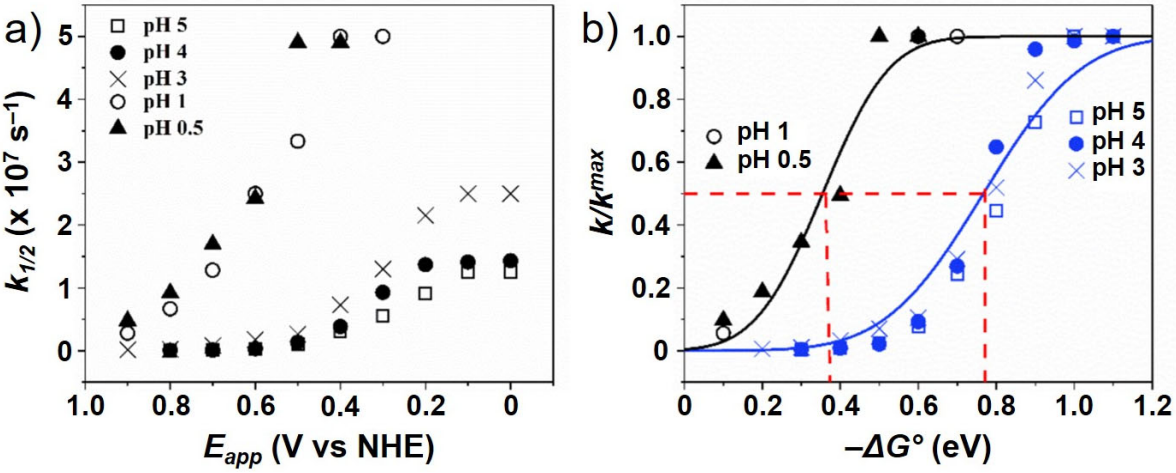

Figure 5.11. a) The $k_{1/2}$ values obtained at different pH values for ITO|-[Ru^{II}(tpy)(4,4′-(CH_2-PO_3H_2)$_2$- bpy)OH_2]$^{2+}$ are shown as function of E_{app}. b) Normalized rate constants (symbols) and fit to Equation 4 (solid lines) for ET (black) and PCET (blue) with λ_{ET} = 0.4 eV and λ_{PCET} = 0.8 eV.

REFERENCES

(1) Dempsey, J. L.; Winkler, J. R.; Gray, H. B. Proton-Coupled Electron Flow in Protein Redox Machines. *Chem. Rev.* **2010**, *110* (12), 7024–7039.

(2) Stubbe, J. A.; Nocera, D. G.; Yee, C. S.; Chang, M. C. Y. Radical Initiation in the Class I Ribonucleotide Reductase: Long-Range Proton-Coupled Electron Transfer? *Chem. Rev.* **2003**, *103* (6), 2167–2201.

(3) Weinberg, D. R.; Gagliardi, C. J.; Hull, J. F.; Murphy, C. F.; Kent, C. A.; Westlake, B. C.; Paul, A.; Ess, D. H.; McCafferty, D. G.; Meyer, T. J. Proton-Coupled Electron Transfer. *Chem. Rev.* **2012**, *112* (7), 4016–4093.

(4) Hammarström, L.; Styring, S. Proton-Coupled Electron Transfer of Tyrosines in Photosystem II and Model Systems for Artificial Photosynthesis: The Role of a Redox Active Link between Catalyst and Photosensitizer. *Energy Environ. Sci.* **2011**, *4* (7), 2379–2388.

(5) Sjödin, M.; Styring, S.; Åkermark, B.; Sun, L.; Hammarström, L. Proton-Coupled Electron Transfer from Tyrosine in a Tyrosine-Ruthenium- Tris-Bipyridine Complex: Comparison with Tyrosinez Oxidation in Photosystem II. *J. Am. Chem. Soc.* **2000**, *122* (16), 3932–3936.

(6) Irebo, T.; Zhang, M. T.; Markle, T. F.; Scott, A. M.; Hammarström, L. Spanning Four Mechanistic Regions of Intramolecular Proton-Coupled Electron Transfer in ARu(Bpy)$_3^{2+}$-Tyrosine Complex. *J. Am. Chem. Soc.* **2012**, *134* (39), 16247–16254.

(7) Mora, S. J.; Odella, E.; Moore, G. F.; Gust, D.; Moore, T. A.; Moore, A. L. Proton-Coupled Electron Transfer in Artificial Photosynthetic Systems. *Acc. Chem. Res.* **2018**, *51* (2), 445–453.

(8) Manbeck, G. F.; Fujita, E.; Concepcion, J. J. Proton-Coupled Electron Transfer in a Strongly Coupled Photosystem II-Inspired Chromophore-Imidazole-Phenol Complex: Stepwise Oxidation and Concerted Reduction. *J. Am. Chem. Soc.* **2016**, *138* (36), 11536–11549.

(9) Hammes-Schiffer, S.; Stuchebrukhov, A. A. Theory of Coupled Electron and Proton Transfer Reactions. *Chem. Rev.* **2010**, *110* (12), 6939–6960.

(10) Odella, E.; Mora, S. J.; Wadsworth, B. L.; Huynh, M. T.; Goings, J. J.; Liddell, P. A.; Groy, T. L.; Gervaldo, M.; Sereno, L. E.; Gust, D.; Moore, T. A.; Moore, G. F.; Hammes-Schiffer, S.; Moore, A. L. Controlling Proton-Coupled Electron Transfer in Bioinspired Artificial Photosynthetic Relays. *J. Am. Chem. Soc.* **2018**, *140* (45), 15450–15460.

(11) Braten, M. N.; Gamelin, D. R.; Mayer, J. M. Reaction Dynamics of Proton-Coupled Electron Transfer from Reduced ZnO Nanocrystals. *ACS Nano* **2015**, *9* (10), 10258–10267.

(12) Valdez, C. N.; Schimpf, A. M.; Gamelin, D. R.; Mayer, J. M. Proton-Controlled Reduction of ZnO Nanocrystals: Effects of Molecular Reductants, Cations, and Thermodynamic Limitations. *J. Am. Chem. Soc.* **2016**, *138* (4), 1377–1385.

(13) Haddox, R. M.; Finklea, H. O. Proton-Coupled Electron Transfer of an Osmium Aquo Complex on a Self-Assembled Monolayer on Gold. *J. Phys. Chem. B* **2004**, *108* (5), 1694–1700.

(14) Madhiri, N.; Finklea, H. O. Potential-, PH-, and Isotope-Dependence of Proton-Coupled Electron Transfer of an Osmium Aquo Complex Attached to an Electrode. *Langmuir* **2006**, *22* (25), 10643–10651.

(15) Costentin, C.; Robert, M.; Savéant, J.-M.; Teillout, A.-L. Concerted and Stepwise Proton-Coupled Electron Transfers in Aquo/Hydroxo Complex Couples in Water: Oxidative Electrochemistry of $[Os^{II}(Bpy)_2(Py)(OH_2)]^{2+}$. *Chem. Phys. Chem* **2009**, *10* (1), 191–198.

(16) Westphal, K. L.; Tommos, C.; Cukier, R. I.; Babcock, G. T. Concerted Hydrogen-Atom Abstraction in Photosynthetic Water Oxidation. *Curr. Opin. Plant Biol.* **2000**, *3* (3), 236–242.

(17) Tommos, C.; Babcock, G. T. Oxygen Production in Nature: A Light-Driven Metalloradical Enzyme Process. *Acc. Chem. Res.* **1998**, *31* (1), 18–25.

(18) Sjödin, M.; Styring, S.; Wolpher, H.; Xu, Y.; Sun, L.; Hammarström, L. Switching the Redox Mechanism: Models for Proton-Coupled Electron Transfer from Tyrosine and Tryptophan. *J. Am. Chem. Soc.* **2005**, *127* (11), 3855–3863.

(19) Ghosh, S.; Soudackov, A. V; Hammes-Schiffer, S. Electrochemical Electron Transfer and Proton-Coupled Electron Transfer: Effects of Double Layer and Ionic Environment on Solvent Reorganization Energies. *J. Chem. Theory Comput.* **2016**, *12*, 2917–2925.

(20) Huang, T.; Rountree, E. S.; Traywick, A. P.; Bayoumi, M.; Dempsey, J. L. Switching between Stepwise and Concerted Proton-Coupled Electron Transfer Pathways in Tungsten Hydride Activation. *J. Am. Chem. Soc.* **2018**, *140* (44), 14655–14669.

(21) Nomrowski, J.; Wenger, O. S. Photoinduced PCET in Ruthenium-Phenol Systems: Thermodynamic Equivalence of Uni- and Bidirectional Reactions. *Inorg. Chem.* **2015**, *54* (7), 3680–3687.

(22) Morris, W. D.; Mayer, J. M. Separating Proton and Electron Transfer Effects in Three-Component Concerted Proton-Coupled Electron Transfer Reactions. *J. Am. Chem. Soc.* **2017**, *139* (30), 10312–10319.

(23) Farnum, B. H.; Morseth, Z. A.; Brennaman, M. K.; Papanikolas, J. M.; Meyer, T. J. Application of Degenerately Doped Metal Oxides in the Study of Photoinduced Interfacial Electron Transfer. *J. Phys. Chem. B* **2015**, *119*, 7698–7711.

(24) Farnum, B. H.; Morseth, Z. A.; Lapides, A. M.; Rieth, A. J.; Hoertz, P. G.; Brennaman, M. K.; Papanikolas, J. M.; Meyer, T. J. Photoinduced Interfacial Electron Transfer within a Mesoporous Transparent Conducting Oxide Film. *J. Am. Chem. Soc.* **2014**, *136* (6), 2208–2211.

(25) Farnum, B. H.; Morseth, Z. A.; Brennaman, M. K.; Papanikolas, J. M.; Meyer, T. J. Driving Force Dependent, Photoinduced Electron Transfer at Degenerately Doped, Optically Transparent Semiconductor Nanoparticle Interfaces. *J. Am. Chem. Soc.* **2014**, *136* (45), 15869–15872.

(26) Klein, A. Transparent Conducting Oxides: Electronic Structure-Property Relationship from Photoelectron Spectroscopy with in Situ Sample Preparation. *J. Am. Ceram. Soc.* **2012**, *96* (2), 331–345.

(27) Concepcion, J. J.; Jurss, J. W.; Templeton, J. L.; Meyer, T. J. One Site Is Enough. Catalytic Water Oxidation by $[Ru(Tpy)(Bpm)(OH_2)]^{2+}$ and $[Ru(Tpy)(Bpz)(OH_2)]^{2+}$. *J. Am. Chem. Soc.* **2008**, *130* (49), 16462–16463.

(28) McHatton, R. C.; Anson, F. C. Electrochemical Behavior of $Ru(Trpy)(Bpy)(OH_2)^{3+}$ in Aqueous Solution and When Incorporated in Nafion Coatings. *Inorg. Chem.* **1984**, *23* (24), 3935–3942.

(29) Takeuchi, K. J.; Thompson, M. S.; Pipes, D. W.; Meyer, T. J. Redox and Spectral Properties of Monooxo Polypyridyl Complexes of Ruthenium and Osmium in Aqueous Media. *Inorg. Chem.* **1984**, *23* (13), 1845–1851.

(30) Trammell, S. A.; Wimbish, J. C.; Odobel, F.; Gallagher, L. A.; Narula, P. M.; Meyer, T. J. Mechanisms of Surface Electron Transfer. Proton-Coupled Electron Transfer. *J. Am. Chem. Soc.* **1998**, *120* (50), 13248–13249.

(31) Kim, D. H.; Losego, M. D.; Peng, Q.; Parsons, G. N. Atomic Layer Deposition for Sensitized Solar Cells: Recent Progress and Prospects. *Adv. Mater. Interfaces* **2016**, *3* (21), 1600354.

(32) Chen, Z.; Vannucci, A. K.; Concepcion, J. J.; Jurss, J. W.; Meyer, T. J. Proton-Coupled Electron Transfer at Modified Electrodes by Multiple Pathways. *Proc. Natl. Acad. Sci. U. S. A.* **2011**, *108* (52), E1461–E1469.

(33) Materna, K. L.; Crabtree, R. H.; Brudvig, G. W. Anchoring Groups for Photocatalytic Water Oxidation on Metal Oxide Surfaces. *Chem. Soc. Rev.* **2017**, *46*, 6099–6110.

(34) Knauf, R. R.; Kalanyan, B.; Parsons, G. N.; Dempsey, J. L. Charge Recombination Dynamics in Sensitized SnO_2/TiO_2 Core/Shell Photoanodes. *J. Phys. Chem. C* **2015**, *119*, 28353–28360.

(35) Argazzi, R.; Bignozzi, C. A.; Heimer, T. A.; Castellano, F. N.; Meyer, G. J. Enhanced

Spectral Sensitivity from Ruthenium(II) Polypyridyl Based Photovoltaic Devices. *Inorg. Chem.* **1994**, *33*, 5741–5749.

(36) Haque, S. A.; Tachibana, Y.; Klug, D. R.; Durrant, J. R. Charge Recombination Kinetics in Dye-Sensitized Nanocrystalline Titanium Dioxide Films under Externally Applied Bias. *J. Phys. Chem. B* **1998**, *102* (10), 1745–1749.

(37) Clifford, J. N.; Palomares, E.; Nazeeruddin, M. K.; Grätzel, M.; Nelson, J.; Li, X.; Long, N. J.; Durrant, J. R. Molecular Control of Recombination Dynamics in Dye-Sensitized Nanocrystalline TiO_2 Films: Free Energy vs Distance Dependence. *J. Am. Chem. Soc.* **2004**, *126* (16), 5225–5233.

(38) Eisenhart, T. T.; Dempsey, J. L. Photo-Induced Proton-Coupled Electron Transfer Reactions of Acridine Orange: Comprehensive Spectral and Kinetics Analysis. *J. Am. Chem. Soc.* **2014**, *136*, 12221–12224.

(39) Glover, S. D.; Parada, G. A.; Markle, T. F.; Ott, S.; Hammarstrom, L. Isolating the Effects of the Proton Tunneling Distance on Protoncoupled Electron Transfer in a Series of Homologous Tyrosine-Base Model Compounds. *J. Am. Chem. Soc.* **2017**, *139* (5), 2090–2101.

(40) Iordanova, N.; Hammes-Schiffer, S. Theoretical Investigation of Large Kinetic Isotope Effects for Proton-Coupled Electron Transfer in Ruthenium Polypyridyl Complexes. *J. Am. Chem. Soc.* **2002**, *124* (17), 4848–4856.

(41) Edwards, S. J.; Soudackov, A. V.; Hammes-Schiffer, S. Analysis of Kinetic Isotope Effects for Proton-Coupled Electron Transfer Reactions. *J. Phys. Chem. A* **2009**, *113* (10), 2117–2126.

(42) Lebeau, E. L.; Binstead, R. A.; Meyer, T. J. Mechanistic Implications of Proton Transfer Coupled to Electron Transfer. *J. Am. Chem. Soc.* **2001**, *123* (43), 10535–10544.

(43) Bard, A. J.; Faulkner, L. R. *Electochemical Method: Fundamentals and Applications*, 2nd ed.; Harris, D., Swain, E., Robey, C., Aiello, E., Eds.; Wiley, 2000.

(44) Marcus, R. A. On the Theory of Oxidation-Reduction Reactions Involving Electron Transfer. I. *J. Chem. Phys.* **1956**, *24* (5), 966–978.

(45) Costentin, C.; Robert, M.; Savéant, J. M. Concerted Proton-Electron Transfer Reactions in Water. Are the Driving Force and Rate Constant Depending on PH When Water Acts as Proton Donor or Acceptor? *J. Am. Chem. Soc.* **2007**, *129* (18), 5870–5879.

(46) Bonin, J.; Costentin, C.; Robert, M.; Routier, M.; Savéant, J. M. Proton-Coupled Electron Transfers: PH-Dependent Driving Forces? Fundamentals and Artifacts. *J. Am. Chem. Soc.* **2013**, *135* (38), 14359–14366.

(47) Schrauben, J. N.; Cattaneo, M.; Day, T. C.; Tenderholt, A. L.; Mayer, J. M. Multiple-Site Concerted Proton-Electron Transfer Reactions of Hydrogen-Bonded Phenols Are Nonadiabatic and Well Described by Semiclassical Marcus Theory. *J. Am. Chem. Soc.* **2012**, *134* (40), 16635–16645.

(48) Savéant, J. M. Electrochemical Approach to Proton-Coupled Electron Transfers: Recent Advances. *Energy Environ. Sci.* **2012**, *5* (7), 7718–7731.

(49) Costentin, C.; Robert, M.; Savéant, J. M. Concerted Proton-Electron Transfers in the Oxidation of Phenols. *Phys. Chem. Chem. Phys.* **2010**, *12* (37), 11179–11190.

(50) Hammes-Schiffer, S. Controlling Electrons and Protons through Theory: Molecular Electrocatalysts to Nanoparticles. *Acc. Chem. Res.* **2018**, *51*, 1975–1983.

(51) Sampaio, R. N.; Troian-Gautier, L.; Meyer, G. J. A Charge-Separated State That Lives for Almost a Second at a Conductive Metal Oxide Interface. *Angew. Chemie* **2018**, *130* (47), 15616–15620.

(52) Spitler, M. T. Effect of Nanometer-Sized Surface Morphology upon Electrochemical Kinetics. *Electrochim. Acta* **2007**, *52* (6), 2294–2301.

CHAPTER 6: KINETIC EVIDENCE THAT THE SOLVENT BARRIER FOR ELECTRON TRANSFER IS ABSENT IN THE ELECTRIC DOUBLE LAYER[16]

6.1 Introduction

It has been known for over 60 years that the dielectric constant, ε, of water molecules at polarized conductive interfaces is dramatically reduced from that of bulk water, $\varepsilon = 80$. For example, several independent capacitance studies have revealed that the first layer of water at a mercury surface had an effective ε between 3 and 8.[1–3] Further studies have shown this to be general to many solid-water interfaces, including non-aqueous electrolytes, behavior attributed to restricted rotational freedom of the solvent dipole.[4–14] Classical dielectric continuum and more sophisticated levels of theory indicate that the solvent, or outer-sphere, reorganization energy, λ_o, approaches zero as ε decreases.[15–18] This is an important prediction as λ_o determines the barrier for most electron transfer reactions of interest in biology, chemistry, and catalysis.[19,20] Despite the importance of these predictions and reports of accelerated electron transfer kinetics near electrode surfaces,[21–27] experimental values of reorganization energies at solid-electrolyte interfaces remain elusive as such measurements are intrinsically difficult to conceive and perform.

Previous studies of interfacial electron transfer have predominantly relied on electrochemical investigations of thermal electron transfer reactions which occurred through

[16]This Chapter previously appeared as two papers in the *Journal of the American Chemical Society*. They are combined here. The original citations are: 1) Bangle, R.E.; Schneider, J.; Piechota, E.J.; Troian-Gautier, L.; Meyer, G.J. *J. Am. Chem. Soc.* **2020**, 142 *(2)*,674-679. 2) Bangle, R.E.; Schneider, J.; Conroy, D.T.; Aramburu-Trošelj, B.; Meyer, G.J. *J. Am. Chem. Soc.* **2020**, 142 *(35)*, 14940-14946.

self-assembled monolayers, SAMs, of long-chain thiols terminated with redox-active molecules on gold electrodes.[21–29] Unfortunately, SAMS with short-chain hydrocarbons have poor stability precluding electron transfer study at short distances. Of note, Chidsey and coworkers have shown that the total reorganization energy, λ, decreased by 30% when interfacial electron transfer occurred ~ 7 Å *versus* ~ 20 Å from a gold surface.[23] Distance-dependent interfacial electron transfer kinetics have also been attributed to interfacial ion concentrations,[24,25,30] to electronic coupling,[27] and to both electronic coupling and λ.[22,23,26] The underlying origin(s) of this SAMS behavior is difficult to experimentally disentangle, however, as both the molecular reduction potentials and the kinetics are distant dependent.[24,30]

In this Chapter, a transparent conductive oxide, tin-doped indium oxide (ITO), combined the advantages of previous electrochemical experiments with the ultrafast timescales accessible by pulsed laser techniques. Transparent conductive oxides are an important class of materials for optoelectronic applications that are utilized here as a powerful analytical tool.[31–33] Through sensitizing mesoporous ITO films with redox-active molecules, pulsed-light-initiated interfacial electron transfer reactions were monitored spectroscopically as a function of the thermodynamic driving force, $-\Delta G°$. The position of the molecules relative to ITO in either acidic aqueous or $LiClO_4$ CH_3CN electrolyte was controlled on an Angstrom scale by layered molecular spacers. Kinetic analysis showed λ to be *near zero* proximate to the electrode surface irrespective of solvent, significantly decreased from λ quantified at larger molecule-electrode distances. This diminished electron transfer barrier was reflected in rapid electron transfer at the ITO surface. Similarly, enhanced electron transfer kinetics were observed with close surface proximity for

intermolecular self-exchange that occurred parallel to a semiconducting TiO_2 surface in aqueous electrolyte. The generality and implications of this finding are discussed.

6.2 Experimental

6.2.1 Materials

All materials were used as received without further purification. Perchloric acid (70%, Sigma-Aldrich), $LiClO_4$ (99.999 %, trace metal basis), zirconyl chloride octahydrate (reagent grade, 98%), methylene diphosphonic acid, titanium(IV) isopropoxide (97%), hydroxypropyl cellulose (average M_W = 80,000, 20 mesh particle size), and polyethyleneglycol Bisphenol A Epichlorohydrin Copolymer (carbowax, 15,000-20,000 Da) were obtained from Sigma-Aldrich. Ethanol (99.5+ %) was obtained from Acros Organics. Acetonitrile was purchased from Brudick and Jackson (Honeywell). In_2O_3:Sn (ITO) nanoparticles (TC8 DE; 20 wt% dispersion in ethanol) were purchased from Evonik. Fluorine-doped tin oxide (FTO) glass substrates (15 Ω/sq) were obtained from Hartford Glass. RuP, $[Ru^{II}(bpy)_2(4,4'\text{-}(PO_3H_2)_2\text{-}bpy)]^{2+}$, where bpy is 2,2'-bipyridine, and TPA, 4-[N,N-di(*p*-tolyl)amino]benzylphosphonic acid, were synthesized as previously reported.[34]

6.2.2 Mesoporous Film Preparation

The In_2O_3:Sn (ITO) sol-gel pastes were generated by combination of colloidal suspensions of ITO nanoparticles (~ 15 nm diameter) in ethanol (20 wt%) with hydroxypropyl cellulose (10 wt%).[31] TiO_2 sol-gel pastes were generated by the combination of carbowax with TiO_2 nanoparticles (15 nm diameter) synthesized by acid digestion of titanium(IV) isopropoxide, as described previously.[34,35] Metal oxide pastes were doctor-bladed onto FTO-coated conductive glass, dried in air for ~ 30 min, and annealed in a tube

furnace at 450 °C under O_2 flow for 30 min. Films generated in this way were measured to be 3-4 μm by a Bruker DektatXT profilometer.

Films were sensitized with layer-by-layer bridge units and redox-active molecules RuP and/or TPA. Films termed ITO|-$(X)_n$-TPA were first sensitized to 50% saturation surface coverage with RuP by reaction of ITO films with 0.1 M $HClO_4$ aqueous solutions of RuP. Surface coverages were controlled through reaction time. Molecular bridge units were assembled by subsequent reactions of films with 0.1 M $HClO_4$ aqueous solutions of 5 mM methylene diphosphonic acid (overnight) then 6 mM $ZrOCl_2$•8 H_2O (2 hours). Multiple bridge units were assembled by repeating the process. Assemblies were terminated by either RuP or TPA by overnight reaction with acidic aqueous or ethanol solutions, respectively.

6.2.3 Mesoporous Film Characterization

ITO and TiO_2 nanoparticles scraped from films were visualized with tunneling electron microscopy (TEM) using a JEOL 2010F FasTEM with a Zirconated tungsten field emission tip and a 2K X 2K Gatan CCD bottom mount camera. UV-vis spectra were obtained with an Agilent Cary 60 UV-Vis spectrometer. Molecular surface coverages, Γ, of RuP and TPA were determined by UV-visible absorbance spectroscopy using a modified Beer-Lambert law, $A = \varepsilon \times \Gamma \times 1000$, where A is the absorbance and ε is the molecular extinction coefficient at a given wavelength. For TPA, surface coverage measurements were obtained after fully oxidizing the TPA in a standard three-electrode cell. Surface coverages are given in Table 6.1.

Table 6.1. Saturated Molecular Surface Coverages, Γ

	RuP Γ (x 10^{-8} mol/cm^3)	TPA Γ (x 10^{-8} mol/cm^3)
ITO|-$(X)_n$-RuP	1.0	-
ITO|-$(X)_n$-TPA	0.5	0.7
TiO_2|-$(X)_n$-RuP	7.0	-
TiO_2|-$(X)_n$-TPA	-	7.0

6.2.4 Quantifying Electron Transfer Distances

Electron transfer distances were estimated from density functional theory (DFT) models of $Ru^{III}P$, TPA^+, and methylene diphosphonic acid shown in Fig. 6.1. Reported *R* values in Table 6.2 represent the distance between the redox centers, Ru for $Ru^{III}P$ and N for TPA^+, and a plane through the O of the anchoring phosphonic acid groups. DFT calculations were completed in Gaussian 16. Molecular geometries were energetically optimized with the B3LYP functional in IEFPCM modelled water and CH_3CN, where the basis set LanL2DZ was applied to ruthenium, and 6-311g was applied to all other atoms. In layer-by-layer assemblies, the interlayer distance of Zr^{4+} flanked by to phosphonate groups has been previously experimentally determined to be ~ 7 Å.[36,37]

6.2.5 Electrochemical and Spectro-electrochemical Measurements

Electrochemical potentials were applied in a standard three-electrode cell in which the metal oxide film of a conductive FTO-glass substrate served as working electrode. Platinum mesh served as counter electrodes. Experiments are performed in either Ar-sparged aqueous 0.1 M $HClO_4$ or 0.1 M $LiClO_4$ CH_3CN, and all potential values are reported *versus* the Normal Hydrogen Electrode (NHE). In aqueous electrolytes, Ag/AgCl reference electrodes were employed, while in CH_3CN electrolytes a silver wire in 0.1 M $LiClO_4$ CH_3CN solution served as a pseudo-reference calibrated versus the ferrocene/ferrocenium reduction potential

measured in 0.1 M *tert*-butyl ammonium perchlorate CH_3CN ($Fc^{+/0}$ $E_{1/2}$ = 630 mV vs NHE). Cyclic voltammetry measurements were performed with a Pine Research Instruments WaveNow Potentiostat controlled by Aftermath software (PRI). For spectro-electrochemistry, this potentiostatic control was coupled with UV-visible absorption spectroscopy measured with an Avantes AvaLight DHc light source and an Avantes StarLine AvaSpec-2048 spectrometer. Formal redox potentials $E°'$ for ITO|-$(X)_n$-$Ru^{III/II}P$ and ITO|-$(X)_n$-$TPA^{+/0}$ were quantified from spectroelectrochemistry by modeling the spectra as a function of applied potential as a sum of the ITO|-$(X)_n$-$Ru^{II}P$ and ITO|-$(X)_n$-$Ru^{III}P$ (or ITO|-$(X)_n$-TPA^0 and ITO|-$(X)_n$-TPA^+) spectra, optimized through linear least squares regression to determine the mole fraction of each species χ. Values of χ as a function of applied potential were fit with Eq. 6.1, where E_{app} is the applied potential and α is non-ideality factor often employed in electrochemistry on mesoporous films.[38]

$$\chi = \frac{1}{1+10^{(E_{app}-E°')/(59.2\alpha)}} \tag{6.1}$$

6.2.6 Transient Absorption Spectroscopy Measurements

Transient absorption spectroscopy was performed with a previously described apparatus.[39] Pulsed light excitation was performed with a Q-switched, pulsed Nd:YAG laser (Quantel U.S.A, Brilliant B, 5-6 ns FWHM) doubled to 532 nm. Laser fluences at the sample were 1-8 mJ/pulse, adjusted to generate the same initial signal amplitude for each sample, at 1 Hz. Signal was probed by a 150 W xenon arc lamp (Applied Photophysics) aligned perpendicular to the pulse beam. The probe lamp was pulsed at 1 Hz with 70 V when measuring on time scales < 100 μs. Signal was detected using a SPEX 1702/04 monochromator optically coupled to a Hamamatsu R928 photomultiplier tube connected LeCroy 9450, Dual 330 MHz digital oscilloscope. In total, the instrument response time was

~ 10 ns. Single wavelength kinetic measurements were generated by averaging the results of at least 90 laser pulses. Transient spectra were generated by combining single wavelength measurements taken approximately every 10 nm over the relevant spectral range. ITO photoelectrodes within standard three-electrode cells as described above were submerged in either Ar-sparged aqueous 0.1 M $HClO_4$ or 0.1 M $LiClO_4$ CH_3CN in a glass cuvette.

Electron transfer kinetics in ITO|-$(X)_n$-RuP and ITO|-$(X)_n$-TPA between injected electrons and oxidized molecules was non-exponential. Electron transfer rate constants k_{IET} were quantified as the inverse of the time required for the initial signal to decay by half. Reorganization energies extracted from kinetic data were insensitive to whether k_{IET} was quantified as the inverse of the time for signal to decay to ½ of the initial or 1/e of the initial signal. Reported uncertainties in kinetic values and reorganization energies represent the standard deviation between at least three independent measurements.

6.2.7 Chronoabsorptometry Measurements

TiO_2 photoelectrodes served as working electrodes in standard three-electrodes cells submerged in Ar-sparged aqueous 0.1 M $HClO_4$ in a glass cuvette as described above. Chronoabsorptometry measurements were obtained using a Pine Research Instruments WaveNow Potentiostat controlled by Aftermath software (PRI), an Avantes AvaLight DHc light source, and an Avantes StarLine AvaSpec-2048 spectrometer. An oxidizing potential was applied to the film and held for several minutes, and the UV-visible absorption spectrum was monitored as a function of time. For TiO_2|-$(X)_n$-RuP, the applied potential, E_{app}, was 0.5 V more positive than the formal reduction potential, $E°'$, of RuP, $E_{app} = E°'(Ru^{III/II}) + 0.5$ V. Oxidative instability of TPA prevented application of $E_{app} = E°'(TPA^{+/0}) + 0.5$ V for the time required to oxidize the entire film. Instead, $E_{app} = E°'(TPA^{+/0}) + 0.15$ V was applied. The rate

of oxidation of the TPA under these conditions was within error the same as the rate of reduction observed when $E_{app} = E°'(TPA^{+/0}) - 0.5$ V was applied to the oxidized films.

Electron diffusion coefficients, D, and self-exchange electron transfer rate constants, k_{SE} were quantified from chronoabsorptometry measurements. To quantify D spectral changes at a characteristic wavelength (460 nm for TiO_2|-$(X)_n$-RuP and 690 nm for TiO_2|-$(X)_n$-TPA) were fit with a variation of the Anson equation given in Eq. 6.2.[40,41]

$$\Delta A = \frac{2\Delta A_f D^{1/2} t^{1/2}}{d\pi^{1/2}} \tag{6.2}$$

In this equation, ΔA is the absorbance change at the specified wavelength, ΔA_f is the total change in absorbance upon fully oxidizing the film, and d is the TiO_2 film thickness in cm measured by profilometry. Values of k_{SE} were calculated from D using Eq. 6.3, where M is the intermolecular spacing between redox-active molecules in cm determined with Eq. 6.4.[40,41]

$$k_{SE} = \frac{4D}{M^2} \tag{6.3}$$

$$M = c_0^{-1/3} \tag{6.4}$$

Here, c_0 is the volume concentration of redox-active molecules, molecules per cm^3, calculated with Eq. 6.5 where N is Avogadro's number and the surface coverage Γ is determined from UV-visible absorption spectroscopy as described above.

$$c_0 = \frac{\Gamma \times N}{d \times \cos 45°} \tag{6.5}$$

Note that this M determination, which results in $M \sim 2$ nm, makes the simplifying assumption that redox-active molecules are evenly distributed through the entire volume of the mesoporous TiO_2 film.

6.3 Results

Mesoporous thin films of ITO nanocrystals were utilized to provide the surface area required for spectroscopic characterization in a transmission mode (Fig. 6.8 in the Associated Content section).[31,42] A pulsed laser excites the ruthenium complex RuP, $[Ru^{II}(bpy)_2(4,4'\text{-}(PO_3H_2)_2\text{-}bpy)]^{2+}$, where bpy is 2,2′-bipyridine, tethered to ITO and immersed in either 0.1 M $HClO_4$ aqueous or 0.1 M $LiClO_4$ CH_3CN solutions (Fig. 6.1). The excited state injects into the ITO,[43] and the subsequent interfacial electron transfer rate constants (k_{IET}) were measured as a function of the thermodynamic driving force ($-\Delta G°$). In some cases, the acceptor was $Ru^{III}P$, while in others it was an oxidized triphenylamine, TPA^+ (4-[N,N-di(*p*-tolyl)amino]benzylphosphonic acid) generated by lateral electron transfer to $Ru^{III}P$ (Fig. 6.1b).[44,45] These acceptors were selected as they have a negligibly small inner-sphere reorganization energy, λ_i, such that $\lambda = \lambda_i + \lambda_o \sim \lambda_o$.[46–48]

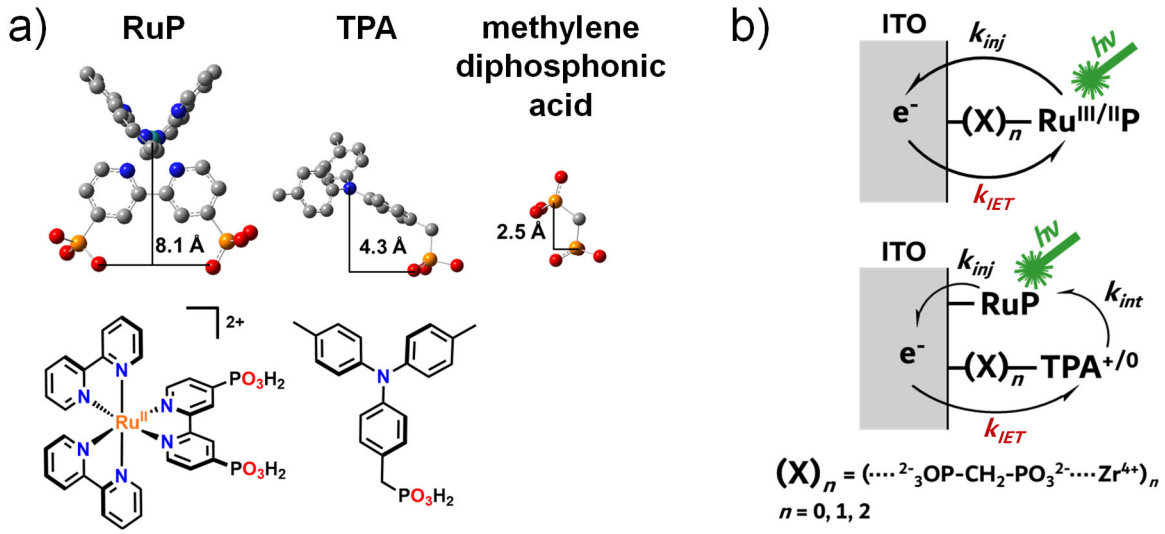

Figure 6.1. a) The molecular structure of RuP, TPA, and spacer with DFT models utilized to estimate *R*. b) Molecules and ITO electrodes where X is methylene diphosphonic acid coordinated to Zr^{4+}that served as an ionic bridge to position RuP or TPA more distance from the interface. Light excitation of RuP initiates excited state injection into ITO, k_{inj}, which is followed by lateral electron transfer, k_{lat}, from TPA if present. Charge recombination occurs through interfacial electron transfer with rate constant k_{IET}.

The redox-active groups were positioned at variable distances from the polarized electrode using a layer-by-layer molecular approach. Bridges comprised of a methylene carbon with two terminal phosphonate groups that underwent Lewis acid-base interactions with a Zr^{4+} cation served as a modular unit to position the redox-active molecules remote from the surface.[36,42,49–52] The bridge unit is represented in Fig. 6.1 as $(X)_n$, where '*n*' is the number of units, to produce the nomenclature ITO|-$(X)_n$-Acceptor. In most cases, the acceptors were reacted with the electrode to reach saturation surface coverage, ~ 1 x 10^{-8} mol/cm^2. For films termed ITO|-$(X)_n$-TPA, electrodes were sensitized to ~50% saturation surface coverage with RuP prior to co-anchoring layer-by-layer assemblies of TPA to saturation. Molecular surface coverages measured by UV-visible absorption are given in Table 6.1. The molecular length scale was estimated by density functional theory (Fig. 6.1a) as described in the Experimental section above. Note that the sp^3-hybridized carbon atom in the TPA positions the nitrogen center only ~ 4.3 Å from the surface.

These molecule-functionalized conductive oxide photo-electrodes differ significantly from previously reported SAMs.[21–23] The SAMs form a hydrophobic organic layer between the gold surface and a redox-active group, where the length of the hydrocarbon chain is known.[23,53] The interfaces interrogated here are more polar, with charged ionic bridges. Further, the gold electrodes of previous studies were generally planar, while spherical ITO nanocrystals (~ 15 nm in diameter, Fig. 6.8 in the Associated Content section) interconnected in a mesoporous thin film were utilized here.[54] The layer-by-layer strategy provides a systematic and well-documented means to control distance between a redox-active molecule and an oxide surface on an Angstrom length scale.[36,49]

Figure 6.2a and 6.9 in the Associated Content section show the visible absorbance spectra of ITO|-(X)$_n$-RuP, ITO|-(X)$_0$-TPA, and unsensitized ITO. The absorbance centered at 460 nm was assigned to the RuP metal-to-ligand charge transfer (MLCT) transitions that were minimally sensitive to n. The neutral TPA did not absorb visible light.[55] The surface-functionalized photo-electrodes were utilized as working electrodes in standard three-electrode cells in either aqueous pH 1 $HClO_4$ or 0.1 M $LiClO_4$ CH_3CN (Fig. 6.2b). Pulsed green light excitation resulted in excited state injection into the ITO, and the subsequent electron transfer from the electrode to the oxidized molecule was monitored spectroscopically.[39] Within the instrument response time, excited state injection and lateral electron transfer from TPA (when present) occurred, i.e. k_{inj} and $k_{lat} > (10\ ns)^{-1}$. Hence, the transient spectra measured at the earliest times were consistent with formation of an injected electron in ITO and $Ru^{III}P$ (or TPA^+) (Figs. 6.2c and 6.9-6.10 in the Associated Content section). Absorbance spectra obtained before and after kinetic measurements revealed no evidence of net photochemistry. Care was taken to adjust the laser irradiance such that approximately equivalent concentrations of $Ru^{III}P$ (or TPA^+) were present at the earliest observation times under all the conditions investigated. This is illustrated by the initial amplitudes of the transient spectral change, ΔA, that are shown without normalization in Fig. 6.11 in the Associated Content section. The subsequent back electron transfer kinetics were quantified as a function of the applied potential, E_{app} (Figs. 6.3 and 6.12-6.14 in the Associated Content section).

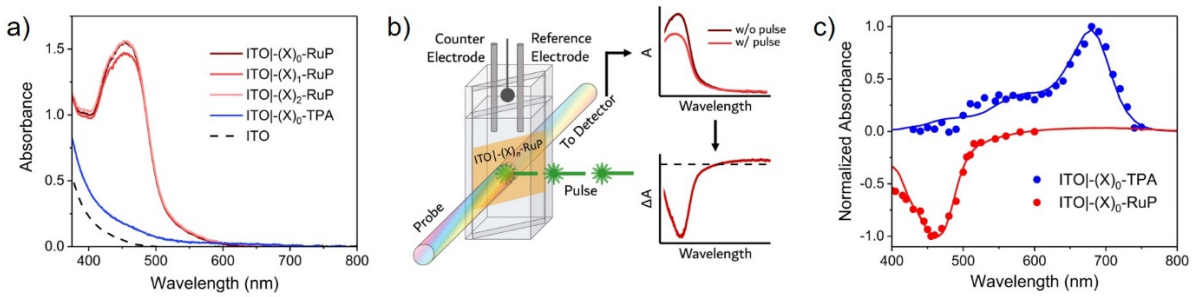

Figure 6.2. a) Visible absorbance spectra of ITO|-(X)$_n$-RuP, ITO|-(X)$_0$-TPA, and unsensitized ITO in aqueous 0.1 M $HClO_4$ solution. b) The rate constant for electron transfer k_{IET} to $Ru^{III}P$ (or TPA^+) was quantified by nanosecond transient absorption spectroscopy as a function of $-\Delta G^o$ in a standard three-electrode cell in either aqueous 0.1 M $HClO_4$ or 0.1 M $LiClO_4$ CH_3CN electrolytes. Green pulsed laser excitation perpendicular to a white light probe initiates electron transfer as evidenced by the decrease in the visible absorption, A, presented as an absorption change, ΔA. c) Transient absorption spectra of ITO|-(X)$_0$-RuP and ITO|-(X)$_0$-TPA measured 1 μs after pulsed 532 nm excitation modelled by the difference between the initial and oxidized absorption spectra (solid lines) in aqueous 0.1 M $HClO_4$.

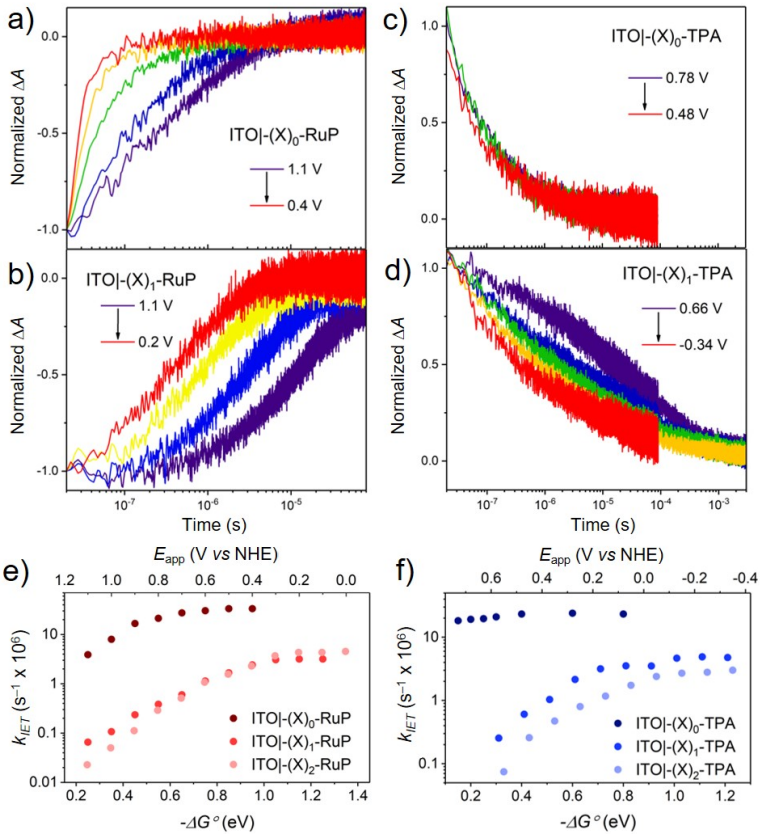

Figure 6.3. Absorption change measured after pulsed 532 nm excitation of ITO|-(X)$_n$-RuP (a-b, 402 nm) and ITO|-(X)$_n$-TPA (c-d, 690 nm) in aqueous 0.1 M $HClO_4$ as a function of the applied potential vs NHE, E_{app}. e-f) Values of k_{IET} increased with $-\Delta G°$ to a limiting value k_{max}, where $-\Delta G° = e(E°' - E_{app})$.

Due to the conductive nature of the ITO, E_{app} controlled the energetic position of the Fermi energy, E_F. This allowed experimental attunement of $-\Delta G°$, defined as $-\Delta G° = eE°' - E_F = e(E°' - E_{app})$, where $E°'$ is the formal reduction potential of the molecular acceptor determined by spectroelectrochemistry or cyclic voltammetry (Figs. 6.15 and 6.16 in the Associated Content section).[31] In aqueous 0.1 M $HClO_4$ solution, $E°'$ for ITO|-$(X)_n$-$RuP^{3+/2+}$ and ITO|-$(X)_n$-TPA were 1.35 V and 0.88 V vs NHE, respectively. In 0.1 M $LiClO_4$ CH_3CN, $E°'$ values were shifted positively: 1.54 V vs NHE for ITO|-$(X)_n$-RuP, and 1.05 V vs NHE for ITO|-$(X)_n$-TPA. Surprisingly, $E°'$ values were insensitive to n, in contrast to observed distance dependence of $E°'$ for redox-active molecules anchored to gold electrodes through SAMs.[24]

As is commonly reported at metal oxide interfaces, the recombination kinetics were non-exponential, and the inverse of the time required for ½ of the initial charged separated states to recombine was taken as a surrogate for the true rate constant, k_{IET}.[56] Equivalent trends in k_{IET} with $-\Delta G°$ were obtained when the inverse of the time required for the number of charge separated states to reach 1/e of the initial amount was used. The kinetic data in Figs. 6.3 and 6.12-14 in the Associated Content section showed that as increasingly negative E_{app} made $-\Delta G°$ more favorable, k_{IET} increased up to a limiting value called k_{max}, given in Table 6.2. Furthermore, charge recombination was most rapid for the acceptors positioned nearest the ITO surface.

Table 6.2. Interfacial Electron Transfer Kinetic Parameters

	R (Å)	0.1 M $HClO_4$ H_2O			0.1 M $LiClO_4$ CH_3CN		
		λ (eV)	k_{max} (s^{-1} x 10^6)	H_{ab}[17] (cm^{-1})	λ (eV)	k_{max} (s^{-1} x 10^6)	H_{ab}[17] (cm^{-1})
ITO|-$(X)_0$-TPA	4.3	0.12 ± 0.04	27	0.6	0.11 ± 0.04	22	0.6
ITO|-$(X)_1$-TPA	15	0.63 ± 0.03	4.8	0.3	0.62 ± 0.03	6.5	0.3
ITO|-$(X)_2$-TPA	24	0.77 ± 0.02	3.0	0.2	0.9 ± 0.1	4.2	0.2
ITO|-$(X)_0$-RuP	8.1	0.53 ± 0.06	33	0.7	0.57 ± 0.02	11	0.4
ITO|-$(X)_1$-RuP	17	0.84 ± 0.03	3.2	0.2	0.85 ± 0.03	2.7	0.2
ITO|-$(X)_2$-RuP	26	0.90 ± 0.04	4.5	0.3	0.94 ± 0.06	2.3	0.2

The kinetic rate constants were analyzed with Marcus-Gerischer theory for interfacial electron transfer, the essential aspects of which are defined in Fig. 6.4. Vital to this model is the energetic overlap between the electronic states in an electrode and a molecule. This model is applicable to both molecular oxidation and reduction by an electrode, but reduction will be elucidated here as an example. Within the Marcus-Gerischer framework, electron transfer can occur between an occupied state in an electrode and an equivalent-energy unoccupied molecular state. Because the metallic electrode consists of a continuum of occupied states, electron transfer reactions occur across an energetic distribution, and the overall rate constant is the integral of the rate constants across all energy E, as expressed in and Eq. 6.6.[15,31,57–59]

$$k = \frac{2\pi}{\hbar}\int_{-\infty}^{\infty} \rho(E) f(E, E_{\mathrm{F}}) |H_{\mathrm{ab}}(E)|^2 W(E) dE \qquad (6.6)$$

[17]Values calculated from k_{max} from ITO electronic densities of states determined in ref. 31 and assuming 1 surface atom involved.

Here, $\rho(E)$ is the density of electronic states in ITO, $f(E,E_F)$ is the Fermi-Dirac distribution, $H_{ab}(E)$ is the molecule-electrode electronic coupling matrix element, $W(E)$ is a Gaussian distribution of activation barriers, k_B is the Boltzmann constant, and $\hbar$ is the reduced Planck constant. Both $\rho(E)$ and $H_{ab}(E)$ are assumed to be independent of E_{app}. In Fig. 6.4, the distribution of activation barriers for electron transfer to a molecular acceptor (Eq. 6.7) is shown relative to the molecular formal reduction potential $E°'$.

$$W(E) = \frac{1}{\sqrt{4\pi\lambda k_B T}} \exp\left(\frac{-(\Delta G° + \lambda)^2}{4\lambda k_B T}\right) \quad (6.7)$$

The width of the distribution is defined by the total reorganization energy, λ. The potential applied to the electrode tunes $-\Delta G°$, and more favorable $-\Delta G°$ leads to increased electron transfer rate constants, k_{IET}. At sufficiently exergonic potentials, k_{IET} reaches a limiting value, k_{max}, which reports on H_{ab} (Eq 6.8).

$$k_{max} = \frac{2\pi}{\hbar} {H_{ab}}^2 \rho \quad (6.8)$$

The metallic nature of the ITO electrodes allowed for direct tuning of $\Delta G°$ by an externally applied potential, E_{app}. The Fermi energy E_F is directly defined by E_{app} such that $-\Delta G° = eE°' - E_F = e(E°' - E_{app})$. Quantification of the change in k_{IET} with $-\Delta G°$ allows evaluation of $W(E)$ and determination of λ, *i.e.* when λ is small, k increases over a narrow $-\Delta G°$ range before reaching k_{max}. Through the assumptions that $\rho(E)$ and $H_{ab}(E)$ are independent of energy and that $f(E,E_F)$ is in the low-temperature limit, substitution of Eq. 6.8 into Eq. 6.6 produces Eq. 6.9, a convenient form for extracting λ from kinetic data, as used in Fig. 6.4b-c and 6.17 in the Associated Content section.

$$\frac{k_{IET}}{k_{max}} = \frac{1}{2}\left[1 - \mathrm{erf}\left(\frac{\Delta G° + \lambda}{2\sqrt{\lambda k_B T}}\right)\right] \quad (6.9)$$

The continuum of states in the conductor results in quantitatively different behavior than that observed for molecular donor-acceptor complexes where inverted kinetic behavior is expected for sufficiently exergonic reactions.[15,60,61] The reorganization energy λ corresponds to $-\Delta G°$ at $\frac{1}{2}k_{max}$, as shown by the dashed lines in Figs. 6.4b-c and 6.17. The λ values extracted in this way were within experimental error insensitive to 0.1, 0.2 or 0.5 M $HClO_4$ ionic strength. For RuP in aqueous 0.1 M $HClO_4$, equal λ values were obtained when electrodes were sensitized to 10% and 100% full saturation surface coverage.

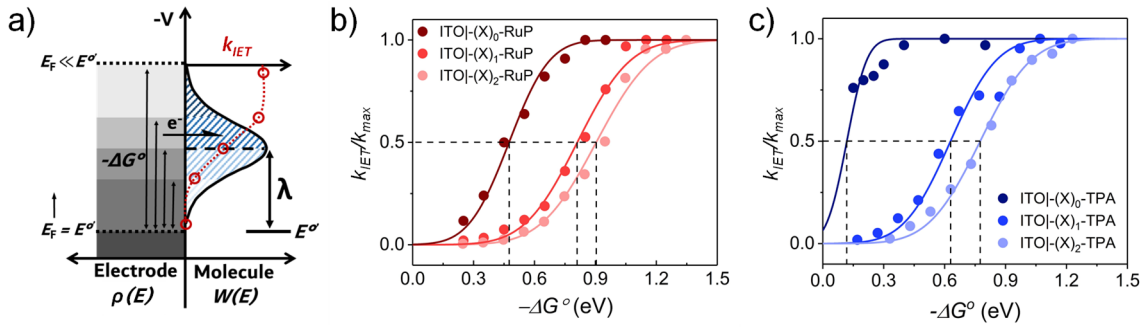

Figure 6.4. a) Illustration of the key principles of Marcus-Gerischer theory. A Gaussian distribution of activation energies, *W(E)*, for electron transfer from electrode states, *ρ(E)*, to a molecule exists with a maximum at $E^{o\prime} - \lambda/e$, where $E^{o\prime}$ is the formal reduction potential, *e* is the number of electrons transferred, and λ is the total reorganization energy. The red dashes and circles represent the expected kinetic behavior when a significant barrier is present; k_{IET} increases to a saturation value at exergonic potentials, k_{max}. b-c) Values of k_{IET} measured in aqueous 0.1 M $HClO_4$ were normalized by k_{max} and fit with Eq. 6.9, represented by solid lines. Dashed lines represent λ values, which are quantified as $-\Delta G°$ when $k_{IET}/k_{max} = 1/2$.

Values of λ exhibited a systematic dependence on the electrode-molecule distance *R*, Fig. 6.5 and Table 6.2, in both aqueous 0.1 M $HClO_4$ and 0.1 M $LiClO_4$ CH_3CN. Values of *R* were estimated as the distance between the redox centers, Ru^{III} for RuP and N^+ for TPA, and a plane through O atoms of the phosphonic acid binding groups using molecular lengths estimated from DFT models shown in Fig. 6.1. In layer-by-layer assemblies, the interlayer distance of Zr^{4+} flanked by two phosphonate groups has been previously reported to be ~ 7 Å.[36,37] At distances greater than 15 Å, $\lambda \approx 0.9$ eV in both aqueous 0.1 M $HClO_4$ and 0.1 M

$LiClO_4$ CH_3CN was approximately equal to the value previously determined for similar molecular donor-acceptor systems in fluid solution.[60] Acceptors positioned more proximate to the electrode showed progressively decreased λ values, such that at less than 5 Å, $\lambda = 0.12$ eV in aqueous 0.1 M $HClO_4$ and $\lambda = 0.11$ eV in 0.1M $LiClO_4$ CH_3CN. These molecules have small inner-sphere reorganization energies, $\lambda_i \sim 0.1$ eV, indicating that the outer-sphere reorganization is negligibly small, i.e., $\lambda_o \sim 0$.[24, 25] This drastically reduced value of λ signifies that the barriers for electron transfer, $\Delta G^{\ddagger} = \lambda/4$ when $\Delta G° = 0$, do indeed approach zero near the polarized interface as predicted theoretically.

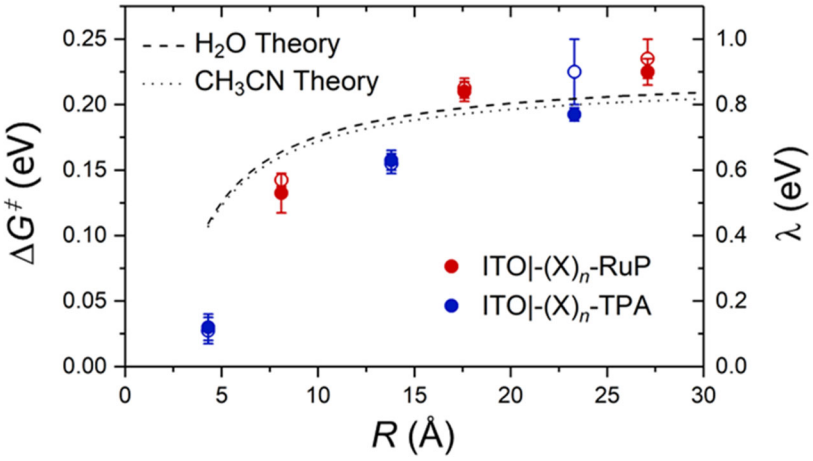

Figure 6.5. The electron transfer barrier, $\Delta G^{\ddagger}$, and λ as a function of the electrode-molecule distance, R in aqueous 0.1 M $HClO_4$ (closed circles) and 0.1 M $LiClO_3$ CH_3CN (open circles). The dashed line represents $\Delta G^{\ddagger}$ and λ values predicted by dielectric continuum theory, Eq. 6.10, assuming $\varepsilon_{st} = 80$ for H_2O and $\varepsilon_{st} = 37.5$ for CH_3CN across all R. The poor fit to experimental data at small R is consistent with a decreased ε_{st} within the electric double and diffuse layers.

Marcus-Gerischer analysis also provides an estimate of the electronic coupling between the electrode and the molecule, H_{ab}. The free energy dependence of the rate constants provides λ, while the saturation rate constant, k_{max}, provides H_{ab}, Eq. 6.8.[31] The kinetic data in Fig. 6.3 and 6.14 in the Associated Content section reveal that H_{ab} decreases as the molecule-electrode separation increases in both aqueous 0.1 M $HClO_4$ and 0.1 M

$LiClO_4$ CH_3CN. Values of H_{ab} decreased exponentially with a decay parameter $\beta \approx 0.2$ Å^{-1}. This unexpectedly small β value indicates weak distance dependence of k_{mac}, consistent with electron transfer through a conductive medium.[25,62–65] Precise determination of H_{ab}, however, requires knowledge of the effective density of states in the electrode and the number of participating surface atoms, both of which are non-trivial. Best estimates of the ITO density of states assuming one surface-atom donor provide small H_{ab} values, < 1 cm^{-1} given in Table 6.2.[31] Such small coupling is consistent with non-adiabatic electron transfer.[19,21,66,67] As shown in Figs. 6.2 and 6.9-6.10 in the Associated Content section, spectral evidence for strong coupling was absent, and the absorption spectra of RuP and TPA^+ were insensitive to their position within the electric double layer. This was further suggestive of small H_{ab} and non-adiabatic electron transfer.[21]

To test generality and understand electron transfer barriers within the electric double layer that do not involve the electrode as an electron source, self-exchange reactions occurring *laterally* across a semiconducting anatase TiO_2 surface were quantified in a standard three-electrode cell in 0.1 M $HClO_4$ water (Fig. 6.6). Like that observed on ITO surfaces, the visible absorption spectra of RuP and TPA^+ were again independent of the number of ionic bridges, indicative of nearly equivalent surface coverages. As depicted in Fig. 6.6b, lateral self-exchange electron transfer was initiated by a potential step sufficient to oxidize the molecules but insufficient to access the TiO_2 valence band, as is well-documented in literature.[68–70] In this manner, electron transfer is initiated at the conductive substrate (FTO) and proceeds across the TiO_2 by lateral self-exchange electron transfer. The direct oxidation of the molecules by TiO_2 is absent because $E°'(TPA^{+/0})$ and $E°'(Ru^{III/II})$ are within the band gap. The accompanying spectral changes were monitored with time and provided

the self-exchange electron transfer rate constant, k_{SE}, as described in the Experimental section (Eqs. 6.2 and 6.3).[70] The data in Fig. 6.7 show that lateral self-exchange occurred more rapidly for molecules near the TiO_2 surface. Values of k_{SE} were approximately 8x larger for molecules directly linked to the surface, while those furthest were indistinguishable between RuP and TPA, indicative of a common outer-sphere solvent barrier to self-exchange. More rapid self-exchange for molecules linked directly to the oxide is consistent with a decreased λ, parallel to the low λ observed for interfacial electron transfer kinetics on ITO where the oxide was the electron donor.

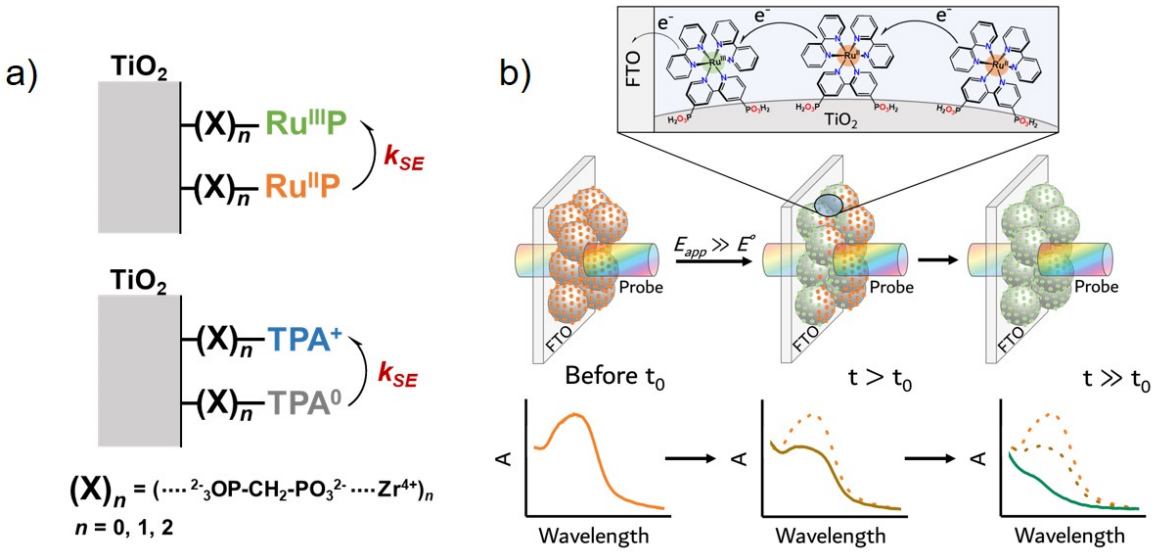

Figure 6.6. a) Scheme of lateral self-exchange electron transfer with rate constants k_{SE} in TiO_2 layer-by-layer assemblies. b) Experimental approach to monitor self-exchange, depicted in the top panel, where a potential step sufficient to oxidize the surface anchored molecules, $E_{app} \gg E^{\circ\prime}$, defines time zero, t_0. Oxidation is initiated at the conductive FTO substrate and continues across the mesoporous thin film. The sensitized TiO_2|-$(X)_n$-RuP or TiO_2|-$(X)_n$-TPA film undergoes a color change as lateral self-exchange occurs, monitored by visible absorption spectroscopy.

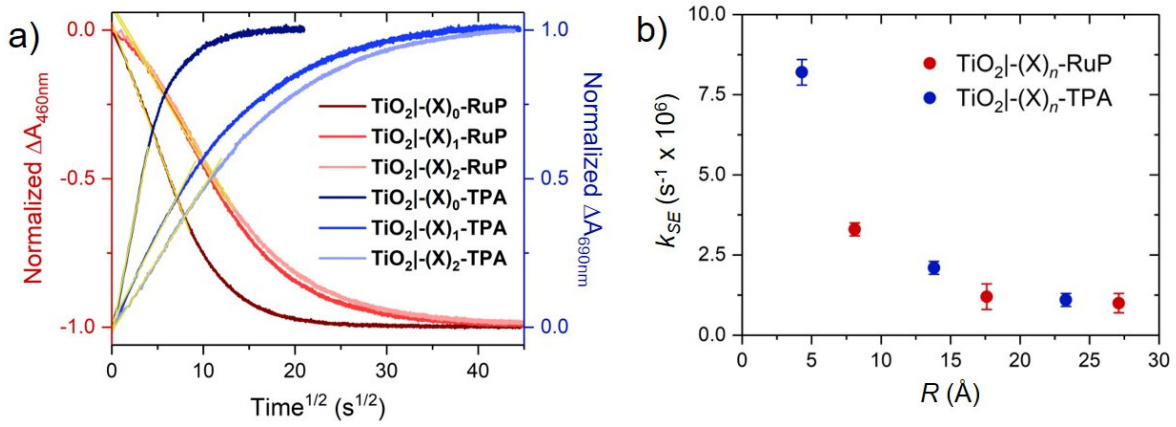

Figure 6.7. a) Absorption change, ΔA, upon application of $E_{app} \gg E^{\circ\prime}$ as a function of time at representative wavelengths for TiO_2|-(X)$_n$-RuP (460 nm, shown in red) and TiO_2|-(X)$_n$-TPA (690 nm, shown in blue) in aqueous 0.1 M $HClO_4$. Yellow lines are fits to Eq. 6.2. b) Values of k_{SE} were quantified from fits in (a) and Eq. 6.3 and plotted vs distance from the electrode, R.

6.4 Discussion

The marked decrease in λ near the polarized interfaces is attributed to the influence of the electric double layer (EDL) on the dielectric constant of water and acetonitrile. While physical descriptions of the EDL have evolved over time, most agree that a strong 10^7 V/cm electrostatic potential is present.[2,57] Solvent molecules and ions directly adsorbed to the electrode comprise the inner-Helmholtz plane, beyond which a layer of solvated ions make up the outer-Helmholtz plane. Further from the electrode is a diffuse layer, where the field is screened by intervening solvent molecules and solvated ions. When directly linked to the oxide, the oxygen atoms of the phosphonate anchoring groups are within the inner-Helmholtz plane, while the redox-active portion of the molecules are within or near the outer-Helmholtz plane. Those linked through ionic bridges probe the diffuse layer. The data reveal that λ_o is absent at the closest distances and approaches bulk solution values at distances > 15 Å.

Dielectric continuum theory predicts a link between λ_o and the interfacial electron transfer distance, R, through Eq. 6.10.[15,57]

$$\lambda_o = \frac{e^2}{4\pi\varepsilon_0}\left(\frac{1}{\varepsilon_{op}} - \frac{1}{\varepsilon_{st}}\right)\left(\frac{1}{a} - \frac{1}{2R}\right) \tag{6.10}$$

Here, ε_{op} and ε_{st} are the optical and static dielectric constants of the solvent, and a is the molecular radius. The dashed and dotted lines in Fig. 6.5 is a dielectric continuum model of λ_o and $\Delta G^{\ddagger}$ using Eq. 6.10 and ε_{st} equal to that of bulk solvent, $\varepsilon_{st} = 80$ for H_2O and $\varepsilon_{st} = 37.5$ for CH_3CN. Note that dielectric continuum theory predicts similar λ_o for these two solvents despite the factor of > 2 difference in their ε_{st}, as both H_2O and CH_3CN have large ε_{st} relative to ε_{op}.[71–73] A physically reasonable radius $a = 4.5$ Å was utilized. As is evident at a distance < 5 Å, the assumption of $\varepsilon_{st} = 80$ or 37.5 fails to predict the negligibly small barrier for electron transfer measured experimentally. To accurately model this data, $\varepsilon_{st} \approx 2$ is required in both cases, in reasonable agreement with both early and recent studies.[1–4] Indeed, the dashed and dotted lines in Fig. 6.5 which represents Eq. 6.10 using the ε_{st} of bulk solvents overestimates λ and $\Delta G^{\ddagger}$ for all distances less than ~ 15 Å. A physical picture similar to that put forward by Bockris is consistent with this data.[2] Within the Helmholtz planes (< 5 Å), the electric field greatly depresses the effective ε_{st} and rigidly orients H_2O and CH_3CN molecules, preventing their reorganization. In fact, the near identical results obtained here between H_2O and CH_3CN reflects the supposition that *any* polar solvent should have a greatly decreased ε_{st} within the Helmholtz planes.[74] In the diffuse layer solvent molecules and ions progressively screen the field. The systematic deviation between predicted and experimental λ values herein thus maps the dielectric constant in the EDL and diffuse layer, a physical picture that has long been difficult to access experimentally.

The kinetic evidence that the solvent barrier is absent in the Helmholtz planes is restricted here to molecular acceptors linked directly to a conductive oxide, with supporting evidence on a semiconducting oxide. Though it is speculative to generalize these results, a number of theoretical and experimental studies have indicated that a dramatically reduced dielectric constant is expected at many solid-electrolyte interfaces.[4,7,8,75–77] If true, the impact on practical and fundamental aspects of solar energy conversion would be tremendous and deserves brief discussion. In molecular electrocatalysis, the data here reveal that both the electronic coupling *and* the reorganization energy are most optimal within the Helmholtz planes. Hence new synthetic methodologies that integrate molecular catalysts into electrode surfaces should enhance molecular electrocatalysis turn over frequencies.[78,79] Further, a common assumption is that λ_o for a surface-anchored molecule is half that measured in fluid solution, presumably because only about half of the molecule is solvated.[57,80] The data herein show that this is a poor assumption, as λ_o is negligibly small within the Helmholtz planes. Finally, photoelectrochemical water oxidation efficiency with molecular catalysts is reported to be most optimal for catalysts far-removed from the electrode surface, where unwanted charge-recombination reactions are minimized.[42,49] Though this approach favors catalysis in kinetic competition with recombination, it fails to exploit the decreased electron transfer barrier within the Helmholtz planes. New electrode architectures with catalysts located at additional interfaces physically separated the from the electrode where reducing equivalents are located are thus expected to provide higher solar water splitting efficiency.

6.5 Conclusions

In conclusion, the rate constants for electron transfer from a conductor to molecular acceptors positioned within an aqueous and an organic electric double layer as a function of the Gibbs free energy change are reported. The absorption spectra and the reduction potentials were insensitive to position, while the electron transfer kinetics and their free energy dependencies were highly sensitive to location within the electric double layer. Application of Marcus-Gerischer theory revealed that the reorganization energy was negligibly small within the Helmholtz planes and increased to bulk values within the diffuse layer, behavior mirrored in lateral self-exchange kinetics. Hence the solvent barrier for electron transfer was absent within the Helmholtz planes. This finding is important for advancing our fundamental knowledge of interfacial electron transfer as it relates to emerging applications in biology, chemistry, and catalysis.

6.6 Acknowledgements

The authors would like to thank Dr. Mark T. Spitler, Dr. Marshall D. Newton, and Dr. Dmitry V. Matyushov for thoughtful conversations. This material is based upon work solely supported by the Alliance for Molecular PhotoElectrode Design for Solar Fuels (AMPED), an Energy Frontier Research Center (EFRC) funded by the U.S. Department of Energy, Office of Science, Office of Basic Energy Sciences under Award Number DE-SC0001011. REB acknowledges the National Science Foundation for an individual Graduate Research Fellowship under Grant No. DGE-1650116.

6.7 Associated Content

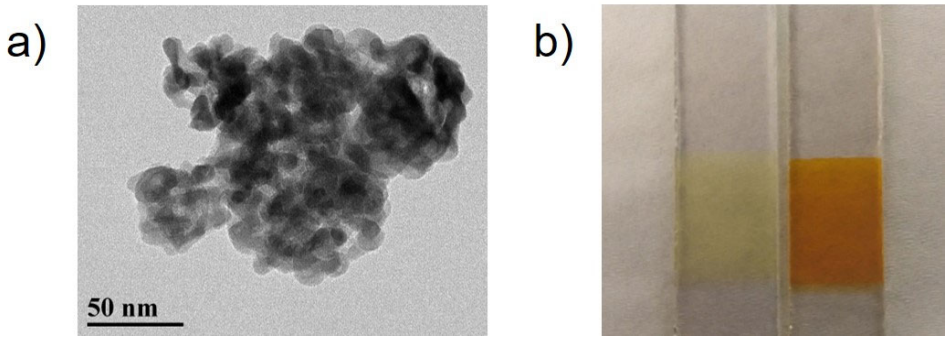

Figure 6.8. a) Transmission electron microscopy imaging of interconnected ITO nanocrystals mechanically removed from an FTO substrate. b) Photograph of unsensitized (left) and RuP-sensitized (right) ITO films illustrating transparency and coloration.

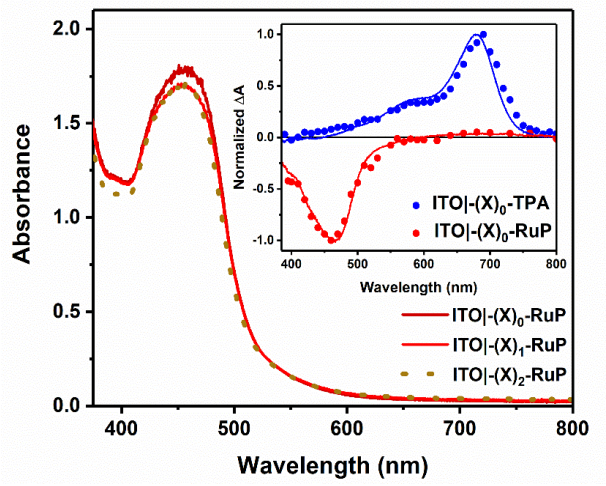

Figure 6.9. Visible absorbance spectra of ITO|-(X)$_n$-RuP in 0.1 M $LiClO_4$ CH_3CN solution. Inset: transient absorption spectra of ITO|-(X)$_0$-RuP and ITO|-(X)$_0$-TPA measured 1 μs after pulsed 532 nm excitation modelled by the difference between the initial and oxidized absorption spectra (solid lines).

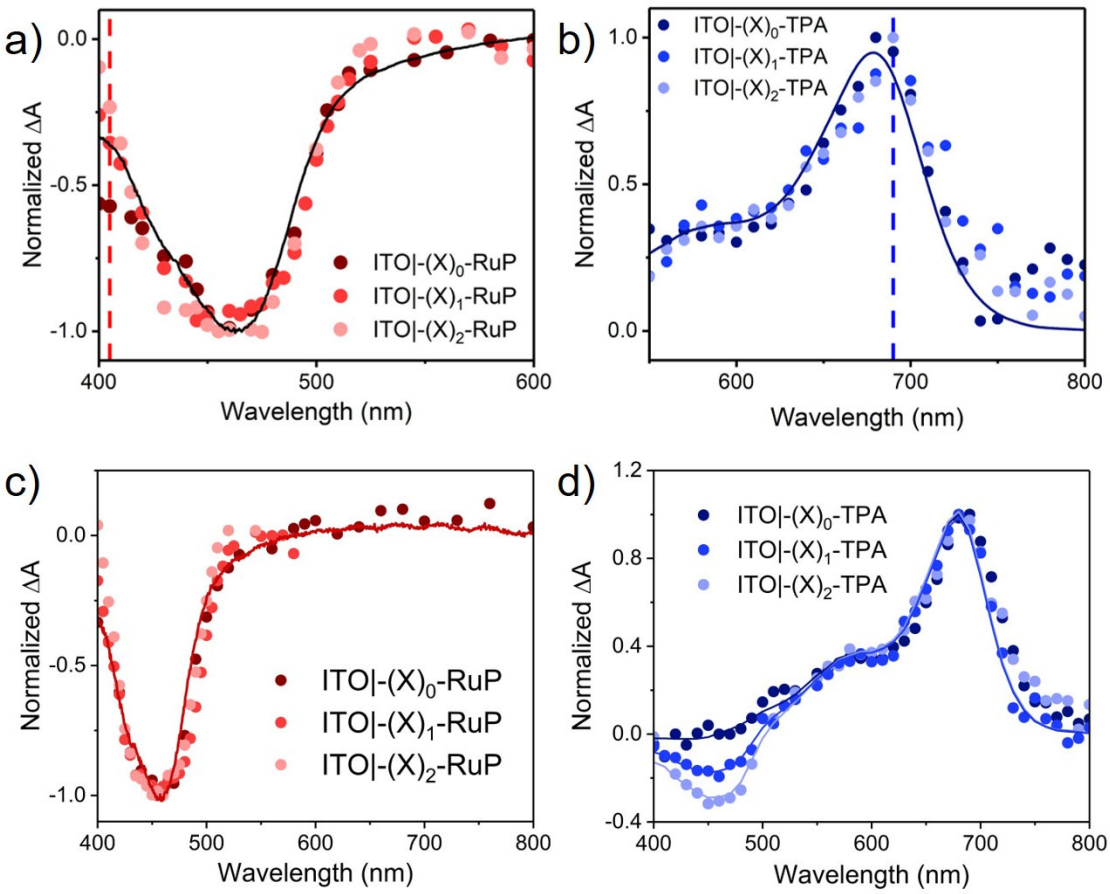

Figure 6.10. Normalized transient absorption difference spectra measured 100 ns after pulsed 532 nm light excitation (points) overlaid with spectral changes that occur upon electrochemical oxidation of a) ITO|-(X)$_n$-RuP in aqueous 0.1 M $HClO_4$, b) ITO|-(X)$_n$-TPA in aqueous 0.1 M $HClO_4$, c) ITO|-(X)$_n$-RuP in 0.1 M $LiClO_4$ CH_3CN, and d) ITO|-(X)$_n$-TPA in 0.1 M $LiClO_4$ CH_3CN.

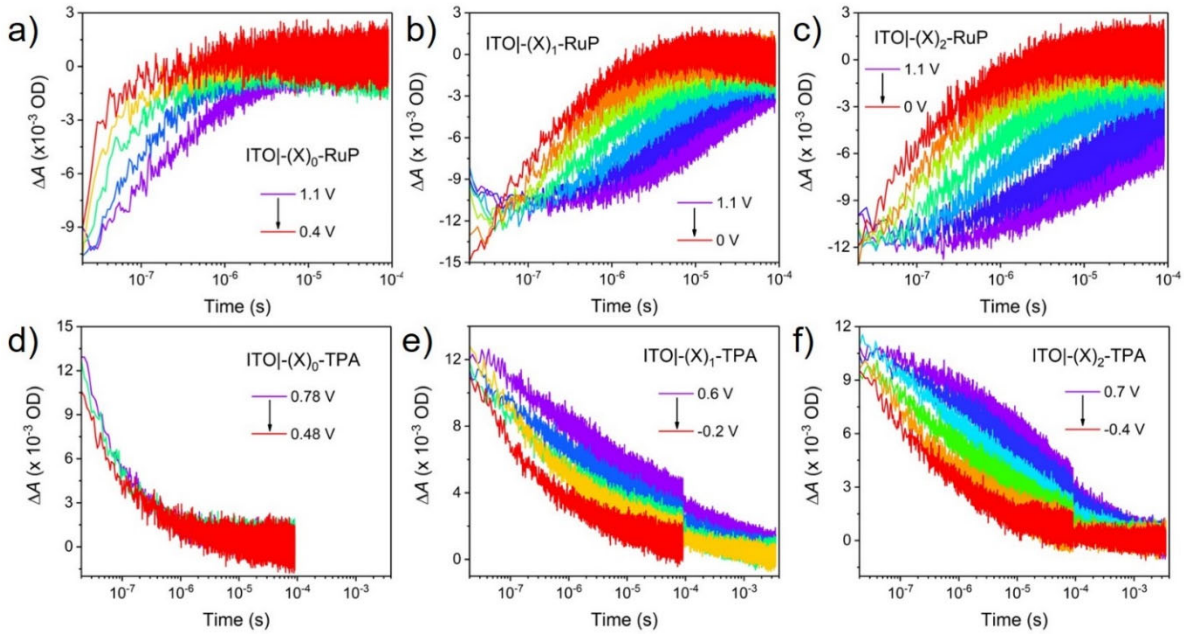

Figure 6.11. Absorption changes monitored at 402 nm (a-c) and 690 nm (d-f) upon 532 nm pulsed light excitation of (a-c) ITO|-(X)$_n$-RuP or (d-f) ITO|-(X)$_n$-TPA where n = 0, 1, or 2 as indicated in 0.1 M aqueous $HClO_4$ as a function of E_{app} vs NHE. Absorption changes are presented without normalization to illustrate that roughly equivalent initial concentrations of $Ru^{III}P$ or TPA^+ were initially present under each E_{app} and n condition. Similar results were obtained in 0.1 M $LiClO_4$ CH_3CN solution.

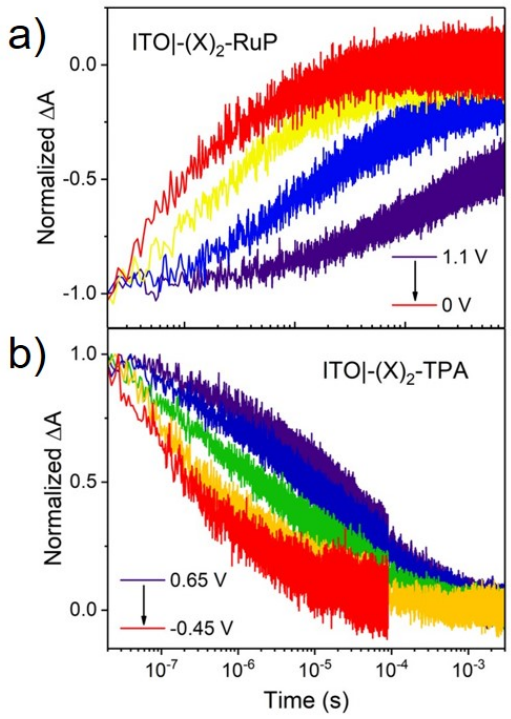

Figure 6.12. Absorption changes monitored at 402 nm (a) or 690 nm (b) following pulsed 532 nm light excitation of a) ITO|-$(X)_2$-RuP or b) ITO|-$(X)_2$-TPA in aqueous 0.1 M $HClO_4$ as a function of E_{app} vs NHE.

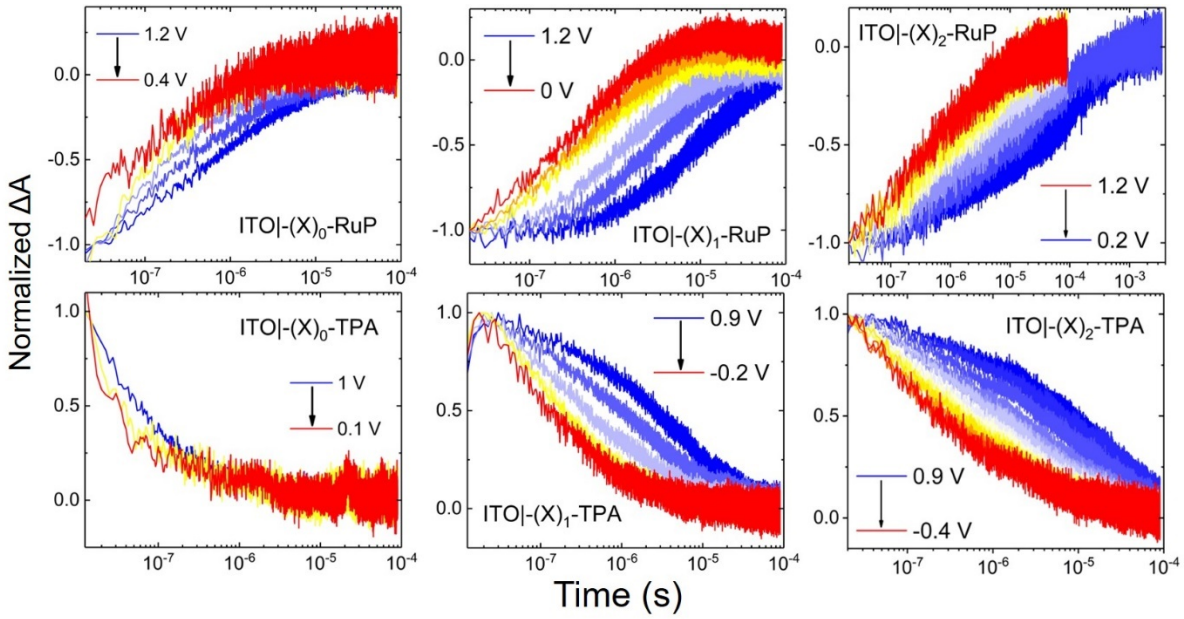

Figure 6.13. Absorption changes monitored at 402 nm (RuP) or 690 nm (TPA) following pulsed 532 nm light excitation of ITO|-$(X)_n$-RuP or ITO|-$(X)_n$-TPA as indicated in 0.1 M $LiClO_4$ CH_3CN as a function of E_{app} vs NHE over the indicated ranges.

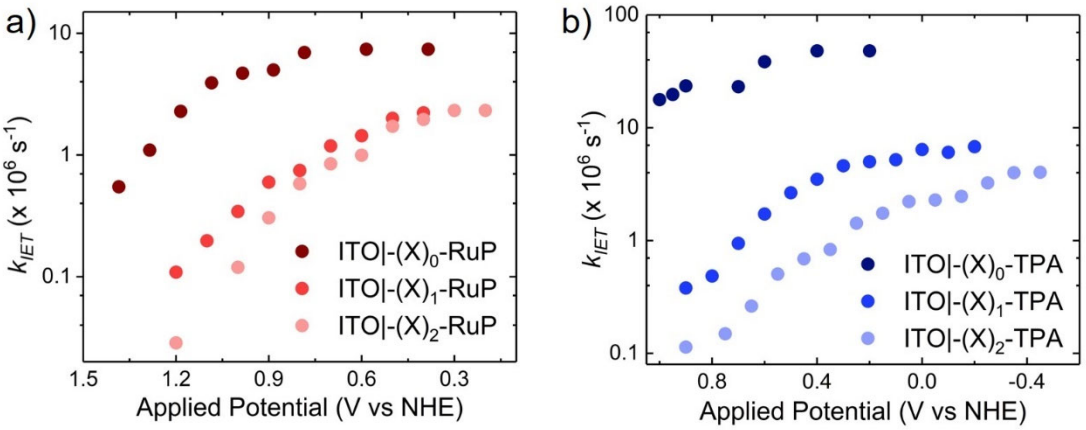

Figure 6.14. Values of k_{IET} extracted as the inverse of the time required for the initial signal to decay by half from single wavelength transient absorption spectroscopy measurements in 0.1 M $LiClO_4$ CH_3CN for a) ITO|-(X)$_n$-RuP and b) ITO|-(X)$_n$-TPA.

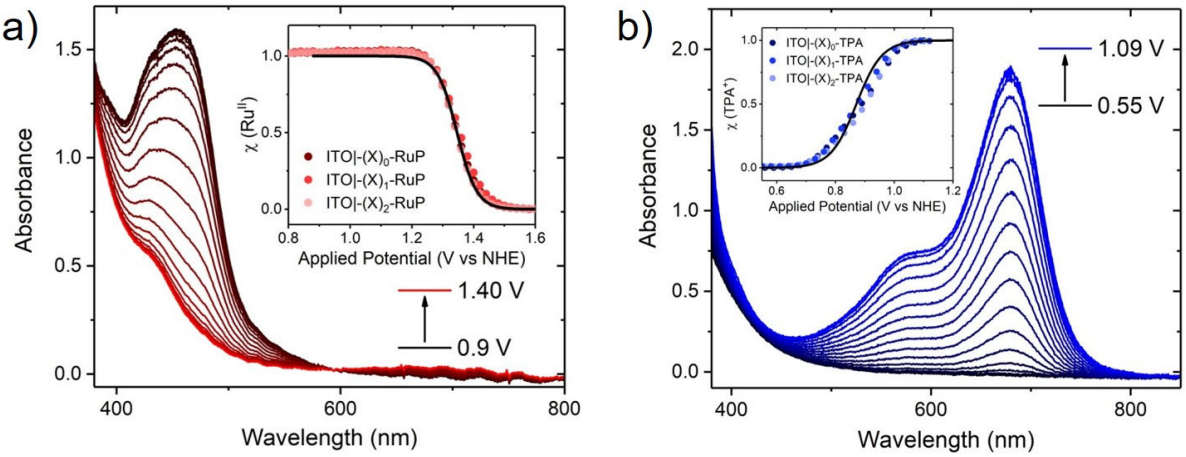

Figure 6.15. Spectroelectrochemical determination of formal reduction potentials in aqueous 0.1 M $HClO_4$. UV-visible absorption spectra in aqueous 0.1 M $HClO_4$ of a) ITO|-(X)$_0$-RuP or b) ITO|-(X)$_0$-TPA upon application of the indicated potentials. Inset is the mole fraction χ of a) $Ru^{II}P$ or b) TPA^+ as a function of applied potential with an overlaid fit to Eq. 6.1 that was utilized to determine the formal reduction potential $E^{\circ\prime}$ of the molecules.

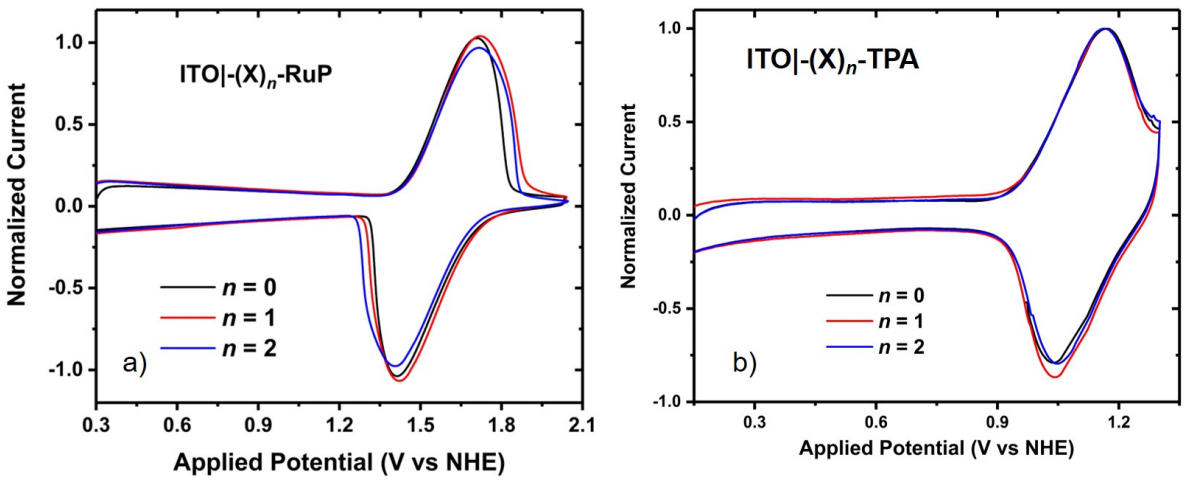

Figure 6.16. Cyclic voltammograms (scan rate 5 mV/sec) of a) ITO|-(X)$_n$-RuP ($Ru^{III/II}$) and b) ITO|-(X)$_n$-TPA ($TPA^{+/0}$) for n = 0, 1, and 2 in a three-electrode cell in 0.1 M $LiClO_4$ CH_3CN are shown. Values of $E^{o\prime}$ were taken to be the midpoint between the oxidative and reductive peaks and matched well those extracted from spectroelectrochemistry. Values of $E^{o\prime}$ were insensitive to n.

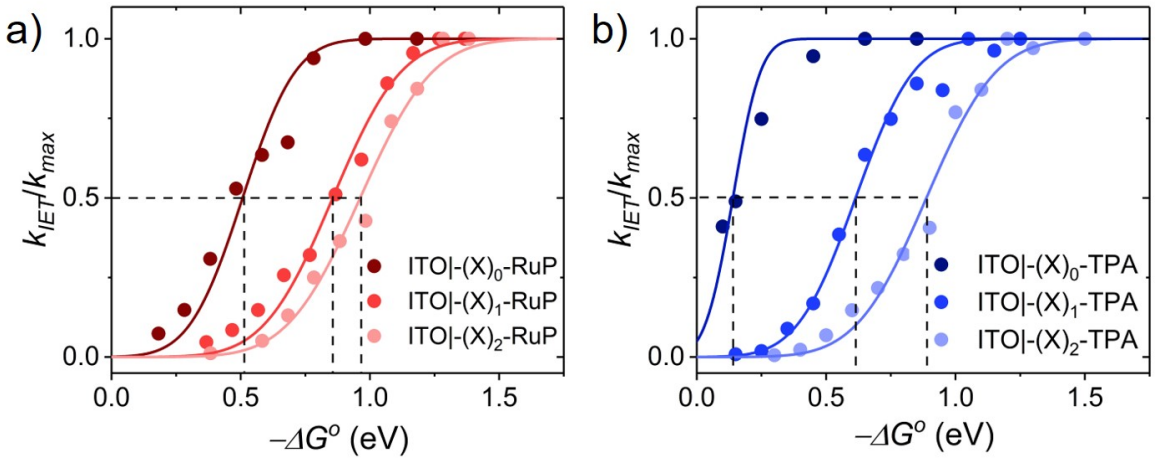

Figure 6.17. Values of k_{IET} measured in 0.1 M $LiClO_4$ CH_3CN were normalized by k_{max} and fit with Eq. 6.9, represented by solid lines. Dashed lines represent λ values, which are quantified as $-\Delta G°$ when $k_{IET}/k_{max} = 1/2$.

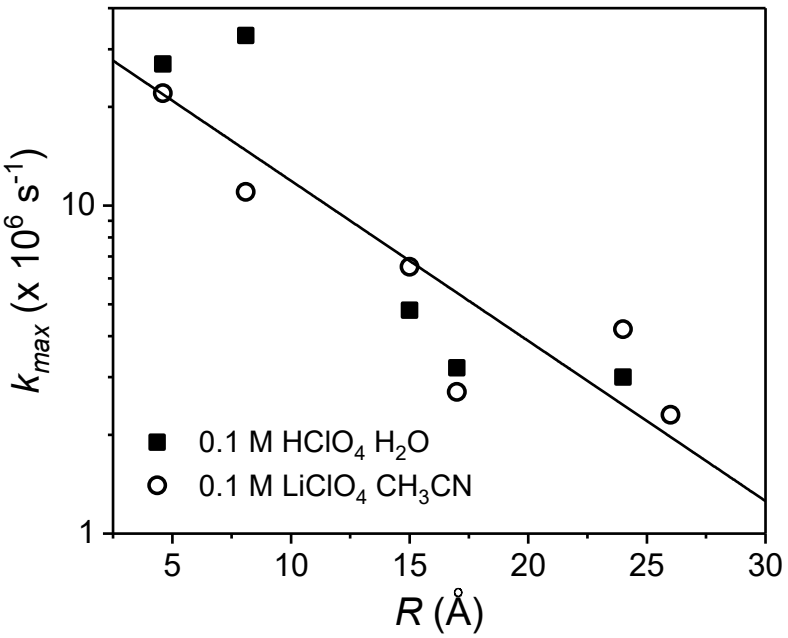

Figure 6.18. The maximum attainable rate constant (k_{max}) as a function of ET distance R for interfacial electron transfer from ITO to oxidized molecules for ITO|-$(X)_n$-RuP and ITO|-$(X)_n$-TPA in 0.1 M $LiClO_4$ CH_3CN and aqueous 0.1 M $HClO_4$ solutions. Values of k_{max} decreased exponentially as a function of R with an exponential decay parameter $\beta \approx 0.2$ Å^{-1}.

REFERENCES

(1) Grahame, D. C. The Electrical Double Layer and the Theory of Electrocapillarity. *Chem. Rev.* **1947**, *41* (3), 441–501.

(2) Bockris, J. O.; Devanathan, M. A. V; Müller, K. On the Structure of Charged Interfaces. *Proc. R. Soc. London. Ser. A. Math. Phys. Sci.* **1963**, *274* (1356), 55–79.

(3) Mott, N. F.; Watts-Tobin, R. J. The Interface between a Metal and an Electrolyte. *Electrochim. Acta* **1961**, *79*, 79–107.

(4) Fumagalli, L.; Esfandiar, A.; Fabregas, R.; Hu, S.; Ares, P.; Janardanan, A.; Yang, Q.; Radha, B.; Taniguchi, T.; Watanabe, K.; Gomila, G.; Novoselov, K. S.; Geim, A. K. Anomalously Low Dielectric Constant of Confined Water. *Science.* **2018**, *360*, 1339–1342.

(5) Hou, Y.; Aoki, K. J.; Chen, J.; Nishiumi, T. Solvent Variables Controlling Electric Double Layer Capacitance at the Metal-Solution Interface. *J. Phys. Chem. C* **2014**, *118* (19), 10153–10158.

(6) Giera, B.; Henson, N.; Kober, E. M.; Squires, T. M.; Shell, M. S. Model-Free Test of Local-Density Mean-Field Behavior in Electric Double Layers. *Phys. Rev. E - Stat. Nonlinear, Soft Matter Phys.* **2013**, *88* (1), 011301.

(7) Velasco-Velez, J. J.; Wu, C. H.; Pascal, T. A.; Wan, L. F.; Guo, J.; Prendergast, D.; Salmeron, M. The Structure of Interfacial Water on Gold Electrodes Studied by X-Ray Absorption Spectroscopy. *Science.* **2014**, *346* (6211), 831–834.

(8) Toney, M. F.; Howard, J. N.; Richer, J.; Borges, G. L.; Gordon, J. G.; Melroy, O. R.; Wiesler, D. G.; Yee, D.; Sorensen, L. B. Voltage-Dependent Ordering of Water Molecules at an Electrode-Electrolyte Interface. *Nature* **1994**, *368* (6470), 444–446.

(9) Fawcett, W. R.; Levine, S.; deNobriga, R. M.; McDonald, A. C. A Molecular Model for the Dielectric Properties of the Inner Layer at the Mercury/Aqueous Solution Interface. *J. Electroanal. Chem.* **1980**, *111* (2–3), 163–180.

(10) Daniels, I. N.; Wang, Z.; Laird, B. B. Dielectric Properties of Organic Solvents in an Electric Field. *J. Phys. Chem. C* **2017**, *121* (2), 1025–1031.

(11) Yeh, I. C.; Berkowitz, M. L. Dielectric Constant of Water at High Electric Fields: Molecular Dynamics Study. *J. Chem. Phys.* **1999**, *110* (16), 7935–7942.

(12) Sorenson, S. A.; Patrow, J. G.; Dawlaty, J. M. Solvation Reaction Field at the Interface Measured by Vibrational Sum Frequency Generation Spectroscopy. *J. Am. Chem. Soc.* **2017**, *139* (6), 2369–2378.

(13) Smith, C. P.; White, H. S. Theory of the Interfacial Potential Distribution and

Reversible Voltammetric Response of Electrodes Coated with Electroactive Molecular Films. *Anal. Chem.* **1992**, *64* (20), 2398–2405.

(14) Brown, M. A.; Abbas, Z.; Kleibert, A.; Green, R. G.; Goel, A.; May, S.; Squires, T. M. Determination of Surface Potential and Electrical Double-Layer Structure at the Aqueous Electrolyte-Nanoparticle Interface. *Phys. Rev. X* **2016**, *6* (1), 011007.

(15) Marcus, R. A. On the Theory of Electron-Transfer Reactions. VI. Unified Treatment for Homogeneous and Electrode Reactions. *J. Chem. Phys.* **1965**, *43* (2), 679–701.

(16) Liu, Y. P.; Newton, M. D. Reorganization Energy for Electron Transfer at Film-Modified Electrode Surfaces: A Dielectric Continuum Model. *J. Phys. Chem.* **1994**, *98* (29), 7162–7169.

(17) Ghosh, S.; Horvath, S.; Soudackov, A. V.; Hammes-Schiffer, S. Electrochemical Solvent Reorganization Energies in the Framework of the Polarizable Continuum Model. *J. Chem. Theory Comput.* **2014**, *10* (5), 2091–2102.

(18) Ghosh, S.; Soudackov, A. V; Hammes-Schiffer, S. Electrochemical Electron Transfer and Proton-Coupled Electron Transfer: Effects of Double Layer and Ionic Environment on Solvent Reorganization Energies. *J. Chem. Theory Comput.* **2016**, *12*, 2917–2925.

(19) Marcus, R. A.; Sutin, N. Electron Transfers in Chemistry and Biology. *Biochim. Biophys. Acta* **1985**, *811*, 265–322.

(20) Warshel, A.; Sharma, P. K.; Kato, M.; Xiang, Y.; Liu, H.; Olsson, M. H. M. Electrostatic Basis for Enzyme Catalysis. *Chem. Rev.* **2006**, *106*, 3210–3235.

(21) Chidsey, C. E. Free Energy and Temperature Dependence of Electron Transfer at the Metal-Electrolyte Interface. *Science.* **1991**, *251* (4996), 919–922.

(22) Finklea, H. O.; Hanshew, D. D. Electron-Transfer Kinetics in Organized Thiol Monolayers with Attached Pentaammine(Pyridine)Ruthenium Redox Centers. *J. Am. Chem. Soc.* **1992**, *114* (9), 3173–3181.

(23) Smalley, J. F.; Feldberg, S. W.; Chidsey, C. E. D.; Linford, M. R.; Newton, M. D.; Liu, Y.-P. The Kinetics of Electron Transfer through Ferrocene-Terminated Alkanethiol Monolayers on Gold. *J. Phys. Chem.* **1995**, *99*, 13141–13149.

(24) Sumner, J. J.; Creager, S. E. Redox Kinetics in Monolayers on Electrodes: Electron Transfer Is Sluggish for Ferrocene Groups Buried within the Monolayer Interior. *J. Phys. Chem. B* **2001**, *105*, 8739–8745.

(25) Eggers, P. K.; Darwish, N.; Paddon-Row, M. N.; Gooding, J. J. Surface-Bound Molecular Rulers for Probing the Electrical Double Layer. *J. Am. Chem. Society* **2012**, *134*, 7539–7544.

(26) Smalley, J. F.; Finklea, H. O.; Chidsey, C. E. D.; Linford, M. R.; Creager, S. E.; Ferraris, J. P.; Chalfant, K.; Zawodzinsk, T.; Feldberg, S. W.; Newton, M. D. Heterogeneous Electron-Transfer Kinetics for Ruthenium and Ferrocene Redox Moieties through Alkanethiol Monolayers on Gold. *J. Am. Chem. Soc.* **2003**, *125* (7), 2004–2013.

(27) Khoshtariya, D. E.; Dolidze, T. D.; Zusman, L. D.; Waldeck, D. H. Observation of the Turnover between the Solvent Friction (Overdamped) and Tunneling (Nonadiabatic) Charge-Transfer Mechanisms for a Au/$Fe(CN)_6^{3-/4-}$ Electrode Process and Evidence for a Freezing Out of the Marcus Barrier. *J. Phys. Chem. A* **2001**, *105* (10), 1818–1829.

(28) Miller, C.; Gratzel, M. Electrochemistry at ω-Hydroxy Thiol Coated Electrodes. 2. Measurement of the Density of Electronic States Distributions for Several Outer-Sphere Redox Couples. *J. Phys. Chem.* **1991**, *95* (13), 5225–5233.

(29) Finklea, H. O.; Liu, L.; Ravenscroft, M. S.; Punturi, S. Multiple Electron Tunneling Paths across Self-Assembled Monolayers of Alkanethiols with Attached Ruthenium(II/III) Redox Centers. *J. Phys. Chem.* **1996**, *100* (48), 18852–18858.

(30) Rowe, G. K.; Creager, S. E. Interfacial Solvation and Double-Layer Effects on Redox Reactions in Organized Assemblies. *J. Phys. Chem* **1994**, *98*, 5500–5507.

(31) Farnum, B. H.; Morseth, Z. A.; Brennaman, M. K.; Papanikolas, J. M.; Meyer, T. J. Application of Degenerately Doped Metal Oxides in the Study of Photoinduced Interfacial Electron Transfer. *J. Phys. Chem. B* **2015**, *119*, 7698–7711.

(32) Edwards, P. P.; Porch, A.; Jones, M. O.; Morgan, D. V.; Perks, R. M. Basic Materials Physics of Transparent Conducting Oxides. *Dalt. Trans.* **2004**, 19, 2995.

(33) Garcia, G.; Buonsanti, R.; Runnerstrom, E. L.; Mendelsberg, R. J.; Llordes, A.; Anders, A.; Richardson, T. J.; Milliron, D. J. Dynamically Modulating the Surface Plasmon Resonance of Doped Semiconductor Nanocrystals. *Nano Lett.* **2011**, *11* (10), 4415–4420.

(34) Troian-Gautier, L.; DiMarco, B. N.; Sampaio, R. N.; Marquard, S. L.; Meyer, G. J. Evidence That $\Delta S^{\ddagger}$ Controls Interfacial Electron Transfer Dynamics from Anatase TiO_2 to Molecular Acceptors. *J. Am. Chem. Soc.* **2018**, *140* (8), 3019–3029.

(35) Bangle, R. E.; Meyer, G. J. Factors That Control the Direction of Excited-State Electron Transfer at Dye-Sensitized Oxide Interfaces. *J. Phys. Chem. C* **2019**, *123* (42).

(36) Katz, H. E.; Scheller, G.; Putvinski, T. M.; Schilling, M. L.; Wilson, W. L.; Chidsey, C. E. D. Polar Orientation of Dyes in Robust Multilayers by Zirconium Phosphate-Phosphonate Interlayers. *Science.* **1991**, *254* (5037), 1485–1487.

(37) Dines, M. B.; DiGiacomo, P. M. Derivatized Lamellar Phosphates and Phosphonates of M(IV) Ions. *Inorg. Chem.* **1981**, *20* (1), 92–97.

(38) Brady, M. D.; Troian-Gautier, L.; Sampaio, R. N.; Motley, T. C.; Meyer, G. J. Optimization of Photocatalyst Excited- and Ground-State Reduction Potentials for Dye-Sensitized HBr Splitting. *ACS Appl. Mater. Interfaces* **2018**, *10* (37), 31312–31323.

(39) Argazzi, R.; Bignozzi, C. A.; Heimer, T. A.; Castellano, F. N.; Meyer, G. J. Enhanced Spectral Sensitivity from Ruthenium(II) Polypyridyl Based Photovoltaic Devices. *Inorg. Chem.* **1994**, *33*, 5741–5749.

(40) Hu, K.; Meyer, G. J. Lateral Intermolecular Self-Exchange Reactions for Hole and Energy Transport on Mesoporous Metal Oxide Thin Films. *Langmuir* **2015**, *31* (41), 11164–11178.

(41) Dimarco, B. N.; Motley, T. C.; Balok, R. S.; Li, G.; Siegler, M. A.; O 'donnell, R. M.; Hu, K.; Meyer, G. J. A Distance Dependence to Lateral Self-Exchange across Nanocrystalline TiO_2. A Comparative Study of Three Homologous Ru III/II Polypyridyl Compounds. *J Phys Chem C* **2016**, *120*, 14226–14235.

(42) Sampaio, R. N.; Troian-Gautier, L.; Meyer, G. J. A Charge-Separated State That Lives for Almost a Second at a Conductive Metal Oxide Interface. *Angew. Chemie* **2018**, *130* (47), 15616–15620.

(43) Farnum, B. H.; Morseth, Z. A.; Lapides, A. M.; Rieth, A. J.; Hoertz, P. G.; Brennaman, M. K.; Papanikolas, J. M.; Meyer, T. J. Photoinduced Interfacial Electron Transfer within a Mesoporous Transparent Conducting Oxide Film. *J. Am. Chem. Soc.* **2014**, *136* (6), 2208–2211.

(44) Hao, Y.; Yang, W.; Zhang, L.; Jiang, R.; Mijangos, E.; Saygili, Y.; Hammarström, L.; Hagfeldt, A.; Boschloo, G. A Small Electron Donor in Cobalt Complex Electrolyte Significantly Improves Efficiency in Dye-Sensitized Solar Cells. *Nat. Commun.* **2016**, *7*, 1–8.

(45) Dimarco, B. N.; Troian-Gautier, L.; Sampaio, R. N.; Meyer, G. J. Dye-Sensitized Electron Transfer from TiO_2 to Oxidized Triphenylamines That Follows First-Order Kinetics. *Chem. Sci.* **2018**, *9*, 940–949.

(46) Biner, M.; Bürgi, H. B.; Ludi, A.; Röhr, C. Crystal and Molecular Structures of $[Ru(Bpy)_3](PF_6)_3$ and $[Ru(Bpy)_3](PF_6)_2$ at 105 K. *J. Am. Chem. Soc.* **1992**, *114* (13), 5197–5203.

(47) Lin, B. C.; Cheng, C. P.; Lao, Z. P. M. Reorganization Energies in the Transports of Holes and Electrons in Organic Amines in Organic Electroluminescence Studied by Density Functional Theory. *J. Phys. Chem. A* **2003**, *107* (26), 5241–5251.

(48) Lambert, C.; Nöll, G. The Class II/III Transition in Triarylamine Redox Systems. *J. Am. Chem. Soc.* **1999**, *121* (37), 8434–8442.

(49) Wang, J. C.; Hill, S. P.; Dilbeck, T.; Ogunsolu, O. O.; Banerjee, T.; Hanson, K.

Multimolecular Assemblies on High Surface Area Metal Oxides and Their Role in Interfacial Energy and Electron Transfer. *Chem. Soc. Rev.* **2018**, *47*, 104–148.

(50) Putvinski, T. M.; Schilling, M. L.; Katz, H. E.; Chidsey, C. E. D.; Mujsce, A. M.; Emerson, A. B. Self-Assembly of Organic Multilayers with Polar Order Using Zirconium Phosphate Bonding between Layers. *Langmuir* **1990**, *6*, 1567–1571.

(51) Farnum, B. H.; Wee, K.-R.; Meyer, T. J. Self-Assembled Molecular p/n Junctions for Applications in Dye-Sensitized Solar Energy Conversion. *Nat. Chem.* **2016**, *8*, 845–852.

(52) Wang, D.; Sampaio, R. N.; Troian-Gautier, L.; Marquard, S. L.; Farnum, B. H.; Sherman, B. D.; Sheridan, M. V.; Dares, C. J.; Meyer, G. J.; Meyer, T. J. Molecular Photoelectrode for Water Oxidation Inspired by Photosystem II. *J. Am. Chem. Soc.* **2019**, *141* (19), 7926–7933.

(53) Bard, A. J.; Abruña, H. D.; Chidsey, C. E.; Faulkner, L. R.; Feldberg, S. W.; Itaya, K.; Majda, M.; Melroy, O.; Murray, R. W.; Porter, M. D.; Soriaga, M. P.; White, H. S. The Electrode/Electrolyte Interface - A Status Report. *J. Phys. Chem.* **1993**, *97* (28), 7147–7173.

(54) Spitler, M. T. Effect of Nanometer-Sized Surface Morphology upon Electrochemical Kinetics. *Electrochim. Acta* **2007**, *52* (6), 2294–2301.

(55) Troian-Gautier, L.; DiMarco, B. N.; Sampaio, R. N.; Marquard, S. L.; Meyer, G. J. Evidence That $\Delta S^{\ddagger}$ Controls Interfacial Electron Transfer Dynamics from Anatase TiO_2 to Molecular Acceptors. *J. Am. Chem. Soc.* **2018**, *140* (8), 3019–3029.

(56) Nelson, J.; Chandler, R. E. Random Walk Models of Charge Transfer and Transport in Dye Sensitized Systems. *Coord. Chem. Rev.* **2004**, *248*, 1181–1194.

(57) Bard, A. J.; Faulkner, L. R. *Electochemical Method: Fundamentals and Applications*, 2nd ed.; Harris, D., Swain, E., Robey, C., Aiello, E., Eds.; Wiley, 2000.

(58) Marcus, R. A. On the Theory of Oxidation-Reduction Reactions Involving Electron Transfer. I. *J. Chem. Phys.* **1956**, *24* (5), 966–978.

(59) Gerischer, H. Electrochemical Techniques for the Study of Photosensitization. *Photochem. Photobiol.* **1972**, *16* (4), 243–260.

(60) Yonemoto, E. H.; Riley, R. L.; Kim, Y. Il; Atherton, S. J.; Schmehl, R. H.; Mallouk, T. E. Photoinduced Electron Transfer in Covalently Linked Ruthenium Tris(Bipyridyl)-Viologen Molecules: Observation of Back Electron Transfer in the Marcus Inverted Region. *J. Am. Chem. Soc.* **1992**, *114* (21), 8081–8087.

(61) Closs, G. L.; Miller, J. R. Intramolecular Long-Distance Electron Transfer in Organic Molecules. *Science.* **1988**, *240* (4851), 440–447.

(62) Wenger, O. S. How Donor - Bridge - Acceptor Energetics Influence Electron

Tunneling Dynamics and Their Distance Dependences. *Acc. Chem. Res.* **2011**.

(63) Weiss, E. A.; Tauber, M. J.; Kelley, R. F.; Ahrens, M. J.; Ratner, M. A.; Wasielewski, M. R. Conformationally Gated Switching between Superexchange and Hopping within Oligo-p-Phenylene-Based Molecular Wires. *J. Am. Chem. Soc.* **2005**, *127*, 11842–11850.

(64) Hines, T.; Diez-Perez, I.; Hihath, J.; Liu, H.; Wang, Z.-S.; Zhao, J.; Zhou, G.; Müllen, K.; Tao, N. Transition from Tunneling to Hopping in Single Molecular Junctions by Measuring Length and Temperature Dependence. *J. Am. Chem. Soc.* **2010**, *132* (33), 11658–11664.

(65) Mott, N. F. Conduction in Glasses Containing Transition Metal Ions. *J. Non. Cryst. Solids* **1968**, *1* (1), 1–17.

(66) Paddon-Row, M. N.; Shephard, M. J.; Jordan, K. D. Predicted Weak Distance Dependence of Through-Bond Mediated Electronic Coupling in n-Alkane Bridges: An Ab Initio Molecular Orbital Study. *J. Phys. Chem.* **1993**, *97* (9), 1743–1745.

(67) Sutin, N. Nuclear, Electronic, and Frequency Factors in Electron Transfer Reactions. *Acc. Chem. Res.* **1982**, *15* (9), 275–282.

(68) Bonhôte, P.; Gogniat, E.; Tingry, S.; Barbé, C.; Vlachopoulos, N.; Lenzmann, F.; Comte, P.; Gra, M. Efficient Lateral Electron Transport inside a Monolayer of Aromatic Amines Anchored on Nanocrystalline Metal Oxide Films. *J. Phys. Chem. B* **1998**, *102*, 1498–1507.

(69) Moia, D.; Vaissier, V.; López-Duarte, I.; Torres, T.; Nazeeruddin, M. K.; O'Regan, B. C.; Nelson, J.; Barnes, P. R. F. The Reorganization Energy of Intermolecular Hole Hopping between Dyes Anchored to Surfaces. *Chem. Sci.* **2014**, *5* (1), 281–290.

(70) Hu, K.; Meyer, G. J. Lateral Intermolecular Self-Exchange Reactions for Hole and Energy Transport on Mesoporous Metal Oxide Thin Films. *Langmuir* **2015**, *31*, 11164–11178.

(71) Fawcett, R. W. *Liquids, Solutions, and Interfaces: From Classical Macroscopic Descriptions to Modern Microscopic Details*, 1st ed.; Oxford University Press: New York, 2004.

(72) Moia, D.; Vaissier, V.; López-Duarte, I.; Torres, T.; Nazeeruddin, M. K.; O'Regan, B. C.; Nelson, J.; Barnes, P. R. F. The Reorganization Energy of Intermolecular Hole Hopping between Dyes Anchored to Surfaces. *Chem. Sci.* **2014**, *5* (1), 281–290.

(73) Marcus, R. A. Chemical and Electrochemical Electron-Transfer Theory. *Annu. Rev. Phys. Chem.* **1964**, *15*, 155–196.

(74) Bangle, R. E.; Schneider, J.; Piechota, E. J.; Troian-Gautier, L.; Meyer, G. J. Electron

Transfer Reorganization Energies in the Electrode-Electrolyte Double Layer. *J. Am. Chem. Soc.* **2020**, *142* (2), 674–679.

(75) Lee, C. Y.; McCammon, J. A.; Rossky, P. J. The Structure of Liquid Water at an Extended Hydrophobic Surface. *J. Chem. Phys.* **1984**, *80* (9), 4448–4455.

(76) Grätzel, M. Light-Induced Charge Separation and Water Cleavage in Microheterogeneous Aqueous Systems. *Faraday Discuss. Chem. Soc.* **1980**, *70* (0), 359–374.

(77) Attard, P. Recent Advances in the Electric Double Layer in Colloid Science. *Curr. Opin. Colloid Interface Sci.* **2001**, *6* (4), 366–371.

(78) Jackson, M. N.; Surendranath, Y. Molecular Control of Heterogeneous Electrocatalysis through Graphite Conjugation. *Acc. Chem. Res.* **2019**, *52* (12), 3432–3441.

(79) Ryu, J.; Surendranath, Y. Tracking Electrical Fields at the Pt/H2O Interface during Hydrogen Catalysis. *J. Am. Chem. Soc.* **2019**, *141* (39), 15524–15531.

(80) Manke, F.; Frost, J. M.; Vaissier, V.; Nelson, J.; Barnes, P. R. F. Influence of a Nearby Substrate on the Reorganization Energy of Hole Exchange between Dye Molecules. *Phys. Chem. Chem. Phys.* **2015**, *17* (11), 7345–7354.

CHAPTER 7: SOLVENT INFLUENCE ON NON-ADIABATIC INTERFACIAL ELECTRON TRANSFER AT CONDUCTIVE OXIDE/ELECTROLYTE INTERFACES[18]

7.1 Introduction

Predictive models to describe electron transfer rate constants at metal-electrolyte interfaces have been invaluable for the development of solar energy conversion technologies, batteries, and electrochemical engineering processes. Semiclassical interfacial electron transfer theory was adapted from related homogeneous electron transfer theory with particular attention to metallic interfaces functionalized with redox active molecular complexes.[1-11] The main conceptual difference between interfacial and intramolecular electron transfer lies in the delocalized continuum of electronic states associated with a metal.[4,11] Each electronic state within the metal can undergo an electron transfer event to or from an isoenergetic electronic state within the molecule. Integration over the continuum of metallic states results in the ensemble interfacial electron transfer rate constant. In other words, the interfacial electron transfer rate constant is determined by the energetic overlap between the continuum of electronic states of the conductor and the molecular distribution (Fig. 7.1). As described by the Fermi golden rule, the degree of energetic overlap, and thus the interfacial electron transfer rate constant, is defined by the same fundamental parameters that govern both interfacial and intermolecular electron transfer kinetics—the Gibbs free

[18]This chapter previously appeared as an article in the *Journal of Chemical Physics*. The original citation is: Aramburu-Trošelj, B.; Bangle, R.E.; Meyer, G.J. *J. Chem. Phys.* **2020**, 153 *(13)*, 134702.

energy $\Delta G°$, the electronic coupling between the donor and acceptor H_{ab}, and the free energy required to reorganize the bonds and surrounding solvent λ.

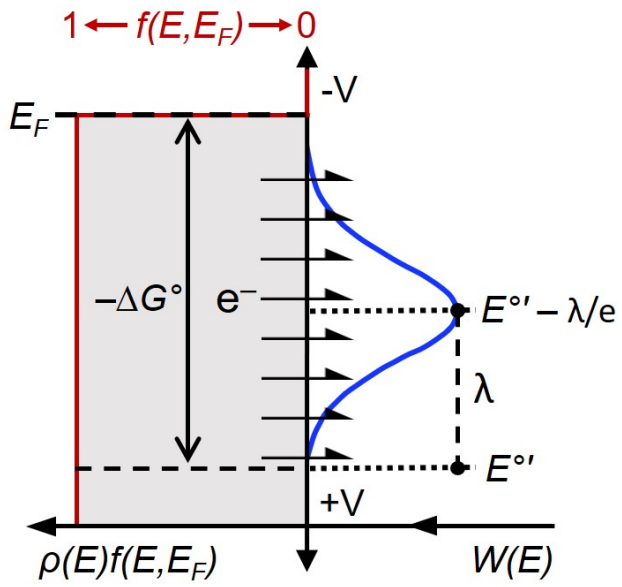

Figure 7.1. A theoretical representation of interfacial electron transfer from a metal to a molecular acceptor. Assuming the low-temperature limit of the Fermi-Dirac distribution $f(E,E_F)$, the interfacial electron transfer rate constant is proportional to the integration over the continuum of electrode states $\rho(E)f(E,E_F)$ and the Fermi's golden rule distribution of activation energies for reduction of the molecule, $W(E)$. The total reorganization energy λ defines the width of $W(E)$. The driving force in eV for a one-electron process is defined as $-\Delta G° = eE°'-E_F = e(E°'-E_{app})$, where $E°'$ is the formal reduction potential of the molecule, E_F is the Fermi level in eV, E_{app} is an externally applied potential, and e is the elementary charge.

This semiclassical framework for the prediction of an interfacial electron transfer rate constant, k_{IET}, from a metal to a molecule is depicted in Fig. 7.1 and described by Eq. 7.1.[3,11,12] The continuum of metal electronic states is represented by $\rho(E)f(E, E_F)$, where $\rho(E)$ is the density of states of the metal, and $f(E, E_F)$ is the Fermi-Dirac distribution describing the occupancy of these states in relation to the electrode Fermi level, E_F. The distribution of activation energies associated with reduction of the molecule is represented by $W(E)$ (Eq. 7.2), with a full-width-at half maximum determined by the reorganization energy, λ.

$$k_{IET} = \frac{2\pi}{\hbar}\int_{-\infty}^{\infty}\rho(E)f(E,E_F)|H_{ab}(E)|^2W(E)dE \qquad (7.1)$$

$$W(E) = \frac{1}{\sqrt{4\pi\lambda k_B T}} \exp\left(\frac{-(\Delta G° + \lambda)^2}{4\lambda k_B T}\right) \quad (7.2)$$

The utilization of an electrode in place of a molecular donor affords a distinct advantage to the study of interfacial electron transfer over that of intramolecular donor-acceptor complexes. Systematic variation of the driving force $-\Delta G°$ in donor-acceptor complexes requires considerable synthetic chemistry. However, in interfacial reactions, $-\Delta G°$ is defined by the difference between the molecular formal reduction potential, $E°'$, and the Fermi level E_F of the metal as described in Eq. 7.3, where e is the elementary charge:

$$-\Delta G° = eE°' - E_F \quad (7.3)$$

Because application of externally applied potentials (E_{app}) to a metallic electrode readily controls the Fermi level, $E_{app} = E_F/e$, $-\Delta G°$ can be precisely tuned with a potentiostat.

Measurement of the kinetic response to $-\Delta G°$ provides a straightforward method to experimentally probe *W(E)* and to quantify both λ and H_{ab}. Contrary to the inverted region theorized and observed in intramolecular electron transfer,[13,14] interfacial electron transfer theory predicts k_{IET} to increase with $-\Delta G°$ to a maximum attainable value, k_{max}, when $-\Delta G° > 2\lambda$. When $-\Delta G° = \lambda$, k_{IET} is ½ k_{max}, and values of k_{IET} normalized to k_{max} provide a convenient means to quantify λ , Eq. 7.4. Assuming the low temperature limit of $f(E, E_F)$, k_{max} reports on H_{ab} and ρ, both of which are also considered to be independent of the applied potential (Eq. 7.5).

$$\frac{k_{IET}}{k_{max}} = \frac{1}{2}\left[1 - \mathrm{erf}\left(\frac{\Delta G° + \lambda}{2\sqrt{\lambda k_B T}}\right)\right] \quad (7.4)$$

$$k_{max} = \frac{2\pi}{\hbar} {H_{ab}}^2 \rho \quad (7.5)$$

The explicit experimental disentanglement of λ, H_{ab}, and $-\Delta G°$ is hence uniquely accessible for interfacial electron transfer through this analysis. This theory has been experimentally

validated through an expansive body of research on thermal electron transfer with gold electrodes with self-assembled monolayers (SAMS).[15–20]

The studies described in Chapters 5 and 6 have utilized transient absorption spectroscopy to quantify interfacial electron transfer kinetics from a transparent conductive oxide (TCO) electrode to surface-anchored molecular acceptors as a function of $-\Delta G°$. This approach requires a means to photo-initiate the desired electron transfer reaction in a standard electrochemical cell. Utilization of the theory described above to analyze the data allowed direct quantification of λ and H_{ab} for interfacial electron transfer to ruthenium-polypyridyl and triarylamine complexes relevant to solar water oxidation.[12,21–23] These studies exemplify how factors such as proton involvement and proximity to the metal surface impact λ and H_{ab}. A somewhat surprising finding in Chapter 6 was the apparent insensitivity of λ, H_{ab}, and k_{IET} to electrolyte concentration. The utilization of aqueous electrolytes with 0.1 M, 0.2 M, and 0.5 M $HClO_4$ as well as a 0.1 M $LiClO_4$ acetonitrile electrolyte resulted in surprisingly similar kinetic behavior. The insensitivity to the electrolyte concentration is in contrast to predictions of Frumkin.[11,24] Similarly, the near parity between acetonitrile and water contrasts with experimental[17,20,24–28] and theoretical[29–39] studies where solvent dynamics were found to play an important role in many interfacial electron transfer reactions.

To explore the impact of solvent on interfacial electron transfer at metal oxide interfaces, kinetic data are reported in this Chapter in the slowly relaxing solvents methanol (MeOH) and benzonitrile (PhCN). The redox-active molecules were positioned within the electric double layer and the diffuse layer of an $Sn:In_2O_3$ (ITO) electrode using a previously reported layer-by-layer approach with ionic bridges.[40] Kinetic analysis with semiclassical interfacial electron transfer theory indicated that in all cases interfacial electron transfer

occurred with very low electronic coupling, indicative of a non-adiabatic mechanism. The kinetic data and analysis are discussed in comparison to recently published results obtained in water and acetonitrile electrolytes.[22,23]

7.2 Experimental

7.2.1 Materials

All materials were used as received without further purification. Perchloric acid (70%, Sigma-Aldrich), zirconyl chloride octahydrate (reagent grade, 98%) and methylene diphosphonic acid were obtained from Sigma-Aldrich. Ethanol (99.5+ %) and methanol (MeOH, 99.8%) were obtained from Acros Organics. Benzonitrile (PhCN, 99%) was purchased from TCI. In_2O_3:Sn (ITO) nanoparticles (VP ITO TC8) were purchased as a powder from Evonik Industries. Fluorine-doped tin oxide (FTO) glass substrates (15 Ω/sq) were obtained from Hartford Glass. RuP, $[Ru^{II}(bpy)_2(4,4'\text{-}(PO_3H_2)_2\text{-}bpy)]^{2+}$, where bpy is 2,2'-bipyridine, and TPA, 4-[N,N-di(*p*-tolyl)amino]benzylphosphonic acid, were synthesized as previously reported.[41]

7.2.2 Oxide Thin Film Preparation

The In_2O_3:Sn (ITO) nanoparticles (20 wt%) were thoroughly sonicated in 100-proof ethanol with 2-[2-(2-Methoxyethoxy)ethoxy]acetic acid (3 wt% compared to ITO) to form a stable dispersion. A sol-gel paste was generated by mixing equal volumes of the 20 wt% ITO dispersion and a 10 wt% hydroxypropyl cellulose/ethanol solution. The paste was doctor-bladed onto FTO-coated conductive glass using two layers of Scotch tape as a spacer to define the ITO film thickness. The paste was then dried in air for ~ 30 min and annealed in a

tube furnace at 450 °C under O_2 flow for 30 min. Films generated in this way were measured to be 3-4 μm thick by a Bruker DektatXT profilometer.

ITO materials were functionalized with redox-active molecules RuP and/or TPA, which were positioned at variable distances from the ITO surface on the Angstrom length scale with ionic bridges as in Chapter 6.[22,23,40,42] Electrodes termed ITO|-$(X)_n$-TPA employed in transient absorption experiments were first sensitized to 50% saturation surface coverage (~ 5 x 10^{-9} mol cm^{-2}) with RuP by reaction of ITO with RuP in methanol.[23] Surface coverages were controlled through reaction time. Molecular bridge units were assembled by subsequent reactions of ITO electrodes with 0.1 M $HClO_4$ aqueous solutions of 5 mM methylene diphosphonic acid (overnight) then 6 mM $ZrOCl_2$•8 H_2O (2 hours). Multiple bridge units were assembled by repeating the process. Bridge assemblies were terminated by redox-active molecules, either RuP or TPA, by overnight reaction with RuP/methanol or TPA/ethanol solutions. For spectroelectrochemical measurements, ITO|-$(X)_n$-TPA electrodes were prepared without first sensitizing the ITO with RuP.

7.2.3 Electrochemical and Spectro-electrochemical Measurements

A standard three-electrode cell with the ITO as a working electrode, a platinum mesh counter electrode, and a silver wire quasi-reference electrode. Experiments were performed in Ar-sparged 0.1 M $LiClO_4$ MeOH or PhCN solutions. All potentials are reported *versus* the Normal Hydrogen Electrode (NHE). For spectroelectrochemical measurements, potentiostatic control was coupled with UV-visible absorption spectroscopy measured with an Avantes AvaLight DHc light source and an Avantes StarLine AvaSpec-2048 spectrometer. The reference utilized for all absorption spectra reported was an ITO electrode that had not been surface functionalized. Formal redox potentials $E^{\circ\prime}$ for ITO|-$(X)_n$-$Ru^{III/II}$P

and ITO|-$(X)_n$-$TPA^{+/0}$ were quantified by modeling the absorption change at 455 nm and 680 nm, respectively, with a modified Nernst equation, Eq. 7.6. Here ΔA is the normalized absorbance change, E_{app} is the applied potential, and α is a non-ideality factor.[43] The $E^{\circ\prime}$ values reported represent the equilibrium potential at which the concentrations of the oxidized and reduced species were equal.

$$\Delta A = \frac{1}{1+10^{(E_{\mathrm{app}}-E^{\circ\prime})/(59.2\alpha)}} \tag{7.6}$$

7.2.4 Transient Spectroscopy Measurements

Transient absorption spectroscopy was performed with a previously described apparatus.[44] Pulsed 532 nm light excitation was provided by a frequency-doubled, Q-switched, pulsed Nd:YAG laser (Quantel U.S.A, Brilliant B, 5-6 ns FWHM). Laser fluences were adjusted between 1-8 mJ/pulse to generate the same initial concentration of reactants. A white light 150 W xenon arc lamp (Applied Photophysics) aligned perpendicular to the excitation served as the probe beam that was pulsed at 1 Hz for time scales < 100 μs. A SPEX 1702/04 monochromator optically coupled to a Hamamatsu R928 photomultiplier tube was used for detection. An optically triggered LeCroy 9450, Dual 330 MHz oscilloscope was utilized to average (typically 90 laser pulses) digitize the transient signal. The instrument response time was ~ 10 ns. Single wavelength kinetic measurements were generated by averaging the results of 90 laser pulses. The samples were an ITO photo-electrode positioned at a 45° angle to the excitation in a standard three-electrode cell in a glass cuvette. The electrolytes were purged with argon gas before all measurements.

7.3 Results

Mesoporous nanocrystalline films of the transparent conducting oxide Sn:In_2O_3 (ITO) were functionalized with RuP, $[Ru^{II}(bpy)_2(4,4'\text{-}(PO_3H_2)_2\text{-}bpy)]^{2+}$, and TPA, 4-[N,N-di(*p*-tolyl)amino]benzylphosphonic acid as illustrated in Fig. 7.2. Molecular acceptors were either directly anchored to the ITO through phosphonic acid groups or were positioned away from the surface through ionic bridge units, represented as X, that consisted of a methylene diphosphonic acid molecule coordinated to a Zr^{4+} Lewis acid.[22,23,40,42] The distance between the ITO surface and the redox active center was controlled through the number of bridging units X to produce films abbreviated as ITO|-$(X)_n$-Acceptor, n= 0, 1 or 2.

The visible absorption spectra of ITO|-$(X)_n$-RuP, display a broad characteristic metal-to-ligand charge transfer absorption band centered near 450 nm when submerged in methanol (MeOH) or benzonitrile (PhCN) (Figs. 7.3d and Fig. 7.9a in the Associated Content section). The neutral TPA does not absorb visible light, however thermal oxidation to yield ITO|-$(X)_n$-TPA^+ is accompanied by a significant color change and the appearance of a prominent absorption band centered at 680 nm. (Figs. 7.3a and Fig. 7.9b in the Associated Content section). The reference spectra were an ITO electrode that had not been surface functionalized. The absorption spectra were within experimental error independent of the number of spacers, n.

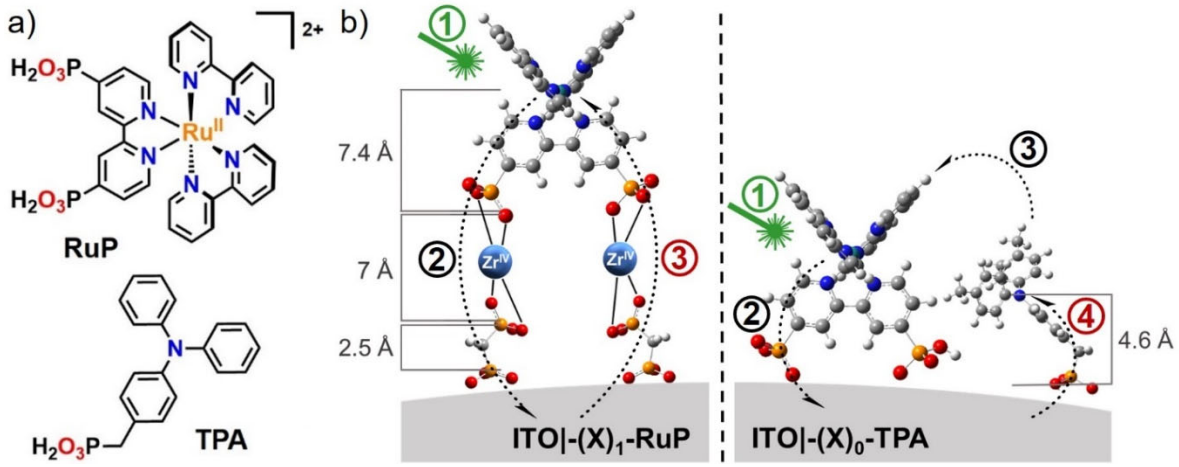

Figure 7.2. a) ITO electrodes were functionalized with the redox-active molecules RuP and TPA. b) Electrodes abbreviated as ITO|-$(X)_n$-RuP were synthesized by a layer-by-layer technique. Each ionic bridge, X, consisted of a methylene diphosphonic acid molecule bound to a Zr(IV) Lewis acidic cation, and the molecule-electrode distance was controlled by the number of linked bridges, n. Kinetic measurements of the electrodes termed ITO|-$(X)_n$-TPA also contained RuP anchored directly to the surface. Electron transfer distances were estimated from DFT models of the molecules and a 7 Å interlayer Zr(IV) spacing. Pulsed light excitation of RuP (1) resulted in excited state electron transfer from RuP to ITO (2). If TPA was present, intermolecular electron transfer from TPA to $Ru^{III}P$ generated TPA^+(black 3). Electron recombination (red 3 or 4) with rate constant k_{IET} was quantified spectroscopically to either $Ru^{III}P$ or TPA^+.

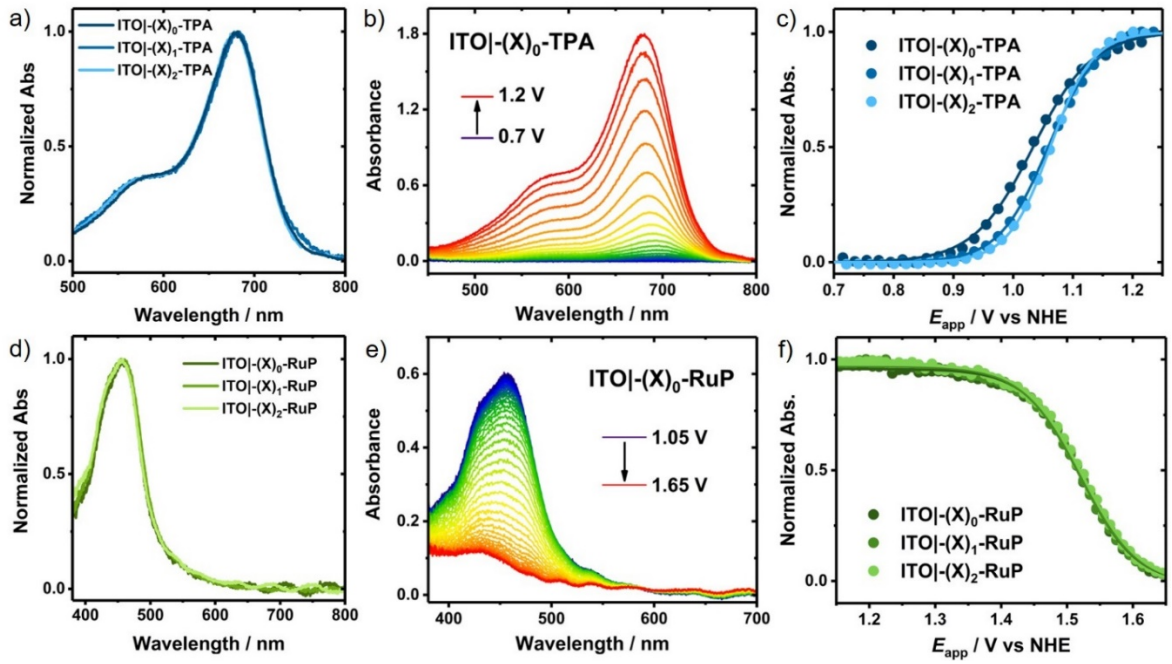

Figure 7.3. The visible absorbance spectra of (a) ITO|-$(X)_n$-TPA^+ and (d) ITO|-$(X)_n$-RuP in 0.1 M $LiClO_4$ MeOH. (b, e) Visible absorbance spectra measured over the indicated applied potential range vs NHE of (b) ITO-$(X)_0$-TPA and (e) ITO|-$(X)_0$-RuP in 0.1 M $LiClO_4$ MeOH. (c,f) The absorbance change ΔA measured at (c) 680 nm for TPA and (f) 455 nm for RuP as a function of applied potential with overlaid fits to a modified Nernst equation, with Eq. 7.6.

The formal reduction potential, $E^{\circ\prime}$, for both $Ru^{III/II}P$ and $TPA^{+/0}$ were determined through spectroelectrochemical experiments with ITO|-$(X)_n$-RuP and ITO|-$(X)_n$-TPA (Figs. 7.3b,e and Figs. 7.10-7.13 in Associated Content). Spectral changes were monitored as a function of the applied potential at 455 nm for ITO|-$(X)_n$-RuP and 680 nm for ITO|-$(X)_n$-TPA and modelled with Eq. 7.6.[22,43,45] Values of $E^{\circ\prime}$ obtained in 0.1 M $LiClO_4$ methanol or benzonitrile were within experimental error insensitive to distance from the ITO surface or the solvent (Figs. 7.3c,f). For ITO|-$(X)_n$-$Ru^{III/II}P$, $E^{\circ\prime}$ = 1.55 V vs NHE, and for ITO|-$(X)_n$-$TPA^{+/0}$, $E^{\circ\prime}$ = 1.02 V vs NHE.

Pulsed 532 nm excitation of RuP resulted in the prompt appearance of the oxidized complex, data consistent with rapid ITO|-$(X)_n$-$Ru^{II}P^*$ → ITO(e^-)|-$(X)_n$-$Ru^{III}P$ excited-state electron injection into ITO, $k_{inj} > 10^8 s^{-1}$. After pulsed light excitation of ITO|-$(X)_n$-TPA, for

which both RuP and TPA were present, rapid intermolecular electron transfer from TPA to light-generated $Ru^{III}P$ occurred within 10 ns to yield ITO|-$(X)_n$-TPA^+. Data collected 50 ns after excitation are shown in Figs. 7.4 and 7.14 in the Associated Content section for n = 0 and 1, while there was no spectroscopic evidence for excited state injection after excitation of ITO|-$(X)_2$-RuP in either methanol or benzonitrile electrolytes.

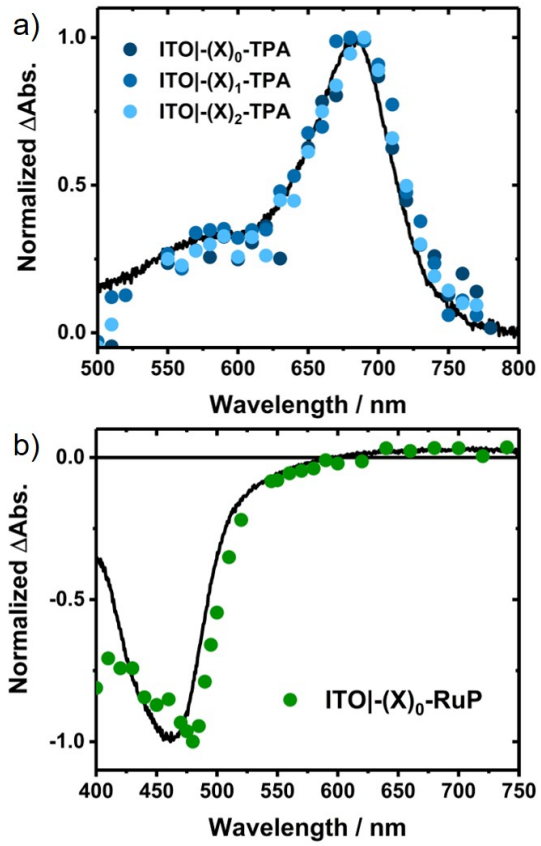

Figure 7.4. Transient absorption spectra measured 50 ns after pulsed 532 nm light excitation (points) for (a) ITO|-$(X)_n$-TPA and (b) ITO|-$(X)_n$-RuP in 0.1 M $LiClO_4$ MeOH. Overlaid as black lines are simulations based on the spectroelectrochemical oxidation of the molecule.

Following excited state injection and (for ITO|-$(X)_n$-TPA) intermolecular electron transfer, the desired interfacial electron transfer reaction was monitored spectroscopically at 402 nm (ITO(e^-)|-$(X)_n$-$Ru^{III}P$ → ITO|-$(X)_n$-$Ru^{II}P$) or 690 nm (ITO(e^-)|-$(X)_n$-TPA → ITO|-$(X)_n$-TPA^+). Kinetics for the interfacial electron transfer were measured as a function of the applied potential (E_{app}). Typical data for ITO|-$(X)_n$-TPA in 0.1 M $LiClO_4$ MeOH are shown

in Fig. 7.5, while data for ITO|-(X)$_n$-TPA in 0.1 M LiClO$_4$ PhCN and ITO|-(X)$_n$-RuP are given in Figs. 7.15-7.16 in the Associated Content section. The kinetic data was non-exponential and the reciprocal of the time required for reaction to reach ½ of the initially formed reactants was taken as an estimate of the interfacial electron transfer rate constant, k_{IET}. The magnitude of k_{IET} increased with increasingly negative E_{app} and was most rapid for molecules anchored directly to the oxide surface. However, the sensitivity of the kinetic data to E_{app} was smallest for ITO|-(X)$_0$-TPA. Note that after pulsed light excitation of ITO|-(X)$_1$-RuP, transient spectral changes indicated that reduction of the RuP* excited state took place, thus lowering the yield of excited state injection (Fig. 7.17 in the Associated Content section).[46] As increasingly negative potentials were applied, the timescales of charge recombination and excited state reduction became similar, precluding accurate k_{IET} quantification. As such, ITO|-(X)$_1$-RuP is excluded from further kinetic analysis.

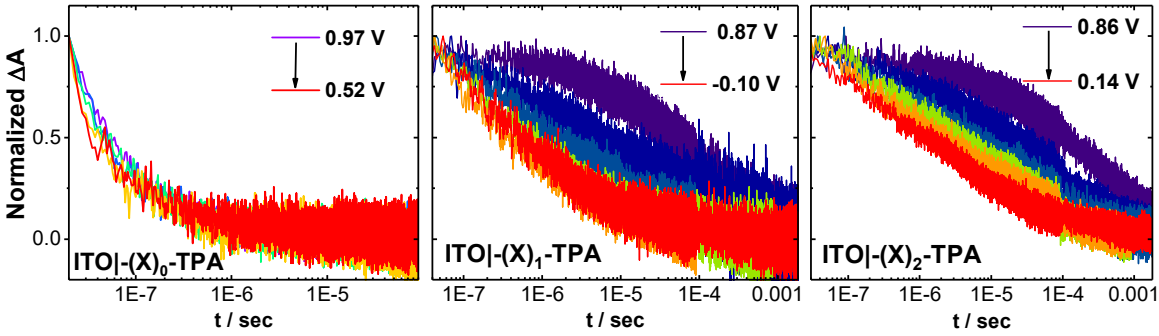

Figure 7.5. The absorption change ΔA measured at 690 nm after pulsed 532 nm light excitation of ITO|-(X)$_0$-TPA (left), ITO|-(X)$_1$-TPA (center) and ITO|-(X)$_2$-TPA (right) immersed in a 0.1 M LiClO$_4$ MeOH as a function of the applied potential *vs.* NHE.

The interfacial electron transfer rate constant k_{IET}, quantified as the inverse half-life, measured as a function of the applied potential are given in Fig. 7.6 and 7.16 in the Associated Content section. For ITO|-(X)$_0$-RuP and ITO|-(X)$_n$-TPA, values of k_{IET} increased with negative E_{app} before reaching a saturation value, k_{max}. Further, for a given E_{app}, k_{IET}

decreased with distance from the ITO surface. Normalization of k_{IET} by k_{max} resulted in plots shown in Figs. 7.6b and Fig. 7.18 in the Associated Content section, which were well-modelled by semiclassical heterogeneous electron transfer theory (Eq. 7.4) to extract the total reorganization energy λ (Table 7.1). Values of H_{ab} were extracted from k_{max} using Eq. 7.5. This equation requires knowledge of the density of electronic states of the electrode, ρ, which has been previously estimated from Drude analysis of the near infrared plasmon absorption to be 0.45 ev^{-1} for mesoporous ITO.[12] This estimate, however, requires knowledge of the number of surface atoms in ITO capable of undergoing interfacial electron transfer with a molecule, which adds uncertainty to calculated H_{ab} values. For the present analysis, a single surface atom was assumed.

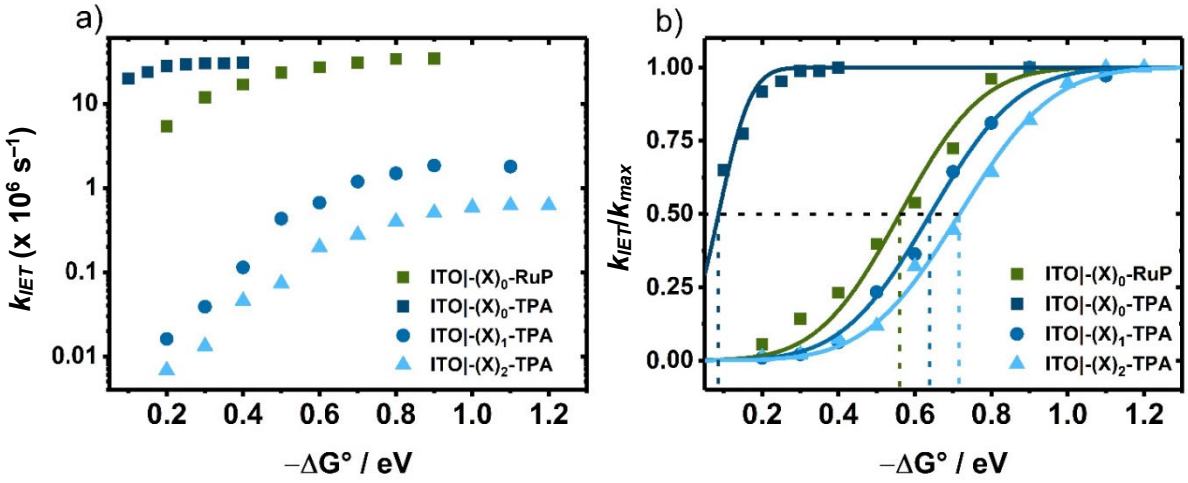

Figure 7.6. (a) Values of k_{IET} quantified as a function of $-\Delta G° = e(E°' - E_{app})$ for kinetic data measured in 0.1 M $LiClO_4$ MeOH. b) Plots of k_{IET} normalized by k_{max} in 0.1 M $LiClO_4$ MeOH with overlaid fits to Eq. 4. When $k_{IET} = ½\ k_{max}$, $-\Delta G° = \lambda$, as illustrated by dashed lines.

Table 7.1. Relevant Interfacial Electron Transfer Kinetic Parameters

		PhCN			MeOH		
	R **/ Å**[19]	λ **/ eV**	k_{max} **/ x 10^6 s^{-1}**	H_{ab} **/ cm^{-1}**	λ **/ eV**	k_{max} **/ x 10^6 s^{-1}**	H_{ab} **/ cm^{-1}**
ITO|-$(X)_0$-RuP	7.4	0.38 ± 0.03	31	0.7	0.56 ± 0.03	33	0.7
ITO|-$(X)_0$-TPA	4.6	0.08 ± 0.04	30	0.7	0.09 ± 0.03	31	1.7
ITO|-$(X)_1$-TPA	15	0.58 ± 0.03	11	0.4	0.63 ± 0.01	2.5	0.2
ITO|-$(X)_2$-TPA	24	0.52 ± 0.04	1.5	0.2	0.72 ± 0.01	0.8	0.1

For ITO|-$(X)_0$-RuP and ITO|-$(X)_n$-TPA, H_{ab} values were within experimental error indistinguishable between MeOH and PhCN. Values of λ, however, were systematically smaller for interfacial electron transfer occurring in PhCN. For ITO|-$(X)_2$-TPA, where λ is expected to approach homogeneous solution values,[11,22,23] $\lambda \approx 0.6$ eV in PhCN, while in MeOH $\lambda \approx 0.75$ eV.

7.4 Discussion

The kinetics for interfacial electron transfer from ITO to acceptors physically located within the electric double layer and the diffuse layer were quantified as function of the free energy change in both benzonitrile (PhCN) and methanol (MeOH). The kinetic approach required a high surface area mesoporous thin film conductive electrode so that the desired reaction could be photoinitiated and quantified as a function of $-\Delta G°$. Marcus-Gerischer analysis provided estimates of the reorganization energy, and the electronic coupling. This

[19]Estimated by DFT in references 22 and 23.

data compliments the measurements of the same materials in water and acetonitrile (MeCN) in Chapter 6, providing an opportunity to evaluate the impact of solvent on interfacial electron transfer at oxide interfaces.[22,23] It is important to emphasize that the formal reduction potentials and absorption spectra of the molecules were insensitive to the number of bridge units and were only weakly solvent dependent. However, the interfacial electron transfer rate constants, k_{IET}, were highly sensitive to the number of bridge units with a more acute solvent dependence. Below we discuss this data, first with regard to the reorganization energy followed by the electronic coupling.

7.4.1 Reorganization Energy

The quantified λ values were largest when the distance from the oxide-electrolyte interface was greatest and decreased to $\lambda \approx 0.1$ eV at the smallest distance. Dielectric continuum theory predicts that λ_o should decrease with the donor-acceptor distance as described by Eq. 7.7.

$$\lambda_o = \frac{q^2}{2}\left(\frac{1}{\varepsilon_{op}} - \frac{1}{\varepsilon_{st}}\right)\left(\frac{1}{a} - \frac{1}{2R}\right) \tag{7.7}$$

Here, ε_{st} and ε_{op} are the solvent static and optical dielectric constants, a is the radius of a spherical cavity occupied by the molecular acceptor,[6,47] and R is the distance between the ITO and the molecule.[11,48] Values of R were estimated as the distance between the redox center of the molecule (N for TPA and Ru for RuP) and a plane through the O atoms of the phosphonic anchoring group as shown in Fig. 7.2. Distances in the RuP, TPA, and diphosphonic acid were estimated by density functional theory and the Zr(IV) interlayer spacing was estimated to be 7 Å.[22,23] Experimental reorganization energies in this study were best modelled with a = 4.8 Å, and are represented as a function of distance in Fig. 7.7 (solid lines), assuming ε_{st} = 32.7 and ε_{op} = 1.76 for MeOH and ε_{st} = 25.2 and ε_{op} = 2.33 for PhCN.[49]

This dielectric continuum expression predicts the smaller λ values observed for PhCN and the decrease in λ near the surface, but fails to predict the vanishingly small λ observed in ITO|-(X)$_0$-TPA, when the redox center of the TPA is a mere ~4.6 Å from the surface. Note that these molecular acceptors have negligibly small inner-sphere reorganization energies (λ_i),[50,51] such that the total reorganization energy λ is approximately equal to the outer-sphere reorganization energy λ_o, *i.e.* $\lambda = \lambda_o + \lambda_i \approx \lambda_o$.

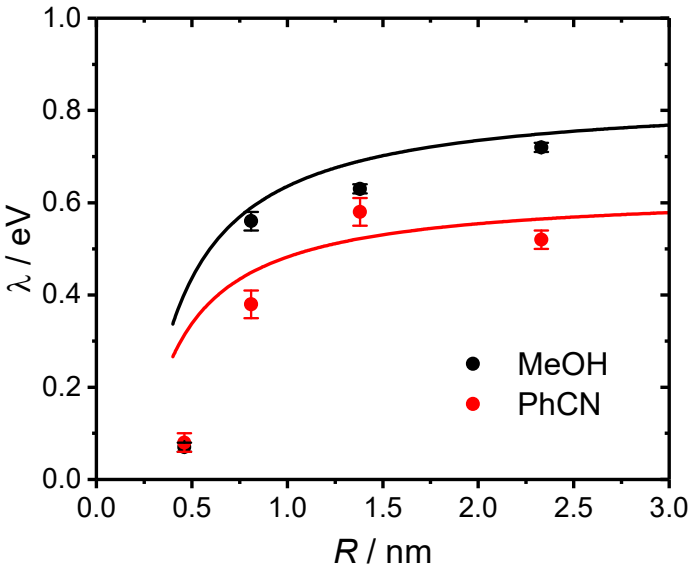

Figure 7.7. Experimentally extracted reorganization energies λ for interfacial electron transfer as a function of distance between the molecule and electrode R in MeOH (black points) and PhCN (red points). Solid lines represent dielectric continuum predictions of λ as a function of R assuming ε_{st} = 32.7 and ε_{op} = 1.76 for MeOH and ε_{st} = 25.2 and ε_{op} = 2.33 for PhCN.

Values of λ near 0 for ITO|-(X)$_0$-TPA in MeOH and PhCN align with recent data obtained in H_2O and MeCN, which also found $\lambda \approx 0.1$ eV.[22,23] That these λ values in MeOH, PhCN, H_2O, and MeCN are within experimental error equal, suggests that inductive effects recently reported by Matyushov,[52] which would predict λ to be significantly larger in bulkier solvents, are not significant here. In these studies, the unexpectedly small λ at the metal oxide/electrolyte interface was attributed to the electric double layer (EDL). Though

descriptions of the EDL have evolved over time, the polarized metal electrode is generally thought to have specifically adsorbed ions and rigidly oriented solvent molecules at the interface.[11,53] This is often called the *inner*-Helmholtz plane. The *outer*-Helmholtz plane, for which a strong electric field is also present, consists of solvated ions. Beyond this, a *diffuse* layer of solvent and solvated ions progressively screens the electric field. Gouy and Chapman's model assumed that the field decays continuously from the metal surface, while Stern separated potential decay in the EDL and the diffuse layer.[54]

Experimental evidence for a loss of the rotational freedom in water molecules within the EDL that drastically reduces ε_{st} has been previously reported,[55–60] although the behavior of non-aqueous interfaces has been less thoroughly explored.[38,61] The dielectric constant in the diffuse layer increased until bulk solvent properties are measured far from the interface. That λ for interfacial electron transfer in ITO|-$(X)_0$-TPA is near zero in H_2O, MeCN, MeOH, and PhCN suggest that within the Helmholtz planes, ε_{st} approaches ε_{op} for each solvent. This manifests in nearly identical electron transfer rate constants for ITO|-$(X)_0$-TPA regardless of solvent (Fig. 7.8). The generality suggests near-activationless interfacial electron transfer to be a general effect within the Helmholtz planes of a conductor-electrolyte interface.

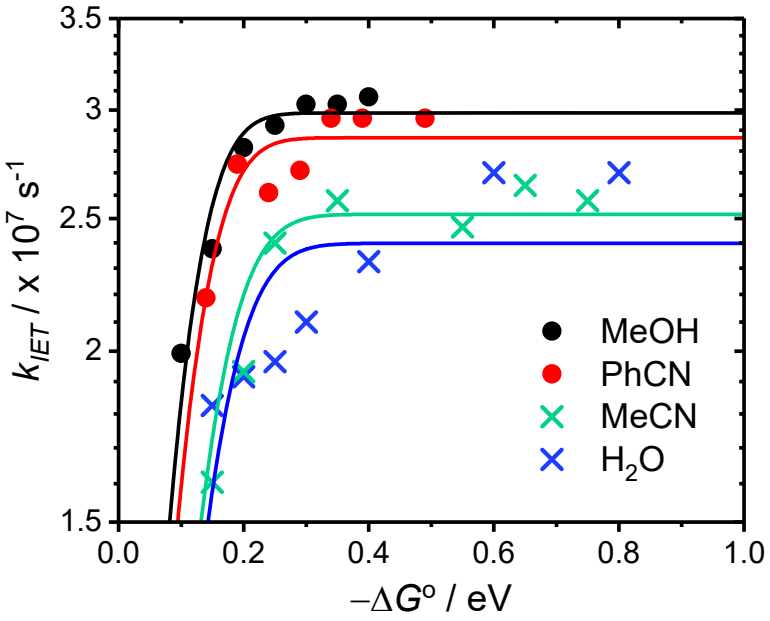

Figure 7.8. Interfacial electron transfer rate constants k_{IET} as a function of $-\Delta G°$ for ITO|-$(X)_0$-TPA in the indicated solvents. Circular points represent data from this work. Blue crosses are taken from ref. [23], and green crosses are taken from ref. [22]. Solid lines represent fits to Eq. 7.8 (see text below) to extract Rips-Jortner kinetic parameters in Table 7.2.

7.4.2 Electronic Coupling

The remarkable solvent insensitivity of the interfacial electron transfer kinetics for ITO|-$(X)_0$-TPA (MeOH, PhCN, H_2O, and MeCN) raises questions about the mechanism of the reaction. As X increases to 1 and 2, a non-adiabatic reaction is reasonably expected over the large distances created by the ionic bridges.[15] However, strong coupling at small distances, *i.e.* for ITO|-$(X)_0$-TPA, might be expected to result in adiabatic electron transfer. While there was no direct spectroscopic evidence for enhanced coupling at short distances in ITO|-$(X)_0$-TPA, researchers have previously identified electron transfer reactions at metal interfaces that depend on the solvent longitudinal relaxation time τ_L, and that have been thus assigned as adiabatic and dynamically controlled.[20,24,27,28] Methanol and PhCN are slowly relaxing solvents with large τ_L, while for H_2O and MeCN solvent motion relaxation occurs ten and twenty times faster, respectively (Table 7.2). As such, if the electron transfer were

dynamically controlled, kinetics should be distinct between the two solvent sets. Further, the slow relaxation of MeOH and PhCN may promote solvent control.[20,30,34,37,39]

Though there are several theoretical treatments to describe the influence of adiabaticity on interfacial electron transfer,[30,32–36,39,62] application of Sumi-Marcus theory as refined by Rips and Jortner is an appealingly straightforward approach, Eq. 7.8.[29,39,63–65]

$$k_A = \frac{k_{IET}}{1+\gamma} \tag{7.8}$$

Here, the non-adiabatic electron transfer rate constant k_{IET} (Eqs. 7.1 and 7.4) is affected by the solvent dynamics through an adiabaticity parameter γ (Eq. 7.9) to yield an adiabaticity-corrected rate constant k_A.

$$\gamma = \frac{4\pi\tau_L H_{ab}^2}{\hbar\lambda} \tag{7.9}$$

When the adiabaticity parameter is small, $\gamma \ll 1$, the reaction is non-adiabatic, and $k_A \propto H_{ab}^2$, as in Eq. 7.5. When $\gamma \gg 1$, however, H_{ab}^2 factors out of the preexponential term, the reaction is adiabatic, and $k_A \propto 1/\tau_L$. For a reaction to be adiabatic in the Rips-Jortner model, a slowly-relaxing solvent environment (large τ_L), high electrode-molecule electronic coupling (large H_{ab}), and/or a small reorganization energy (λ) is required.

To analyze the degree of adiabaticity for interfacial electron transfer in ITO|-(X)$_0$-TPA in each solvent, values of k_{IET} quantified from transient spectral changes as a function of $-\Delta G°$ were modelled with Eq. 7.8 (Fig. 7.8). As in modelling with Eq. 7.4, the range over which the kinetics are sensitive to E_{app} reflects λ, and k_{max} reflects the preexponential factor, now assumed to contain information on both H_{ab} and γ. Values of λ, H_{ab}, and γ quantified using Eq. 7.8-7.9 are given in Table 7.2. Values of τ_L depend on ε_{st} as described in Eq. 7.10, where ε_∞ is the high-frequency dielectric constant and τ_D is the Debye relaxation time.

$$\tau_L = \frac{\varepsilon_\infty}{\varepsilon_{st}}\tau_D \tag{7.10}$$

This means τ_L is likely significantly affected by the EDL. As such, γ values (Table 7.2) were calculated both with the ε_{st} of the bulk solvent and the decreased ε_{st} required to model the experimental λ values in Table 7.1 with Eq. 7.7. These produce a lower and upper limit of γ, respectively. Interestingly, λ and H_{ab} values quantified by Eq. 7.8 were within experimental uncertainty equal to those quantified in the non-adiabatic limit (Eq. 7.4). Values of H_{ab} were all exceptionally small, < 1 cm^{-1}. Though large τ_L values in MeOH and PhCN yielded γ values roughly 5–20x greater than those for H_2O and MeCN, even the upper limit γ values were all $\ll 1$. This indicates the observed electron transfer at these ITO surfaces, even within the Helmholtz planes and in slowly relaxing solvents, is non-adiabatic.

Table 7.2. Solvent Characteristics and Kinetic Parameters Extracted with Rips-Jortner Theory

Solvent	ε_{st}	ε_{op}[20]	τ_L **(ps)**	λ **(eV)**	H_{ab} **(cm^{-1})**	γ **(x 10^{-3})** [21]
MeOH	32.7 [20] (2.2) [22]	1.76	4.39 [23] (66) [24]	0.08	0.7	8.2 (120)
PhCN	25.2 [20] (3.3) [22]	2.33	5.72 [23] (44) [24]	0.09	0.7	8.6 (66)
H_2O	78.5 [20] (2.5) [22]	1.78	0.48 [23] (15) [24]	0.12	0.6	0.4 (14)
MeCN	35.9 [20] (2.5) [22]	1.80	0.20 [23] (3) [24]	0.11	0.6	0.2 (3)

The assignment of a non-adiabatic interfacial electron transfer with this Rips-Jortner analysis is consistent with the observed similarity between the interfacial electron transfer

[20]Values taken from reference 49.

[21] Calculated from Eq. 7.9 using two τ_L values. The first value is calculated using the ε_{st} of the bulk solvent, to generate a lower limit of κ. For values in parentheses, τ_L is calculated using the ε_{st} required to model experimentally determined λ values, as to represent an upper limit of κ.

[22] Values required to model experimental λ values in Table 7.1 with Eq. 7.7.

[23] Calculated with Eq. 7.10 using bulk ε_{st} values from reference 49.

[24] Calculated with Eq. 7.10 using ε_{st} values that best model experimental λ.

rate constants for ITO|-(X)$_0$-TPA in each solvent. No systematic dependence of k_{IET} on solvent τ_L was observed (Fig. 7.19 in the Associated Content section). Further, k_{IET} depended exponentially on distance from the electrode irrespective of solvent (Fig. 7.20 in the Associated Content section), and the absorbance spectra of RuP and TPA were insensitive to the molecules' position in the EDL (Figs. 7.1 and Fig. 7.9 in the Associated Content section). All of these experimental measures point to small H_{ab} and non-adiabatic electron transfer. Very weak coupling results in non-adiabatic electron transfer, even when the EDL lowers ε_{st} values to slow the solvent longitudinal relaxation and virtually eliminate λ—both factors that promote adiabaticity. Why H_{ab} in these functionalized transparent conductive oxide materials is so low is not readily apparent, as electron transfer reactions between molecules and metallic electrodes on similar length scales are generally considered to be adiabatic.[20,24,27,28] It may be that the *s* orbitals which comprise the conduction band states of ITO couple poorly to anchored molecules.[66] It is also possible that surface heterogeneity leads to a subset of electron transfer events that occur non-adiabatically, while others with larger H_{ab} occur adiabatically within the 10 ns instrument response time. While a small fraction of the interfacial electron transfer may occur on shorter time scales, the data reported in this Chapter are fully in line with a non-adiabatic mechanism.

7.5 Conclusions

Interfacial electron transfer was observed as a function of $-\Delta G°$ from a mesoporous ITO electrode to tethered, redox-active molecules positioned at various distances from the conductor-electrolyte interface. Absorbance spectra and formal reduction potentials of the molecules were independent of their physical location. Analysis with semiclassical electron

transfer theory revealed the reorganization energy λ for the electron transfer to be significantly smaller in PhCN than in MeOH when molecules were distant from the interface in the diffuse layer. Values of λ decreased as molecules approached the interface and were vanishingly small, $\lambda \approx 0.1$ eV, at the shortest attainable distances. The near-activationless electron transfer was attributed to the strong electric field in the Helmholtz planes of the electric double layer, which drastically reduced the solvent static dielectric constant. The impact of the electric double layer on the reorganization energy has now been quantified in MeOH, PhCN, H_2O, and MeCN, suggesting that activationless electron transfer in the Helmholtz planes may be generalizable to all polar solvents. Exceptionally low coupling between the ITO and the redox-active molecules resulted in non-adiabatic electron transfer, even at the shortest distances and conditions which would promote adiabaticity, as revealed by Rips-Jortner analysis. This non-adiabaticity manifest in electron transfer rate constants that show no systematic dependence on the solvent τ_L between MeOH, PhCN, H_2O, and MeCN. The data reveal that electron transfer barriers are dramatically diminished within the Helmholtz planes of the conductive oxide-electrolyte electric double layer.

7.6 Acknowledgements

The authors appreciate Dr. Eric Piechota's valuable insight on the subtleties of electron transfer theories. This material is based upon work solely supported by the Alliance for Molecular PhotoElectrode Design for Solar Fuels (AMPED), an Energy Frontier Research Center (EFRC) funded by the U.S. Department of Energy, Office of Science, Office of Basic Energy Sciences under Award Number DE-SC0001011. REB acknowledges

the National Science Foundation for an individual Graduate Research Fellowship under Grant No. DGE-1650116.

7.7 Associated Content

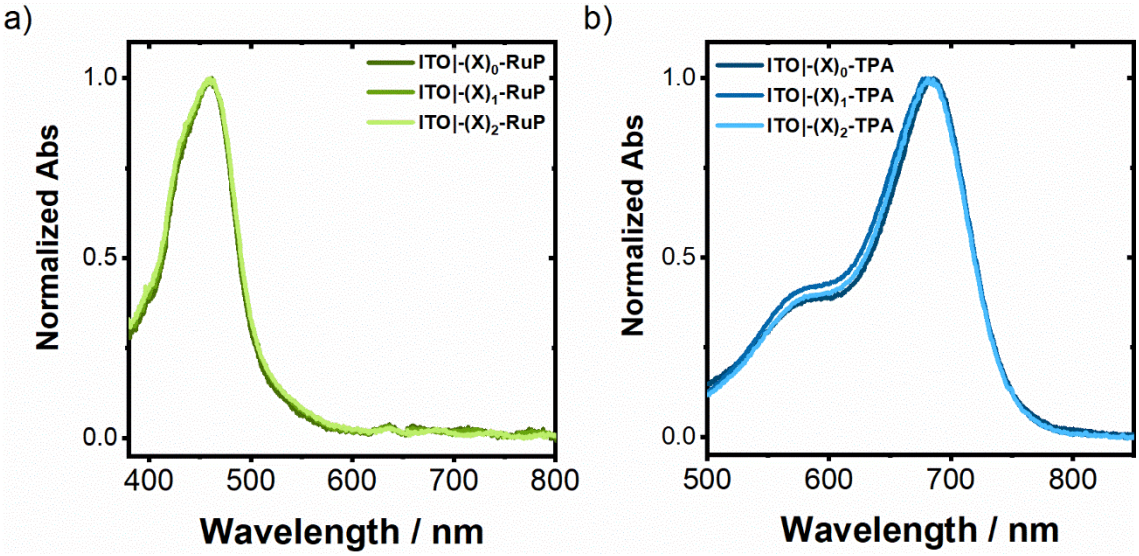

Figure 7.9. Visible absorption spectra of ITO|-(X)$_n$-RuP (a) and oxidized ITO|-(X)$_n$-TPA (b) in PhCN 0.1 M $LiClO_4$.

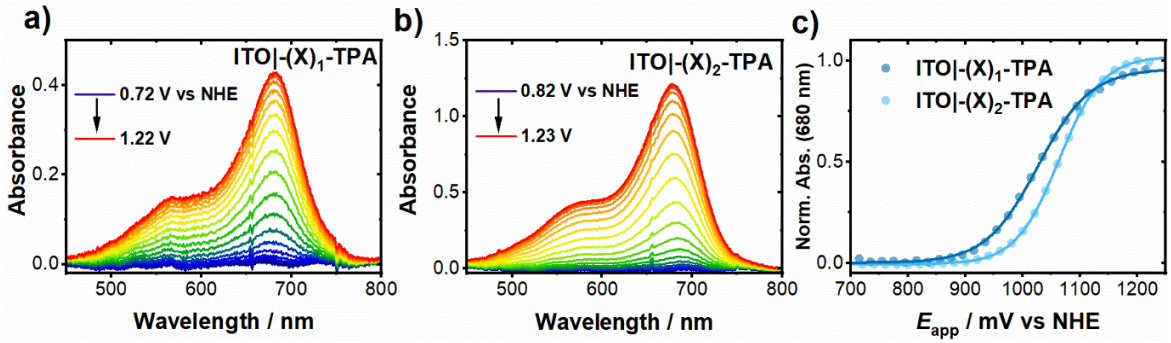

Figure 7.10. Oxidative visible spectroelectrochemistry of ITO|-(X)$_n$-TPA for n = 1, (a), and n = 2, (b), in MeOH 0.1 M $LiClO_4$. c) Normalized absorption changes measured at 680 nm extracted from a) and b) as a function of applied potential for ITO|-(X)$_n$-TPA (n = 1, 2) with an overlaid fit to Eq. 7.5.

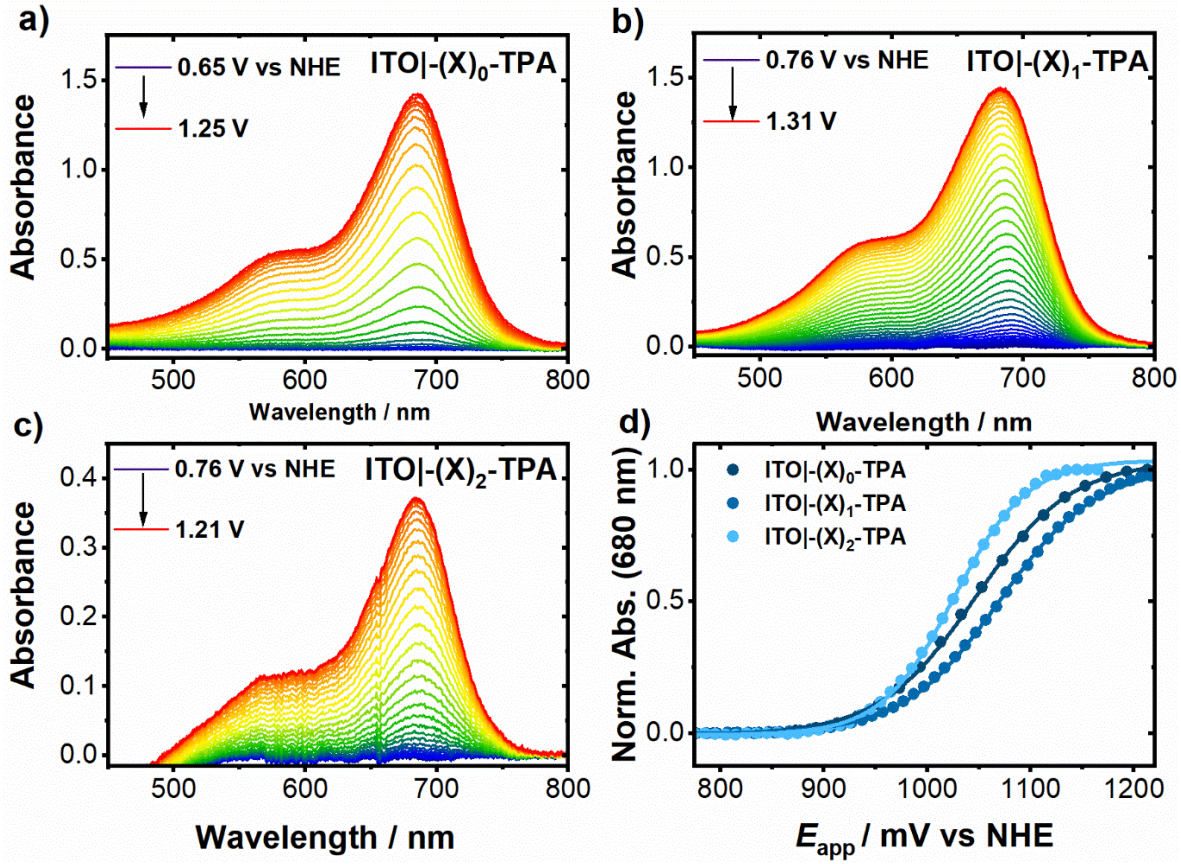

Figure 7.11. Oxidative visible spectroelectrochemistry of ITO|-(X)$_0$-TPA (a), ITO|-(X)$_1$-TPA (b) and ITO|-(X)$_2$-TPA (c) in PhCN 0.1 M $LiClO_4$. d) Normalized absorption change at 680 nm extracted from a), b), and c) as a function of the applied potential for ITO|-(X)$_n$-TPA (n = 0, 1, 2) with an overlaid fit to Eq. 7.5.

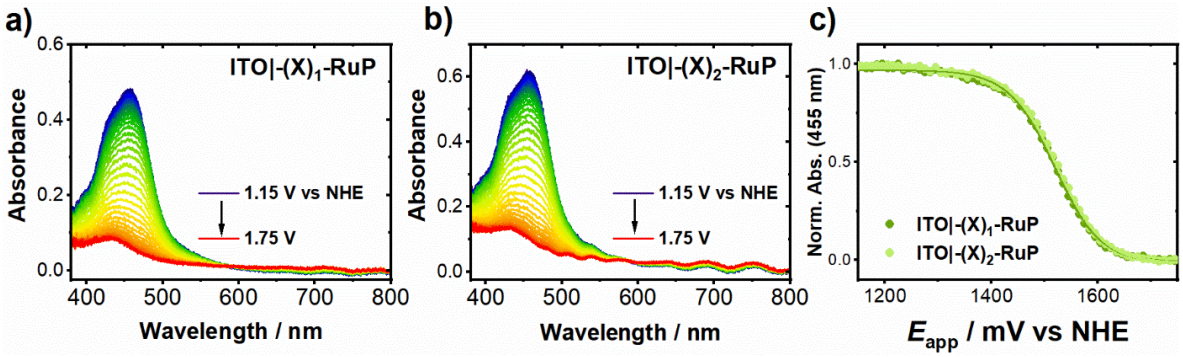

Figure 7.12. Oxidative visible spectroelectrochemistry of ITO|-(X)$_n$-RuP for n = 1, (a), and n = 2, (b), in MeOH 0.1 M $LiClO_4$. c) Normalized absorption change at 455 nm extracted from Figures a) and b) as a function of applied potential for ITO|-(X)$_n$-RuP (n = 1, 2) with an overlaid fit to Eq. 7.5.

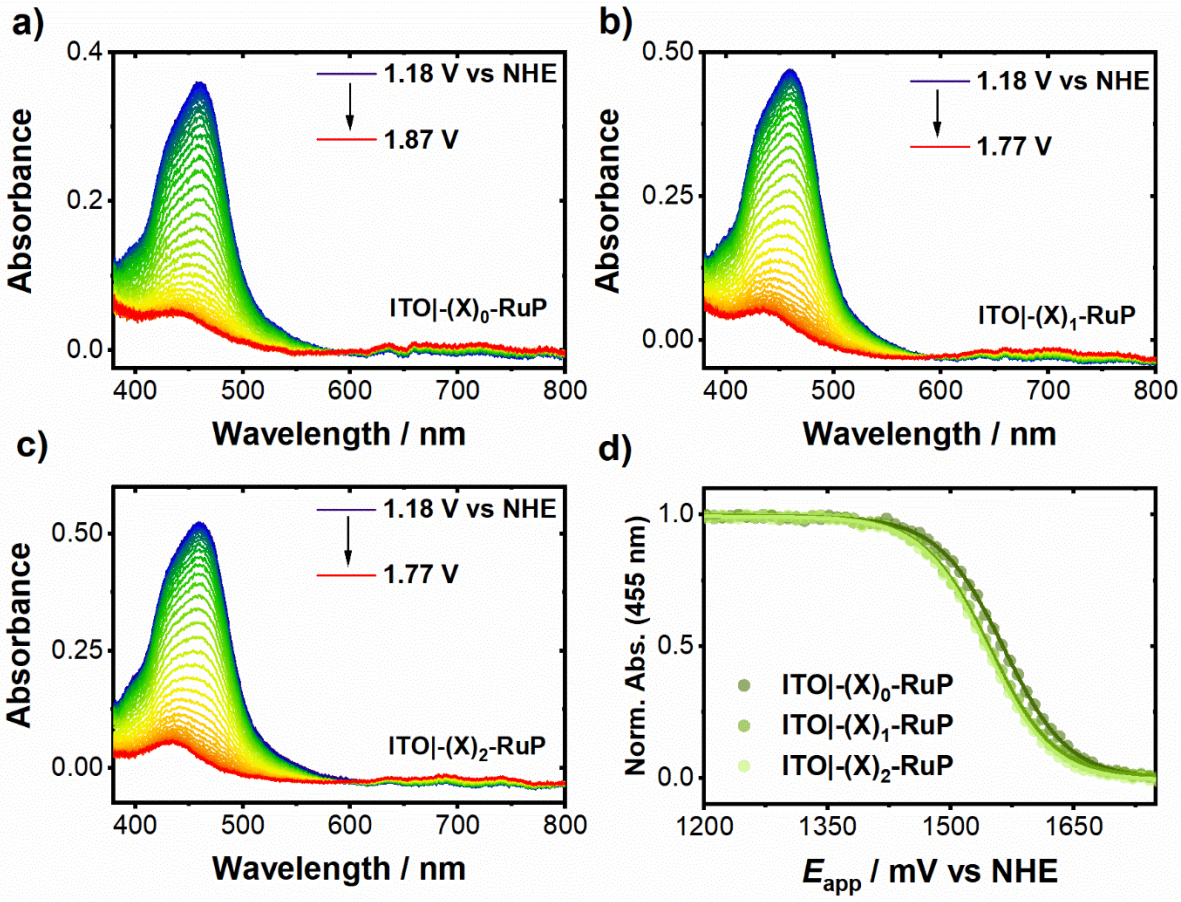

Figure 7.13. Oxidative visible spectroelectrochemistry of ITO|-(X)$_0$-RuP (a), ITO|-(X)$_1$-RuP (b) and ITO|-(X)$_2$-RuP (c) in PhCN 0.1 M $LiClO_4$. d) Absorption changes at 455 nm extracted from Figures a), b), and c) as a function of applied potential for ITO|-(X)$_n$-RuP with an overlaid fit to Eq. 7.5.

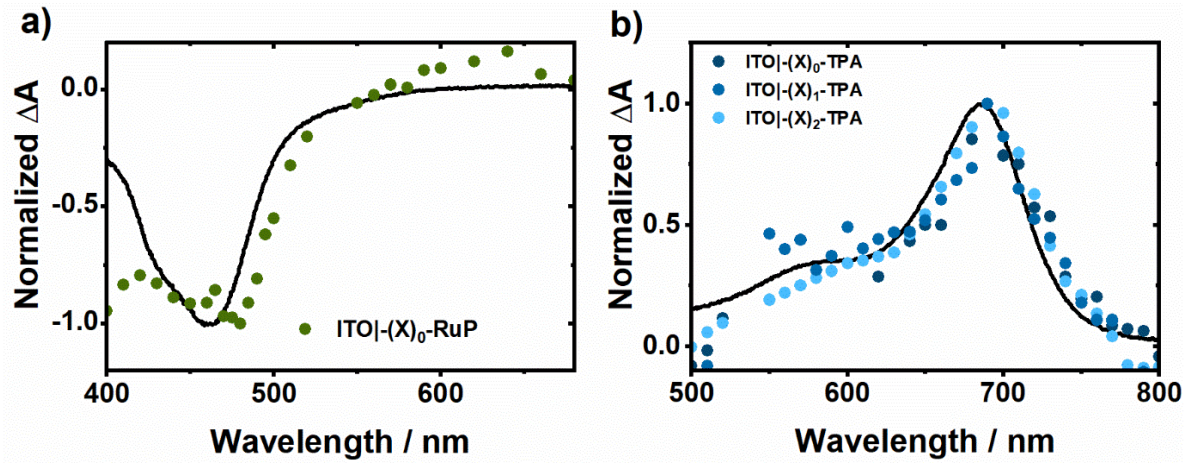

Figure 7.14. Transient absorption spectra measured 50 ns after pulsed 532 nm light excitation (points) for (c) ITO|-(X)$_n$-TPA and (d) ITO|-(X)$_n$-RuP for the indicated value of n in 0.1 M $LiClO_4$ PhCN. The solid lines are simulations based on spectroelectrochemical data.

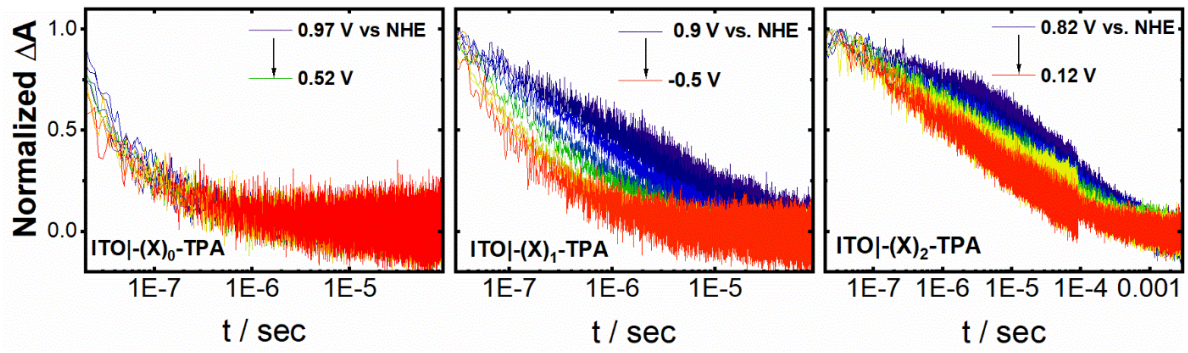

Figure 7.15. The absorption change Δ*A* measured after pulsed 532 nm light excitation monitored at 690 nm for ITO|-(X)$_0$-TPA (left), ITO|-(X)$_1$-TPA (center) and ITO|-(X)$_2$-TPA (right) in 0.1 M $LiClO_4$ PhCN as a function of the applied potential *vs.* NHE.

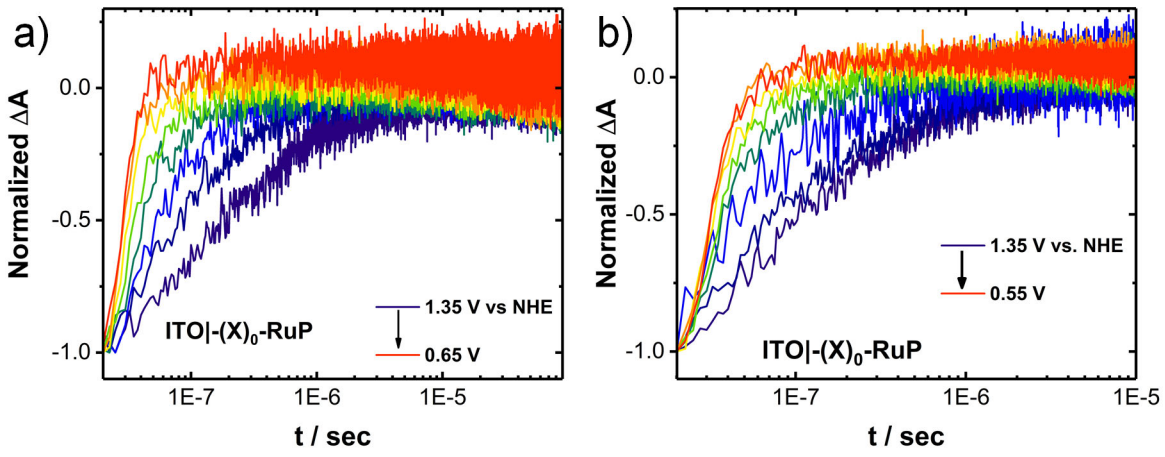

Figure 7.16. The absorption change Δ*A* at 402 nm measured after pulsed 532 nm light excitation of ITO|-(X)$_0$-RuP in 0.1 M $LiClO_4$ MeOH (left) and PhCN (right) as a function of the applied potential *vs.* NHE.

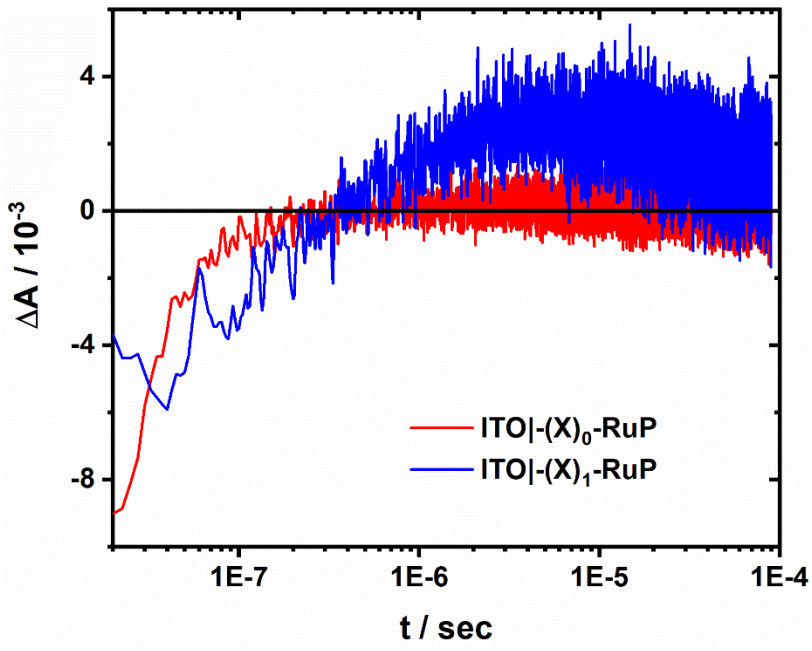

Figure 7.17. The absorption change ΔAbs monitored at 402 nm after pulsed 532 nm light excitation of ITO|-(X)$_0$-RuP (red) and ITO|-(X)$_1$-RuP (blue) 0.1 M $LiClO_4$ MeOH measured at the negative applied potential required to reach k_{max}, -0.6 V vs NHE for ITO|-(X)$_0$-RuP and 0 V vs NHE for ITO|-(X)$_1$-RuP. The positive ΔAbs feature present for ITO|-(X)$_1$-RuP is consistent with excited state reduction of RuP that prevented accurate determination of k_{IET}. The positive feature is absent for ITO|-(X)$_0$-RuP.

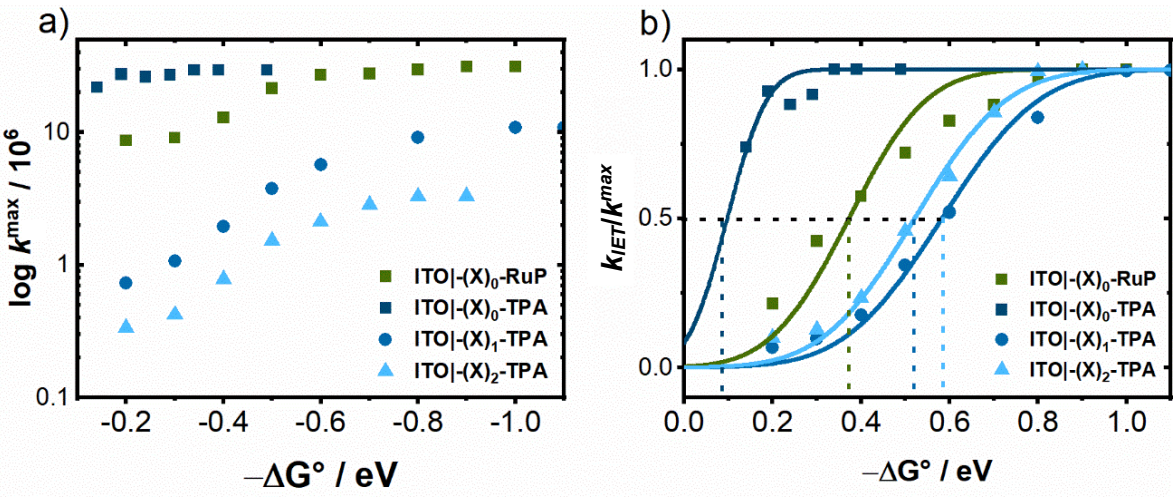

Figure 7.18. Logarithmic plots of k_{IET} vs E_{app} vs NHE for ITO|-(X)$_0$-RuP and ITO|-(X)$_n$-TPA (n = 0, 1, 2) (a), and their corresponding plots of k_{et}/k_{max} vs -ΔG° (b) with overlaid fits to Eq. 7.4. All data were acquired in PhCN 0.1 M $LiClO_4$.

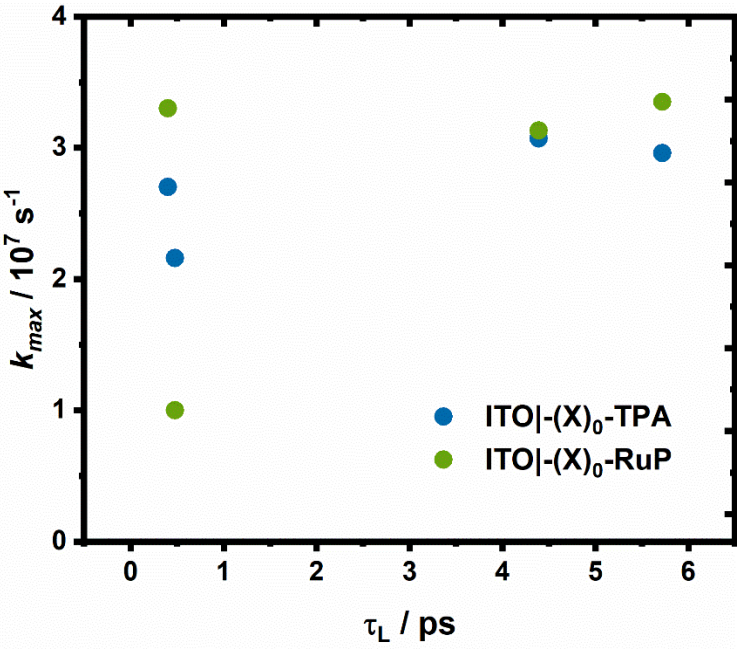

Figure 7.19. Plot of the experimentally extracted k_{max} values vs τ_L for MeCN (0.20 ps), H_2O (0.48 ps), PhCN (5.72 ps) and MeOH (4.39 ps) for ITO|-(X)$_0$-TPA and ITO|-(X)$_0$-RuP.

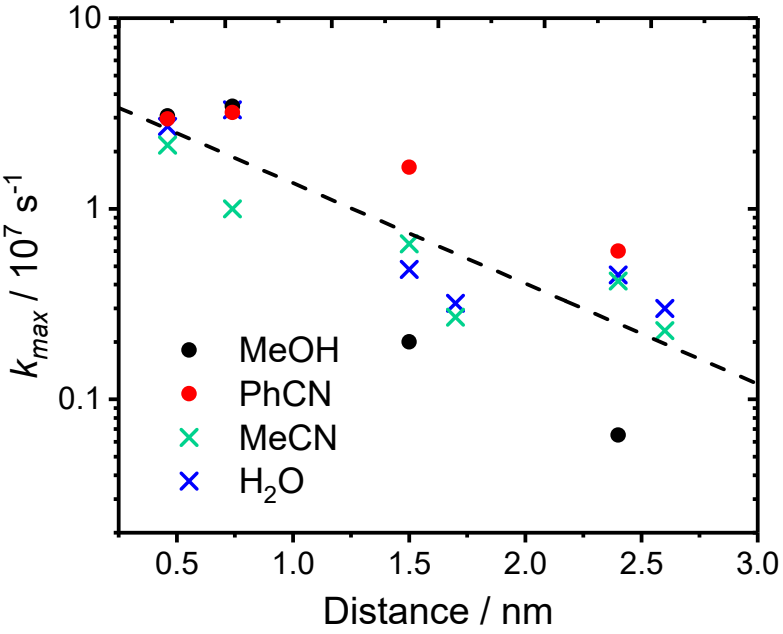

Figure 7.20. A logarithmic plot of k_{max} *vs* distance in the indicated solvents.

REFERENCES

(1) Marcus, R. A. On the Theory of Oxidation-Reduction Reactions Involving Electron Transfer. I. *J. Chem. Phys.* **1956**, *24* (5), 966–978.

(2) Marcus, R. A. Theory of Electron-Transfer Reaction Rates of Solvated Electrons. *J. Chem. Phys.* **1965**, *43* (10), 3477–3489.

(3) Schmickler, W.; Santos, E. *Interfacial Electrochemistry*, 2nd ed.; Springer: Berlin, 2010.

(4) Gerischer, H. Electrochemical Techniques for the Study of Photosensitization. *Photochem. Photobiol.* **1972**, *16* (4), 243–260.

(5) Hush, N. S. Homogeneous and Heterogeneous Optical and Thermal Electron Transfer. *Electrochim. Acta* **1968**, *13*, 1005–1023.

(6) Liu, Y. P.; Newton, M. D. Reorganization Energy for Electron Transfer at Film-Modified Electrode Surfaces: A Dielectric Continuum Model. *J. Phys. Chem.* **1994**, *98* (29), 7162–7169.

(7) Hush, N. S. Adiabatic Rate Processes at Electrodes. I. Energy-Charge Relationships. *J. Chem. Phys.* **1958**, *28* (5), 962–972.

(8) Hush, N. S. Electron Transfer in Retrospect and Prospect 1: Adiabatic Electrode Processes. *J. Electroanal. Chem.* **1999**, *460* (1–2), 5–29.

(9) Henstridge, M. C.; Laborda, E.; Rees, N. V.; Compton, R. G. Marcus-Hush-Chidsey Theory of Electron Transfer Applied to Voltammetry: A Review. *Electrochim. Acta* **2012**, *84*, 12–20.

(10) Levich, V. G. Present State of the Theory of Oxidation-Reduction in Solution (Bulk and Electrode Reactions). In *Advances in Electrochemistry and Electrochemical Engineering*; Delahay, P., Ed.; Interscience Publishers: New York, 1966; pp 249–371.

(11) Bard, A. J.; Faulkner, L. R. *Electochemical Method: Fundamentals and Applications*, 2nd ed.; Harris, D., Swain, E., Robey, C., Aiello, E., Eds.; Wiley, 2000.

(12) Farnum, B. H.; Morseth, Z. A.; Brennaman, M. K.; Papanikolas, J. M.; Meyer, T. J. Application of Degenerately Doped Metal Oxides in the Study of Photoinduced Interfacial Electron Transfer. *J. Phys. Chem. B* **2015**, *119*, 7698–7711.

(13) Closs, G. L.; Miller, J. R. Intramolecular Long-Distance Electron Transfer in Organic Molecules. *Science.* **1988**, *240* (4851), 440–447.

(14) Yonemoto, E. H.; Riley, R. L.; Kim, Y. Il; Atherton, S. J.; Schmehl, R. H.; Mallouk,

T. E. Photoinduced Electron Transfer in Covalently Linked Ruthenium Tris(Bipyridyl)-Viologen Molecules: Observation of Back Electron Transfer in the Marcus Inverted Region. *J. Am. Chem. Soc.* **1992**, *114* (21), 8081–8087.

(15) Chidsey, C. E. Free Energy and Temperature Dependence of Electron Transfer at the Metal-Electrolyte Interface. *Science.* **1991**, *251* (4996), 919–922.

(16) Smalley, J. F.; Feldberg, S. W.; Chidsey, C. E. D.; Linford, M. R.; Newton, M. D.; Liu, Y.-P. The Kinetics of Electron Transfer through Ferrocene-Terminated Alkanethiol Monolayers on Gold. *J. Phys. Chem.* **1995**, *99*, 13141–13149.

(17) Smalley, J. F.; Finklea, H. O.; Chidsey, C. E. D.; Linford, M. R.; Creager, S. E.; Ferraris, J. P.; Chalfant, K.; Zawodzinsk, T.; Feldberg, S. W.; Newton, M. D. Heterogeneous Electron-Transfer Kinetics for Ruthenium and Ferrocene Redox Moieties through Alkanethiol Monolayers on Gold. *J. Am. Chem. Soc.* **2003**, *125* (7), 2004–2013.

(18) Finklea, H. O.; Hanshew, D. D. Electron-Transfer Kinetics in Organized Thiol Monolayers with Attached Pentaammine(Pyridine)Ruthenium Redox Centers. *J. Am. Chem. Soc.* **1992**, *114* (9), 3173–3181.

(19) Creager, S.; Yu, C. J.; Bamdad, C.; O'Connor, S.; MacLean, T.; Lam, E.; Chong, Y.; Olsen, G. T.; Luo, J.; Gozin, M.; Kayyem, J. F. Electron Transfer at Electrodes through Conjugated "Molecular Wire" Bridges. *J. Am. Chem. Soc.* **1999**, *121* (5), 1059–1064.

(20) Khoshtariya, D. E.; Dolidze, T. D.; Zusman, L. D.; Waldeck, D. H. Observation of the Turnover between the Solvent Friction (Overdamped) and Tunneling (Nonadiabatic) Charge-Transfer Mechanisms for a Au/$Fe(CN)_6^{3-/4-}$ Electrode Process and Evidence for a Freezing out of the Marcus Barrier. *J. Phys. Chem. A* **2001**, *105* (10), 1818–1829.

(21) Schneider, J.; Bangle, R. E.; Swords, W. B.; Troian-Gautier, L.; Meyer, G. J. Determination of Proton-Coupled Electron Transfer Reorganization Energies with Application to Water Oxidation Catalysts. *J. Am. Chem. Soc.* **2019**, *141* (25), 9758–9763.

(22) Bangle, R. E.; Schneider, J.; Piechota, E. J.; Troian-Gautier, L.; Meyer, G. J. Electron Transfer Reorganization Energies in the Electrode-Electrolyte Double Layer. *J. Am. Chem. Soc.* **2020**, *142* (2), 674–679.

(23) Bangle, R. E.; Schneider, J.; Aramburu-Trošelj, B. M.; Conroy, D. T.; Meyer, G. J. Kinetic Evidence That the Solvent Barrier for Electron Transfer Is Absent in the Electric Double Layer. *J. Am. Chem. Soc.* **2020**, *142* (35), 14940–14946.

(24) Pyati, R.; Murray, R. W. Solvent Dynamics Effects on Heterogeneous Electron Transfer Rate Constants of Cobalt Tris(Bipyridine). *J. Am. Chem. Soc.* **1996**, *118* (7), 1743–1749.

(25) Eggers, P. K.; Darwish, N.; Paddon-Row, M. N.; Gooding, J. J. Surface-Bound

Molecular Rulers for Probing the Electrical Double Layer. *J. Am. Chem. Society* **2012**, *134*, 7539–7544.

(26) Sumner, J. J.; Creager, S. E. Redox Kinetics in Monolayers on Electrodes: Electron Transfer Is Sluggish for Ferrocene Groups Buried within the Monolayer Interior. *J. Phys. Chem. B* **2001**, *105*, 8739–8745.

(27) Winkler, K.; McKnight, N.; Fawcett, W. R. Electron Transfer Kinetics of Tris(1,10-Phenanthroline)Ruthenium(II) Electrooxidation in Aprotic Solvents. *J. Phys. Chem. B* **2000**, *104* (15), 3575–3580.

(28) Fawcett, W. R.; Opallo, M. The Kinetics of Heterogeneous Electron Transfer Reaction in Polar Solvents. *Angew. Chemie Int. Ed.* **1994**, *33* (21), 2131–2143.

(29) Sumi, H.; Marcus, R. A. Dynamical Effects in Electron Transfer Reactions. *J. Chem. Phys.* **1986**, *84* (9), 4894–4914.

(30) Smith, B. B.; Hynes, J. T. Electronic Friction and Electron Transfer Rates at Metallic Electrodes. *J. Chem. Phys.* **1993**, *99* (9), 6517–6530.

(31) Weaver, M. J. Dynamical Solvent Effects on Activated Electron-Transfer Reactions: Principles, Pitfalls, and Progress. *Chem. Rev* **1992**, *92*, 480.

(32) Schmickler, W. A Theory of Adiabatic Electron-Transfer Reactions. *J. Electroanal. Chem.* **1986**, *204*, 31–43.

(33) Dogonadze, R. R.; Kuzntesov, A. M.; Vorotentsev, M. A. The Kinetics of Adiabatic and Nonadiabatic Reactions at the Metal and Semiconductor Electrodes. *Croat. Chem. Acta* **1972**, *44*, 257–273.

(34) Zusman, L. D. Outer-Sphere Electron Transfer Reactions at an Electrode. *Chem. Phys.* **1987**, *112* (1), 53–59.

(35) Kuznetsov, A. M. A Unified Model of the Adiabatic Reactions of Electron Transfer at Metal Electrodes. *J. Electroanal. Chem.* **1988**, *241*, 45–56.

(36) Feldberg, S. W.; Sutin, N. Distance Dependence of Heterogeneous Electron Transfer through the Nonadiabatic and Adiabatic Regimes. *Chem. Phys.* **2006**, *324*, 216–225.

(37) Ghosh, S.; Soudackov, A. V; Hammes-Schiffer, S. Electrochemical Electron Transfer and Proton-Coupled Electron Transfer: Effects of Double Layer and Ionic Environment on Solvent Reorganization Energies. *J. Chem. Theory Comput.* **2016**, *12*, 2917–2925.

(38) Gorodyskii, A. V.; Karasevskii, A. I.; Matyushov, D. V. Adiabatic Outer Sphere Electron Transfer through the Metal-Electrolyte Interface. *J. Electroanal. Chem.* **1991**, *315* (1–2), 9–28.

(39) Matyushov, D. V. Solvent Reorganization Energy of Electron-Transfer Reactions in Polar Solvents. *J. Chem. Phys.* **2004**, *120* (16), 7532–7556.

(40) Wang, J. C.; Hill, S. P.; Dilbeck, T.; Ogunsolu, O. O.; Banerjee, T.; Hanson, K. Multimolecular Assemblies on High Surface Area Metal Oxides and Their Role in Interfacial Energy and Electron Transfer. *Chem. Soc. Rev.* **2018**, *47*, 104–148.

(41) Troian-Gautier, L.; DiMarco, B. N.; Sampaio, R. N.; Marquard, S. L.; Meyer, G. J. Evidence That $\Delta S^{\ddagger}$ Controls Interfacial Electron Transfer Dynamics from Anatase TiO_2 to Molecular Acceptors. *J. Am. Chem. Soc.* **2018**, *140* (8), 3019–3029.

(42) Sampaio, R. N.; Troian-Gautier, L.; Meyer, G. J. A Charge-Separated State That Lives for Almost a Second at a Conductive Metal Oxide Interface. *Angew. Chemie* **2018**, *130* (47), 15616–15620.

(43) Hu, K.; Meyer, G. J. Lateral Intermolecular Self-Exchange Reactions for Hole and Energy Transport on Mesoporous Metal Oxide Thin Films. *Langmuir* **2015**, *31* (41), 11164–11178.

(44) Argazzi, R.; Bignozzi, C. A.; Heimer, T. A.; Castellano, F. N.; Meyer, G. J. Enhanced Spectral Sensitivity from Ruthenium(II) Polypyridyl Based Photovoltaic Devices. *Inorg. Chem.* **1994**, *33*, 5741–5749.

(45) Piechota, E. J.; Troian-Gautier, L.; Sampaio, R. N.; Brennaman, M. K.; Hu, K.; Berlinguette, C. P.; Meyer, G. J. Optical Intramolecular Electron Transfer in Opposite Directions through the Same Bridge That Follows Different Pathways. *J. Am. Chem. Soc.* **2018**, *140* (23), 7176–7186.

(46) Bangle, R. E.; Meyer, G. J. Factors That Control the Direction of Excited-State Electron Transfer at Dye-Sensitized Oxide Interfaces. *J. Phys. Chem. C* **2019**, *123* (42), 25967–25976.

(47) Vaissier, V.; Barnes, P.; Kirkpatrick, J.; Nelson, J. Influence of Polar Medium on the Reorganization Energy of Charge Transfer between Dyes in a Dye Sensitized Film. *Phys. Chem. Chem. Phys.* **2013**, *15* (13), 4804–4814.

(48) Marcus, R. A. On the Theory of Electron-Transfer Reactions. VI. Unified Treatment for Homogeneous and Electrode Reactions. *J. Chem. Phys.* **1965**, *43* (2), 679–701.

(49) Fawcett, R. W. *Liquids, Solutions, and Interfaces: From Classical Macroscopic Descriptions to Modern Microscopic Details*, 1st ed.; Oxford University Press: New York, 2004.

(50) Lambert, C.; Nöll, G. The Class II/III Transition in Triarylamine Redox Systems. *J. Am. Chem. Soc.* **1999**, *121* (37), 8434–8442.

(51) Biner, M.; Bürgi, H. B.; Ludi, A.; Röhr, C. Crystal and Molecular Structures of $[Ru(Bpy)_3](PF_6)_3$ and $[Ru(Bpy)_3](PF_6)_2$ at 105 K. *J. Am. Chem. Soc.* **1992**, *114* (13), 5197–5203.

(52) Matyushov, D. V. Electron Transfer in Nonpolar Media. *Phys. Chem. Chem. Phys.* **2020**, *22* (19), 10653–10665.

(53) Bockris, J. O.; Devanathan, M. A. V; Müller, K. On the Structure of Charged Interfaces. *Proc. R. Soc. London. Ser. A. Math. Phys. Sci.* **1963**, *274* (1356), 55–79.

(54) Stern, O. Zur Theorie Der Elektrolytischen Doppelschicht. *Zeitschrift für Elektrochemie* **1932**, *30* (21–22), 508–516.

(55) Grahame, D. C. The Electrical Double Layer and the Theory of Electrocapillarity. *Chem. Rev.* **1947**, *41* (3), 441–501.

(56) Mott, N. F.; Watts-Tobin, R. J. The Interface between a Metal and an Electrolyte. *Electrochim. Acta* **1961**, *79*, 79–107.

(57) Fawcett, W. R.; Levine, S.; deNobriga, R. M.; McDonald, A. C. A Molecular Model for the Dielectric Properties of the Inner Layer at the Mercury/Aqueous Solution Interface. *J. Electroanal. Chem.* **1980**, *111* (2–3), 163–180.

(58) Fumagalli, L.; Esfandiar, A.; Fabregas, R.; Hu, S.; Ares, P.; Janardanan, A.; Yang, Q.; Radha, B.; Taniguchi, T.; Watanabe, K.; Gomila, G.; Novoselov, K. S.; Geim, A. K. Anomalously Low Dielectric Constant of Confined Water. *Science.* **2018**, *360*, 1339–1342.

(59) Velasco-Velez, J. J.; Wu, C. H.; Pascal, T. A.; Wan, L. F.; Guo, J.; Prendergast, D.; Salmeron, M. The Structure of Interfacial Water on Gold Electrodes Studied by X-Ray Absorption Spectroscopy. *Science.* **2014**, *346* (6211), 831–834.

(60) Toney, M. F.; Howard, J. N.; Richer, J.; Borges, G. L.; Gordon, J. G.; Melroy, O. R.; Wiesler, D. G.; Yee, D.; Sorensen, L. B. Voltage-Dependent Ordering of Water Molecules at an Electrode-Electrolyte Interface. *Nature* **1994**, *368* (6470), 444–446.

(61) Hou, Y.; Aoki, K. J.; Chen, J.; Nishiumi, T. Solvent Variables Controlling Electric Double Layer Capacitance at the Metal-Solution Interface. *J. Phys. Chem. C* **2014**, *118* (19), 10153–10158.

(62) Morgan, J. D.; Wolynes, P. G. Adiabaticity of Electron Transfer at an Electrode. *J. Phys. Chem.* **1987**, *91* (4), 874–883.

(63) Matyushov, D. V. Dynamical Effects in Protein Electrochemistry. *J. Phys. Chem. B* **2019**, *123* (34), 7290–7301.

(64) Rips, I.; Jortner, J. Dynamic Solvent Effects on Outer-Sphere Electron Transfer. *J.*

Chem. Phys. **1987**, *87* (4), 2090–2104.

(65) Jortner, J.; Bixon, M. Intramolecular Vibrational Excitations Accompanying Solvent-Controlled Electron Transfer Reactions. *J. Chem. Phys.* **1988**, *88* (1), 167–170.

(66) Klein, A. Transparent Conducting Oxides: Electronic Structure-Property Relationship from Photoelectron Spectroscopy with in Situ Sample Preparation. *J. Am. Ceram. Soc.* **2012**, *96* (2), 331–345.